b
UNIVERSITÄT
BERN

Development of a Laser Ionisation Mass Spectrometer for In-Situ Investigations on the Lunar Surface

Inaugural dissertation
of the Faculty of Science,
University of Bern

presented by

Peter Keresztes Schmidt

Supervisor of the doctoral thesis:
Prof. Dr. Peter Wurz

Space Research and Planetary Sciences (WP)
Physics Insitute, University of Bern

Development of a Laser Ionisation Mass Spectrometer for In-Situ Investigations on the Lunar Surface

Inaugural dissertation
of the Faculty of Science,
University of Bern

presented by

Peter Keresztes Schmidt

Supervisor of the doctoral thesis:
Prof. Dr. Peter Wurz

Space Research and Planetary Sciences (WP)
Physics Insitute, University of Bern

Accepted by the Faculty of Science.

Bern, 2nd May 2025

The Dean
Prof. Dr. Jean-Louis Reymond

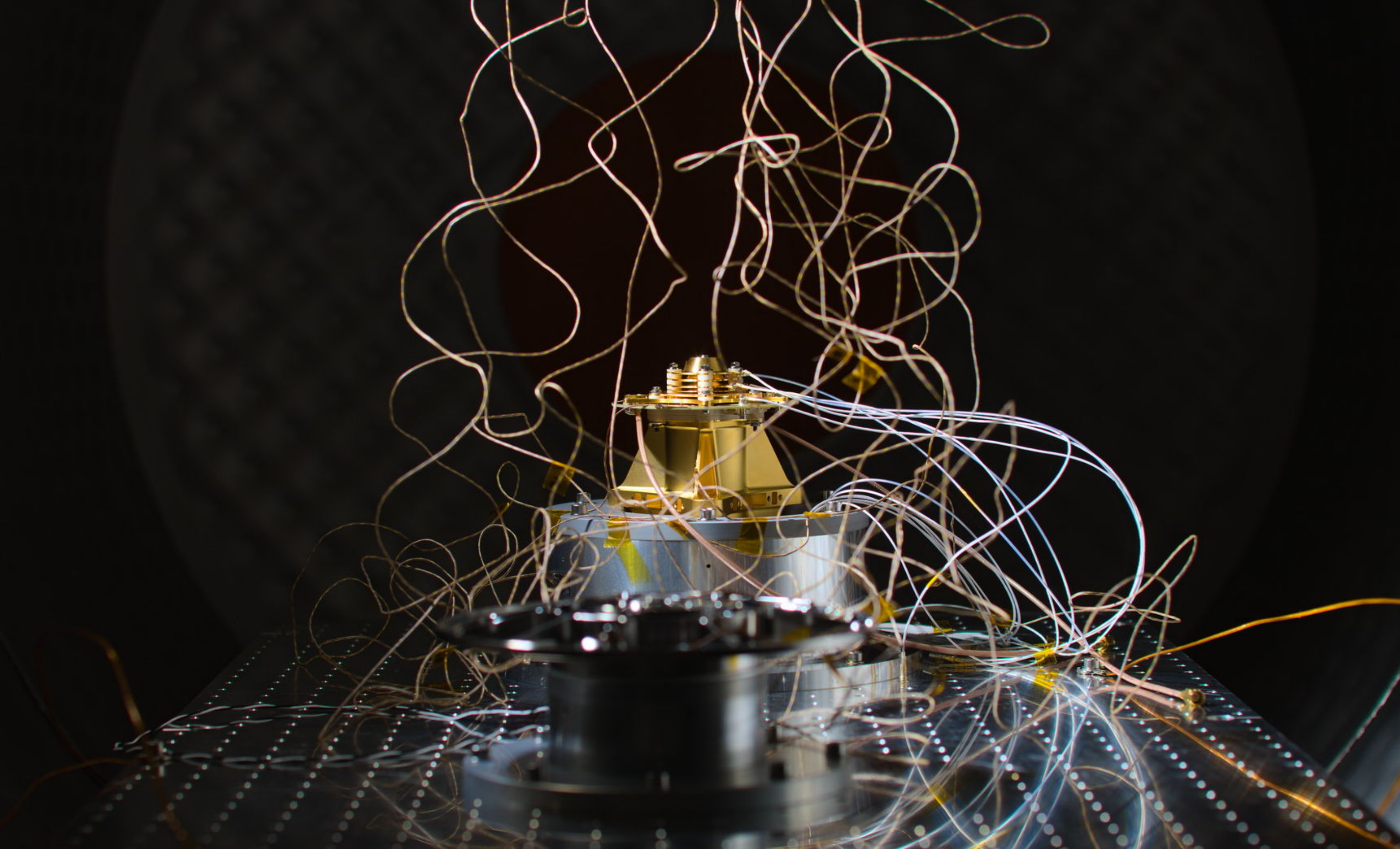

The CLPS-LIMS instrument's Engineering Qualification Model (EQM) Mass Analyser and Sample Handling Carousel during thermal vacuum testing in the beginning of 2025.

Abstract

In recent years, there has been a growing interest in the in-situ exploration of the Moon, particularly in the lunar south pole region, which is into planetary formation and in-situ resource utilisation. As part of these efforts, the University of Bern has been invited by NASA to develop and provide a scientific instrument for the sensitive chemical analysis of lunar regolith.

This thesis describes the development of the CLPS-LIMS instrument, a Laser Ionisation Time-of-Flight Mass Spectrometer designed for deployment on the lunar surface through NASA's Commercial Lunar Payload Services (CLPS) programme. The instrument aims to perform high-sensitivity element and isotope analysis of lunar regolith, aiding in the understanding of its composition and evolution.

A key aspect of this thesis has been the prototype development to validate the measurement technique that will be implemented in the flight instrument. This involved the selection and testing of the laser source, a critical component for laser ablation ionisation and the initial design of the laser optical system, integrating the laser source with the laboratory mass analyser. Preliminary tests using lunar regolith simulant materials were performed which revealed challenges in sample handling and required modifications to the mass analyser to ensure compatibility with lunar regolith analysis.

Beyond prototype development, significant contributions were made to the design of the flight version of CLPS-LIMS. These include studies defining the requirements for the instrument's sample handling system, ensuring it can prepare and deliver lunar regolith samples effectively for LIMS analysis. The compatibility between the sample handling system and the LIMS analysis process has been validated, confirming that regolith samples can be successfully analysed under the expected mission conditions.

Additionally, work was carried out on the commissioning of the CLPS-LIMS engineering model, focusing on the development of ground support equipment (both hardware and software) to facilitate the integration and testing of engineering-quality subsystems into a fully functional instrument. Finally, during an end-to-end test of the engineering model, measurements on two prospective reference materials selected for flight were successfully performed. These tests demonstrated the overall functionality of the instrument, providing confidence in its readiness for future lunar deployment.

Through the presented efforts, the CLPS-LIMS instrument has undergone extensive development and validation, ensuring its capability to deliver high-quality in-situ chemical analyses of the lunar surface, supporting upcoming lunar exploration missions.

Contents

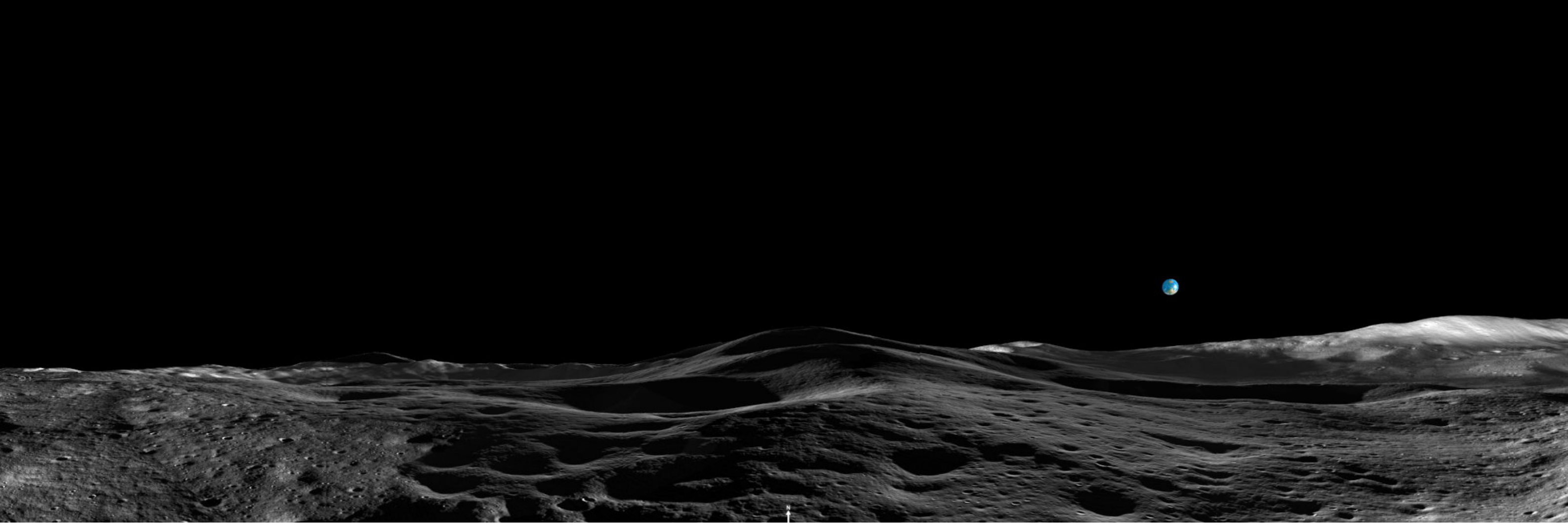

Panorama of the lunar surface at the designated landing site of the CLPS-LIMS instrument near Haworth crater in the Moon's south pole region. The picture was assembled from images taken by the narrow- and wide-angle cameras on board the Lunar Reconnaissance Orbiter.

1 Introduction

1.1 The Moon

The Moon, Earth's only natural satellite, is a geologically diverse celestial body shaped by billions of years of meteoroid impacts, volcanic activity, and space weathering (Heiken et al. 1991). Its surface is covered by a layer of loose, fragmented material known as lunar regolith, which plays a crucial role in scientific exploration and future lunar missions. Additionally, the Moon's extreme physical environment, including temperature fluctuations, ionising radiation, and electrostatic charging, presents unique challenges for robotic and human operations.

1.1.1 Lunar Regolith

Lunar regolith was formed over billions of years through continuous meteoroid impacts, solar wind exposure, and space weathering processes. Since the Moon lacks an atmosphere, meteoroid impacts on the surface occur at high velocities, shattering rocks into fine particles and producing impact melt. This continuous bombardment results in a layer of loose, fragmented material covering the solid bedrock, typically several meters thick in older regions of the Moon (Li et al. 2024; Shkuratov 2001).

Table 1.1: Average regional lunar surface oxide chemistry based on returned samples from the Apollo programme. Concentrations are in wt%. Adapted from Slabic et al. 2024

Region	SiO_2	TiO_2	Al_2O_3	FeO	MgO	CaO	Na_2O	K_2O
Highlands	45.62	0.84	24.47	6.6	6.98	14.65	0.48	0.2
High-Ti Mare	41.27	7.48	12.5	16.47	9.75	11.26	0.39	0.11
Low-Ti Mare	45.62	2.09	13.2	16.45	10.19	10.65	0.42	0.19

Space weathering further alters the regolith's properties by exposing surface grains to solar wind ions and micrometeorite impacts. These processes create a unique component called agglutinates, which are glassy, partially melted regolith particles.

Lunar regolith composition varies across different regions as can be seen from the chemical composition shown in Table 1.1. The Moon's surface is broadly divided into two main terrains:

Lunar Highlands

Dominated by anorthosite, rich in calcium-rich feldspar (plagioclase), and containing lower concentrations of iron and titanium.

Lunar Maria

Basaltic in nature, with higher iron (Fe) and titanium (Ti) content.

The primary chemical constituents of lunar regolith include:

- Oxygen (O) — 40 wt% to 45 wt% (bound in oxides)
- Silicon (Si), Aluminium (Al), Magnesium (Mg), Calcium (Ca), and Iron (Fe) oxides
- Titanium (Ti) oxides (especially in mare basalts)
- Minor constituents such as sodium (Na), and potassium (K)

Unlike terrestrial soils, lunar regolith lacks water-bearing minerals, organic material, and oxidation-driven alterations due to the absence of an atmosphere and liquid water (Heiken et al. 1991).

Due to its formation mechanism lunar regolith exhibits a broad grain size distribution as shown in Figure 1.1. Coarse fragments (>1 mm) include rock fragments and larger breccias. The regolith's median grain size ranges from 40 µm to 130 µm, with an average of 70 µm. Roughly 10 % to 20 % is finer than 20 µm. A thin layer of dust consisting of submicron particles, created by impact processes and space weathering, contributing to the regolith's adhesive nature.

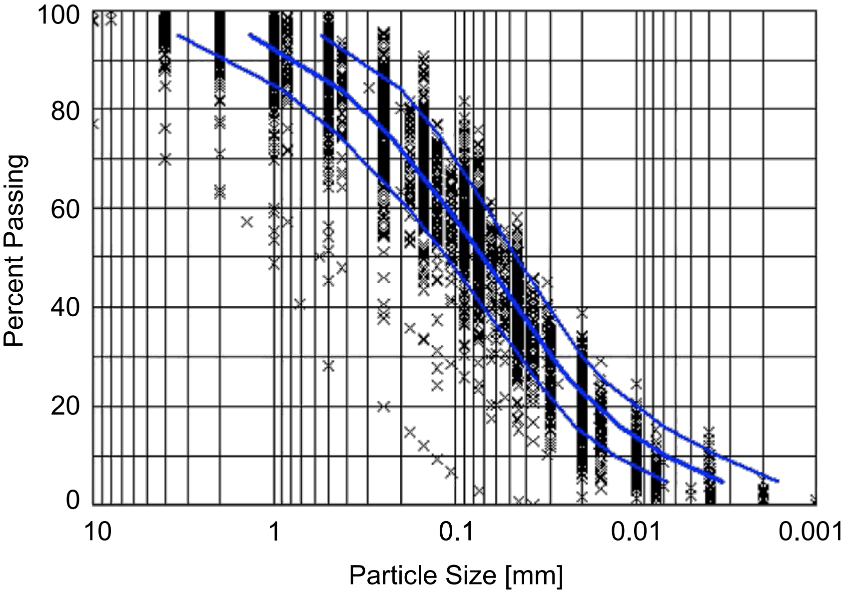

Figure 1.1: Particle size distribution of lunar regolith. The middle blue curve shows the average distribution, the outer curves show ±1σ. Adapted from Carrier 2003.

This fine, and when illuminated by sunlight, electrostatically charged dust poses a significant challenge for exploration, as it sticks to surfaces and can cause mechanical wear on equipment and spacesuits.

1.1.2 The Lunar Surface Environment

The absence of a substantial atmosphere leads to extreme temperature variations on the lunar surface. Temperature changes are driven by the long lunar day (~29.5 Earth days), with two weeks of continuous sunlight followed by two weeks of darkness. Daytime Temperatures can reach about 400 K on sunlit surfaces. Nighttime Temperatures drop as low as 95 K in non-illuminated regions (Williams et al. 2017). The Permanently Shadowed Regions (PSRs) located at the lunar poles remain in permanent darkness and can reach temperatures as low as 20 K making them cold traps for volatiles such as water ice (Brown et al. 2022; Paige et al. 2010; Siegler et al. 2015).

This extreme temperature range poses challenges for electronic components, mechanical systems, and human exploration, requiring thermal management strategies for lunar habitats and instruments.

The Moon's surface can develop electrostatic charging due to interactions with the space environment, particularly solar wind and the lunar day-night cycle (Fenner et al. 1973;

Heiken et al. 1991; Knott 1973; Stubbs et al. 2014). The main sources of electrostatic charging are:

Photoemission by solar illumination
Solar ultraviolet (UV) and X-ray radiation eject electrons from the surface, resulting in a net positive charge on the sunlit side.

Solar Wind Plasma
The Moon is continuously bombarded by solar wind electrons and protons, creating localised negative or positive charging depending on surface conditions. This effect can only be observed in shadowed regions or on the Moon's night side, since in illuminated regions charging by photoemission is dominant.

Plasma Wake Effects
On the nightside and in shadowed regions, an excess of electrons can accumulate, leading to strong negative surface charging.

This electrostatic environment can lead to dust levitation and transport, especially near the terminator (the boundary between day and night), where strong electric fields may lift fine dust particles (Colwell et al. 2007).

The Moon lacks a protective atmosphere and global magnetic field, exposing its surface to high levels of plasma precipitation and ionising radiation from multiple sources:

Solar Wind
Continuous stream of charged particles (protons, electrons, and alpha particles) from the Sun, with energies typically up to a few keV per nucleon.

Solar Particle Events (SPEs)
Sporadic bursts of high-energy protons and heavy ions from solar flares with energies in the MeV range, which pose significant radiation hazards to astronauts and equipment.

Galactic Cosmic Rays (GCRs)
High-energy charged particles originating from outside the solar system with energies in the GeV range, including protons, helium nuclei, and heavy ions, capable of penetrating deep into materials.

The lack of atmospheric shielding means that lunar habitats and equipment must incorporate radiation protection measures, such as regolith-based shielding or electromagnetic deflection systems, to mitigate the risks associated with prolonged exposure (George et al. 2024; Mazur et al. 2015; Reitz et al. 2012; S. Zhang et al. 2020).

The Moon presents a unique and extreme environment shaped by its lack of atmosphere, exposure to space weather, and long-term geological evolution. The lunar regolith, formed through impact-driven fragmentation and space weathering, serves as both a scientific record of the Moon's history and a critical material for future lunar exploration. However, challenges such as electrostatic charging, temperature extremes, and radiation exposure must be addressed during the development of space instrumentation destined for the lunar surface.

1.2 LMS - Overview and Principle of Operation

The Laser Mass Spectrometer (LMS) is a miniaturised laser ablation and ionisation time-of-flight mass spectrometer (LI-TOF-MS) developed at the University of Bern (Rohner 2004; Rohner et al. 2003). The LMS instrument was initially designed and developed for its application on the lander module of ESA's *BepiColombo* mission, meant to investigate the surface composition of Mercury. The mission's lander module was unfortunately cancelled in 2003 due to budgetary constraints (*Critical decisions on Cosmic Vision* 2003). Nonetheless, the development of LMS continued at the University of Bern continued, to expand its capabilities with regards to the sensitive chemical analysis of solids (A. Riedo, Bieler, et al. 2013; A. Riedo, Meyer, et al. 2013; Andreas Riedo, Neuland, et al. 2013; Tulej, Andreas Riedo, et al. 2012), thus widening the instruments field of applications. Since 2019 a variation of the LMS instrument called ORIGIN (**OR**ganics **I**nformation **G**athering **IN**strument) is being developed, focusing on the detection and identification of organic molecules in the context of the search for life in our solar system (Boeren, Gruchola, et al. 2022; Boeren, Keresztes Schmidt, et al. 2024, 2025; K. A. Kipfer et al. 2022; N. F. W. Ligterink, Grimaudo, et al. 2020). A general introduction into the operation principles of LMS is given here.

Laser Ablation Ionisation Mass Spectrometry (LIMS), the fundamental measurement principle employed by the LMS instrument, is an analytical technique for the spatially resolved determination of the chemical composition of solids. As in every mass spectrometric technique, an ion source is required. In LIMS, a focused, pulsed laser beam interacts with the solid surface, causing ablation of a thin layer of material as depicted in Figure 1.2. This process generates an expanding plasma plume consisting of ablated particles and directly ionised species. In the case of LMS, this ion source is directly coupled to a time-of-flight (TOF) mass analyser, which separates the generated ions based on their mass-to-charge ratio (m/q). The ions' respective flight times are recorded by a detector and signal acquisition system, allowing for mass spectrum reconstruction. A more detailed introduction to the principles of TOF-MS is provided in the next section.

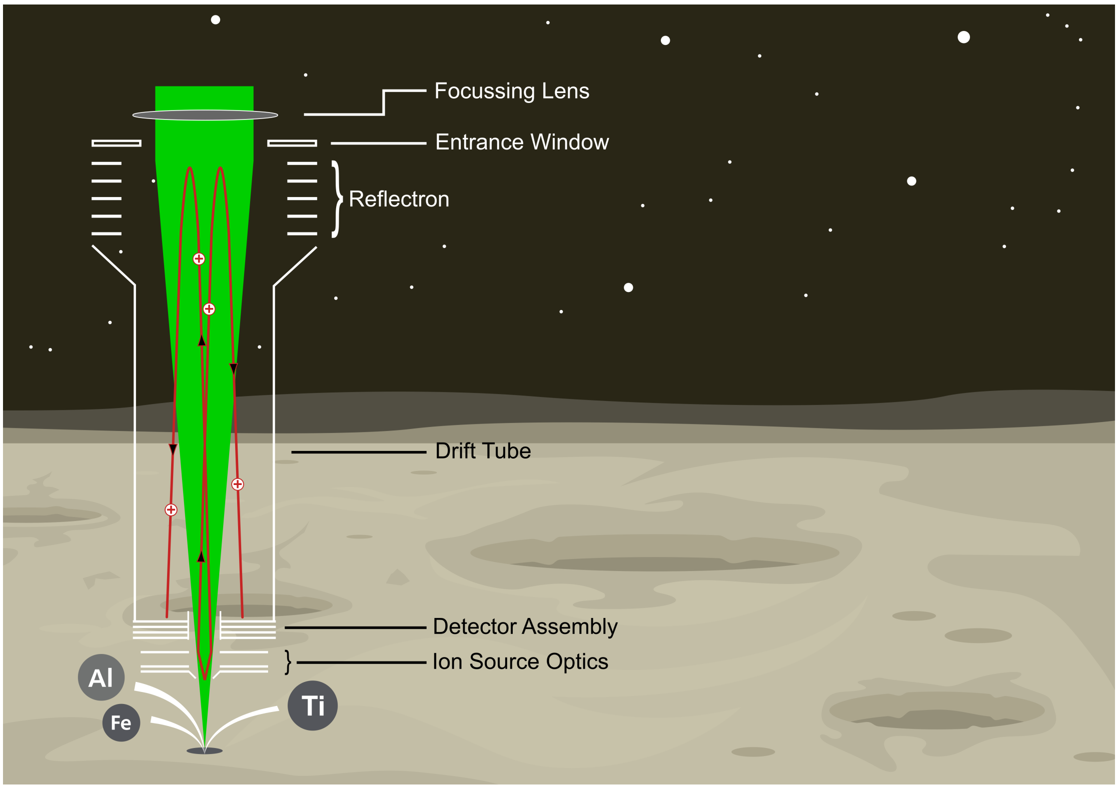

Figure 1.2: Schematic overview of the LMS instrument while analysing material on the lunar surface. The laser beam (green) and flight paths of ions (red lines) are shown.

A key advantage of coupling a pulsed laser ionisation source with TOF mass spectrometry is that TOF-MS inherently requires pulsed ion generation, which is naturally provided by the pulsed laser beam.

The ablation conditions, primarily dictated by laser irradiance, influence the type of information extracted from LIMS.

- At moderate laser irradiances ($10\,\mathrm{MW\,cm^{-2}}$ to $100\,\mathrm{MW\,cm^{-2}}$ with nanosecond lasers), LIMS can detect molecules and molecular fragments.
- At higher irradiances ($\mathrm{GW\,cm^{-2}}$ for nanosecond lasers, $\mathrm{TW\,cm^{-2}}$ for femtosecond lasers), the laser energy leads to atomisation, allowing for element and isotope analysis of the sample material.

However, quantitative analysis with LIMS remains challenging due to different ionisation yields of the elements caused by non-stoichiometric plasma formation. The efficiency of laser ablation and ionisation varies depending on material properties and laser absorption characteristics, which must be addressed with suitable calibration constants in element quantification. These effects are particularly pronounced when using nanosecond (ns) lasers.

To mitigate these challenges, femtosecond (fs) lasers have been increasingly employed in LIMS (Hergenröder et al. 2006; Andreas Riedo, Neuland, et al. 2013; Tulej, N. F. Ligterink, et al. 2021). Due to their non-thermal ablation, fs-lasers induce a more stoichiometric plasma, reducing variations in the ionisation of elements and matrix-dependent biases (Garcia et al. 2008; Hermann et al. 2010; Russo et al. 2013). As a result, fs-laser-based LIMS can provide more accurate quantitative results compared to ns-laser systems. A main limitation of fs-laser systems is their size and power consumption, making them currently unsuitable for space applications.

1.2.1 Fundamentals of Time-of-Flight Mass Spectrometry (TOF-MS)

The concept of separating ions with different mass-to-charge ratios (m/q) based on their time-of-flight in field-free region was first introduced by Stephens in 1946 ("Proceedings of the American Physical Society" 1946). Since its inception, TOF-MS has undergone continuous advancements, particularly in terms of mass resolution. A significant breakthrough came in 1973 with the introduction of the reflectron by Alikhanov (Alikhanov 1957). This innovation improved mass resolution by compensating for energy dispersion among ions, ensuring that those with the same m/q but different initial kinetic energies reached the detector simultaneously.

Compared to traditional scanning mass spectrometers like quadrupole or magnetic sector instruments, TOF-MS offers several distinct advantages:

Broad mass range

Unlike scanning instruments, TOF-MS does not impose strict limitations on the detectable mass range. The only constraints are defined by the instrument's geometry and data acquisition system.

Low weight and simple construction

TOF-MS instruments have relatively straightforward designs, requiring fewer heavy parts (e.g. electromagnets) than other mass spectrometers, making them ideal for spaceflight applications and portable analysis systems.

Rapid data acquisition

TOF-MS records a complete mass spectrum with each ion extraction event, eliminating the need for scanning across different masses.

High mechanical tolerances

The performance of a TOF-MS depend primarily on electronic circuits rather than mechanical alignment of the ion-optical elements (e.g. quadrupoles), reducing the complexity of construction and lowering production costs.

High sensitivity

TOF-MS is highly sensitive, capable of detecting even single ions. In systems utilising grid-less ion-optics, 100 % ion transmission can be achieved, maximising detection efficiency and analytical performance.

Today, TOF-MS is a widely used analytical technique in various fields, playing a crucial role in methods such as Matrix-Assisted Laser Desorption/Ionisation (MALDI-TOF-MS), Secondary Ion Mass Spectrometry (SIMS-TOF), and Laser Ablation Inductively Coupled Plasma TOF-MS (LA-ICP-TOF-MS) (Becker 2007). These techniques leverage TOF-MS's ability to rapidly acquire full mass spectra with high sensitivity, making it an essential tool in applications ranging from classical analytical chemistry to materials science and planetary exploration.

The general operating principle of a TOF mass analyser is based on the acceleration of the to be analysed ions to a defined kinetic energy E_k, their spatial separation within a field-free region and subsequent detection of their time of flight.

With the assumption that the initial kinetic energy of the generated ions is zero, E_k after passing an acceleration potential U is given by

$$E_{acc} = qU = \frac{mv^2}{2} = E_k \tag{1.1}$$

where q is the ion's charge, m the ion's mass and v its velocity after acceleration. With Equation 1.1 rearranged for v yields

$$v = \sqrt{\frac{2qU}{m}}. \tag{1.2}$$

From Equation 1.2 it is evident that lighter ions are accelerated to a higher velocity than heavier ones, thus after passing a field free region of length d, spatial separation has occurred. From this the ions' time of flight t through the field free region can be calculated as

$$t = \frac{d}{v} = d\sqrt{\frac{m}{2qU}} \Rightarrow t \propto \sqrt{\frac{m}{q}}. \tag{1.3}$$

Equation 1.3 describes the fundamental principle by which a TOF mass analyser separate ions according to m/q.

1.3 NASA's Artemis Programme and the CLPS initiative

Figure 1.3: The official logo of NASA's Artemis programme under which humans shall return to the lunar surface.

NASA's Artemis programme is a multi-phase initiative aimed at returning humans to the Moon and establishing a sustainable lunar presence in preparation for future Mars exploration (Creech et al. 2022; Smith et al. 2020). The programme's primary objectives include landing the first woman and the next man on the Moon, developing long-term infrastructure for lunar exploration, and fostering international and commercial partnerships. Artemis focuses on utilising the Moon's south pole, a region of scientific interest due to it being uncharted territory and potentially harbouring water ice and other volatiles. NASA's *Surveyor* and *Apollo* missions, Russia's *Luna* programme as well as the more recent Chinese *Chang'e* missions, landed in equatorial regions of the Moon. India's *Chandrayaan-3* mission was the first to soft land in the lunar south pole region with a latitude of 69° S (Karanam et al. 2023). Since then, Intuitive Machine's *IM-1* mission launched as part of NASA's Artemis programme, remained the only other (partially) successful mission to the south pole region. Hence, most of the knowledge we have about the lunar south pole and its unique features, such as permanently shadowed regions (PSRs), where potentially water ice can be found, stems from remote observations (Vondrak et al. 2010). The Artemis programme is expected to provide numerous opportunities to bring instrumentation to the lunar surface and perform in-situ studies.

A key component of Artemis is the Commercial Lunar Payload Services (CLPS) initiative, which leverages private-sector partnerships to deliver scientific instruments, technology demonstrations, and payloads to the lunar surface (Schonfeld 2023). CLPS is designed to accelerate lunar exploration by using commercial landers and rovers to support NASA's objectives. These missions shall provide essential data on the lunar environment, in-situ resource utilisation (Anand et al. 2012; Sanders et al. 2008), and surface conditions, which will guide future crewed missions.

1.4 The CLPS-LIMS Instrument

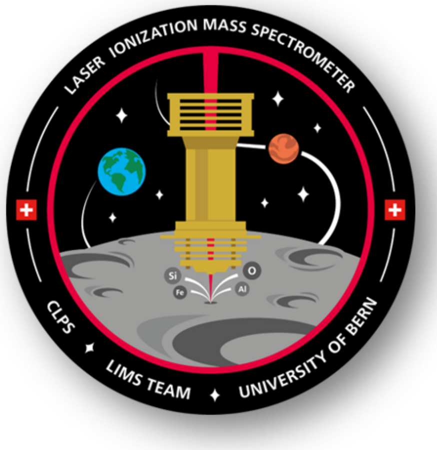

Figure 1.4: Mission patch of the CLPS-LIMS instrument destined for the lunar south pole.

One of the scientific instruments included in the CLPS payloads is the CLPS-LIMS instrument, designed for the in-situ chemical analysis of lunar regolith. The design of the CLPS-LIMS instrument is driven by the questions asked by the scientific community as formulated in the Artemis Science Definition Team (SDT) report (*Artemis III Science Definition Team Report* 2020). The main goals for the Artemis programme are as follows:

1. Understanding planetary processes
2. Understanding character and origin of lunar polar volatiles
3. Interpreting the impact history of the Earth-Moon system
4. Revealing the records of the ancient Sun and our astronomical environment
5. Observing the Universe and the local space environment from a unique location
6. Conducting experimental science in the lunar environment
7. Investigating and mitigating exploration risks

Based on the capabilities of LIMS, the instrument is expected to contribute information concerning the geochemistry of lunar surface and regolith material, which represents the overall scientific objective of the CLPS-LIMS payload. This objective is embedded within Goals 1 and 4 of the SDT report. Part of Goal 1 and 4 are the following objectives:

1 b-1. Determine the extent and composition of the primary feldspathic crust, KREEP layer, and other products of planetary differentiation.

1e. Understand impact processes: basins, craters, mixing of the crust

1f. Utilise the Moon as natural laboratory for understanding regolith processes and weathering on anhydrous bodies

4c. Understand changing compositions of impactors with time, and the nature of the early Earth.

Due to the dynamic nature of the CLPS programme, the details of the mission profile, apart from the CLPS-LIMS instrument's concept of operations, remain unknown at the time of writing this thesis. Based on the requirements, with the different payloads selected for the lander, the CLPS vendor will consolidate these requirements and develop the mission profile. The mission's general outline will most likely follow profiles the first two, already launched CLPS missions, namely Intuitive Machine's *IM-1* and Astrobotic's *Peregrine Mission One*, both launched in the beginning of 2024.

The lander on which the CLPS-LIMS instrument will be integrated will be launched by a commercial launch provider into an Earth orbit, from which a trans-lunar injection (TLI) will be performed, sending the spacecraft towards the Moon. This is followed by a cruise phase of multiple days to a few weeks, depending on the specific transfer orbit. At the Moon, the spacecraft is captured into a lunar satellite orbit, from which the decent to the surface is initiated. Once landed, the scientific part of the mission will commence and last for about one lunar day (corresponding to about 14 Earth days). As of writing this thesis, it is not expected that the lander, and thus the payloads, will survive the lunar night.

Landing site selection for a mission can be a challenging task. This is especially true, when the landing site is located in the south pole region of the Moon. The high latitudes result in very low Sun and Earth angles above the horizon. Combined with the highly variable topography of the lunar surface, requirements like continuous line of sight with Earth over the mission's duration for communication and continued solar illumination are challenging to fulfil. Scientifically, the CLPS-LIMS instrument's goal is to analyse material from the early phases of the Moon's development (pre-Nectarian). In collaboration with the teams of the other scientific instruments and their specific requirements, the selected landing site for the mission with the CLPS-LIMS instrument will be on the rim of the impact crater Haworth, as shown in Figure 1.5.

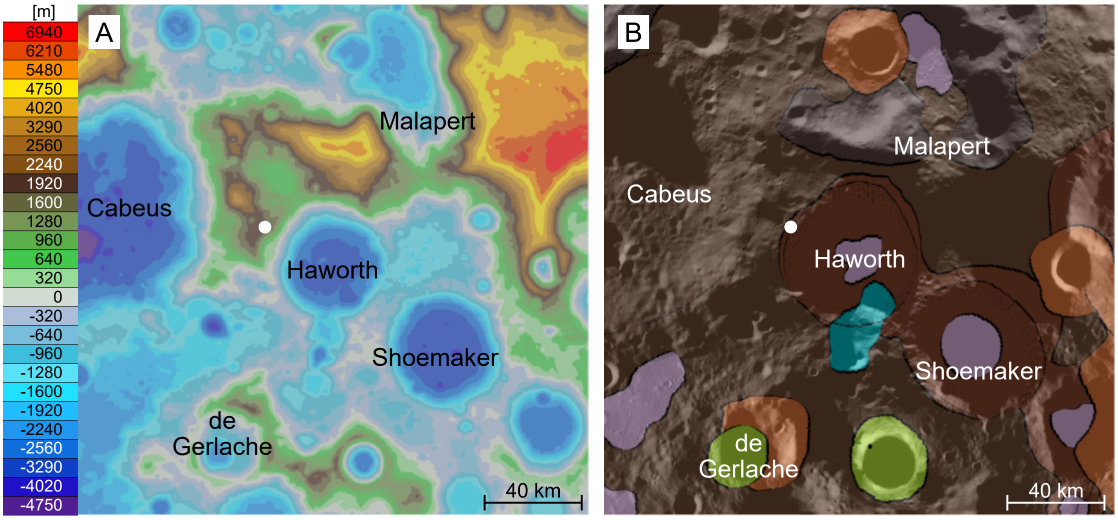

Figure 1.5: (A) Topographic map of the Haworth crater and its surrounding structures. The location marked with a white dot is the currently selected landing site for the mission with the CLPS-LIMS instrument. **(B)** Geological map of the landing site. Brown-shaded regions, in which the landing site lies, are of pre-Nectarian age. Based on Spudis et al. 2008.

1.5 Thesis Outline

The kick-off the CLPS-LIMS project roughly coincided with the start of my PhD project. The work presented here spans the time frame from the very early prototyping phase until the first functional engineering model of the actual flight-capable CLPS-LIMS instrument were tested in the laboratory.

Accordingly, the thesis is organised into three, mostly chronological, chapters. In Chapter 2 the technological adaptations to the existing laboratory LIMS instrument were explored, that are necessary before constructing a fight-capable instrument for the analysis of lunar regolith. Chapter 3 introduces the design of the CLPS-LIMS instrument and how the different sub-systems were prototyped and tested in the laboratory. Finally, Chapter 4 describes the commissioning process of the CLPS-LIMS engineering model, and the various tests conducted to validate the model's performance.

2 Prototyping the CLPS-LIMS concepts

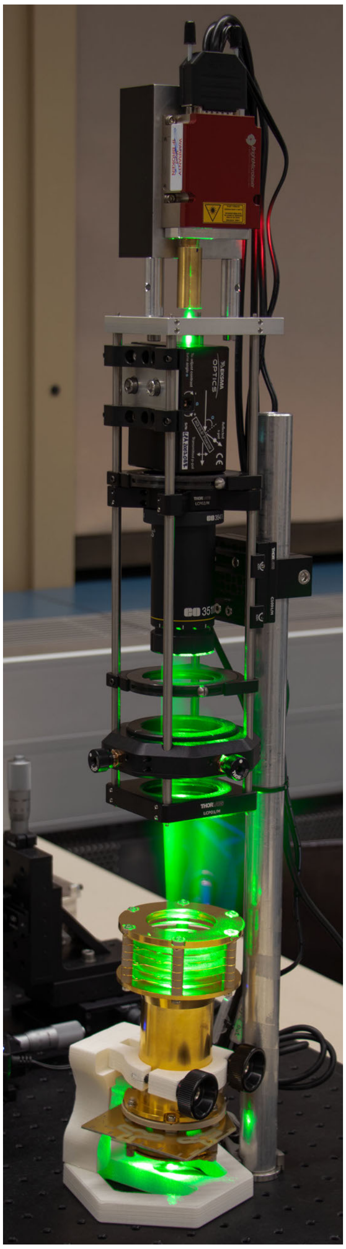

Before designing a LIMS instrument capable of operating autonomously on the lunar surface, foundational laboratory studies were necessary to identify critical design adaptations and develop the measurement concepts required for LIMS analysis of lunar regolith. These studies focused on understanding the specific challenges posed by the lunar environment and regolith properties, ensuring that the instrument could perform reliably under real mission conditions.

A key aspect of this prototyping phase was the development of a compact laser system, serving as the basis from which a flight-ready design could be derived.

Additionally, initial studies with lunar regolith simulant materials were conducted to investigate the material's behaviour under LIMS measurement conditions. The findings from these tests were used to define the requirements for a flight-ready sample handling system, ensuring that regolith can be prepared and analysed in a controlled and reproducible manner.

This chapter details the prototyping efforts undertaken to bridge the gap between laboratory LIMS instrumentation and a fully autonomous lunar flight instrument, laying the groundwork for the final CLPS-LIMS design.

2.1 Flight-prototype Optical System Design

The main challenge for a LIMS system applicable for in-situ research on planetary bodies is the pulsed laser system used to ablate, atomise, and ionise sample material. The output energy in the right wavelength regime must be high enough to allow for these processes to happen in a stable manner. Pulse lengths must be short enough for a high peak power ($\mathrm{MW\,cm^{-2}}$ to $\mathrm{GW\,cm^{-2}}$). The requirements must be combined with a small volume, low weight, and low power consumption of the overall laser system to be suitable for a space mission.

Therefore, the laser system represents the critical part of the design process. Recent technological advances shifted the performance envelope of passive Q-switched Nd:YAG microchip laser systems (J. Zayhowski 2013; J. J. Zayhowski 2000) into the range usable for LIMS measurements. Being sufficiently small, with unit sizes at the cm-level, makes these types of lasers a good choice for this application.

In addition, a laser beam manipulation system was needed, that could guide the laser pulses from the laser through the mass analyser to the sample surface. Its design should be suitably compact and robust from the beginning, to aid its conversion in later stages of the project to a flight-ready system. To be suitable for LIMS measurements, the beam must be focussed to a spot size in the range of 10s of µm to reach the necessary irradiance on the sample surface. An additional functional requirement of the system is its ability to adjust the energy of the laser pulses. Depending on sample material properties, different laser pulse energies are required to obtain optimal conditions for chemical analysis by LIMS.

In the following sections, the selection of a suitable laser, the development of the necessary test setups, and the design of a laser optical system that fulfils the above-mentioned requirements are discussed.

2.1.1 Laser Source

Laser sources suitable for LIMS are characterised by a combination of key requirements:

- The laser source must be pulsed, so that the ablation process is sufficiently short to form compact ion packets for the separation by TOF-MS. This limits the pulse widths to the low ns range.
- The laser's wavelength must be short enough to be absorbed by the sample and therefore have a high ablation and ionisation efficiency. Hence, lasers with wavelengths in the visible, or better in the UV range are preferred.

- The laser's pulse energy must be high enough to, considering its pulse width, reach peak powers in the kW regime. These powers are required to reach the irradiances in the range of $\mathrm{GW\,cm^{-2}}$ on the sample surface, which are needed for good ablation and ionisation conditions.
- The laser's pulse-to-pulse energy stability must be as high as possible to ensure similar plasma properties during ablation and ionisation from shot to shot. As laser ablation and ionisation is a non-linear process, small variations in the pulse energy lead to large variations in mass spectrometric signal intensity.
- The laser's repetition rate must lower than the inverse of the maximally expected time of flight but should be high enough to allow for fast analysis of the sample. With the current mass spectrometric setup, this sets the optimal repetition rate in the range of 100s of Hz to low kHz.
- The laser's lifetime should be long enough to support the expected mission duration.

In addition, to control the effective pulse energy reaching the sample surface is needed within a range of about a factor of 10, as the ablation conditions must be optimised according to the specific sample. This energy adjustment can be part of the laser source itself or, e.g., a separate beam attenuator within the laser optical system.

Recent technological advances shifted the performance envelope of passively Q-switched Nd:YAG microchip laser systems with a fundamental wavelength in the IR of 1064 nm into the range usable for LIMS measurements. Being sufficiently small, with unit sizes at the cm-level and power consumption <10 W, makes these types of lasers a good choice for this application. Second-harmonic generation with sufficient pulse energies for LIMS, leading to an output wavelength of 532 nm in the visible range, can be carried out within the same mechanical envelope.

Table 2.1: Technical specifications of the procured SB1-532-40-0.1 laser. σ denotes the standard deviation of a value μ the mean.

Wavelength [nm]	532	λ
Pulse Energy [µJ]	>40	E
Pulse Energy Stability [%]	<0.3	σ_E/μ_E
Pulse Width [ns]	<1.5	t_W
Peak Power [kW]	>26	P_p
Repetition Rate [Hz]	100	f

Based on these requirements, a commercial SB1-532-40-0.1 laser (Bright Solutions Srl., Italy) was procured. Its technical parameters are summarised in Table 2.1.

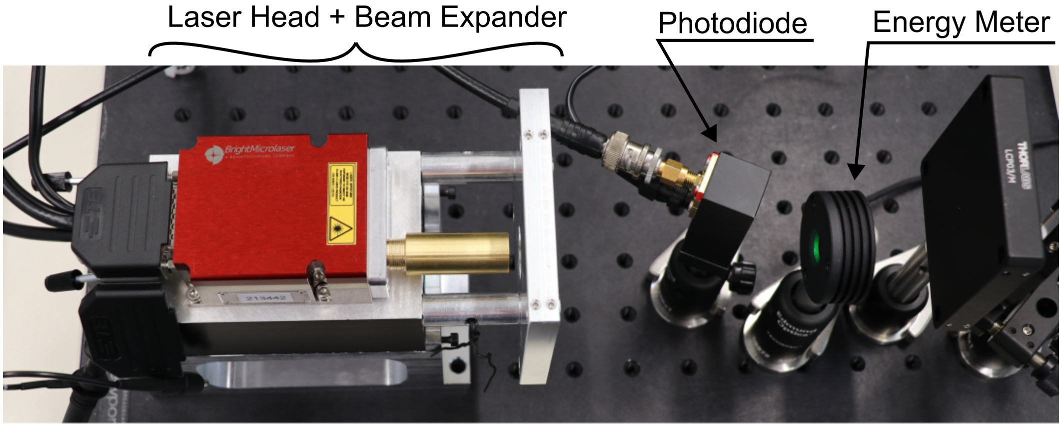

Figure 2.1: Test setup to characterise the dynamic behaviour of the 532 nm SB1 microchip laser system.

To ensure that the obtained laser is compliant with its specifications, validation studies were conducted using the setup shown in Figure 2.1. With a J-10MB-LE pulse energy meter (Coherent Inc., USA) the maximal pulse energy and its variation were determined under various operation conditions. Additionally, by measuring the reflected light from the energy meter's surface with a UPD-50-UP fast photodiode (ALPHALAS GmbH, Germany) connected to a MSO64B (Tektronix Inc., USA) oscilloscope, the beam's temporal profile could be analysed.

The pulse energy shows a distinct deviation from the nominal value for the first about 5 pulses at the beginning of each laser burst. This behaviour is depicted in Figure 2.2.

Inside the laser, the pump diode and the second harmonics generation crystal must be kept within a narrow temperature window for optimal performance. This is accomplished by two independent thermo-electric coolers (TECs, Peltier elements) controlled by separate PID loops. As the heat dissipation of both components is different while producing laser pulses, a transient at the beginning of a burst can be expected until the component temperatures have stabilised. This behaviour is inherent to the laser's design. The heating and cooling power of the TECs is limited, as well as the heat conduction from the TECs to the actual temperature stabilised components, thus, explaining the pulse energy instabilities when activating laser light emission. For the application of this laser the maximally seen instabilities of about 1 % within the first 5 pulses, are not deemed critical. After the stabilisation phase, the variations of the laser energy drop to about 0.1 %. Depending on the specific scientific question and the applied LIMS measurement procedure, it might become necessary to omit the affected mass spectra from further analysis until the laser has stabilised.

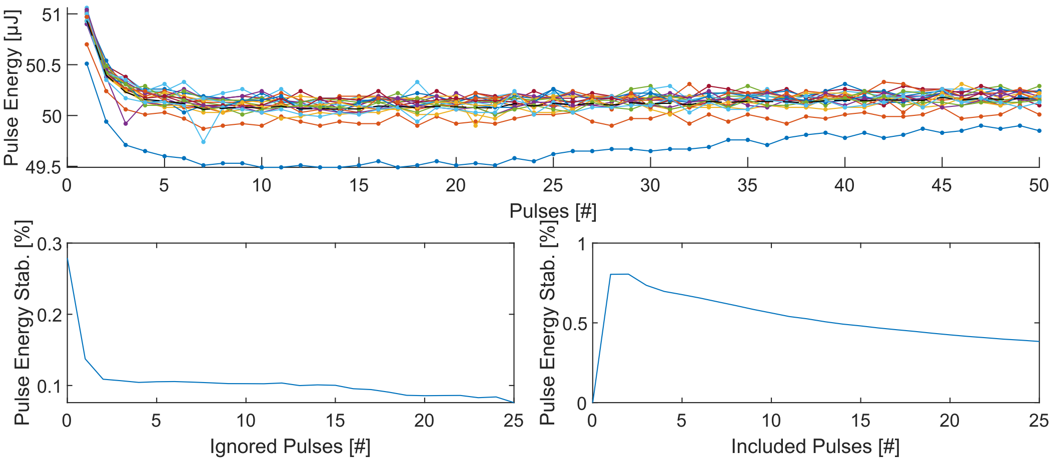

Figure 2.2: (Top) Measured pulse energy of the SB1-532 laser for the first 50 pulses after triggering a burst. **(Bottom, Left)** Pulse energy stability after ignoring the first k pulses, thus allowing to measure the performance after stabilisation. **(Bottom, Right)** Pulse energy stability of k included pulses, emphasising the maximum instability during the stabilisation phase.

The obtained temporal profile of multiple laser pulses is shown in Figure 2.3. The laser's pulse width is calculated as the FWHM of the temporal profile and is found to be (1.20 ± 0.02) ns. The measured value is below the maximally allowed 1.5 ns as required by LIMS and specified by the manufacturer, therefore the laser meets this requirement.

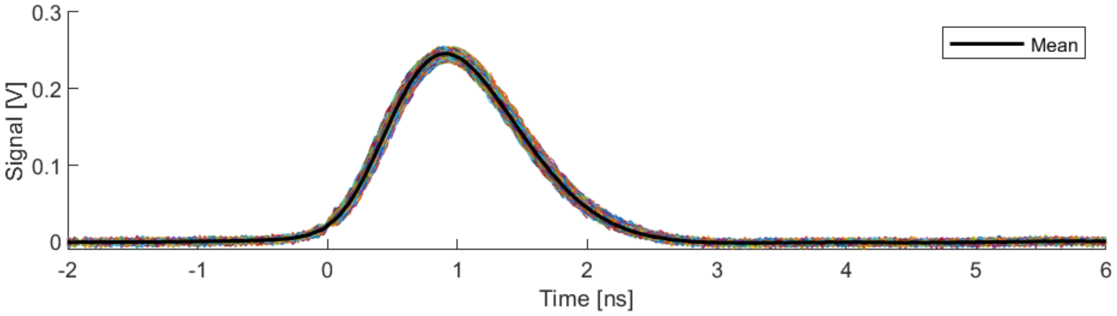

Figure 2.3: Temporal profiles of 1000 pulses emitted by the SB1-532 laser. The mean FWHM is (1.20 ± 0.02) ns.

The performed tests validated the laser's performance and its potential suitability for LIMS.

2.1.2 Supporting Electronics and Software

For a SB1-type laser to properly integrate with the laboratory mass spectrometric setup, a custom interface and controller board was built and the associated firmware as well as the user-facing control interface were developed.

A main limitation of the SB1 laser's integrated control electronics is the lack of a burst mode, in which a precisely defined count of laser pulses with a set frequency is generated. Operating the laser in such a mode is universally implemented within the laboratory laser systems of other existing LMS-type instruments. The SB1 laser does offer an external trigger input, to which a logic TTL signal can be applied, inducing the generation of a single laser pulse. By applying a fixed-length pulse train to the trigger input, the laser will emit the appropriate number of laser pulses. In addition, the laser provides a synchronisation output on which a TTL signal is generated at the instance a laser pulse is fired, allowing to synchronise the recording of a mass spectrum with the laser emission.

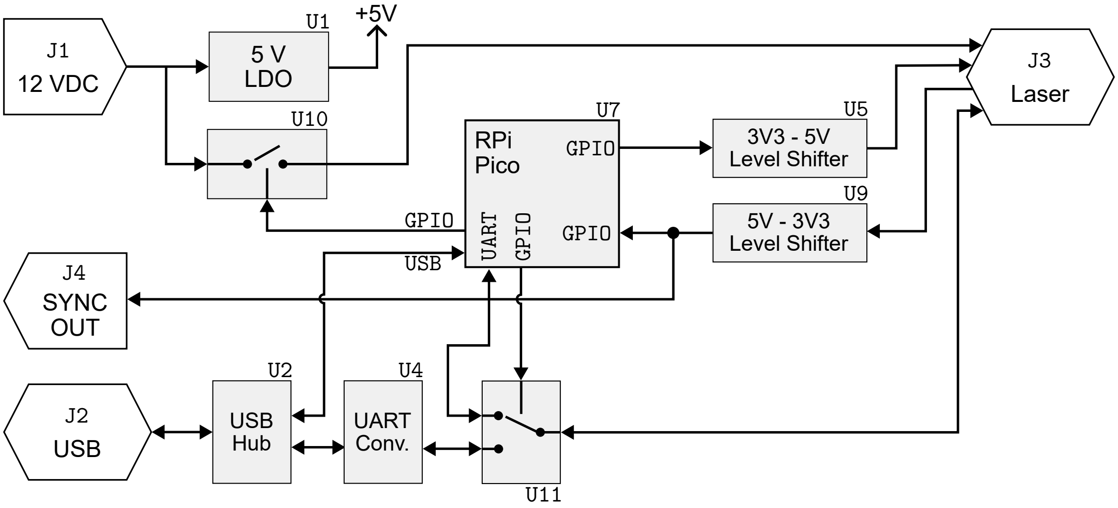

Figure 2.4: Block diagram of the developed and built SB1 controller board.

Based on these requirements, the "SB1 Laser Controller" was developed, whose block diagram is shown in Figure 2.4. The main control logic is implemented using a RP2040 microcontroller-based RPi Pico (Raspberry Pi Ltd., United Kingdom) board (Figure 2.4, **U7**). The Pico has all the necessary supporting electronics, such as voltage converters and flash memory on-board, making the overall integration of the microcontroller unit (MCU) simpler. The controller board interfaces via the DB15 connector **J3** with the laser. It carries all the necessary signals to control the laser. These are:

Power Supply voltage for the laser electronics and separately for the laser diode. The latter can be switched on/off under MCU control via the MOSFET U10, ensuring no laser emission can take place.

Logic I/Os TTL-level logic signals from the MCU to the laser, such as the laser trigger signal and status signals from the laser to the MCU, as well as the synchronisation signal on laser pulse emission.

Communication Universal Asynchronous Receiver Transmitter (UART) interface to control and configure the laser electronics.

As shown in Figure 2.5, power to the controller is supplied using connector **J1**. Via connector **J2** a USB-based connection is established between a controlling computer and the SB1 controller board. The connection allows for communication with the MCU and the laser via an integrated USB-UART converter (**U4**). The laser synchronisation signal generated by the laser is buffered, so it can drive a 50 Ω load, such as a high-speed digitisers trigger input that can be connected via the BNC connector **J4**.

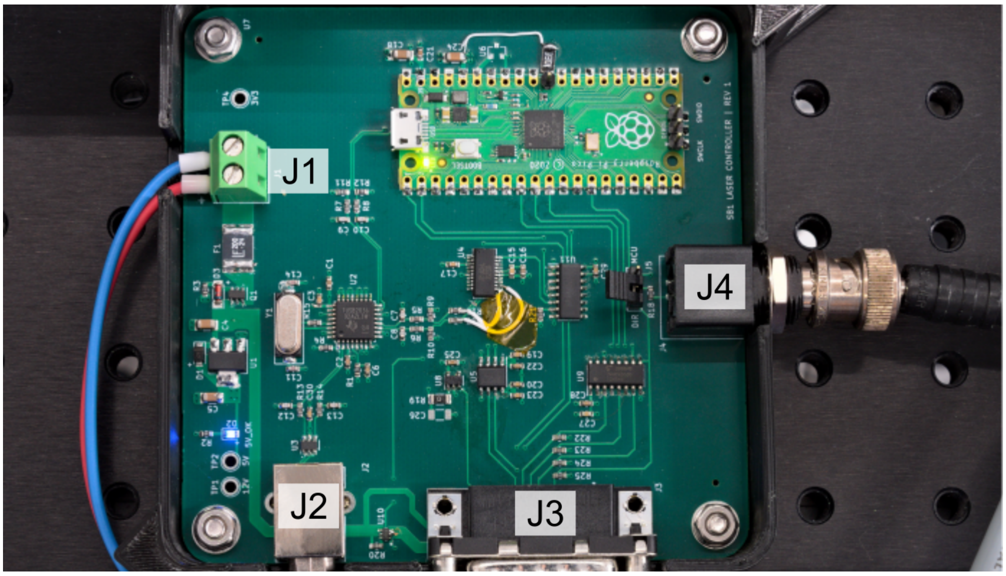

Figure 2.5: Revision 1 of the designed and built control board for SB1 type lasers. It contains a microcontroller-based trigger pulse generator and the necessary interfacing electronics to communicate via one USB connection (**J2**) with the laser and the controller.

The firmware for the controller was developed in C++ and implements a simple ASCII-based protocol via which the various inputs and outputs can be read or set, and via which the laser burst generation is configured and triggered.

For interaction with the user, a GUI written in Python was developed. A screenshot is shown in Figure 2.6. The developed programme features an application programming interface (API), through which already existing control software of the ORIGIN setup can communicate with the controller board.

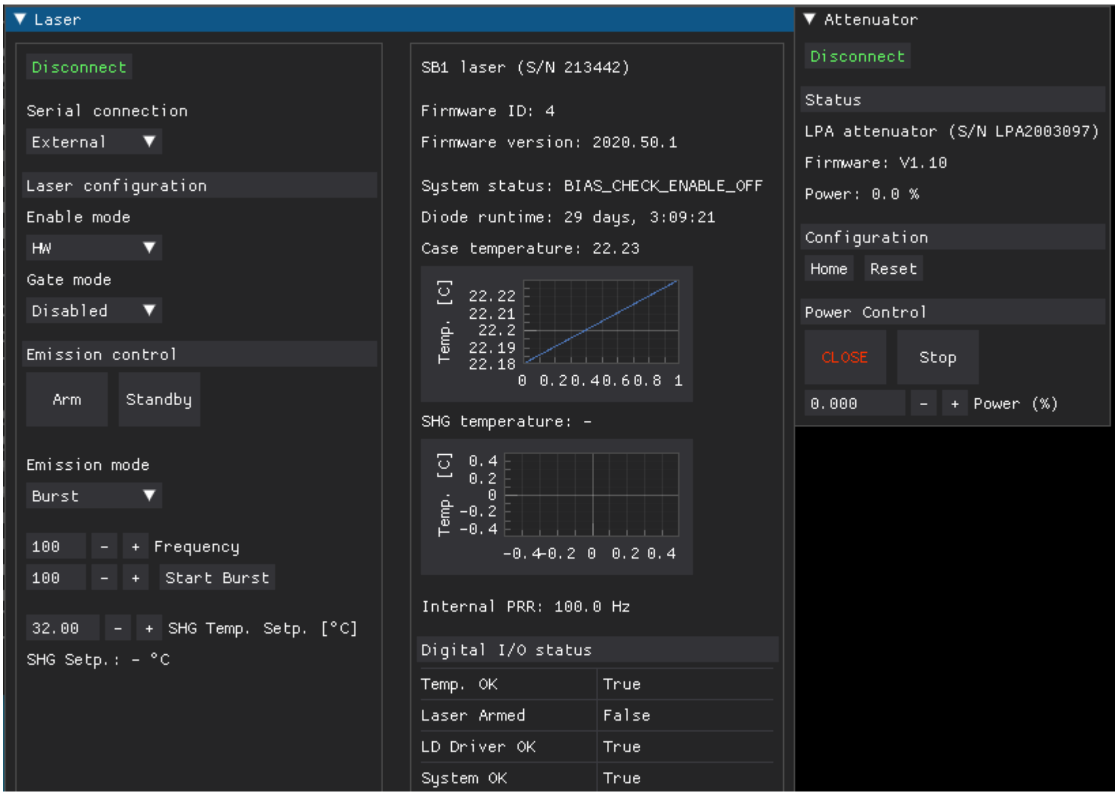

Serial connection
External

Laser configuration
Enable mode
HW
Gate mode
Disabled

Emission control

Emission mode
Burst

100 Frequency
100

32.00 SHG Temp. Setp. [°C]
SHG Setp.: - °C

SB1 laser (S/N 213442)

Firmware ID: 4
Firmware version: 2020.50.1

System status: BIAS_CHECK_ENABLE_OFF
Diode runtime: 29 days, 3:09:21
Case temperature: 22.23

SHG temperature: -

Internal PRR: 100.0 Hz

Digital I/O status

Temp. OK	True
Laser Armed	False
LD Driver OK	True
System OK	True

Status
LPA attenuator (S/N LPA2003097)
Firmware: V1.10
Power: 0.0 %

Configuration

Power Control

0.000 Power (%)

Figure 2.6: Screenshot of the user interface to control the SB1 type lasers and the associated control board, as well as the laser power attenuator mounted within the laser optical path of the prototype laser system.

2.1.3 Beam Shaping and Guiding System

The output of a laser source is usually a collimated beam with a defined diameter. For laser ablation and ionisation conditions using ns-pulse lasers, irradiances in the range of GW cm^{-2} at the sample surface are necessary. Due to its geometrically compact form, the LMS mass analyser has an upper limit of number of ions it can separate within an ion packet, before space charge effects impede the spectral quality. The number of produced ions is influenced by the area in which the laser beam's irradiance is above the material's ablation threshold. Due to this additional constraint, the light-matter interaction of interest should take place in a limited area with a diameter in the range of 10 µm to 20 µm, which is typically about 2 orders of magnitude smaller than the beam diameter at the laser's output. The purpose of the beam shaping and guiding system is to manipulate the laser's output optically, such that the above-mentioned constraints are fulfilled on the sample surface.

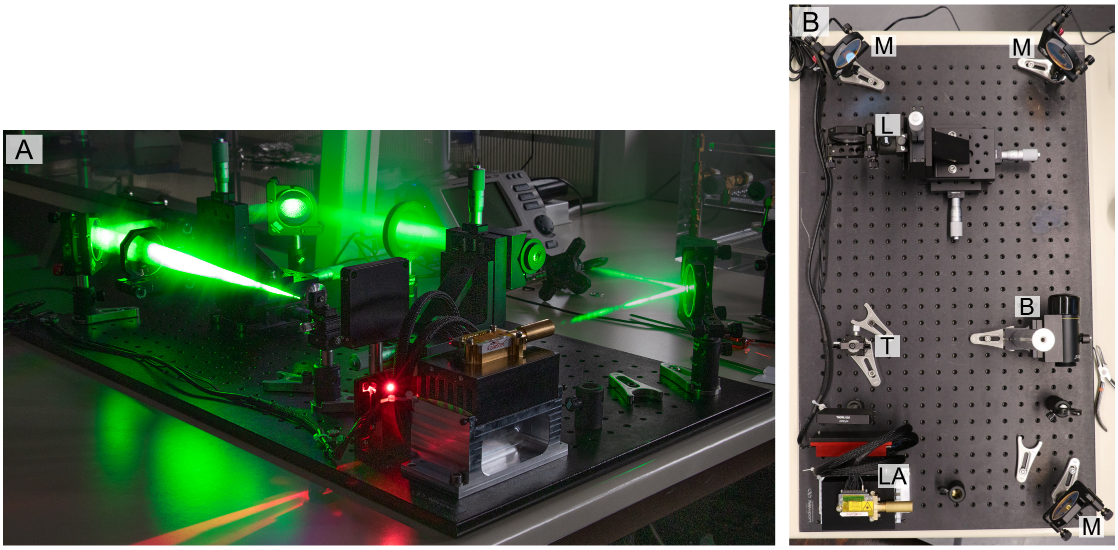

Figure 2.7: Breadboard-type test setup for the beam shaping and guiding system for a microchip laser. Panel A visualises the beam path through the optics. Panel B shows a top-view of the setup with the different components marked. **LA**: laser with primary beam expander, **M**: mirror, **B**: secondary beam expander, **L**: focussing lens, **T**: ablation sample.

The general design of such a system involves the focussing of the collimated laser beam by means of a concave lens in such a way that a beam diameter of the required size is reached in the focal spot. The minimal focal spot size d_{min} in the diffraction limited case can be estimated by

$$d_{min} \approx \frac{4}{\pi} \lambda F_{\#} \tag{2.1}$$

with λ the wavelength of the light, and $F_{\#}$ the focussing lens's F-number according to

$$F_{\#} = f/d \tag{2.2}$$

with f being the focal length of the lens and d the beam's input diameter. Hence, to minimise d_{min}, f must be minimised and d maximised.

Based on these concepts, a new beam guiding system for the integration of the SB1-532 laser was prototyped. In an additional step the system was refined, eliminating superfluous optical components and optimising its implementation. The breadboard implementation of the system is shown in Figure 2.7. It consists of the laser source **LA**, which has a collimated beam diameter at its output of about 4 mm. The main focussing element **L** is a spherical plan-convex lens with a focal length $f = 300$ mm. The lens's focal length is given due to the mechanical constraints of the ORIGIN setup, into which the laser system should be integrated. As the optical system is located outside the vacuum chamber, no lens with a shorter focal length could be utilised. To reach the required focal spot diameter of <20 µm, the laser's output beam must be expanded first. A 5x Galilean telescope-type beam expander **B** is used for this purpose, expanding the laser beam's diameter to 20 mm. For verification of the ablation condition, a sample **T** is placed in the focal spot of the lens **L**. According to the above given first-order approximation, a focal spot with diameter $d_{min} \approx 10\,\mu\text{m}$ can be reached with this setup.

Initial tests conducted with this setup using a stainless steel plate as sample resulted in audibly and visibly discernible ablation conditions at atmospheric pressures. Parametric studies of the crater shapes to determine the necessary laser irradiance to remove sample material, a prerequisite for LIMS measurements, were conducted using the setup. The resulting crater profiles and diameters were determined using a ContourGT-K (Bruker Nano Inc., USA) white light interferometer. As the laser pulse energy needed to be varied for these measurements, a laser beam attenuator was added in the beam path before the beam expander **B**. The sample was mounted on a PT3 XYZ manual linear translation stage (Thorlabs Inc., USA). This allowed to move the sample along the system's optical axis, which corresponds to the Z axis.

Initially, the focal position of the optical system determined by moving the sample in discrete steps of $dz = 250\,\mu\text{m}$ closer to the laser along the optical axis. At each distance 100 laser shots at a pulse energy of 8.0 µJ (attenuator transmission $T = 20\,\%$) were deposited. The resulting craters were microscopically evaluated as shown in Figure 2.8, panel A. The crater at distance $z = 0\,\text{mm}$ was determined to be closest to the system's focal position, as it shows optically the most confined crater shape. The out of focus craters show a diminishing central ablation craters, while the discoloured heat affected zones, typical for ns pulse ablation, grow. This trend matches the expectations, as the beam's peak irradiance decreases when moving away from the focal position. As ablation takes only place if an irradiance threshold is surpassed, the decrease in peak irradiance leads to effectively smaller ablation craters when keeping the laser pulse energy constant, as shown in Figure 2.9. For in-focus conditions, the crater diameter approached the laser beam diameter. At sample positions $z < -1\,\text{mm}$ a fringe pattern in the heat affected zone is observable, as shown in Figure 2.8, panel B. This is consistent with measured aberrations present in the laser beam after the focal position, most likely due to using a spherical lens as focussing element.

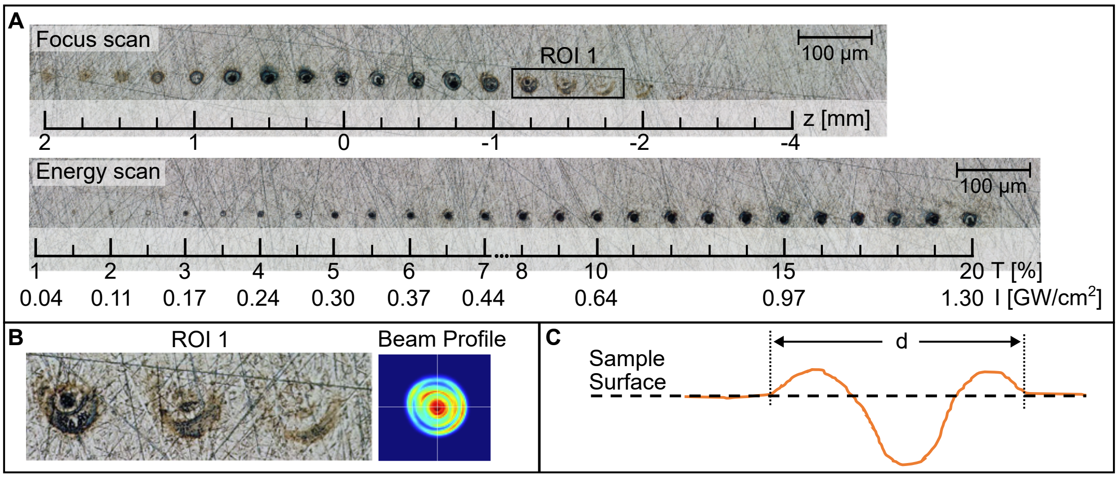

Figure 2.8: **(A)** Microscopic image of ablation craters produced by the breadboard laser system on a stainless steel sample. A focus scan at high irradiance if $I = 1.30\,\mathrm{GW\,cm^{-2}}$ was performed by moving the sample closer to the laser through the laser focus. The ablation crater corresponding to the laser focus ($z = 0\,\mathrm{mm}$) was determined optically, having the most confined crater shape. The evolution of the craters in focus was studied at different laser irradiances. **(B)** Enlarged microscopic image of craters created at distances closer to the laser than the focus. Comparing the produced craters and discolourations with the corresponding beam profile, the fringes due to aberrations in the optical system become evident. **(C)** Exemplary crater profile as observed after ablation of the stainless steel. For the determination of the crater diameter d, the outermost part of the change of topology is considered.

To determine the minimally needed laser irradiance for ablation, a laser pulse energy scan with the sample placed at $z = 0\,\mathrm{mm}$ was performed. Using a CCD beam profiler, the laser beam width was determined to be 23.7 µm in focus, thus resulting in applied irradiances of $0.04\,\mathrm{GW\,cm^{-2}}$ to $1.30\,\mathrm{GW\,cm^{-2}}$. The obtained craters are shown in Figure 2.8, panel A. Interferometrically, crater formation was observed at irradiances $>0.3\,\mathrm{GW\,cm^{-2}}$ with the crater diameter increasing with increasing irradiance, as shown in Figure 2.9. For high irradiances the crater diameter was roughly equal to the laser beam diameter.

From these studies performed using stainless steel as sample material, the following initial requirements for the laser optical system were derived:

- The peak irradiance must be $>0.3\,\mathrm{GW\,cm^{-2}}$ at every possible sample position.
- To achieve ablation craters $<20\,\mu\mathrm{m}$, the laser beam diameter must not exceed 20 µm.

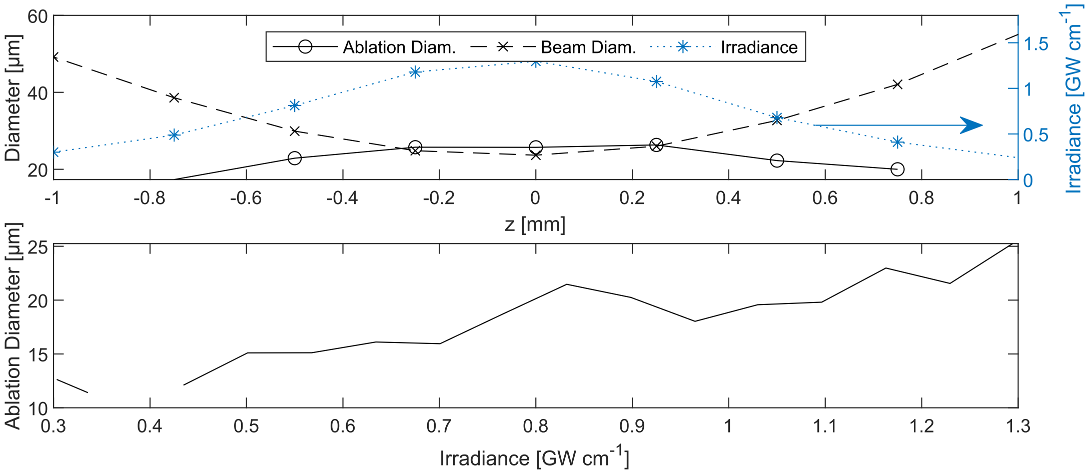

Figure 2.9: (Top) Crater and laser beam diameter of the breadboard setup depending on the distance from the focal position z. **(Bottom)** Ablation crater diameter depending on the laser irradiance with the sample being at $z = 0\,\mathrm{mm}$.

An equally structured measurement campaign was performed using granite as sample material. With the granite sample being a dielectric, a higher ablation threshold is expected which should more closely match the ablation threshold for lunar regolith material than the threshold derived from stainless steel. For the granite a minimum ablation threshold of $0.6\,\mathrm{GW\,cm^{-2}}$ was determined. The crater size didn't exceed the laser beam diameter even for irradiances as high as $4.5\,\mathrm{GW\,cm^{-2}}$.

In conclusion, to account for all possible pulse energy losses in the complete mass spectrometric system due to additional optical surfaces, the laser optical system shall generate irradiances at least in the range of $0.1\,\mathrm{GW\,cm^{-2}}$ to $1.0\,\mathrm{GW\,cm^{-2}}$.

Based on the validated concept, a simplified version of the beam guiding system was developed. It combines all necessary optical components into a linear cage system, called to optical tower, making alignment and integration onto the mass spectrometric setup very easy.

In addition to the necessary secondary beam expander and focusing lens, a variable beam attenuator is integrated to allow tuning the laser irradiance in accordance with the needs of the specific LIMS measurement. The CAD model and a picture of the built laser optics tower are shown in Figure 2.10. As all optical components are mounted linearly, no intermediate mirrors are needed, eliminating all degrees of freedom for alignment. Custom designed and produced holders for the beam attenuator and the laser ensure the optical axis of all elements is co-linear by design.

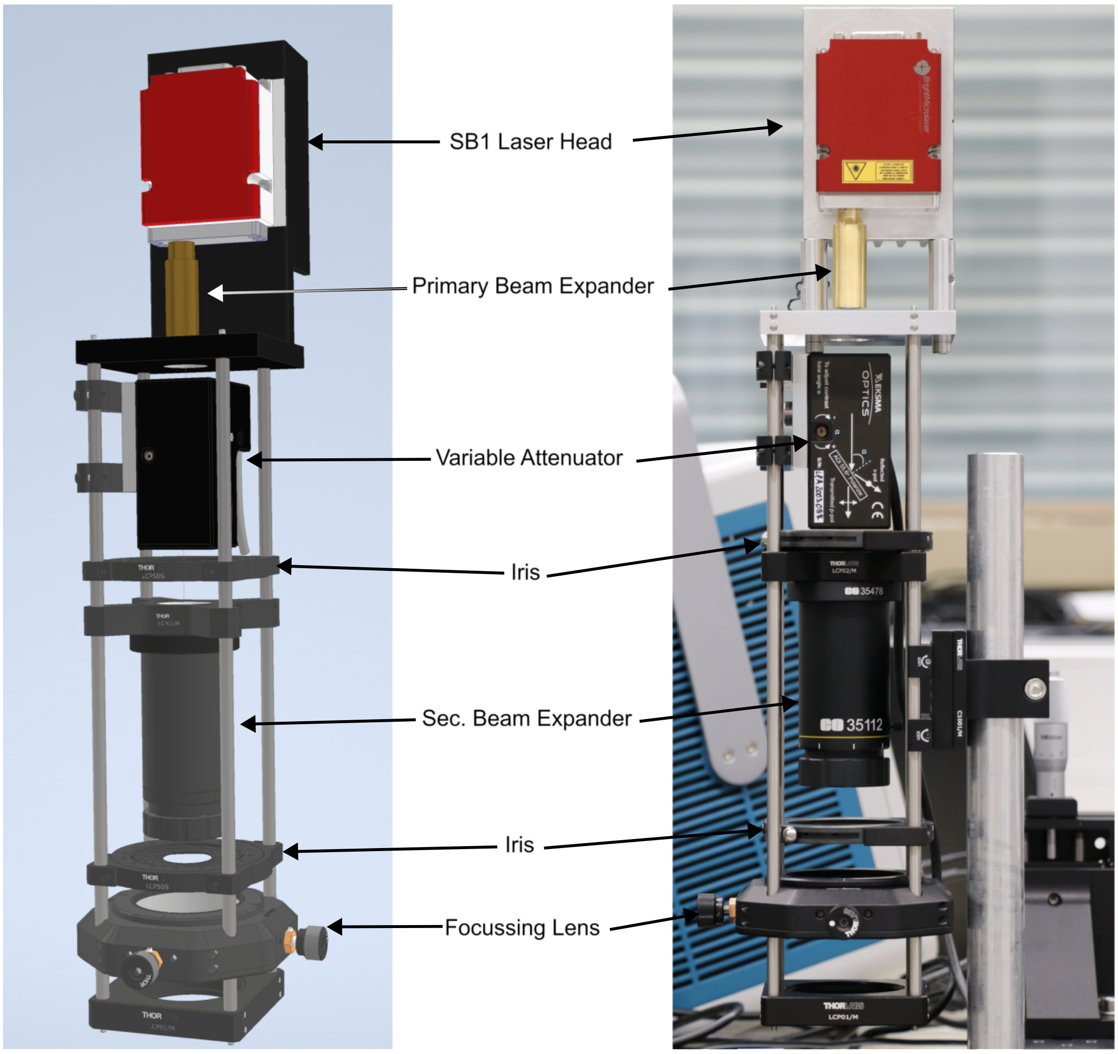

Figure 2.10: CAD model (left) of the laser optical tower system and image of the assembled version (right). The optical path follows the same structure as the breadboard setup shown in Figure 2.7, excluding the mirrors.

The completed optical design was simulated in Ansys Zemax OpticStudio to verify that the inclusion of the beam attenuator does not reduce the quality of the focal spot. The diameter of the focal spot is calculated to be 12.8 µm, as can be seen in in Figure 2.11. Since the numerical simulations are based on accurate physical wave propagation calculations and proper models of all involved optical components, the difference to the previously calculated first-order approximation of $d_{min} \approx 10\,\mu\text{m}$ for the focus diameter is expected.

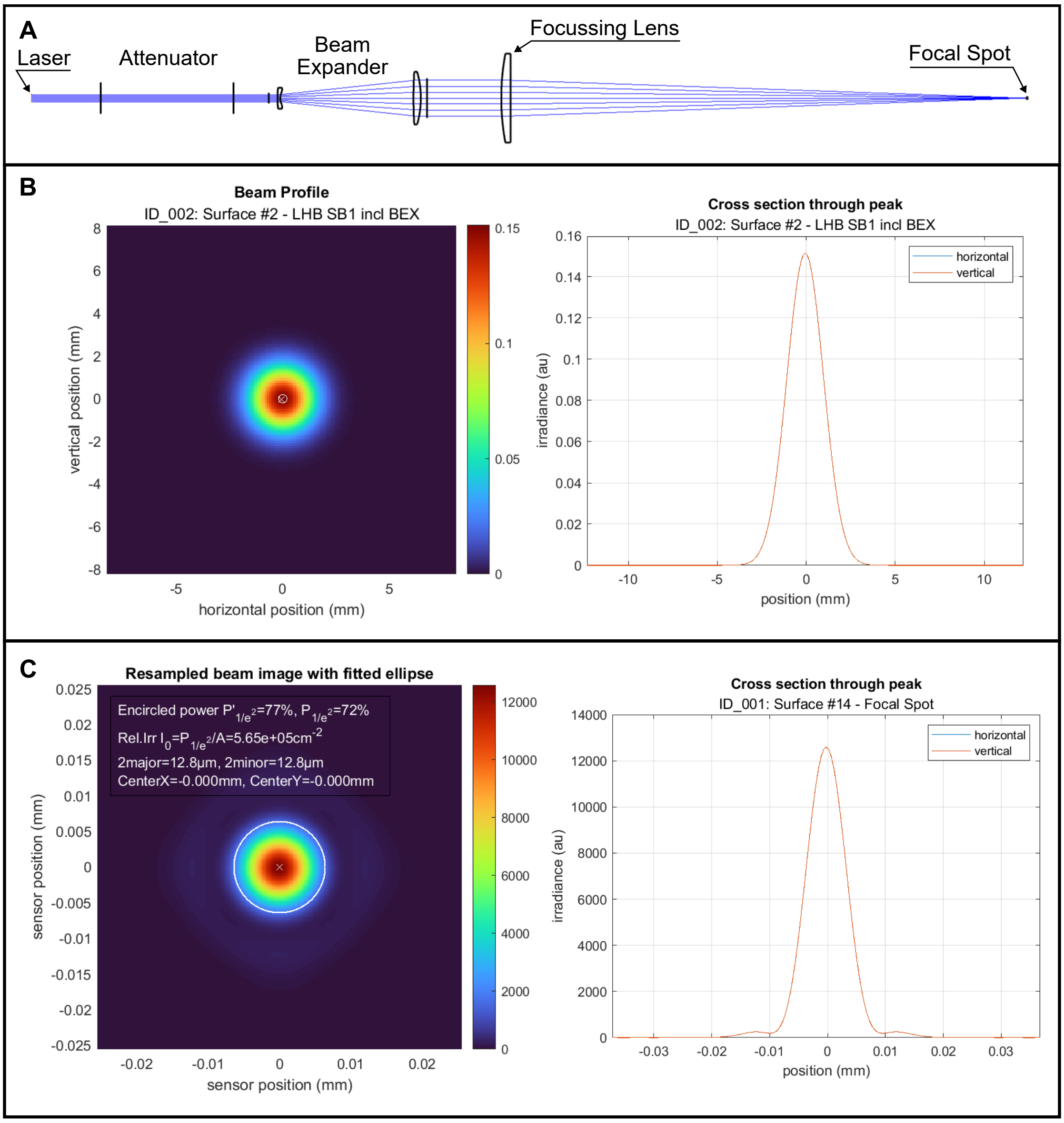

Figure 2.11: Simulations of the tower-design's optical performance. **(A)** Beam path from the laser to the focal spot with all simulated optical surfaces. **(B)** Beam profile at the output of the SB1 laser. Its parameters are derived from data provided by laser's data sheet. **(C)** Calculated beam in the focal spot. A beam diameter of 12.8 µm is reached.

The developed tower-system design provides all the necessary features to be suitable for the integration into a flight-capable LIMS system. Based on its general structure, the concept study as shown in Figure 2.12 was designed by the institute's mechanical engineering team.

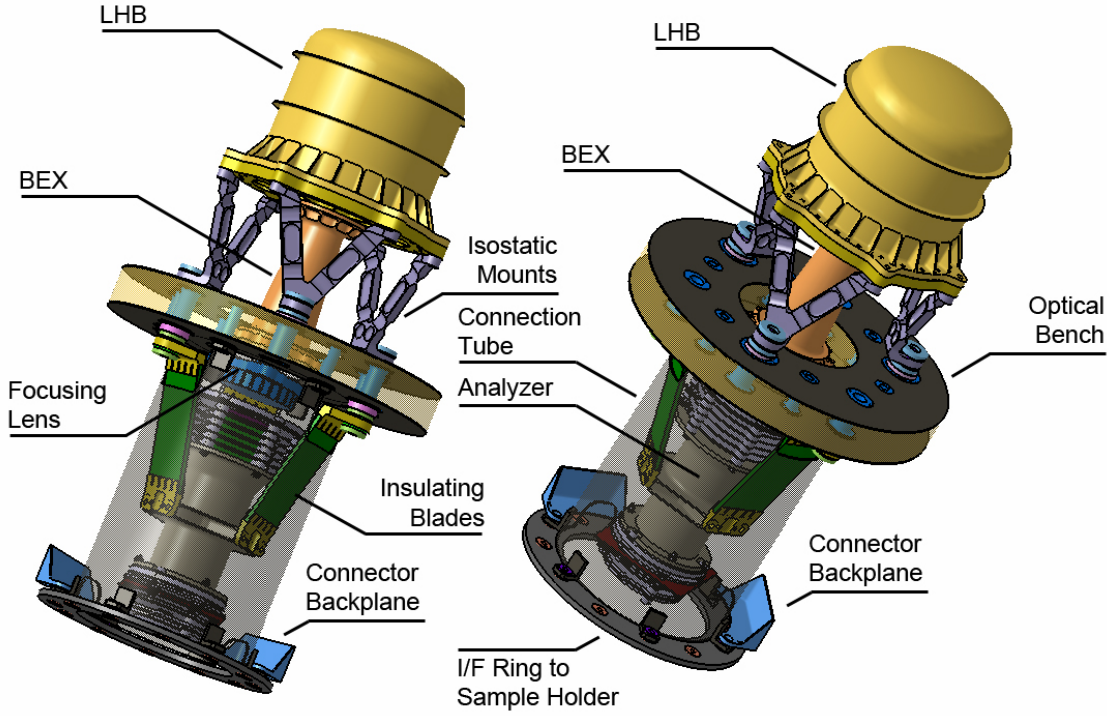

Figure 2.12: Initial conceptual design of a flight-capable LIMS system, based on the results of the studies discussed in this thesis.

The central part of the design is an optical bench that support and maintains the co-alignment of all elements. It also provides the mechanical platform to the spacecraft. The laser is housed in a pressurised container, filled with synthetic dry air. This avoids the need for using vacuum compatible components within the laser source and thus simplifying its implementation. A beam expander (BEX) widens the beam, so that a smaller focal spot can be created by the subsequent focussing lens.

This concept study served as the baseline design from which the CLPS-LIMS instrument evolved. Critical requirements regarding the instrument's optical design were derived from the studies described in this thesis.

2.2 Sample Observation System

All the initial mass spectrometric measurements conducted during the prototyping phase of the CLPS-LIMS project used the ORIGIN setup. For sample positioning, the setup features a XYZ linear stage consisting of three AG-LS25-27V6 (Newport Corp., USA) actuators with maximal motion ranges of 27 mm. As the actuators are open-loop, the absence of position feedback in the stage limits the accuracy and reproducibility of sample positioning. To address this limitation, a camera-based sample observation system was developed to enhance sample positioning accuracy, enable real-time observation of the ablation process, and facilitate laser system alignment.

The camera system provides visually accurate sample positioning and allows for direct observation of the laser ablation process. This capability is particularly relevant for the studies conducted in this project, as they involve lunar regolith simulant — a material that has not previously been investigated in this context. Furthermore, the system enables high-resolution determination of the laser beam position relative to the mass analyser, improving alignment accuracy and simplifying the alignment procedure.

Figure 2.13: ORIGIN chamber with two orthogonal viewports. The cameras of the observation system are mounted to the setup using dovetail rails for alignment purposes and point towards the ablation region.

The system is implemented using two orthogonally mounted G1-319m CMOS cameras (Allied Vision Technologies GmbH, Germany). A key design constraint was the requirement for a minimal working distance of 200 mm, as the cameras needed to be positioned outside the vacuum chamber. Additionally, the field-of-view had to be greater than 27 mm to fully cover the stage's motion range. To meet these requirements, a C-35-F2.0-10MP

(Allied Vision Technologies GmbH, Germany) objective with a 35 mm focal length was selected, providing a horizontal field-of-view of 33.4 mm, while achieving a pixel resolution of 16 µm.

The completed setup, shown in Figure 2.13, is mounted using optical dovetail rails, allowing precise alignment of the cameras. An image captured by the front camera during the ablation process (Figure 2.14) demonstrates the system's capabilities. The ablation location in relation to both the sample and the sample holder is clearly visible, facilitating accurate sample positioning. Additionally, the laser beam's position relative to the mass analyser entrance can be observed, enabling precise alignment of the laser through the centre of the mass analyser. The ablation region itself is also clearly visible, allowing for real-time visual observation of laser-matter interactions.

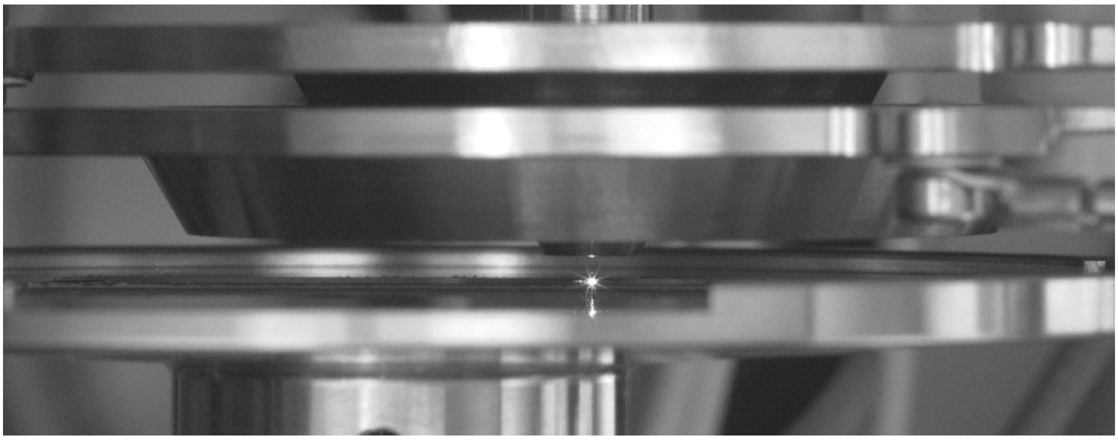

Figure 2.14: Ablation region as imaged by the front camera. The location of the laser beam in relation to the mass analyser entrance and the sample is clearly visible.

The camera system is fully integrated into the instrument's control software, enabling automatic video recording and the capture of snapshots at predefined events within the measurement procedure. This integration enhances the overall functionality of the system, providing a robust and reliable tool for sample alignment, laser positioning, and process monitoring.

The camera system proved as an invaluable tool during the studies investigating the behaviour of the lunar regolith simulant, as the next section will show. It provided input to the CLPS-LIMS instruments design, minimising the risk of malfunction when analysing grainy, loose material, such as lunar regolith.

2.3 The Sample: Lunar Regolith Simulant

The CLPS-LIMS instrument is designed to perform chemical composition analysis of lunar regolith at the Moon's south pole. To develop the measurement procedures and guide the CLPS-LIMS instrument's design, a suitable sample material is necessary for laboratory testing. However, actual lunar regolith is available only in limited quantities, primarily from the Apollo missions, necessitating the use of high-fidelity lunar regolith simulant materials.

In the context of the CLPS-LIMS project, lunar regolith simulant materials serve as substitutes for real lunar soil, replicating its chemical and mechanical properties for different testing purposes:

Method Development
Simulant materials must mimic the chemical composition of lunar regolith to enable accurate calibration and validation of the instrument's analytical capabilities.

Engineering and Sample Handling Tests
Simulant materials must approximate the mechanical properties of lunar soil to assess sample collection, processing, and handling mechanisms.

Although lunar regolith simulant materials are carefully designed to approximate the properties of real lunar soil, fundamental differences remain due to their terrestrial origins and artificial processing methods. These differences arise from variations in formation processes, chemical composition, and mechanical properties.

Lunar regolith is the product of billions of years of meteoroid impacts, space weathering, and solar wind interactions. These processes create highly irregular, sharp-edged grains and introduce unique components such as glass-mineral agglutinates, and solar wind-implanted ions (Brinckerhoff et al. 2000; Cudnik 2023; Hapke 2001; O'Brien et al. 2021). In contrast, simulant materials are manufactured from naturally occurring terrestrial minerals, sourced from specific geological deposits and ground to match the size distribution of lunar regolith.

Chemically, lunar regolith and simulant materials exhibit distinct differences (Slabic et al. 2024). Terrestrial materials often contain hydrated minerals, sulfates, and clays, which do not exist on the Moon due to its anhydrous environment (Heiken et al. 1991). Conversely, lunar regolith contains components absent in terrestrial materials, such as pyroclastic glass from ancient volcanic activity (Heiken et al. 1991; McIntosh et al. 2024), micrometeorite impact features at both millimetre and µm scales, and surfaces that have been fundamentally altered by space weathering (Pieters et al. 2016).

Mechanically, lunar regolith simulant materials struggle to reproduce the highly irregular grain morphologies found in real lunar soil. Lunar regolith grains exhibit sharp, angular surfaces due to continuous fracturing from meteoroid impacts, whereas simulant grains, even when crushed and processed, tend to be more rounded. This discrepancy influences the behaviour of the material in engineering tests, particularly for experiments involving transport, adhesion, and mechanical interactions with equipment.

To accommodate both methodological and engineering testing needs, two specific lunar regolith simulant materials are utilised, both provided by Space Resource Technologies, USA:

LHS-1 (Lunar Highlands Simulant)

Used for methodological development due to its high chemical fidelity.

LHS-1E (Lunar Highlands Engineering Simulant)

- Used for engineering purposes, particularly for developing and testing the sample handling mechanisms.
- Geotechnically equivalent to LHS-1 but with a simplified chemical composition, making it less representative for analytical testing by LIMS but suitable for mechanical evaluations.

For the remainder of this chapter, only LHS-1 will be considered, as the studies described were all conducted in the context of LIMS measurements.

Mineralogically and chemically, LHS-1 is designed to mimic the composition of the lunar highlands. Since it is expected that the lunar south pole region is geologically similar to the lunar highlands (Spudis et al. 2008; Wang et al. 2024), this simulant was obtained. No simulant developed specifically to mimic the presumed geological composition of the lunar south pole region was available at that time. LHS-1 is predominantly composed of anorthositic material, high in plagioclase feldspar with lower iron and titanium content, compared to simulant materials that mimic lunar mare regolith. For element analysis by LIMS, the chemical composition of the sample material is of particular interest. The concentrations of the specified metal oxides as measured by X-ray diffraction (XRD) are given in Table 2.2. The corresponding element concentrations have been calculated. The simulant's grain size distribution follows well the general distribution of lunar regolith, as determined from the Apollo sample, as can be seen in Figure 2.15.

Table 2.2: Chemical composition of LHS-1 as determined by XRD according to the datasheet (see Appendix B). LOI denotes loss on ignition.

Oxide	Oxide wt%	Corresponding Element	Element At. Fraction
SiO_2	51.2	Si	23.9 %
TiO_2	0.6	Ti	0.36 %
Al_2O_3	26.6	Al	14.1 %
FeO	2.7	Fe	2.1 %
MnO	0.1	Mn	800 ppm
MgO	1.6	Mg	1.0 %
CaO	12.8	Ca	9.1 %
Na_2O	2.9	Na	2.2 %
K_2O	0.5	K	0.4 %
P_2O_5	0.1	P	400 ppm
LOI	0.4	-	-
Total	99.4	-	-

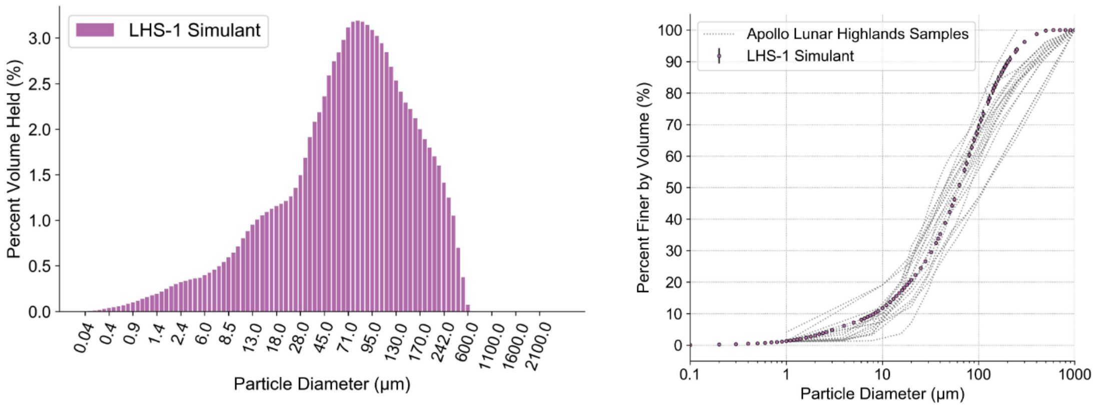

Figure 2.15: (Left) Grain size distribution of LHS-1 simulant. **(Right)** Comparison with Apollo Lunar Highland samples. Adapted from LHS-1 datasheet.

The following studies present the first attempts in analysing lunar regolith with a laboratory LIMS setup. The purpose of these studies was to gain experience with lunar regolith, in particular how it behaves physically during analysis by LIMS, to guide the necessary design choices for the CLPS-LIMS instrument.

2.3.1 Behaviour during LIMS measurements

Initial measurements of lunar regolith simulant, specifically LHS-1, using the laboratory LIMS instrument ORIGIN were performed.

The setup was equipped with the previously described laser optical tower using the SB1 532 nm laser. The sample was prepared on an unmodified sample holder, which is usually used for the analysis of organic films (Boeren, Keresztes Schmidt, et al. 2025; N. F. W. Ligterink, Kristina A. Kipfer, et al. 2022). The sample holder has 5 round cavities arranged in a row, as can be seen in Figure 2.16. Each cavity has a diameter of 3 mm and a depth of 200 µm. Regolith simulant was filled into the 3 central cavities and compressed manually with a spatula. Excess material was removed, making sure the surroundings of the cavities were free from sample material.

The sample was placed in the instrument's vacuum chamber and evacuated. LIMS measurements were performed with pulse energies of about 0.9 µJ at the sample surface. In total, 100 000 laser shots were applied to the surface while continuously moving along the axis of the sample cavities. The state of the sample and sample holder after this measurement campaign is shown in Figure 2.16. The sample material has clearly spread out of the cavities, leaving the cavities partially empty.

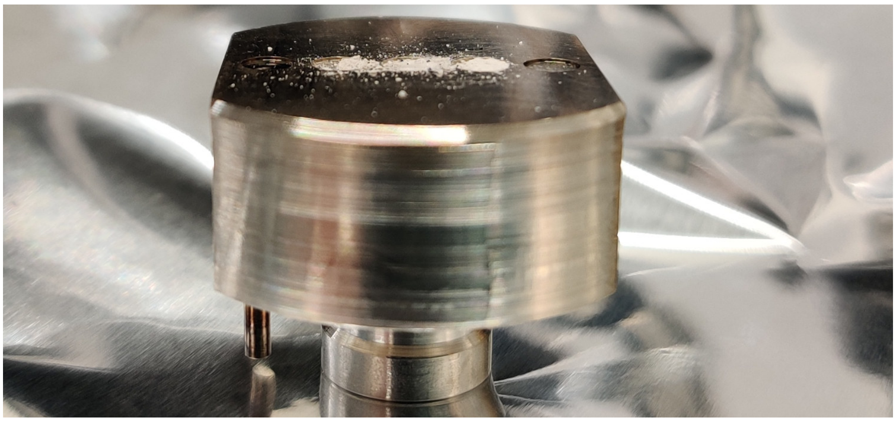

Figure 2.16: LHS-1 regolith simulant on a sample holder with 200 µm deep cavities after being subjected to analysis by LIMS.

These measurements showed clearly that the methodology needed to be improved. The thin layer of sample material within the cavity had a very low cohesion, allowing the laser pulses to liberate particles from the bulk sample. A possible second mechanism for the sample to spread could be the ionisation of a macroscopic sample particle, which is then influenced by the downwards extending electric fields of the mass analyser, leading to pickup of the particle and subsequent redeposition. Additionally, to the unwanted sample spread during measurement, the shallow cavities caused a bias towards smaller grain sizes, as particles extending beyond the surface of the sample holder were removed during sample preparation.

To address these issues, a new sample holder was designed to minimise sample loss, accommodate a wider range of grain sizes, and improve overall measurement consistency. The key features of the new design include:

- **Five sample channels**, allowing for the analysis of multiple samples or different preparation methods within a single measurement.
- **Increased cavity depth of** 1.2 mm, enabling the accommodation of particles up to 1 mm in diameter, aligning with the size distribution of LHS-1 regolith simulant and the lunar regolith.
- **Larger surface area**, allowing for extended rastering of the laser beam across pristine sample areas.
- **Extended surrounding area**, designed to catch any ejected sample material, reducing contamination of the vacuum chamber and other components.
- **Cutouts along the rim**, providing an unobstructed view of the ablation region for the sample observation system, allowing real-time monitoring and analysis of the laser-material interaction.

Additionally, an improved sample preparation procedure was developed to enhance sample preparation consistency and simulate the preparation conditions of a future sample handling system on the CLPS-LIMS. The process follows these steps:

1. **Filling the channels**: The sample material is poured into the cavities, ensuring complete coverage.
2. **Overfilling and scraping**: Excess regolith simulant is added to overfill the channels, followed by careful scraping to remove excess material extending above the surface of the sample holder. This step ensures a uniform surface level across all channels.
3. **No additional compaction**: To simulate a worst-case scenario in which the sample material has minimal cohesion, no further compression or consolidation is performed. This approach preserves the natural behaviour of loosely packed regolith and allows for the evaluation of potential sample displacement during measurements.

The developed and manufactured sample holder is shown in Figure 2.17. Two of the five channels are filled with LHS-1. The front view highlights the well-defined sample surface.

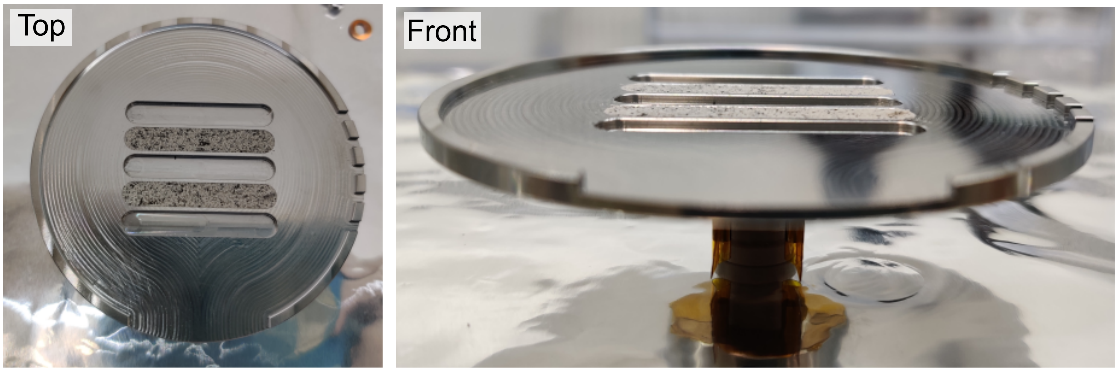

Figure 2.17: New sample holder specifically designed for the analysis of lunar regolith simulant. Two of the 1.2 mm deep, 5 mm, wide and 27 mm long channels are filled with LHS-1.

During continued usage of the system a significant issue was identified related to the interaction between ejected sample particles and the mass analyser's electrodes. In particular, sample grains could become stuck between the ground electrode and the subsequent acceleration electrode, as shown schematically in Figure 2.18 (panel A).

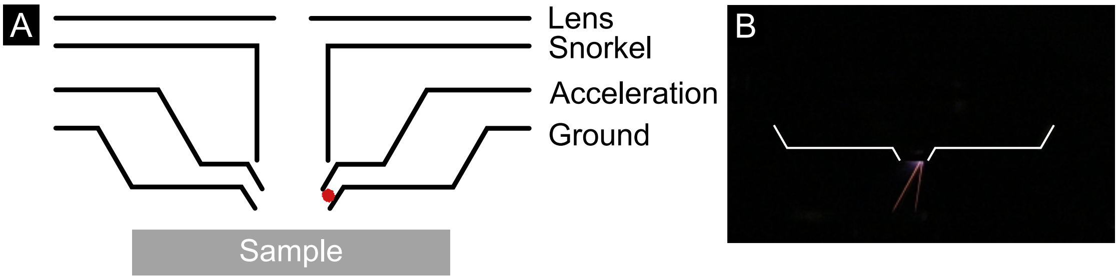

Figure 2.18: (A) Schematic of the mass analyser's entrance electrodes. A regolith simulant grain lodged between the ground and acceleration electrode is drawn in red. **(B)** Picture of an induced discharge to dislodge the stuck grain. The outlines of the ground electrode are highlighted.

The consequences of this contamination varied depending on the mineral composition and electrical properties of the trapped grain:

- **Loss of Spectral Signal:** If the trapped grains were electrically conductive, it could create electrical discharges, disrupting the electric field and preventing proper ion acceleration. This resulted during measurement in a complete loss of measurable signal, rendering the mass spectrometric analysis impossible.

- **Measurement Instability:** Even in cases where no immediate discharge occurred, the presence of a foreign particle within the electrode gap introduces the risk of signal fluctuations or degradation over time.

To restore nominal performance of the instrument, the contamination had to be removed. Normally, this was performed by venting the vacuum chamber and manually removing the stuck particle.

Additionally, a potential last-resort method for clearing the obstruction has been identified. By temporarily increasing the acceleration voltage beyond normal operation conditions, controlled discharges can be induced, as shown in Figure 2.18 (panel B). This process can dislodge the stuck particle and restore proper mass analyser functionality. While this approach is viable in emergency situations, it carries inherent risks, including potential long-term damage to the electrodes or power supplies. Therefore, it is considered a contingency measure, nevertheless one that can be performed during flight without local human interaction.

To mitigate the inherent risk of simulant grains become stuck, the minimum distance between the ground electrode and the acceleration electrode was increased from 0.3 mm to 0.6 mm. This change significantly reduces the likelihood of a grain becoming trapped within the gap, as fewer particles from the lunar regolith fall within this critical size range. Following the implementation of this design change into the instrument, roughly an order of magnitude more measurements were conducted with LHS-1 and no stuck grains were detected. As a risk mitigation strategy, this design change has been carried over to the CLPS-LIMS instrument.

2.4 Impact on related research

2.4.1 Laser-Based Mass Spectrometry for Organics Detection

The developed instrumentation presented in this chapter, mainly the microchip laser system and the sample observation system, are now fully integrated into the ORIGIN setup.

ORIGIN, in its nominal configuration, is mainly used for research concerning the detection and identification of bio-molecular signatures of life. Based on laser desorption, organic molecules known as building blocks of life, such as amino acids or different groups of lipids, can be detected.

The samples of interest are drop-cast into sample holders containing up to 25 cavities with diameters of 3 mm. Prior to the integration of the sample observation system, the only way to accurately position the sample under the laser beam was for the user to observe the sample through the viewports of the vacuum chamber while moving the sample stage. As the sample observation system delivers orthogonal side-on views of the sample holder, accurate positioning in all three axes via the delivered camera images is possible. In the following publication this feature is highlighted. In the future, this system can be extended to automatically detect features on the sample holder, which it can use as reference points, making fully automatic positioning of the sample holder possible.

For the desorption of molecules, a laser in the UV range is highly advantageous, as most molecules do not absorb light in the visible range. At the time of writing, a second optical tower with a SB1-based 266 nm laser was constructed to fully replace the active Q-switched laser system of the ORIGIN setup. The main advantage of this new laser system is the increased pulse-to-pulse energy stability of <1 %, making new measurement protocols feasible. A description of these is beyond the scope of this thesis.

doi:10.2533/chimia.2025.70 Chimia 79 (2025) 70–76

Life Detection Beyond Earth: Laser-Based Mass Spectrometry for Organics Detection on Solar System Objects

Andreas Riedo[a,b]*, Nikita J. Boeren[a,b], Peter Keresztes Schmidt[a], Marek Tulej[a], and
Peter Wurz[a,b]*

Abstract: The detection and identification of the building blocks of life, from amino acids to more complex molecules such as certain lipids, is a crucial but highly challenging task for current and future space exploration missions in our Solar System. To date, Gas Chromatography Mass Spectrometry has been the main technology applied. Although it has shown excellent performance in laboratory research, it has not yet been able to provide a conclusive answer regarding the presence or absence of a signature of life, extinct or extant, in space exploration. In this contribution we present the current measurement capabilities of our space prototype laser-based mass spectrometer for organics detection. The developed mass spectrometer currently allows the detection and identification of small organic molecules, such as amino acids and nucleobases, at sample concentrations at the level of femtomole mm^{-2}, using the same measurement protocol. The latter is highly relevant to space exploration, since with the instrumentation in use so far only one class of organics can be measured with one instrument configuration.

Keywords: Laser desorption mass spectrometry · Life detection · LIMS · Organics · Space exploration

Andreas Riedo received his PhD in Physics in 2014 from the University of Bern, Switzerland. In 2016 he received an SNSF fellowship that allowed him to conduct his research in Astrobiology at the Leiden University, The Netherlands. He extended his stay with an MCSA fellowship for another two years before he moved in 2019 to the Free University Berlin after receiving the Einstein fellowship. In 2020 he moved to University of Bern, received his *Venia Docendi* in 2022, and is currently appointed as project leader for a LIMS instrument to be deployed on a CLPS mission within NASA's Artemis program.

Nikita J. Boeren received her BSc in Analytical Chemistry from the University of Applied Sciences Leiden and an MSc jointly from the University of Amsterdam and Vrije Universiteit Amsterdam, The Netherlands. As a PhD candidate at the University of Bern, her research focuses on the detection of biosignatures using the ORIGIN setup for *in situ* space exploration targeting Mars, Europa, and Enceladus.

Peter Keresztes Schmidt received his BSc and MSc in Chemistry at the ETH Zürich, Switzerland. He is currently working as a PhD student in Bern, Switzerland, where he is developing a new LIMS instrument for *in situ* studies on the lunar surface.

Marek Tulej received a PhD in Physical Chemistry from the University of Basel, in 1999. After his postdoctoral period at Paul Scherrer Institute (PSI), he joined in 2008 the University of Bern as an instrument scientist for space missions, including Phobos-Grunt, Marco Polo-R, Luna-Resurs, and JUICE.

Peter Wurz has a degree in electronic engineering (1985), an MSc and a PhD in Physics from Technical University of Vienna, Austria (1990). He has been a postdoctoral researcher at Argonne National Laboratory, USA until 1992, after which he joined the University of Bern and became a full Professor of physics in 2008. From 2015–2022 he was the head of the Space Science and Planetology division, and since 2022 director of the physics institute. He has been Co-I and PI for many science instruments for space missions of ESA, NASA, ISRO, CNSA, Roscosmos, and JAXA.

1. Introduction

With the two Viking spacecraft that landed on Mars in the 1970s,[1] humanity began the challenging endeavour of detecting and identifying signatures of life in our Solar System. The landers were equipped with highly sophisticated payloads at that time, which included Gas Chromatography Mass Spectrometric (GC-MS) systems for molecular signature identification.[2-5] Unfortunately, *in situ* measurements of Martian surface material using the Viking science instrumentation did not provide conclusive evidence of the presence of life. Since then, other exploration mis-

---

Correspondence: PD Dr. A. Riedo, E-mail: andreas.riedo@unibe.ch, Physics Institute, University of Bern, Bern, CH-3012 Bern, Switzerland

sions have been or will be launched to search for life in our Solar System. NASA's Curiosity[6] and Perseverance rovers[7] are currently operating on the surface of Mars to better understand habitability conditions and search for life, and are the best equipped rovers ever operated in space science. In addition, the Perseverance rover is currently collecting sample material and sealing it in tubes, in preparation for later collection and transfer to Earth for detailed laboratory analysis as part of the Mars Sample Return Mission.[8–9]

There are different categories into which signatures of life can be grouped. The Mars 2020 Science Definition Team has defined six promising groups, ranging from isotope fractionation to macroscopic signatures visible to camera systems.[10–11] Building blocks of life, such as amino acids or lipids, are arguably a prominent category of life signatures. Their detection could indicate the presence of life as we know it. Consequently, the astrobiology community has been pushing for detection capabilities for these molecules on past, present, and future missions.[12–13] So far, GC-MS systems have been widely used in exploration missions because of their measurement capabilities,[14] *e.g.* L and D amino acids can be distinguished with the appropriate GC column, and their excellent performance in laboratory research. However, since the Viking missions to Mars, the GC-MS systems have not provided conclusive evidence of the presence of life. As a result, the space science community is looking for alternative and sensitive measurement technologies for future use.

Since the beginning of 2000, the Mass Spectrometry Group of the Institute for Space Research and Planetary Sciences at the University of Bern has been working on the design and investigation of laser-based mass spectrometers for the chemical (elements, isotopes, and molecules) analysis of samples for their potential application on future exploration missions.[15,16] In this contribution, we highlight the current measurement capabilities of our ORganics Information Gathering INstrument (ORIGIN),[17] which has been designed for *in situ* detection and identification of various groups of organics. ORIGIN is a Laser Ablation Ionisation Mass Spectrometry (LIMS) system that operates in the laser desorption mode to gently desorb organic molecules from sample surfaces. Based on the current measurement capabilities, several international groups have shown interest in using this technology on future missions, ranging from signature detection in the Venusian cloud to lipids on the Martian surface.

2. ORIGIN – Laser-based Mass Spectrometry

2.1 *System Description*

ORIGIN is a LIMS system operating in the laser desorption mode (highly reduced irradiance compared to the laser ablation mode) for the sensitive detection and identification of organic molecules. The system is described in more detail in previous publications,[17–19] so only a brief overview of the measurement principles is given here. The schematics and operating principle are shown in (Fig. 1). The system consists of a miniature reflection-type time-of-flight mass analyser[16] coupled to a pulsed nanosecond laser system (Nd:YAG, τ ~ 3 ns, λ = 266 nm, laser pulse repetition rate of 20 Hz, actively Q-switched). The simple beam delivery system placed on an optical table directs the laser pulses to the lens system which focuses the laser beam through the mass

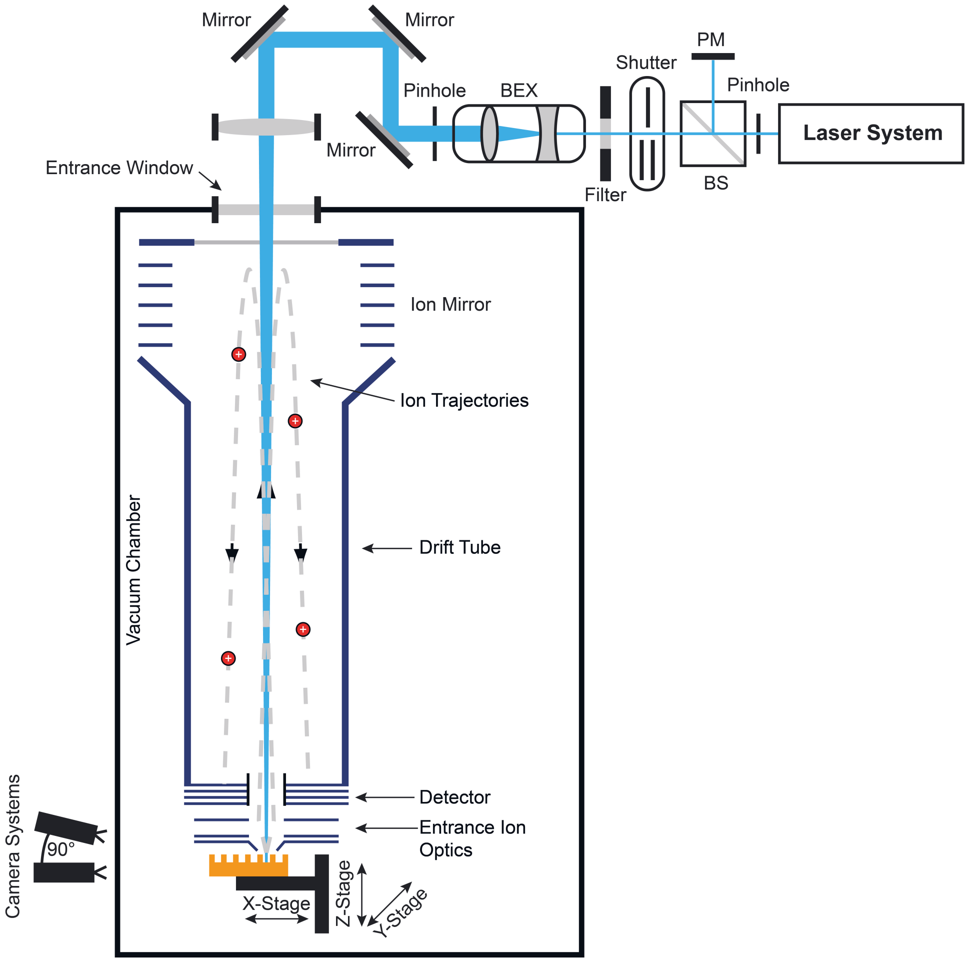

Fig. 1. Operating principle and schematics of the ORIGIN LIMS setup used for organics detection and identification.

analyser onto the sample surface to spot sizes of about 30 μm in diameter. Pulse energies in the range of about 1–5 μJ (at the surface) are typically applied in mass spectrometric studies, resulting in laser irradiances in the order of MW/cm^2. Each laser pulse gently desorbs and ionises the analyte of interest, allowing the positively charged species to enter the entrance ion optical elements of the mass analyser. The species are accelerated and confined towards the drift tube, reflected at the ion mirror towards the multichannel plate (MCP) detector system[20] through the drift tube a second time. The species arrive at the detector system sequentially according to their mass-to-charge ratio (Time of Flight (TOF) measurement principle). Read-out-electronics with a sampling rate of up to 2 GS/s record the TOF spectrum (length of 20 μs) for each laser pulse, which is then stored on the host computer for post processing. Software packages written in-house are used for subsequent data analysis.[21] Empty TOF spectra (*i.e.* no mass peak detected above the noise floor, typically 6 sigma) are not considered for analysis. The sample holder is placed on an XYZ stage to allow for accurate positioning of the holder below the mass analyser aperture. Two cameras mounted orthogonally allow for visual feedback of the sample holder position. In Fig. 2 the visual imaging of the sample holder together with the entrance ion optics of the mass analyser from one of the cameras is shown. The bright white spot visible below the mass analyser corresponds to the focus of the laser beam and the induced plasma (here laser ablation conditions).

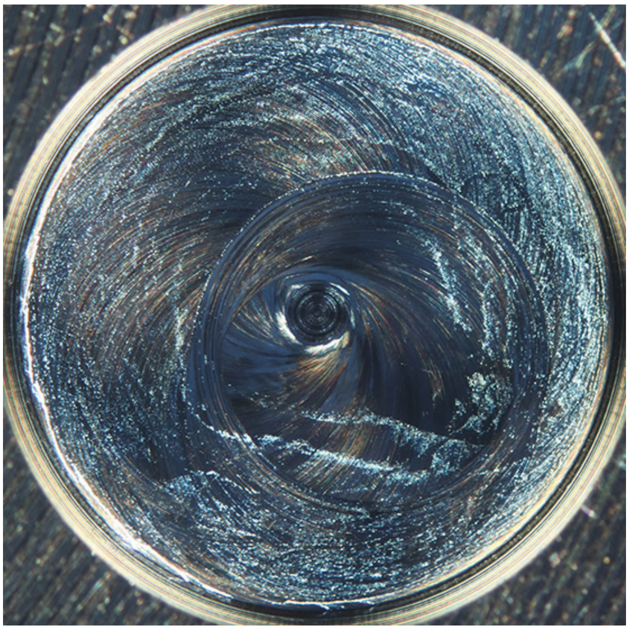

Fig. 3. Optical microscopy image of a sample cavity containing adenine (1 mM concentration, in solution). Adapted from Boeren *et al.* ref. [19].

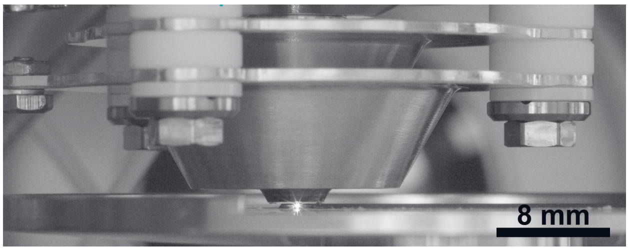

Fig. 2. *In situ* imaging during LIMS measurements. The bright spot below the mass analyser aperture corresponds to the focused laser beam.

2.2 *Measurement Protocol*

Typically, 1 μL of sample analyte is drop cast into a cavity (0.2 mm × Ø 3 mm) of a sample holder. It is important to note that in contrast to MALDI no matrix is present within the cavity. Prior to integration into the vacuum chamber, the sample holder is placed on a clean bench (ISO5) where the water or other solvent containing the analyte of interest can evaporate in a clean environment. The sample holder with the remaining organic residue film is then placed in the vacuum chamber, the chamber is evacuated, and once a low enough pressure is reached (~ 5×10^{-7} mbar) the mass spectrometric measurements are initiated. Each cavity is typically spot-wise investigated over 40 surface positions (can be adapted to the scientific needs), considering the inhomogeneous distribution of the residue film (see Fig. 3). A Python control package conducts the measurements autonomously according to user input.

3. Detection and Identification of Organics

3.1 *Amino Acids*

After the design and manufacturing phase of ORIGIN, the first measurements were conducted in 2019 on up to 20 biotic and abiotic amino acids, drop cast into cavities of a stainless steel holder at various concentrations (1 μl drop cast of 100–1 μM solutions, corresponding to 14–0.14 pmol mm^{-2}, or 100–1 pmol / g ice), mixtures thereof, and contaminated with NaCl salt.[17] The aforementioned gram of ice corresponds to a sample received during a mission on an icy moon, *e.g.* Europa Lander mission.[12] The measurements showed that each amino acid can be identified in the mass spectra by its simple and unique fragmentation pattern induced by the laser-molecule interaction. The current setup does not allow differentiation between isomers, *e.g.* iso-leucine and leucine, or measurement of the enantiomeric excess (L/D). The top panel of Fig. 4 shows a mass spectrum of aspartic acid (Asp, 100 μM, in solution, 100 pmol / g ice, 14 pmol mm^{-2}) measured using the typical measurement protocol. The recorded mass spectrum shows three distinct mass peaks of Asp, allowing the amino acid to be reliably identified. When distributed over the 40 surface positions, variations in intensities are observed, as expected, due to the inhomogeneous distribution of the molecule 'film' over the cavity. However, the ratio between the fragments remains almost constant (within one sigma, see Fig. 2 in Ligterink *et. al*. 2020),[17] allowing an identification by fragment ratio analysis, comparable to element isotope analysis. Consequently, this information can be used to feed a database that allows the simulation of amino acid patterns. The lower panel of Fig. 4 shows such a simulation of Asp, simulating the three major fragments observed for Asp. It is planned to consolidate the software routine (not yet finalised) for post-analysis of the presence and abundances of species within a more complex mixture by fragment ratio analysis and least- square fitting. In addition, the first large measurement campaign carried out on up to 20 amino acids using the ORIGIN setup, has shown that there is a linear correlation between fragment intensity and amino acid concentration. In Fig. 5 the linear correlation between the drop cast concentration and one of the major fragments (at mass *m/z* of 110) of histidine (His) is shown. This is extremely valuable information as it allows a rough estimation of the abundances of the molecules detected. It should be noted that such a correlation can only be derived for thin films or low concentrations of organics, as we expect to receive on *e.g.* Mars or the ice moons Europa and Enceladus.[12–13] Above a certain concentration, resulting in a thick layer of organics, we expect a saturation effect due to a maximum limit in desorbed sample material per laser shot using our current measurement protocol.

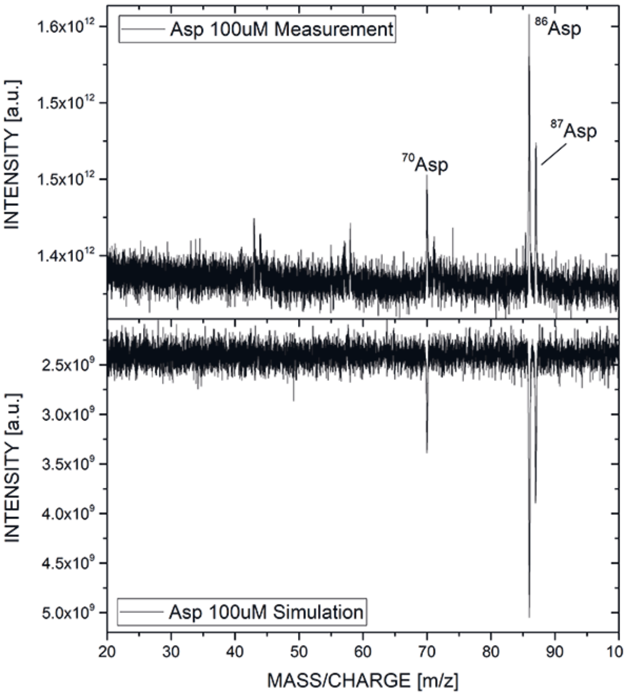

Fig. 4. Top: measured mass spectrometric pattern of aspartic acid (Asp), drop cast with a concentration in solution of 100 µM. Bottom: simulated spectra of Asp.

For space exploration missions, an instrument is typically designed to detect and identify only one class of molecules, for example amino acids. This minimises the complexity of the instrument and the associated risks in manufacturing and operation, as well as the costs overall. The disadvantage of this approach is that it is pre-selective, *i.e.* other molecule classes may not be detected. This is particularly true when using the current gold standard in organic analytics, the GC-MS instrumentation, where the selected column defines which class of molecules can be detected *in situ* on the planetary object. Therefore, and after exploring the detection of amino acids in more detail, *e.g.* using network analysis to separate matrix and signal from molecules,[23] it was logical for our team to explore how the measurement protocol developed for amino acids could be applied to different and more complex organic molecules.

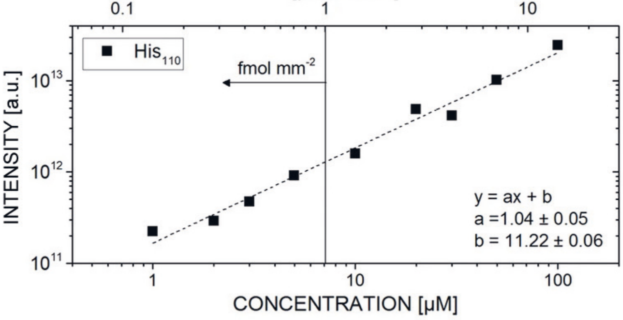

Fig. 5. Correlation between amino acid concentration and recorded fragment intensity of the amino acid histidine. Here, one of the major fragments of His with mass *m/z* of 110 was used for the correlation. Image taken and adapted from Ligterink *et al.* ref. [17].

3.2 *Polycyclic Aromatic Hydrocarbons (PAHs)*

So far, the measurement protocol has allowed the detection of Polycyclic Aromatic Hydrocarbons (PAHs),[22] which are representative of more complex molecules, lipids,[18] and more recently, nucleobases,[19] the latter two being linked to life as we know it. PAHs do not have the same importance for life as amino acids or lipids, as they are abundant in the Interstellar Medium (ISM), however they could be precursor molecules important for life, see discussion in Kipfer *et al.* and references therein or Ehrenfreund *et al.*[22,24] In Fig. 6 the successful detection of four different PAHs (anthracene ($C_{14}H_{10}$), pyrene ($C_{16}H_{10}$), perylene ($C_{20}H_{12}$), and coronene ($C_{24}H_{12}$), 100 µM in solution (100 pmol / g ice, or 14 pmol mm^{-2}), measured at 4 µJ laser pulse energy) using ORIGIN and the identical measurement protocol as for amino acids is shown. In contrast to amino acids, the parent (for anthracene, perylene, and coronene) or protonated (pyrene) mass spectrometric peaks were detected directly, allowing their easy identification. Of the five PAHs analysed, coronene had the clearest mass spectrum by means of fragmentation. The robust aromatic ring structures of PAHs and the improved coupling with UV wavelengths clearly enhance the laser desorption process. For the investigated PAHs, limits of detection (3 sigma) of only a few tens of fmol mm^{-2} were observed, and, similar to amino acids, the abundance can be derived from the detected peak signals (see Figs. 7 and 8, respectively, in Kipfer *et al.*).

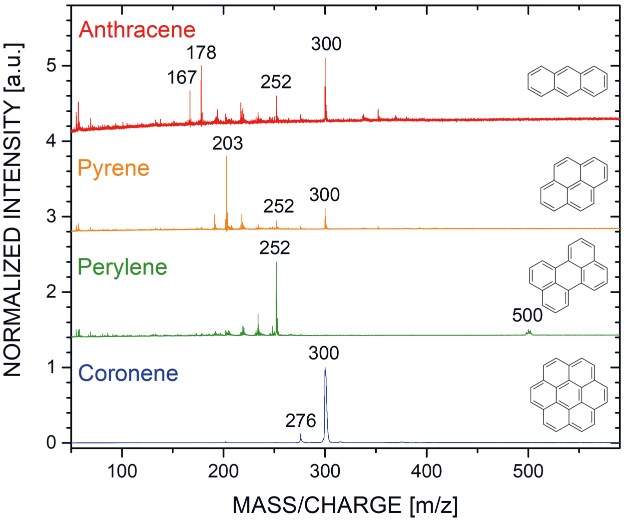

Fig. 6. The PAHs anthracene, pyrene, perylene and coronene (100 µM, in solution) were successfully detected and identified using the same measurement protocol as for the amino acids. Image adapted from Kipfer *et al*. ref. [22].

3.3 *Lipids*

In Boeren *et al.*[18] six different lipids were studied in detail, including cholecalciferol, phyllo-quinone, menadione, 17α-ethynylestradiol, α-tocopherol, and retinol. In Fig. 7 the mass spectra of α-tocopherol (430.71 g mol^{-1}), phylloquinone (450.70 g mol^{-1}), and 17α-ethynylestradiol (296.40 g mol^{-1}) are shown (taken and adapted from Boeren *et al.*).[18] The molecules shown had a concentration of 400 µM (400 pmol / g ice, or 56 pmol mm^{-2}), which allowed a better understanding of their detectability with ORIGIN. Similar to the PAH study, each lipid investigated showed its own unique fragmentation pattern with its parent peak and a few minor fragment peaks. While for 17α-ethynylestradiol and α-tocopherol the parent peak is the most abundant signal in the recorded spectrum (see Fig. 7), a much lower intensity was observed for phylloquinone, having the most intense peak at [M-2]$^+$. Concentration scans conducted in the range of 7 fmol mm^{-2} to 28 pmol mm^{-2} on the three presented lipids, allowed the derivation of the theoretical limit of detection (at the 3 sigma level, $LOD_{3\sigma}$). The $LOD_{3\sigma}$ values for α-tocopherol, phylloquinone, and 17α-ethynylestradiol of 34 fmol mm^{-2}, 85 fmol mm^{-2}, and 0.2 fmol mm^{-2}, respectively, were derived from this campaign (< 100 fmol mm^{-2}, 710 fmol / g ice). In Boeren *et al.* we also demonstrated the reliable detection and identification of mixtures of the three classes of organic molecules studied so far, namely amino acids, PAHs, and lipids (see Fig. 4 in said publication),[18] which represents a real milestone in the application of this detection technology.

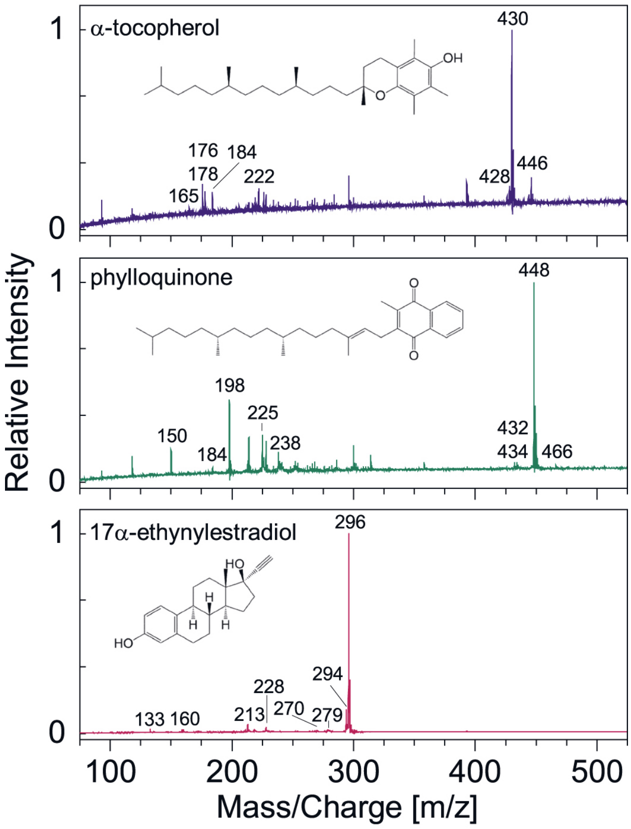

Fig. 7. Laser desorption mass spectra of α-tocopherol, phylloquinone, and 17α-ethynylestradiol standards are shown. The standards examined had a concentration of 400 µM. Image taken and adapted from Boeren *et al.* ref. [18].

3.3 *Nucleobases*

More recently, the identical measurement protocol was used for the successful detection and identification of nucleobases with ORIGIN, investigating single nucleobases and mixtures of several nucleobases, at various concentrations.[19] In Fig. 8, laser desorption mass spectra of adenine (135.1 g mol^{-1}), guanine (151.1 g mol^{-1}), uracil (112.1 g mol^{-1}), thymine (126.1 g mol^{-1}), cytosine (111.1 g mol^{-1}), and 5-methylcytosine hydrochloride (161.6 g mol^{-1}) are shown. Minimal fragmentation can be observed and in almost all cases the parent or protonated parent peak was detected. The more stable aromatic ring structure of the studied compounds, in comparison to a typical amino acid, is one reason why a limited fragmentation is observed. Interestingly, significantly more signal, thus better ionisation was observed for 5-methylcytosine than for cytosine, despite the difference of only one methyl group. This study also showed that increasing the number of sample surface positions from a nominal 40 to several hundred increases the detection sensitivity of the instrument by a decade (see Fig. 4 in the same publication). For example, an $LOD_{3\sigma}$ of 50 fmol mm^{-2} (~ 350 fmol / g ice) was derived for adenine, which is well in line with the mission requirements for ExoMars with the detection of ≤ 1 nmol with signal-to-noise ratio (SNR) ≥ 10[25] corresponding to 141 fmol mm^{-2}, or the Europa Lander mission study with 1 pmol / g ice corresponding to 141 fmol mm^{-2}.[12] Also of note is the clean background compared to previous studies. The introduction of argon sputtering of the sample holder prior to drop casting of the analyte significantly reduced the carry-over from previous studies, allowing improved detection and a better understanding of the signatures of the molecules studied.[19] Note, argon ion sputtering cannot and will be not applied during a space mission; it allows the re-use of sample holders during laboratory tests.

3.4 *Matrix Effects and Identification Strategies*

Laser desorption measurements have been conducted so far on organic compounds mixed with NaCl,[17] and on KCl,[17] $(NH_4)_2SO_4$, $MgSO_4$, and $CaCO_3$.[26] Typically, only the cation of each matrix (*e.g.* Na$^+$) was detected as the system is operated in the positive ion mode. These mass lines typically do not interfere with the mass lines for organic compound identification. A slight interference with Ca$^+$ is observed with the pattern of the amino acid alanine (compare Fig. 1 in Ligterink *et al.*[17] with Fig. 4 in Ligterink *et al.*[26]). In the presence of NaCl slightly higher pulse energies were required to reliably detect the amino acids. The salt crust might reduce the desorption and ionization efficiency of the amino acids present in the salt/organics mixture.[17]

For the identification of molecular structures that interfere with each other, an increase in pulse energy might provide further insights into the compounds present. The increased pulse energy results in increased fragmentation, whereas the energy thresholds at which this occurs, are compound specific. As a consequence, the newly generated fragments might allow a better insight into the molecules present.

4. Future Applications

The measurement protocol using ORIGIN is currently based on the availability of an organic residue film on a preferably conductive surface, to support the laser desorption ionisation process. Extraction of organics from soil or mineral matrices using laser ablation conditions (elevated laser irradiances at the level of GW/cm^2 or higher) would severely fragment the organic structures and consequently limit their detection. Therefore, for the application of the current measurement protocol, we are either dependent on a solvent-based organic extraction unit or the organics are in a liquid phase, such as ice or droplets, which can be collected. After receiving or collecting the material, the liquid phase may evaporate through the application of heat and/or vacuum conditions, leaving a residual film of organics. Due to the versatile measurement capabilities and high detection sensitivity of our space prototype mass spectrometer for the detection of organics, several international partners have expressed interest in using the instrument on future space exploration missions targeting different objects in the Solar System, including missions to Venus and Mars.

We are actively participating in the Morning Star Mission program, which aims to find signatures of life in the Venusian atmosphere.[27–29] The presence of life in the atmosphere, which might act as a life-supporting habitat, could explain some observations that cannot be explained otherwise. The middle and lower cloud deck, at about 50 to 60 km above the surface, has milder temperature conditions of about 60°C and about 1 bar of pressure compared to the harsh environment at the surface (hundreds of Celsius and tens of bars).[28] The current mission scenario foresees using

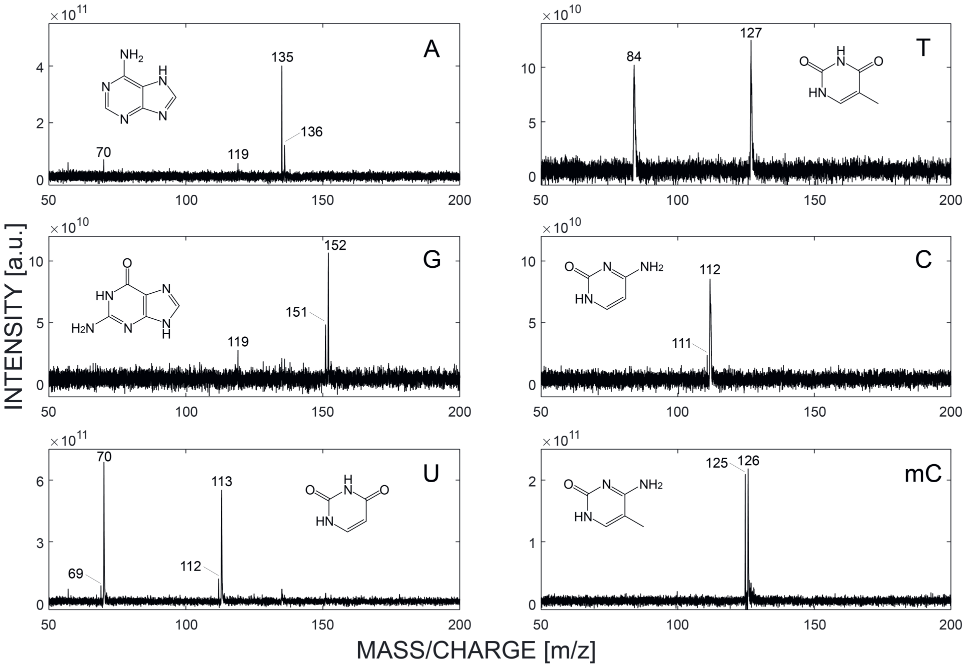

Fig. 8. Laser desorption mass spectra of adenine (A), guanine (G), uracil (U), thymine (T), cytosine (C), and 5-methylcytosine (mC) using ORIGIN. Concentrations: 5 pmol mm^{-2} for A, 14 pmol mm^{-2} for G, C, and mC, 707 pmol mm^{-2} for U, and 141 pmol mm^{-2} for T. Image adapted from Boeren *et al*. ref. [19].

a flight version of ORIGIN, where droplets will be collected in the wet atmosphere using a sampling system to be designed. Subsequently, the media in which the organics are expected, mainly sulfuric acid, will be removed by thermal heating and application of vacuum conditions (vacuum desiccation). The remaining film with possible organic material will then be analysed by ORIGIN using the measurement protocol described above.

Because of its history, Mars is one of the most promising candidates in our Solar System that still might host life or contains signatures of past life in the Martian subsurface. Together with colleagues from NASA Ames Research Center, we are working on the Abzu lander mission to Mars, that focuses on the detection of lipid signatures. NASA Ames has developed and further validated an extraction unit, named Extractor for Chemical Analysis of Lipid Biomarkers in Regolith (ExCALiBR).[30–31] ExCALiBR accepts soil material and by solvent extraction provides a concentrated lipid extract. In Abzu,[30] both ExCALiBR and ORIGIN are integrated into a sample carousel containing a number of sample cavities. The extract from ExCALiBR is drop cast onto a sample cavity within the sample carousel, which is then evacuated to rough vacuum conditions. The rough vacuum conditions allow the used solvents to be removed, and turning the sample cavity towards ORIGIN allows the extract to be analysed.

The icy moons Europa and Enceladus, moons of Jupiter and Saturn respectively, are other promising candidates in our Solar System[32] where ORIGIN could find its application. The current scientific community strongly believes that the liquid oceans represent habitats where life could have flourished and been sustained. Through cracks in the ice sheets, existing life or its signatures can escape from the oceans[33] and form deposits on the ice crust, which can be studied much more easily with a landed mission than directly in the ocean. The Europa Lander Study Report[12] and the Enceladus Orbilander Mission Concept[13] outline the mission objectives and for example, the required detection sensitivity of future payloads for the detection of organics. The current measurement capabilities of ORIGIN meet several mission requirements, such as detection limits or the detection of different molecule classes or molecules of such a class.[12,17]

5. Conclusions

The detection and identification of signatures of life, past or present, on a planetary body is one of the major goals of current space research and planetary exploration. A conclusive detection of signatures of life would have a tremendous impact on science and the general public, as we would know for the first time that life is not unique to Earth. In this contribution, we have demonstrated the current measurement capabilities of our space prototype mass spectrometry system ORIGIN – a laser-based ionisation mass spectrometer operated in the desorption mode. The system has recently been developed for the detection and identification of organics related to life. To date, the gentle desorption without matrix application allows the identification of amino acids, PAHs, lipids, and nucleobases using the same measurement protocol. The measurement methodology is based on the spot-wise chemical analysis of a residual organic film and the acquisition of mass spectra for each laser shot applied. Through molecule specific fragments or the detection of the parent peak, reliable identification of the organic species is possible, even within a mixture. The current measurement versatility, together with the high detection sensitivity, allows the payload requirements to be met, for example for a landed mission on Europa or Enceladus. The system can therefore be of real added value for future space exploration missions dedicated to the detection of life.

Acknowledgements

A.R. acknowledges support from the European Union’s Horizon 2020 research and innovation program under the Marie Skłodowska-Curie grant agreement No. 750353. This work has been carried out within the framework of the NCCR PlanetS supported by the Swiss National Science Foundation under grants 51NF40_182901 and 51NF40_205606.

Author Contributions

AR, NJB, and PKS were involved in conceptualization, formal analysis, investigation, methodology, and validation. AR was involved in supervision, funding acquisition, and writing the original draft. PKS was involved in software activities. PW was involved in supervision and funding acquisition. All were involved in reviewing and editing of the manuscript.

Received: November 7, 2024

[1] G. A. Soffen, C. W. Snyder, *Science* **1976**, *193*, 759, https://doi.org/10.1126/science.193.4255.759

[2] V. I. Oyama, B. J. Berdahl, G. C. Carle, M. E. Lehwalt, H. S. Ginoza, *Origins Life* **1976**, *7*, 313, https://doi.org/10.1007/BF00926949.

[3] V. I. Oyama, *Icarus* **1972**, *16*, 167, https://doi.org/10.1016/0019-1035(72)90144-3.

[4] G. V. Levin, P. A. Straat, *Biosystems* **1977**, *9*, 165, https://doi.org/10.1016/0303-2647(77)90026-0.

[5] N. H. Horowitz, J. S. Hubbard, G. L. Hobby, *Icarus* **1972**, *16*, 147, https://doi.org/10.1016/0019-1035(72)90142-X.

[6] J. P. Grotzinger, J. Crisp, A. R. Vasavada, R. C. Anderson, C. J. Baker, R. Barry, D. F. Blake, P. Conrad, K. S. Edgett, B. Ferdowski, R. Gellert, J. B. Gilbert, M. Golombek, J. Gómez-Elvira, D. M. Hassler, L. Jandura, M. Litvak, P. Mahaffy, J. Maki, M. Meyer, M. C. Malin, I. Mitrofanov, J. J. Simmonds, D. Vaniman, R. V. Welch, R. C. Wiens, *Space Sci. Rev.* **2012**, *170*, 5, https://doi.org/10.1007/s11214-012-9892-2.

[7] K. A. Farley, K. H. Williford, K. M. Stack, R. Bhartia, A. Chen, M. de la Torre, K. Hand, Y. Goreva, C. D. K. Herd, R. Hueso, Y. Liu, J. N. Maki, G. Martinez, R. C. Moeller, A. Nelessen, C. E. Newman, D. Nunes, A. Ponce, N. Spanovich, P. A. Willis, L. W. Beegle, J. F. Bell, A. J. Brown, S.-E. Hamran, J. A. Hurowitz, S. Maurice, D. A. Paige, J. A. Rodriguez-Manfredi, M. Schulte, R. C. Wiens, *Space Sci. Rev*. **2020**, *216*, 142, https://doi.org/10.1007/s11214-020-00762-y.

[8] B. K. Muirhead, A. Nicholas, J. Umland, IEEE Aerospace Conf. **2020**, p. 1, https://doi.org/10.1109/AERO47225.2020.9172609.

[9] G. Kminek, M. A. Meyer, D. W. Beaty, B. L. Carrier, T. Haltigin, L. E. Hays, *Astrobio*. **2021**, *22*, S, https://doi.org/10.1089/ast.2021.0198.

[10] J. F. Mustard, M. Adler, A. Allwood, D. S. Bass, D. W. Beaty, J. F. Bell III, W. B. Brinckerhoff, M. Carr, D. J. Des Marais, B. Drake, K. S. Edgett, J. Eigenbrode, L. T. Elkins-Tanton, J. A. Grant, S. M. Milkovich, D. Ming, C. Moore, S. Murchie, T. C. Onstott, S. W. Ruff, M. A. Sephton, A. Steele, A. Treiman, 2013, Report of the Mars 2020 Science Definition Team, 154 pp., posted July, 2013, by the Mars Exploration Program Analysis Group (MEPAG) at http://mepag.jpl.nasa.gov/reports/MEP/Mars_2020_SDT_Report_Final.pdf.

[11] L. E. Hays, H. V. Graham, D. J. D. Marais, E. M. Hausrath, B. Horgan, T. M. McCollom, M. N. Parenteau, S. L. Potter-McIntyre, A. J. Williams, K. L. Lynch, *Astrobiology* **2017**, *17*, 363, https://doi.org/10.1089/ast.2016.1627.

[12] K. P. Hand, A. E. Murray, J. B. Garvin, W. B. Brinckerhoff, B. C. Christiner, K. S. Edgett, B. L. Ehlmann, C. R. German, A. G. Hays, T. M. Hoehler, S. M. Horst, J. I. Lunine, K. H. Nealson, C. Paranicas, B. E. Schmidt, D. E. Smith, A. R. Rhoden, M. J. Russel, A. S. Templeton, P. A. Willis, R. A. Yingst, C. B. Phillips, M. L. Cble, K. L. Craft, A. E. Hofmann, T. A. Nordheim, R. P. Pappalardo, and the Project Engineering Team (2017): Report of the Europa Lander Science Definition Team. Posted February, **2017**.

[13] S. M. MacKenzie, M. Neveu, A. F. Davila, J. I. Lunine, K. L. Craft, M. L. Cable, C. M. Phillips-Lander, J. D. Hofgartner, J. L. Eigenbrode, J. H. Waite, C. R. Glein, R. Gold, P. J. Greenauer, K. Kirby, C. Bradburne, S. P. Kounaves, M. J. Malaska, F. Postberg, G. W. Patterson, C. Porco, J. I. Núñez, C. German, J. A. Huber, C. P. McKay, J.-P. de Vera, J. R. Brucato, L. J. Spilker, *Planet. Sci. J*. **2021**, *2*, 77, https://doi.org/10.3847/PSJ/abe4da.

[14] P. R. Mahaffy, C. R. Webster, M. Cabane, P. G. Conrad, P. Coll, S. K. Atreya, R. Arvey, M. Barciniak, M. Benna, L. Bleacher, W. B. Brinckerhoff, J. L. Eigenbrode, D. Carignan, M. Cascia, R. A. Chalmers, J. P. Dworkin, T. Errigo, P. Everson, H. Franz, R. Farley, S. Feng, G. Frazier, C. Freissinet, D. P. Glavin, D. N. Harpold, D. Hawk, V. Holmes, C. S. Johnson, A. Jones, P. Jordan, J. Kellogg, J. Lewis, E. Lyness, C. A. Malespin, D. K. Martin, J. Maurer, A. C. McAdam, D. McLennan, T. J. Nolan, M. Noriega, A. A. Pavlov, B. Prats, E. Raaen, O. Sheinman, D. Sheppard, J. Smith, J. C. Stern, F. Tan, M. Trainer, D. W. Ming, R. V. Morris, J. Jones, C. Gundersen, A. Steele, J. Wray, O. Botta, L. A. Leshin, T. Owen, S. Battel, B. M. Jakosky, H. Manning, S. Squyres, R. Navarro-González, C. P. McKay, F. Raulin, R. Sternberg, A. Buch, P. Sorensen, R. Kline-Schoder, D. Coscia, C. Szopa, S. Teinturier, C. Baffes, J. Feldman, G. Flesch, S. Forouhar, R. Garcia, D. Keymeulen, S. Woodward, B. P. Block, K. Arnett, R. Miller, C. Edmonson, S. Gorevan, E. Mumm, *Space Sci. Rev.* **2012**, *170*, 401, https://doi.org/10.1007/s11214-012-9879-z.

[15] U. Rohner, J. A. Whitby, P. Wurz, *Meas. Sci. Technol*. **2003**, *14*, 2159, https://doi.org/10.1088/0957-0233/14/12/017.

[16] A. Riedo, A. Bieler, M. Neuland, M. Tulej, P. Wurz, *J. Mass Spectro*m **2013**, *48*, 1, https://doi.org/10.1002/jms.3104.

[17] N. F. W. Ligterink, V. Grimaudo, P. Moreno-Garcia, R. Lukmanov, M. Tulej, I. Leya, R. Lindner, P. Wurz, C. S. Cockell, P. Ehrenfreund, A. Riedo, *Sci. Rep*. **2020**, *10*, 9641, https://doi.org/10.1038/s41598-020-66240-1.

[18] N. J. Boeren, S. Gruchola, C. P. de Koning, P. Keresztes Schmidt, K. A. Kipfer, N. F. W. Ligterink, M. Tulej, P. Wurz, A. Riedo, *Planet. Sci. J.* **2022**, *3*, 241, https://doi.org/10.3847/PSJ/ac94bf.

[19] N. J. Boeren, P. Keresztes Schmidt, M. Tulej, P. Wurz, A. Riedo, *Planet. Sci. J*. **2024**, (in press), https://doi.org/10.3847/PSJ/ad9de9.

[20] A. Riedo, M. Tulej, U. Rohner, P. Wurz, *Rev. Sci. Instrum.* **2017**, *88*, 045114, https://doi.org/10.1063/1.4981813.

[21] S. Meyer, A. Riedo, M. B. Neuland, M. Tulej, P. Wurz, *J. Mass Spectrom*. **2017**, *52*, 580, https://doi.org/10.1002/jms.3964.

[22] K. A. Kipfer, N. F. W. Ligterink, J. Bouwman, L. Schwander, V. Grimaudo, C. P. de Koning, N. J. Boeren, P. Keresztes Schmidt, R. Lukmanov, M. Tulej, P. Wurz, A. Riedo, *Planet. Sci. J*. **2022**, *3*, 43, https://doi.org/10.3847/PSJ/ac4e15.

[23] L. Schwander, N. F. W. Ligterink, K. A. Kipfer, R. A. Lukmanov, V. Grimaudo, M. Tulej, C. P. de Koning, P. Keresztes Schmidt, S. Gruchola, N. J. Boeren, P. Ehrenfreund, P. Wurz, A. Riedo, *Front. Astron. Space Sci*. **2022**, *9*, https://doi.org/10.3389/fspas.2022.909193.

[24] P. Ehrenfreund, S. Rasmussen, J. Cleaves, L. Chen, *Astrobiology* **2006**, *6*, 490, https://doi.org/10.1089/ast.2006.6.490.

[25] F. Goesmann, W. B. Brinckerhoff, F. Raulin, W. Goetz, R. M. Danell, S. A. Getty, S. Siljeström, H. Mißbach, H. Steininger, R. D. Arevalo, A. Buch, C. Freissinet, A. Grubisic, U. J. Meierhenrich, V. T. Pinnick, F. Stalport, C. Szopa, J. L. Vago, R. Lindner, M. D. Schulte, J. R. Brucato, D. P. Glavin, N. Grand, X. Li, F. H. W. van Amerom, *Astrobiology* **2017**, *17*, 655, https://doi.org/10.1089/ast.2016.1551.

[26] N. F. W. Ligterink, K. A. Kipfer, S. Gruchola, N. J. Boeren, P. Keresztes Schmidt, C. P. de Koning, M. Tulej, P. Wurz, A. Riedo, *Aerospace* **2022**, *9*, 312, https://doi.org/10.3390/aerospace9060312.

[27] S. Seager, J. J. Petkowski, C. E. Carr, D. Grinspoon, B. Ehlmann, S. J. Saikia, R. Agrawal, W. Buchanan, M. U. Weber, R. French, P. Klupar, S. P. Worden, 'Venus Life Finder Mission Study ', a. e-prints, **2021**.

[28] S. Seager, J. J. Petkowski, C. E. Carr, D. H. Grinspoon, B. L. Ehlmann, S. J. Saikia, R. Agrawal, W. P. Buchanan, M. U. Weber, R. French, P. Klupar, S. P. Worden, D. Baumgardner, *Aerospace* **2022**, *9*, 385, https://doi.org/10.3390/aerospace9070385.

[29] D. Duzdevich, J. J. Petkowski, W. Bains, H. J. Cleaves, C. E. Carr, E. I. Borowska, A. Azua-Bustos, M. L. Cable, G. E. Dorrington, D. H. Grinspoon, N. F. W. Ligterink, A. Riedo, P. Wurz, S. Seager, *Aerospace* **2022**, *9*, 597, https://doi.org/10.3390/aerospace9100597.

[30] M. B. Wilhelm, A. Ricco, D. Oehler, D. Buckner, A. Rodriguez, P. Mahaffy, J. Eigenbrode, M. Ditzler, J. G. Blank, M. Nuevo, P. Sobron, E. Eshelman, A. Nawaz, A. Southard, R. H. Williams, G. Komatsu, P. M. Furlong, T. Smith, T. Fong, J. Koehne, L. Jahnke, D. D. Marais, M. Chin, T. Boone, T. Chinn, K. Sridhar, T. McClure, T. Hoac, M. J. Anderson, L. Radosevich, A. Rademacher, L. Friend, S. Baird, T. Evans, J. Bookbinder, M. Bicay, *Bull. AAS* **2021**, *53*, https://doi.org/10.3847/25c2cfeb.10b58580.

[31] D. K. Buckner, M. J. Anderson, S. Wisnosky, W. Alvarado, M. Nuevo, A. J. Williams, A. J. Ricco, Anamika, S. Debic, L. Friend, T. Hoac, L. Jahnke, L. Radosevich, R. Williams, M. B. Wilhelm, *Astrobiology* **2023**, *24*, 1, https://doi.org/10.1089/ast.2023.0012.

[32] J. I. Lunine, *Acta Astronaut.* **2017**, *131*, 123, https://doi.org/https://doi.org/10.1016/j.actaastro.2016.11.017.

[33] K. Bywaters, C. R. Stoker, N. Batista Do Nascimento, L. Lemke, *Life* **2020**, *10*, 40, https://doi.org/10.3390/life10040040.

License and Terms

2.4.2 Additive Manufacturing in Space Research

During the CLPS-LIMS project substantial knowledge in additive manufacturing was gained, as lots of instrument and subsystem models, as well as miscellaneous laboratory tools were produced using 3D printing.

This cumulated in the idea of manufacturing parts of the LMS instrument's ion-optical system with the help of fused filament fabrication (Singh et al. 2020). The availability of electrically conductive and isolating filaments made it possible to produce the complete reflectron of the ion-optical design without the need for conventionally machined parts.

The following publication describes the production process and subsequent tests of the new reflectron, proving it being ion-optically equivalent to the conventionally produced one.

The described technique holds the potential to rapidly prototype new ion-optical designs, allowing for fast-iteration laboratory tests of those.

JAAS

TECHNICAL NOTE

Cite this: DOI: 10.1039/d4ja00392f

Additive manufacturing in space research: hybrid mass analyser for laser ablation ionisation mass spectrometry

Andreas Riedo, *[ab] Peter Keresztes Schmidt, [a] Nikita J. Boeren, [ab] Salome Gruchola, [a] Luca N. Knecht, [a] Marek Tulej [a] and Peter Wurz [ab]

Received 29th October 2024
Accepted 29th January 2025

DOI: 10.1039/d4ja00392f

rsc.li/jaas

Additive manufacturing has found its way into many industrial and academic areas. In this contribution, we present an additively manufactured reflectron, integrated in a space-prototype mass analyser used in laser ablation ionisation mass spectrometry. Fused deposition modelling technology was applied to produce the reflectron's ion optical system. For the insulating parts, polylactic acid filament was used as printing material, while the conductive ion optical parts were printed using polylactic acid impregnated with carbon. Measurements were conducted on a stainless steel sample (AISI 316 L, 1.4435) and NIST SRM 661 sample to validate the performance of the reflectron. We found that this system performed nominally in terms of mass resolution and detection sensitivity. This demonstrates the suitability of 3D printing for rapid prototyping in laboratory environments. The latter is of considerable importance for future space exploration missions, as the methodology allows testing of new designs time efficiently and at reduced costs.

Introduction

With the availability of affordable 3D printers offering excellent print quality, additive manufacturing is increasingly being used in industrial and academic activities.[1–4] In recent years, the technology has also been applied in analytical chemistry, *e.g.*, supporting daily laboratory work (*e.g.*, tools for sample preparation or mechanical structures used in measurement setups) and is now increasingly utilised in mass spectrometry and spectroscopy. To give just a few examples, additive manufacturing has been successfully applied to separation technologies,[5] ion guides for Electro Spray Ionisation (ESI) sources to improve ion transport to the mass analyser,[6,7] microfluid[8,9] and microreactor[10] systems, ion sources and Thin Layer Chromatography (TLC) chips,[9] an electron impact gas ioniser for compact mass spectrometry,[11] ceramic cylindrical ion trap mass analyser chips,[12] and the backbone of a ceramic quadrupole mass spectrometer.[13] Additive manufacturing has also been used to print specific reference materials, such as Pt group element reference materials.[14] For reviews on additive manufacturing in mass spectrometric applications and technologies in general, and as well as on different additive manufacturing technologies, we refer readers to the listed publications.[1,2,4,9]

Typically, a space-prototype system used in a laboratory environment requires significant technical adaptation before it can be deployed on a space exploration mission. For example, the high mechanical loads during rocket launch would damage such a system, which must be avoided at all costs. These adaptations can include changes to the spacings between or geometries of the electrodes in the mass analyser's ion optical system, which can affect the instrument's performance. Until now, adapted designs have been produced conventionally, for example using 5-axis CNC machining, and tested with the existing laboratory hardware to identify any problems with the new design before final production of a flight system. This process is time consuming and dependent on the availability of many resources. To overcome this limitation during design testing, we explored additive manufacturing as a rapid prototyping and risk reducing approach in space research using a design of one of our space prototype mass analysers.

In this contribution, we demonstrate for the first time, to the best of our current knowledge, a fully additively manufactured ion mirror consisting of an entrance window integrated with the remaining and conventionally manufactured space-prototype mass analyser (hereafter referred to as the hybrid mass analyser). The ion-optical design represents the core of our Laser Ablation Ionisation Mass Spectrometric (LIMS) system, which is currently being flight-qualified for its deployment on the lunar surface through NASA's Artemis programme.[15–17] LIMS measurements using the hybrid mass analyser demonstrate the suitability of additive manufacturing in this area of space science and mass spectrometry. This is highly relevant to our

---

[a] *Space Research and Planetary Sciences, Physics Institute, University of Bern, 3012 Bern, Switzerland. E-mail: andreas.riedo@unibe.ch*

[b] *NCCR PlanetS, University of Bern, 3012 Bern, Switzerland*

field, as design verification can be carried out more efficiently prior to final flight system production. Moreover, new ion optical designs, which so far have not been tested in the laboratory environment, can be produced cheaper, faster, and more independently, which as a result opens new perspectives in this field.

Experimental

Sample material

For the validation of the mass spectrometric performance a stainless steel sample (AISI 316L, 1.4435) and the NIST SRM 661 reference material were used. The NIST SRM 661 sample was fixed with UHV compatible copper tape on the sample holder. Measurements on stainless steel were conducted on the sample holder directly, as it is manufactured of said material. The used stainless steel alloy is a standardised material and minimum and maximum values for element abundances are given (all wt%): C (max. 0.03%), N (max. 0.10%), Si (max 1.0%), P (max. 0.045%), S (max. 0.03%), Cr (17.0–19.0%), Mn (max. 2.0%), Ni (12.5–15.0%), and Mo (2.5–3.0%). The chemical composition of NIST SRM 661 is certified and the respective abundances can be found in the corresponding certificate of analysis.

LIMS instrument

Laser Ablation Ionisation Mass Spectrometric (LIMS) measurements were conducted using the ORganics Information Gathering INstrument (ORIGIN) instrument setup, which is originally designed for the detection of organic molecules. ORIGIN is described in detail in recent publications.[18,19] Therefore, only a brief description is given here. The setup consists of a miniature reflectron-type time-of-flight mass analyser and a pulsed nanosecond laser system ($\lambda = 532$ nm, $\tau = 1.3$ ns, laser pulse repetition rate of 100 Hz, laser pulse energy of up to about 40 μJ per pulse) used as laser ablation ion source. The latter is different to the nominal ORIGIN setup where we typically operate a UV ($\lambda = 266$ nm) nanosecond laser system for molecular studies. The mass analyser integrated in ORIGIN is based on a design developed earlier, for the elemental and isotope analysis of solids.[20,21] We are currently in the design and manufacturing process of a flight LIMS system consisting of the mass analyser design used in this study. Note, that for the flight system only space proven materials and manufacturing processes will be used. The LIMS instrument shall be deployed through a Commercial Lunar Payload Service (CLPS) mission within NASA's Artemis program for the chemical analysis of lunar regolith at locations near the lunar south pole.[16,17] In said CLPS mission, we will fly a flight version of the microchip laser system used in this study here. The commercially available microchip laser system used in this study is shown in panel A in Keresztes Schmidt *et al.*, 2022.[15] In this study here, we integrated the same optical tower as shown in Keresztes Schmidt *et al.*, 2022 (ref. 15) on the vacuum chamber, in which the mass analyser is located. The optical tower consists of a beam attenuator and a single lens focusing system. The laser pulses are guided towards the entrance window of the vacuum chamber, through the ion optical system of the mass analyser, onto the sample surface. A laser focus diameter of about 20 μm is obtained. Once the positively charged species are generated through the ablation and ionisation process, they are accelerated and confined into the interior of the mass analyser and are reflected at the reflectron towards the detector system of ORIGIN.[22] Positively charged species arrive in time sequence at the detector system, according to their mass-to-charge ratio (TOF measurement principle). A high-speed read-out-electronic system is used to record the signal generated by the detector system, and in-house written software is used for data analysis.[23]

The reflectron investigated in this study here consists of five equidistant electrode rings. On top of the reflectron, an active electrode (referred to as backplane) is integrated containing the entrance window of the mass analyser (not to be confused with the entrance window of the vacuum chamber), through which the laser beam is guided. The reflectron is integrated above the drift tube of the mass analyser. In Riedo *et al.*, 2013 (ref. 21) a typical set of voltages applied to the ion optical system, including the reflectron, is provided.

Additively manufactured reflectron

For the additive manufacturing process of the reflectron, we applied the Fused Deposition Modelling (FDM) technology. This technology is one of the most common processes for printing of 3D components. For a full description of the process and other printing technologies, we refer to *e.g.*, Agrawaal *et al.*, 2021,[1] Grajewski *et al.*, 2021.[4] In short, the printing filament is heated up sufficiently (material dependent temperature) and pressed through a printing head (extruder) towards the printing bed. The structure is subsequently printed layer by layer according to the need of the user (*e.g.*, speed, layer thickness, quality, *etc.*).

For this study, a Sidewinder X1 (Artillery 3D Technology Co., Ltd.) was used for the manufacturing of the reflectron parts. This model allows to print structures with a maximal precision of 50 μm and 100 μm in lateral and vertical directions, respectively. The extruder was equipped with a 0.4 mm nozzle. For the insulating parts (spacers between ion optical elements, insulating tubes, top part of entrance window assembly), normal PLA material (Purefil PLA filament, 1.75 mm core diameter, Fabru GmbH, Switzerland) was used, which showed an electric resistance at the level of MΩ (simple 2-point measurements). Note, screws that go through the insulating parts and ion optical components are used for the integration of the reflectron; they are insulated with the insulating tubes. For active ion optical elements (electrode rings, bottom part of entrance window assembly), conductive PLA material (Protopasta Conductive PLA, Protoplant, Inc., Canada) was used. This material is impregnated with carbon and has an electric resistance at the level of few kΩ per 10 cm of filament (2-point measurements). This is sufficiently low for the operation of our ion optical elements, as they are floated at high voltage and are not power consumers. CAD drawings (STEP files) of each part of the reflectron were imported to the slicer software (PrusaSlicer, Prusa Research a.s., Czech Republic), providing the controlling G-code for the 3D printer. In Table 1, detailed information on the printed parts is listed. For simplicity, normal metallic pins for the electrical contacts are screwed to the ion optical components of the reflectron, to which vacuum compatible cables are subsequently attached. In a more advanced design, even the electrical connections can be realised by the 3D printing process. The additive manufactured reflectron is shown in Fig. 1.

Similar to CNC machined parts, all manufactured structures were inspected in view of conformity (no PLA whiskers/strings, no overflow of PLA, *etc.*) prior to assembly. After assembly of the additively manufactured reflectron and before integration into the conventional manufactured body of the mass analyser, the reflectron was placed in the ORIGIN vacuum chamber under UHV conditions, to facilitate outgassing. Note, this process is applied as well to conventionally produced parts, allowing a more efficient evacuation of a vacuum chamber prior to instrument operation. After outgassing, which was complete in less than 48 h, the conventional manufactured reflectron was replaced by the additively manufactured one, followed by the integration of the assembled mass analyser into the vacuum chamber of the ORIGIN setup. In Fig. 2, the conventional and hybrid versions of the mass analyser are shown. Reaching the operational vacuum conditions (mid-10^{-7} mbar level) the voltages for the operation of the reflectron were carefully ramped up to the nominal values used in the past before conducting the first LIMS measurements.

Measurements

Proof-of-concept measurements were conducted on the stainless steel sample. For initial tests, laser pulse energies at the level of about 0.50 μJ (~120 MW cm^{-2}) were tested on the steel substrate and several thousands of TOF spectra were recorded. For these measurements and to avoid possible damages during operation, the LIMS system was not pushed to its limits, *e.g.*, the voltages applied at the detector system were at the lower end.

For the quantification of the measurement performance (mass resolution and detection sensitivity) of the hybrid mass analyser, a pulse energy scan was conducted on NIST SRM 661. Laser pulse energies ranging from about (0.42–0.58) μJ ((103–142) MW cm^{-2}, values at the surface) were tested, corresponding to pulse energies just at the ablation threshold of sample material and to conditions where space charge effects impact the measurement capabilities of the mass analyser. The major space charge effects are charging of the surface and coulombic repulsion effects in the plasma plume. For the lower pulse energies applied ((0.42–0.52) μJ) up to 20 000 mass spectra were recorded for each pulse energy. For the two highest pulse energies tested (0.55 μJ and 0.58 μJ) up to 30 000 mass spectra were recorded. For comparison of the performance of the hybrid mass analyser (detection sensitivity and mass resolution), measurements at comparable instrument conditions were conducted on NIST SRM 661 using the conventional mass analyser.

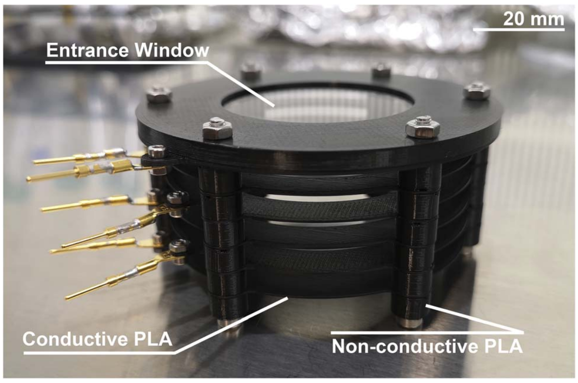

Fig. 1 Additively manufactured reflectron of the mass analyser used in LIMS.

Results and discussion

In Fig. 3 and 4, the proof-of-concept measurements (Fig. 3) and measurements conducted on NIST SRM 661 (Fig. 4) using the additively manufactured reflectron are shown. Firing the laser on the stainless steel sample directly resulted in well resolved mass spectra at high sensitivity. This was not expected, as typically the ion optical settings need to be slightly adjusted when new hardware is installed at the mass analyser, which was not the case here.

In Fig. 3, a histogrammed mass spectrum of the stainless steel sample is shown. The spectrum consists of 1100 single laser shot mass spectra and was recorded at a laser pulse energy of (0.43 ± 0.02) μJ. In this spectrum, we do see all expected mass peaks (metallic elements), even ^{63}Cu just above the noise floor (see inset in the panel). Note, Cu does not belong to the certified

Table 1 Additive manufactured parts with their corresponding printing parameters

Part	First layer [mm]	Other layers [mm]	Nozzle temp. [°C]	Bed temp. [°C]
Electrode rings	0.2	0.15	230	50
Insulating spacers	0.25	0.15	200	60
Insulating tube	0.2	0.2	200	60
Bottom side, entrance window	0.25	0.15	230	50
Top side, entrance window	0.2	0.2	200	60

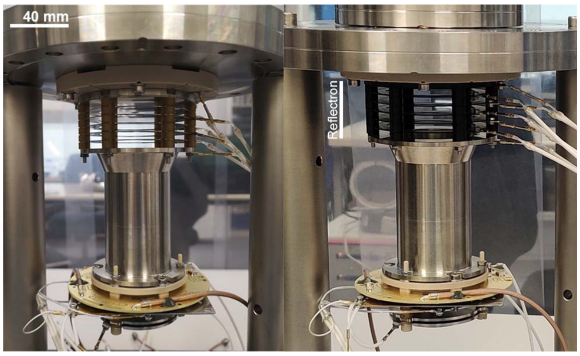

Fig. 2 The conventional mass analyser (left) and the hybrid mass analyser with the additively manufactured reflectron in black (right). The mass analyser is integrated into an adapter PEEK plate, which is connected to the top flange of the vacuum chamber.

list of elements of this stainless steel but abundances of up to 1wt% are accepted according to EN 10088-1. Elements with a high first ionisation potential, such as C or S, are not observed in this proof-of-concept measurement. This observation can be attributed to the applied laser wavelength of $\lambda = 532$ nm (see *e.g.*, discussion in Riedo *et al.*, 2013 (ref. 24)).

In Fig. 4 two histogrammed (20 000 single laser shot spectra) mass spectrum of NIST SRM 661 are shown. The mass spectrum in the upper panel was recorded using the hybrid mass analyser while the mass spectrum in the lower panel (intensities inverted) was measured using the conventional mass analyser. Both spectra were recorded at comparable laser irradiances at the level of about 110 to 120 MW cm^{-2}. Note, at higher laser irradiances peak broadening due to space charge effects is observed. Moreover, higher laser irradiances lead to higher peak intensities, which at some point affect the peak-to-peak baseline separation. Latter effect can be observed for ^{56}Fe (Fe being the main constituent of SRM 661), affecting the ^{57}Fe peak.

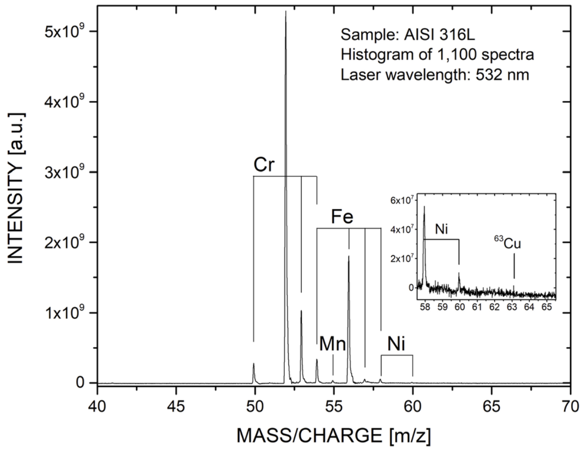

Fig. 3 Mass spectrum of stainless steel (AISI 316L, 1.4435) recorded with the mass analyser equipped with the additively manufactured reflectron.

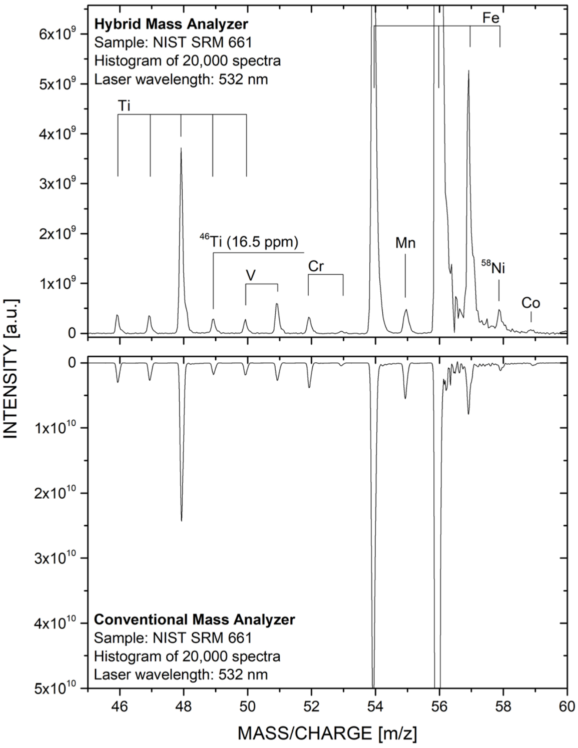

Fig. 4 Mass spectrum of NIST SRM 661 recorded with the hybrid mass analyser (upper panel) and conventional mass analyser (lower panel, inverted). Similar measurement performance, such as mass resolution and detection sensitivity, is observed.

By comparing both spectra with each other, a high spectral similarity is apparent. For example, no significant difference in term of mass resolution can be observed; the mass resolution $m/\Delta m$ of ^{48}Ti is slightly above 400, which is in line with previous studies (see *e.g.*, Riedo *et al.*, 2013 (ref. 21)). Further, the detection sensitivity is not affected by the additively manufactured reflectron. For example, ^{46}Ti, which has a certified atomic fraction of 16.5 ppm, is well above the noise floor in both spectra (*e.g.*, a signal-to-noise ratio of about 100 for the mass spectrum in the upper panel). The quality of the mass spectrum shown here, together with the detection sensitivity quantifiable with NIST SRM 661 (see Fig. 4), is only possible because the additive manufactured reflectron performs as a full-fledged ion optical element perfectly integrating with the ion optics of the remaining mass analyser. Therefore, the printing and integration of the additive manufactured reflectron can be concluded as successful and qualifies the additive manufacturing with the applied FDM technique for mass spectrometric prototyping in this field.

As with conventional CNC machining of ion optical components for high performance mass spectrometric systems, parameters such as surface quality (*e.g.*, planarity and surface roughness), sharp edges, materials used, manufacturable geometries, *etc.* that affect electric fields, need to be investigated in detail in future studies using additive manufacturing.

Imperfections in such components could, for example, lead to discharges between ion optical components and thus cause serious damage to mass spectrometric systems. The additive manufactured reflectron presented in this study may not be the most complicated ion optical system, but it is a first and important step towards the validation and application of more sophisticated ion optical parts for high performance mass spectrometric systems.

Implications for space applications

Once a proposed mass spectrometric system is selected for a space exploration mission, only a laboratory prototype system is typically available. To make this system flight ready, many engineering steps need to be mastered, ranging from material selection, making the system light and robust, to coatings on the structures to make the system inert against the harsh environmental conditions in space. As a consequence, many tests need to be successfully concluded at sub-unit level before the complete system will be manufactured, assembled, and tested. Unfortunately, this requires many production steps as well, which impact the required testing activities. From mass spectrometry point of view, distances and shapes of ion optical components of the laboratory prototype-system need to be adapted to make the mass spectrometer flight ready. To minimise the technical risks associated with the implemented changes on the mass spectrometric unit, additive manufacturing could be integrated in the manufacturing and testing phases prior to final flight hardware production using flight proven materials and machining. In case the design is not working as expected, the part can be adapted and printed without human interaction using additive manufacturing. The part can be then integrated and verified once the setup is ready for follow-up test activities. This allows for rapid iterations in the development process, optimising the available time for the project.

Conclusions

Space research instrumentation has to survive high mechanical and thermal stresses during their application in space. Consequently, many sub-unit tests must be successfully concluded before integration and testing of a full payload. This also holds for mass spectrometric instrumentation, which measure the chemical composition of *e.g.*, solids on the Martian surface. To make a mass spectrometric system flight-ready starting from a laboratory system design, almost every part of the instrument needs to be adapted, potentially affecting the measurement performance of the system. In this study, the reflectron of a space-prototype LIMS mass analyser design was additively manufactured using FDM technology. Laser ablation studies were conducted on stainless steel and NIST SRM 661 samples. The measurements conducted show that mass spectral quality was not affected by the integration of the additively manufactured reflectron. This represents a true success, as this opens doors for follow-up strategies in mass spectrometry in space science and in general, including rapid prototyping in the laboratory environment and development of ion optical designs that might be too complicated to manufacture using conventional CNC machining.

Data availability

Data for this article are available at Bern Open Repository and Information System at **https://doi.org/10.48620/74876**.

Author contributions

AR was involved in conceptualisation, formal analysis, investigation, methodology, validation, visualization, and writing original draft. PKS was involved in investigation, methodology, and reviewing and editing of the manuscript. NJB, SG, LNK, and MT were involved in reviewing and editing of the manuscript. PW was involved in funding acquisition, project administration, resources, and reviewing and editing of the manuscript.

Conflicts of interest

There are no conflicts to declare.

Acknowledgements

This work has been carried out within the framework of the NCCR PlanetS supported by the Swiss National Science Foundation under grants 51NF40_182901 and 51NF40_205606.

References

1 H. Agrawaal and J. E. Thompson, *Talanta Open*, 2021, **3**, 100036.

2 W. Chen, B. Zhang, M. M. Stevanović, L. Huang and K. Qian, *LabMed Discovery*, 2024, **1**(1), 100010.

3 V. N. Lednev, P. A. Sdvizhenskii, R. D. Asyutin, R. S. Tretyakov, M. Y. Grishin, A. Y. Stavertiy and S. M. Pershin, *Addit. Manuf.*, 2019, **25**, 64–70.

4 M. Grajewski, M. Hermann, R. D. Oleschuk, E. Verpoorte and G. I. Salentijn, *Anal. Chim. Acta*, 2021, **1166**, 338332.

5 M. Belka and T. Bączek, *Trac. Trends Anal. Chem.*, 2021, **142**, 116322.

6 B. M. Marsh, S. Rahman, V. M. Benkowski, S. Tichy and R. G. Cooks, *Int. J. Mass Spectrom.*, 2021, **468**, 116637.

7 A. Kachkine and L. F. Velásquez-García, *J. Am. Soc. Mass Spectrom.*, 2024, **35**, 862–870.

8 E. Gal-Or, Y. Gershoni, G. Scotti, S. M. E. Nilsson, J. Saarinen, V. Jokinen, C. J. Strachan, G. Boije af Gennäs, J. Yli-Kauhaluoma and T. Kotiaho, *Anal. Methods*, 2019, **11**, 1802–1810.

9 H. Guillén-Alonso, I. Rosas-Román and R. Winkler, *Anal. Methods*, 2021, **13**, 852–861.

10 G. Scotti, S. M. E. Nilsson, V.-P. Matilainen, M. Haapala, G. Boije af Gennäs, J. Yli-Kauhaluoma, A. Salminen and T. Kotiaho, *Heliyon*, 2019, **5**, e02002.

11 C. Yang and L. F. Velásquez-García, *J. Phys. D: Appl. Phys.*, 2019, **52**, 075301.

12 P. Roman, X. Chen, W. K. Jones, A. Karbasi, C. M. Newton, T. Bates, J. Denkins and S. Bhansali, *J. Microelectron. Electron. Packag.*, 2016, **13**, 113–120.

13 C. C. Eckhoff, N. K. Lubinsky, L. J. Metzler, R. E. Pedder and L. F. Velásquez-García, *Adv. Sci.*, 2024, **11**, 2307665.

14 C. K. Sio, T. Parsons-Davis, E. Lee, J. Wimpenny, A. J. Pascall, J. D. Kuntz, J. J. Goodell, K. E. Roberts, B. B. Bandong and N. R. Bennett, *Rapid Commun. Mass Spectrom.*, 2020, **34**, e8627.

15 P. Keresztes Schmidt, A. Riedo and P. Wurz, *Chimia*, 2022, **76**, 257.

16 P. Wurz, T. Bandy, P. Mandli, S. Studer, S. Havoz, M. Blaukovitsch, B. G. Plet, M. Tulej, D. Piazza, P. Keresztes Schmidt, S. Riedo and A. Riedo, *2023 IEEE Aerospace Conference*, 2023, pp. 1–10, DOI: **10.1109/AERO55745.2023.10115714**.

17 P. Keresztes Schmidt, S. Hayoz, D. Piazza, T. Bandy, P. Mändli, M. Blaukovitsch, M. Althaus, B. G. Plet, S. Riedo, S. Studer, O. Studer, M. Bieri, M. Tulej, A. Riedo and P. Wurz, *2024 IEEE Aerospace Conference*, 2024, pp. 1–10, DOI: **10.1109/AERO58975.2024.10521190**.

18 N. F. W. Ligterink, V. Grimaudo, P. Moreno-Garcia, R. Lukmanov, M. Tulej, I. Leya, R. Lindner, P. Wurz, C. S. Cockell, P. Ehrenfreund and A. Riedo, *Nat. Sci. Rep.*, 2020, **10**, 9641.

19 N. J. Boeren, S. Gruchola, C. P. de Koning, P. Keresztes Schmidt, K. A. Kipfer, N. F. W. Ligterink, M. Tulej, P. Wurz and A. Riedo, *Planet. Sci. J.*, 2022, **3**, 241.

20 U. Rohner, J. A. Whitby and P. Wurz, *Meas. Sci. Technol.*, 2003, **14**, 2159.

21 A. Riedo, A. Bieler, M. Neuland, M. Tulej and P. Wurz, *J. Mass Spectrom.*, 2013, **48**, 1–15.

22 A. Riedo, M. Tulej, U. Rohner and P. Wurz, *Rev. Sci. Instrum.*, 2017, **88**, 045114.

23 S. Meyer, A. Riedo, M. B. Neuland, M. Tulej and P. Wurz, *J. Mass Spectrom.*, 2017, **52**, 580–590.

24 A. Riedo, M. Neuland, S. Meyer, M. Tulej and P. Wurz, *J. Anal. At. Spectrom.*, 2013, **28**, 1256–1269.

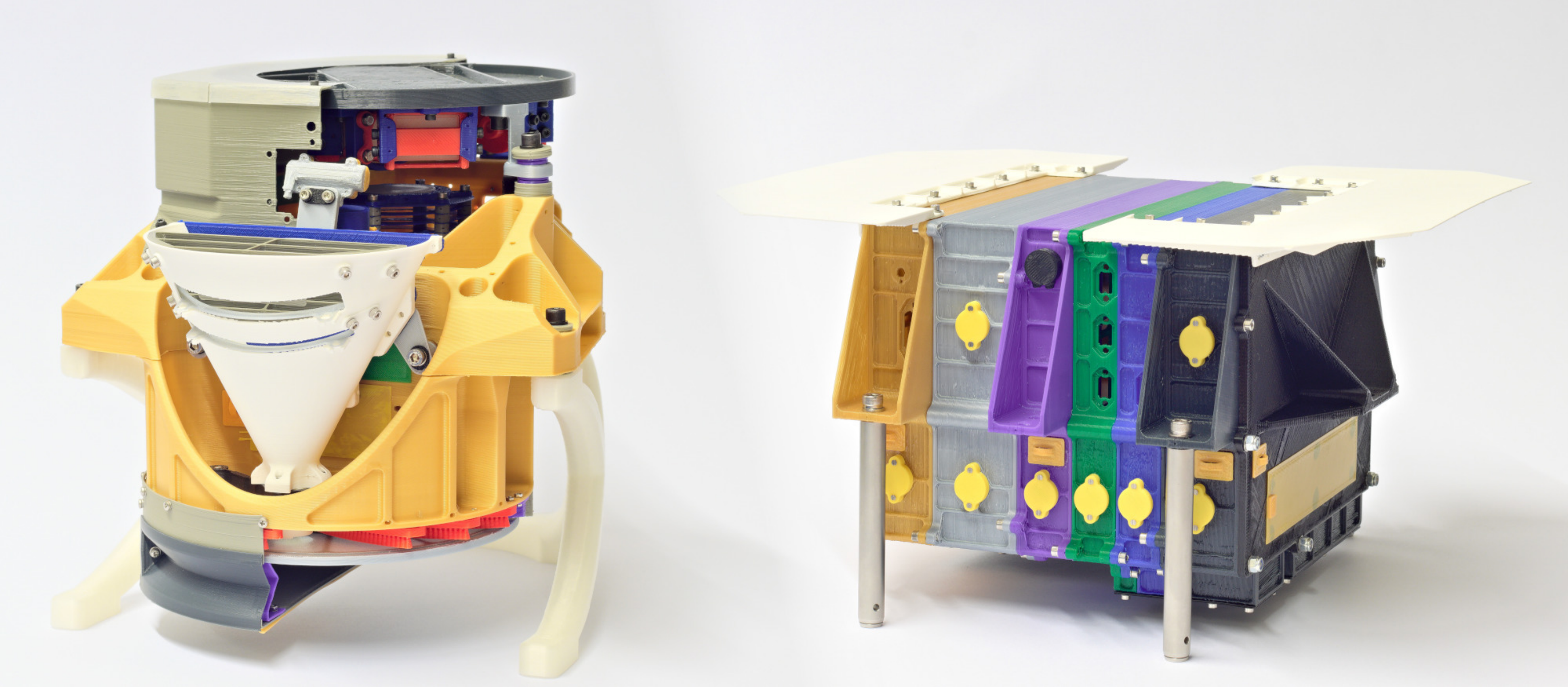

Additively manufactured (scale 1:1) Spectrometer Unit (SMU, left panel) and Electronics Unit (ELU, right panel) of the CLPS-LIMS instrument, as presented during the Preliminary Design Review (PDR) in May 2024 to NASA.

3 From the Laboratory to the Moon: The CLPS-LIMS Instrument

Based on concepts that were explored during the prototyping phase of the CLPS-LIMS project and the requirements formulated by NASA's CLPS mission concept, a flight ready version of the laboratory LIMS instrument has been created. This chapter outlines the challenges that had to be overcome in the design and development process of the CLPS-LIMS instrument and how the laboratory LIMS instrument evolved to become a spaceflight design.

Diven by the scientific objectives as outlined in the introduction of this thesis, the CLPS-LIMS instrument was designed for the analysis of lunar regolith grains up to a diameter of1 mm. It measures the element and isotope composition of those grains by means of Laser Ablation Ionisation Mass Spectrometry (LIMS). This information will lead to a better understanding of the geochemical environment of the investigated landing site.

The CLPS-LIMS instrument is developed in an agile manner. Hence, its design was subject to multiple design iterations, ensuring compliance to all requirement changes the instrument was subjected to during the project's initial phase. Nonetheless, the high-level concept of operations remained the same:

1. **Sample loading**

   For the CLPS-LIMS instrument to perform chemical analysis, the to be analysed material must be loaded into the instrument. Regolith sample material is transported from the lunar surface to a sample inlet provided by the instrument. It is processed according to the needs of the subsequent LIMS analysis.

2. **Chemical composition analysis of the sample**

   The loaded sample material is presented to the analysis system of the instrument. A pulsed, focussed laser beam is directed onto the sample surface, where sample material is ablated and ionised. The mass analyser performs separation according to the mass-to-charge ratio of the ionised species, and the detector system registers the signal.

3. **Sample discharge**

   The remnant sample material is removed from the analysis section of the instrument and discharged to the lunar surface. A new sample analysis cycle can be triggered.

Based on these fundamental concepts and the scientific goals, an instrument design was developed, which is presented in the following sections. Since testing of several Elegant Breadboards (EBB) of the instrument's Electronics Unit (ELU) is an integral part of this thesis, a more detailed description of the design requirements for those units is given in the last section of this chapter.

3.1 In-Situ Lunar Regolith Analysis by LIMS

The following publication describes the concepts by which in-situ analysis of lunar regolith by LIMS can be performed. The discussed instrument design is at the core of further iterations through which it has been refined and adapted to changing programmatic constraints of the CLPS program me.

At the time this publication was written, the design baseline foresaw that the CLPS-LIMS instrument is fully responsible for the sample collection from the lunar surface and the transport of said sample to the instrument. Thus, a sample introduction system based on the electrostatic collection of lunar regolith particles has been studied and tested by using a breadboard system to demonstrate its feasibility and efficiency in dust collection.

The publication summarises the general concepts by which in-situ chemical analysis of lunar regolith using LIMS can be performed and presents an instrument design implementing the concepts. A sample introduction system based on an electrically-biased conveyor belt was prototyped, suitable for collecting regolith grains from the lunar surface and transporting them for analysis to the instrument.

I contributed the described performance analysis of the laser system, as well as the results of the presented successful end-to-end test. It shows that the chemical analysis of lunar regolith simulant by LIMS is possible, and mass spectra can be recorded with the prototype system.

In Situ Lunar Regolith Analysis by Laser-Based Mass Spectrometry

Peter Wurz
Physics Institute, University of Bern, Sidlerstrasse 5, 3012 Bern, Switzerland
peter.wurz@unibe.ch

Sébastien Hayoz
Physics Institute, University of Bern, Sidlerstrasse 5, 3012 Bern, Switzerland
sebastien.hayoz@unibe.ch

Daniele Piazza
Physics Institute, University of Bern, Sidlerstrasse 5, 3012 Bern, Switzerland
daniele.piazza@unibe.ch

Timothy Bandy
Physics Institute, University of Bern, Sidlerstrasse 5, 3012 Bern, Switzerland
timothy.bandy@unibe.ch

Matthias Blaukovitsch
Physics Institute, University of Bern, Sidlerstrasse 5, 3012 Bern, Switzerland
matthias.blaukovitsch@unibe.ch

Peter Keresztes Schmidt
Physics Institute, University of Bern, Sidlerstrasse 5, 3012 Bern, Switzerland
peter.keresztes@unibe.ch

Patrik Mändli
Physics Institute, University of Bern, Sidlerstrasse 5, 3012 Bern, Switzerland
patrik.maendli@unibe.ch

Benoît Gabriel Plet
Physics Institute, University of Bern, Sidlerstrasse 5, 3012 Bern, Switzerland
benoit.plet@unibe.ch

Sven Riedo
Physics Institute, University of Bern, Sidlerstrasse 5, 3012 Bern, Switzerland
sven.riedo@unibe.ch

Simon Studer
Physics Institute, University of Bern, Sidlerstrasse 5, 3012 Bern, Switzerland
simon.studer@unibe.ch

Marek Tulej
Physics Institute, University of Bern, Sidlerstrasse 5, 3012 Bern, Switzerland
marek.tulej@unibe.ch

Andreas Riedo
Physics Institute, University of Bern, Sidlerstrasse 5, 3012 Bern, Switzerland
andreas.riedo@unibe.ch

Abstract—**We are developing laser-based mass spectrometry (LIMS) for the in situ investigation of the chemical and mineralogical composition of the lunar regolith. The current development of our LIMS instrument is for an application on a robotic mission within the Artemis CLPS program of NASA. The CLPS lander will be placed in the south polar region. The LIMS system consists of a time-of-flight mass analyzer (TOF-MS), a laser system (LSS) providing nano-second laser pulses focused to µm spots on the sample surface, electronics (ELU) for operating the LIMS system, and a sample handling system (SHS). The TOF-MS, LSS, and ELU are according to our established design presented earlier. The SHS is specially designed for the CLPS lander to collect regolith grains from the lunar surface in the vicinity of the lander. The SHS design foresees rotating steel brushes that free regolith grains from the surface into ballistic trajectories. A conveyor belt collects these grains, which is electrically biased to improve its collection efficiency. Adjusting the speed of the brushes and the voltage on the conveyor belt allow to optimize the collection efficiency of the grains. The conveyor belt transports the grains to the entrance of the mass analyzer where grain by grain analysis will be performed.**

The main scientific objective for the LIMS instrument is the geochemical analysis of the lunar regolith, by the analysis of individual regolith grains and assessing their mineralogical diversity. In addition, this investigation will also address technical aspects of sampling a planetary surface at or near a landed spacecraft, i.e., the effect the plume of the retrorockets has on the regolith underneath the lander. Of particular interest is the chemical contamination of the surface by the spent fuel, and the amount of removal grains by the gas drag.

TABLE OF CONTENTS

1. INTRODUCTION

We are developing laser-based mass spectrometry (LIMS) for the investigation of the chemical, element, isotope, and mineralogical composition of the lunar regolith to be performed in situ on a landed robotic platform. Regolith is a mixture of grains with a typical size distribution of 30 – 250 µm, with an average size of 60 µm, and grains larger than 1 cm constituting about 1% [1, 2]. Moreover, regolith is a mixture of grains from different geographic origin, from near and far of the sampling site, resulting from the constant bombardment of the lunar surface with micro-meteorites and larger bolides. Therefore, the set of analyzed regolith grains will be of different geographic origin, from near and far of

978-1-6654-9032-0/23/$31.00 ©2023 IEEE

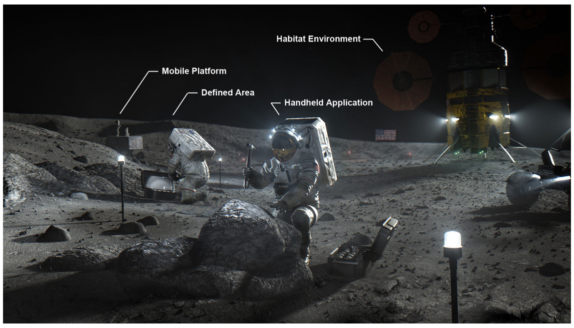

Figure 1: Depending on the task, LIMS instruments may be operated in different environments, including instruments operated autonomously on a robotic platform, as part of an instrument suite on an outpost in a predefined area, in the laboratory section of a habitat, on a mobile platform, or directly in situ by the Astronaut as a handheld analytical tool. Image adapted and from NASA.

the sampling site, and provide information on the contribution of different geological units to the investigated location, along with chemical and mineralogical mixing between different terranes and different crustal depths. The depth of the lunar regolith layer is between several meters to tens of meters [1, 2], depending on location on the Moon.

During landing, the exhaust of the retrorockets will interact with the regolith layer and possibly chemically contaminate an area of several times the dimensions of the landing spacecraft, see for example the Morpheus lander project of NASA [3]. Also, the fast-flowing gas of the rocket exhaust during landing will remove some of the regolith at the landing site. This removal and the alteration of the regolith is part of the investigation performed by this LIMS instrument. A good way to study this alteration is to have a drill that allows access to the sub-surface to about 1 m to reach unperturbed regolith material.

The LIMS instrument allows for the analysis of many individual regolith grains collected from the close vicinity of the landed spacecraft. Thereby, the LIMS measurements allow for the analysis of grains from different minerals, and from different provenances on the lunar surface, as they present themselves in the mix of collected regolith grains. Impacting meteoroids spread the regolith grains over large distances and, more general, distribute the ejecta material centro-symmetrically around the impact crater, typically within <2.5 crater diameters from the center of the impact [1]. Depending on the details of the landing site, potential for a very diverse mix of grain origin can be expected.

The current development of our LIMS instrument is for an application on a robotic mission, within the Commercial Lunar Payload Services (CLPS) framework, which is part of NASA's Artemis program. The CLPS lander will be placed in the south polar region, on the lunar far side. Possible future applications of the LIMS instrument are within the manned lunar program, so-called Artemis missions, to support the field studies of the astronauts (see Figure 1).

The LIMS measurement provides detailed chemical analysis within seconds, detection of trace elements at the ppm level and below, isotope abundances with high accuracy, for dating rocks. All this is achieved without sample preparation to support investigations ranging from pure scientific interest all the way to support in situ resource utilization (ISRU) activities and related tasks.

Our LIMS system is compact, features simple and robust operation, and is based on current measurement capabilities of a real-size prototype system. The instrument can be part of the payload of a lander, on a rover, or can be portable for field excursions of astronauts, or be part of an instrument suite in a laboratory at the lunar base for detailed on site investigations of samples collected in the field (see Figure 1).

Our miniature LIMS system is suited for studies conducted on solid sample materials that are encountered during in situ space exploration. That includes e.g., the identification of the mineralogy of heterogeneous samples, as well as element and isotope studies conducted on lunar and chondritic meteorites, which allows studies of in situ radio-isotope geochronology.

The scientific goal is the chemical analysis of individual regolith grains and deriving their mineralogical makeup. By analyzing 100 grains (minimal goal) to several 1,000 grains (nominal scenario) the chemical and mineralogical makeup of the landing site and its surroundings can be explored. Because of the grain-by-grain chemical analysis, sorting of the different grains by mineral composition, and inferences of their origin on the lunar surface is possible during data analysis. In addition, because of the laser ablation process that allows to drill up to about 50 µm deep below the sample surface of a grain, depending on material and laser pulse energy [4,5], the chemical investigation of the grains can be performed below the space-weathered outer surface of the grains [6,7] to derive the true, unaffected mineral composition of each grain.

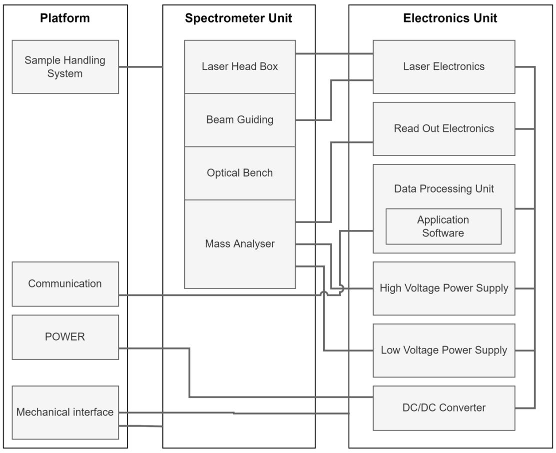

Figure 2: Main block diagram for the CLPS-LIMS and Artemis-LIMS systems.

While currently little is known about the alteration of the regolith during landing, sampling the surface material below or near the landing site is often considered for planetary landers [e.g., 8], either for in situ investigations or for sample return. Because samples can only be collected from areas affected by the plume of the retro-rocket engine used for landing, the processing of the regolith by the landing activities can be studied. The chemicals used in the retro rocket are known, and are clearly distinct from the regolith composition. Thus, from detailed chemical analysis, the amount of chemical contamination and alteration of the regolith grains can be derived. Moreover, if a drill is available to collect samples below the surface at several depths, the range of influence of the contamination can be assessed in more detail.

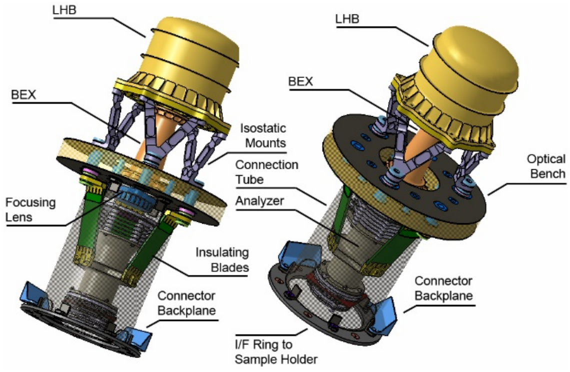

Figure 3: Design study of the LIMS instrument for an application on a CLPS platform. A similar design is foreseen for LIMS instrument for the field work of the astronauts.

NASA's Artemis program will lead humanity forward to the Moon and prepare for the manned exploration of Mars [9]. Initial investigations delivered by CLPS providers will study the lunar surface and available resources near the lunar poles. Starting in 2023, NASA will send science instruments and technology experiments to the lunar surface several times per year on CLPS flights.

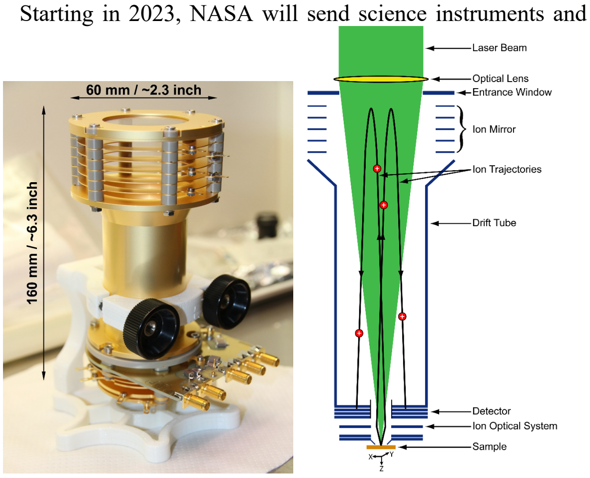

Figure 4: The core part of the LIMS instrument, the mass analyzer. Left panel shows the prototype instrument, right panel shows the schematics.

2. INSTRUMENT DESCRIPTION

The LIMS system consist of three major subsystems: the Spectrometer Unit (SMU), the Sample Handling System (SHS), and the Electronics Unit (ELU), which are shown in Figure 2. The SHS is different for the CLPS instrument and the manned Artemis implementation. For the CLPS-LIMS instrument a sample introduction system that collects regolith particles from the surface is foreseen, which is discussed below. For the Artemis-LIMS system rocks or pieces of rock collected by the astronauts will be inserted in the instrument manually.

The SMU of the LIMS instrument consists of the actual Mass Analyzer (MA) and the Laser Sub System (LSS). An early design study of the system is shown in Figure 3, where the actual laser (LHB), the laser optics (BEX), and the ion-optical system are joined to one unit.

The ELU houses all the electronics of the LIMS instrument. The individual electronics units for CLPS LIMS are the laser electronics, the read-out-electronics, the data processing unit, the high voltage electronics, the low-voltage electronics, and the DC/DC converter. For Artemis-LIMS also a battery system and a WiFi communication module are foreseen to allow for independent operation of the LIMS instrument by the astronauts on their field trips.

The Laser Ablation/Ionization Mass Spectrometer

LIMS is designed for the sensitive, chemical analysis of solid matter as an analytical instrument on a landed spacecraft [10,11]. The LIMS instrument is a reflectron-type time-of-flight mass spectrometer coupled to a pulsed laser (of nanosecond or femtosecond pulse duration) for ablation and ionization of sample material for mass spectrometric analysis of solid samples (see Figure 4) [12,13,14]. The LIMS instrument has a mass resolution up to 900, with an accuracy of the mass scale of 500 ppm [15], a mass range from m/z 1 to ~1,000 [16], a detection limit around 10 ppb depending on mass [11], and an instantaneous dynamic range of 8 decades [17]. The LIMS instrument allows for quantitative composition measurements of solid surfaces of almost all elements in laser ablation mode [18,19]. With every laser pulse a small amount of sample material is removed, about femto-grams per laser shot. Thus, when ablating with the laser at the same spot the sequence of mass spectra resulting from these laser pulses can be used to derive a depth profile of the atomic composition at the sampled location [20]. This allows, for example, to penetrate through the space weathered layer on grains and rocks [4,7] to access the true chemical composition of the material. Furthermore, LIMS can be operated in laser desorption mode to detect complex molecules located on the sample surface [21]. This operation mode is particularly useful in studying the chemical contamination of the regolith grains by the exhaust of the retrorockets.

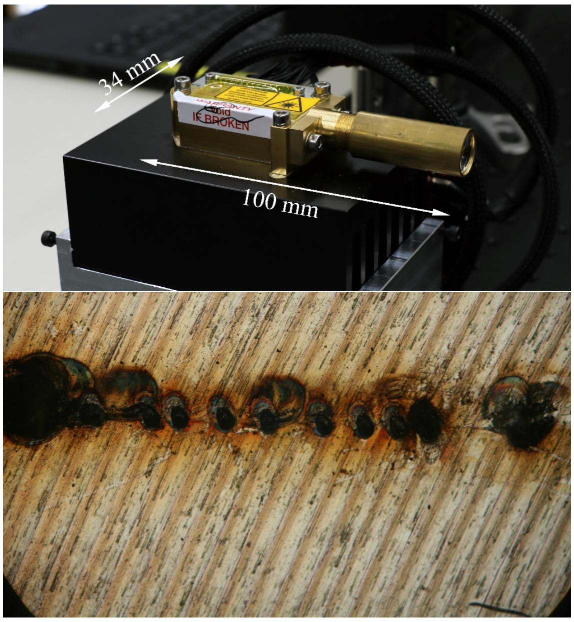

Figure 5: Top panel: Prototype micro-chip laser system with the beam expander telescope in test setup, bottom panel: laser ablation test sequence with stainless steel as sample surface (532 nm, 100 Hz, ~40 µJ, beam diameter Ø ~30 µm).

Laser Sub System (LSS)

For laboratory experiments using LIMS we operated various laser systems, providing nano-second or femto-second pulses at various wavelengths ranging from IR to UV. The nano-second laser system is a pulsed Nd:YAG laser (20 Hz, at 1064 nm, and the harmonics 532 nm, 355 nm, 266 nm, GW/cm^2, Ø ~ 20 µm). The femtosecond pulsed laser system is a Ti:Sapphire system with optional frequency doubling and tripling (1 kHz, at 775 nm, 387 nm, 258 nm, TW/cm^2, Ø ~ 10–20 µm). Using these laser systems, their different pulse durations, and their different wavelengths, we investigated the influence of these parameters on the results of chemical composition analysis. This allows us to select the best laser system for a LIMS instrument. We find that the femto-second laser system is clearly superior to the nano-second laser system [22,23], and that the shorter the wavelength the better is the analytical capability for quantitative analysis [11,16]. With all laser systems we accomplished quantitative analysis of samples, however, with different effort in calibration of the system.

Given the constraints for a flight system being mass, power, thermal, complexity, autonomous operations, and the highly compressed schedule of a CLPS mission, we chose a frequency-doubled Nd:YAG micro-chip laser system operated at 532 nm, the first harmonic, providing 1.4 ns laser pulses, with a repetition frequency of 100 Hz. This laser system is compact, has affordable power consumption, and the company producing it has flight heritage in NASA's OSIRIS-Rex mission [24]. Figure 5, top panel, shows a prototype microchip laser system with the beam expander mounted at the laser exit. Figure 5, bottom panel, shows the capability of this laser system to cause significant ablation on stainless steel samples, which corresponds to intensities of GW/cm^2, with spot sizes of Ø ~ 30 µm.

For Artemis-LIMS we are developing a fiber-based femto-second laser system based on a commercial system. The wavelength should be as short as possible, ideally in the UV range, and the pulse repetition frequency should be in the range of 100 Hz – 1 kHz, with a laser intensity measured at the surface of TW/cm^2, and a spot size of Ø ~ 10 µm. In case this system is not flight-ready in time, the nano-second Nd:YAG micro-chip laser system will be used again.

Electronics Box

The electronics box houses all the electronics of the instrument, aside from some minor proximity electronics at the detector and the laser head. There are six individual electronics modules for CLPS-LIMS system, which are: i) laser electronics, ii) read-out electronics (RoE), iii) data processing unit (DPU), iv) high-voltage electronics (HVPS), v) low-voltage electronics (LVPS), and vi) DC/DC converter. For the Artemis-LIMS instrument there are two additional electronics modules foreseen to allow for independent field operations of the instrument. These modules are vii) battery system, and viii) WiFi communication module.

Laser electronics—Dedicated electronics to operate the laser, to adjust the laser pulse energy, to control the operation temperature of the Nd:YAG and the frequency doubling crystal, and to record all laser housekeeping data.

Read-out-Electronics—recording of detector signal, analog-to-digital (ADC) conversion, and histogramming of recorded time-of-flight spectra. The foreseen ADC (TI ADC12D1620QML) supports dual-channel digitization with a 12-bit vertical resolution and 1.6 GS/s per detector channel. Optionally, time-interleaved digitization with a sampling frequency of 3.2 GS/s on one channel is possible. Given by the mass-analyzer dimensions a sampling duration of 12 µs is necessary to capture a time-of-flight spectrum covering the full mass range.

Data Processing Unit—is the computer system that handles all the instrument operations, the calibration on the lunar surface, the optimization of the performance, the collection of science and housekeeping data, the data compression, and the communication with the spacecraft (telecommand and telemetry). The Gaisler GRC712RC dual-core LEON3FT SPARC V8 processor, on which the system is based, is a proven and tested integrated circuit for space applications. Added non-volatile memory for science data allows to implement a store-and-forward mechanism to comply with the data rates as specified by the mission profile. Communication with the spacecraft will be handled via a RS-422 interface.

High voltage electronics—Provides 7 high voltages up to –2.5 kV, with 14-bit resolution, to operate the ion-optical system, and it records its housekeeping data.

Low voltage electronics— Provides eight low voltages in the range from –500 V to +500 V, with 12-bit resolution, to operate the ion-optical system, and it records its housekeeping data.

DC/DC converter—Provides all the voltages to power the various electronic components (+3.3 V, –5 V, +5 V, +15 V, +12 V).

Battery system—For the field operation electrical power will be provided by a built-in battery system that supports field operations of the instrument up to eight hours. Upon return to the astronauts' habitat the instruments will be connected to a docking station to recharge the batteries.

WiFi communication module—Data collected by the instruments will be transferred via a WiFi connection to the astronauts' habitat in almost real time. Thus, the collected data will be available in the habitat for local analysis. From the habitat the data will be downlinked to Earth.

3. SAMPLE INTRODUCTION SYSTEM

On the CLPS platform we are responsible to collect the sample from the surface ourselves. The goal is to collect regolith, i.e., small dust grains from the immediate vicinity of the lander and perform grain by grain analysis. The typical size of these grains is about 60 µm, with sizes ranging from µm to cm. The largest grain size CLPS-LIMS can handle is about 0.5 mm.

The system we selected for the CLPS mission for sample access, collection, and introduction into the instrument is an electrically biased conveyor belt that collects dust particles mechanically released from the surface and transports these regolith grains from the collection area to the analysis area of the instrument. Mineral dust, which is usually an isolating material, is always somewhat electrically charged because of triboelectric effects. In addition, the precipitating plasma and solar UV irradiation cause additional charging of exposed grains on the surface [25]. Once airborne, the charged dust grains are attracted by the electric field of the conveyor belt and are deposited there. Even if the regolith grains are not electrically charged, the airborne particles would be attracted to the biased conveyer belt because of dielectric polarization of the grains in the electric field of the conveyor belt and the resulting attractive (Coulomb) force [30]. The idea of collecting regolith grains with an electrically biased conveyor belt is based on a sample collection mechanism that we studied for an earlier instrument that was part of an asteroid lander [11].

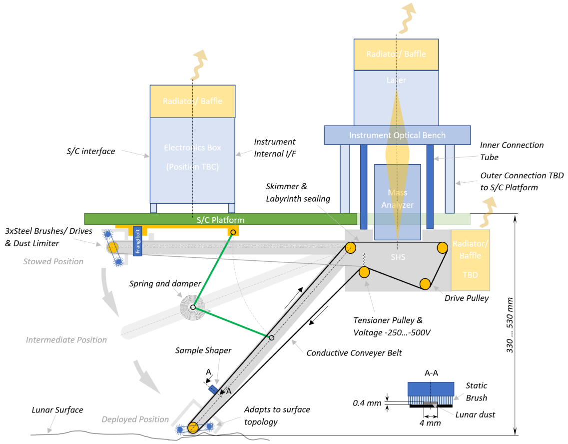

2022.06.27. For conceptual information only

Figure 6: Conceptual study of the sample handling system of the LIMS instrument for the application on the CLPS platform.

A conceptual design of the sample introduction system is shown in Figure 6. The conveyor belt extends over an arm that is lowered to the lunar surface underneath the lander. During flight, the conveyor belt arm is in its transport position attached to the spacecraft platform. Upon successful landing the launch lock of the arm is released via a frangibolt mechanism and lowered to the lunar surface by a spring-loaded mechanism restrained by a damping element. This system allows to accommodate distances from the spacecraft platform to the lunar surface in the range of 350 – 530 mm, which accommodates the topographic terrain uncertainty of the landing site.

At the surface end of the conveyor belt arm there are three steel brushes. When operated, the rotating steel brushes release the regolith grains from the surface that are attracted to the electrically charged conveyor belt and stick there upon landing. The rotation speed of the brushes can be adjusted to optimize the loading of the conveyor belt with regolith grains, and to adapt for the encountered regolith being loose or compacted, the latter possibly by the activity of the retrorocket during landing. In worst case, the brush can be operated to be slightly abrasive to release particles from a more compacted object. In case two of three brushes fail there is still chance to transport lunar dust towards the mass analyzer with the remaining brush.

The moving conveyor belt transports the collected regolith grains to the measurement location of the LIMS instrument where each grain is analyzed individually. LIMS analysis of a grain takes about 1–2 minutes, thus thousands of grains can be analyzed during a lunar day. If the data rate allows, even depth profiles of a grain can be recorded.

4. PROTOTYPE TESTING

Mass Spectrometer

We developed two highly miniaturized Laser Ablation Ionization Mass Spectrometry (LIMS) instruments for in situ planetary research [12,13,14]. These were originally intended for a lander on Mercury as part of the BepiColombo mission of ESA [26]. For almost two decades, we continuously improved the larger of the two LIMS instruments in preparation for future landed missions for versatile use on lunar, asteroid, Mars, and other planetary surfaces [10,27].

Currently, we have three prototype instruments in operation in our laboratory. Thanks to our continuous development, LIMS has advanced towards a true alternative for the sensitive and quantitative chemical analysis of solid materials with high spatial resolution. We achieved a performance comparable to state-of-the-art laboratory techniques, such as SIMS, LA-ICP-MS or GD-TOF-MS, see review [26,28].

In preparation for the CLPS mission, we developed prototypes or test setups for several sub-units of the LIMS instrument, which were necessary to address all the requirements for a CLPS lander on the lunar surface. These are discussed below.

We investigated the performance of the LIMS prototype mass spectrometer with lunar analogue material, the Lunar Highlands Simulant (LHS-1) [29], which has a mean particle size of 90 µm matching the mean particle size distribution encountered during the Apollo missions. The mineral composition of the lunar simulant material consists of Anorthosite, Glass-rich basalt, Ilmenite, Olivine, and Pyroxene grains. This mix of mineral grains results in a bulk chemistry of: SiO_2 (51.2%), TiO_2 (0.6%), Al_2O_3 (26.6%), FeO (2.7%), MnO (0.1%), MgO (1.6%), CaO (12.8%), Na_2O (2.9%), K_2O (0.5%), P_2O_5 (0.1%), and others (0.4%).

For the measurement a 1 mm deep cavity on the surface of a stainless steel sample holder was filled with lunar analogue material while assuring that sample height differences were kept minimal by levelling the surface with a spatula. Care was taken to not compress the sample material. This resembles the expected received sample from the sample handling system.

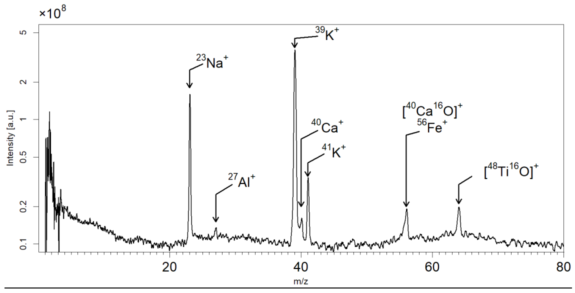

Figure 7: Sample mass spectrum of the LHS-1 lunar analogue material recorded with the laboratory prototype LIMS instrument.

The optical and ion-optical subsystem optimization was accomplished by performing measurements of the stainless steel sample holder. Parameters were tuned to maximize signal intensity while retaining mass resolution and symmetric peak shapes. Measurements were performed at a laser irradiance of ~0.2 GW/cm^2 and 100 Hz laser frequency. The sample was continuously moving below the mass analyzer with a speed of ~0.8 mm/s, matching the operation of the sample handling system.

In Figure 7 we show a histogrammed mass spectrum of LHS-1 consisting of 100 single shot mass spectra recorded during one of our preliminary test campaigns of the laser optical subsystem. With this setup a mass resolution $M/\Delta M \sim 400$ was achieved. All major elements or their oxides present in LHS-1, except Si, were detected. Due to the mix of grains in the analogue material and the short travel distance of ~0.8 mm during this measurement, it can be expected that predominantly Si-lacking grains were measured, likely ilmenite grains. Contributions from the sample holder to the mass spectrum were not detected.

By optimizing the ion optics directly on the lunar analogue material, improvements to the spectral quality are expected. This will result in a more stable signal allowing for more single shot spectra to be histogrammed and thus improving SNR. This is a prerequisite for detecting the trace elements present in the sample.

Laser Sub System

Since the analytical performance of the LIMS instrument is strongly dependent on the operation parameters of the laser system, it was necessary to characterize the micro-chip laser accordingly.

The ablation and ionization of the sample material, regolith grains or larger solids, is highly dependent on the applied laser irradiance (W/cm^2). This measure is directly tied to energy emitted within a laser pulse and the corresponding pulse duration. Thus, the stability of the pulse energy over longer time periods of continuous operation, typically in the range of minutes and short-term variations in the pulse energy had also to be quantified. Figure 8 shows a result of such a measurement. Due to the passive Q-switch technology of the pulsed laser, no significant variations in pulse duration are possible.

Single laser pulse energies were measured using a Coherent J-10MB-LE energy sensor coupled with the Coherent LabMax-TOP evaluation unit. No additional optical elements were placed between the laser head and the laser energy meter.

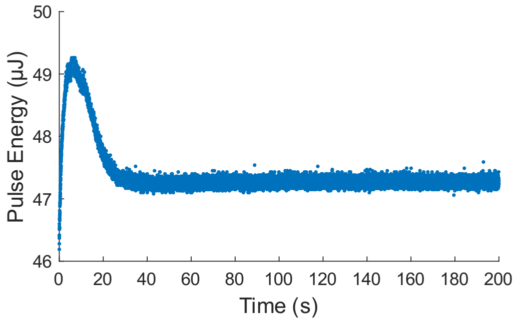

Figure 8: Laser pulse energy measurements within a 200 s long burst with a laser repetition frequency of 100 Hz.

The laser pulse duration was verified, and it matches the manufacturer specifications using a Alphalas UPD-50-UP fast photodiode as temporal detector and using a Tektronix MSO64B oscilloscope to record the signal. Subsequent analysis of the pulse shape agreed with the company specified value of ~1.4 ns.

A pulse energy profile of a representative laser burst is shown in Figure 8. The specification of an average pulse energy of 40 µJ are fully met with an average of 47.4 ± 0.4 µJ. The initial instability in the first ~30 s of the bursts is attributed to the reaction time within the temperature control system of the laser. Acceptance criteria defined for the LIMS instrument require a pulse energy stability of <2 % over the first 20,000 shots in a burst. Considering the initial instability, pulse energy stabilities of <1 % are achieved. After reaching steady state pulse energy stabilities of <0.2 % are observed, meeting the specification needed for quantitative chemical analysis of the samples.

Dust Collection System

The dust collection system is a new development for the lunar application, thus the working principle itself, its collection efficiency must be tested and verified, and operation scenarios must be developed. For that purpose, we developed a test setup for the regolith particle collection. The design of this test setup is shown in Figure 9. The test setup consists of a dust tray filled with lunar analog material (emulating the lunar regolith surface), the steel brush driven by a motor with adjustable rotation speed, and a piece of conveyor belt, the collection foil, mounted on an articulated section of a circle to collect the released particles. The collection foil can be electrically biased from 0 V up to –1,000 V. The test setup (see Figure 10) is accommodated in a vacuum chamber operated at 1 mbar. The setup was used already for many test runs. The dust tray was filled with lunar regolith analogue material, the Lunar Highlands Simulant (LHS-1) [29].

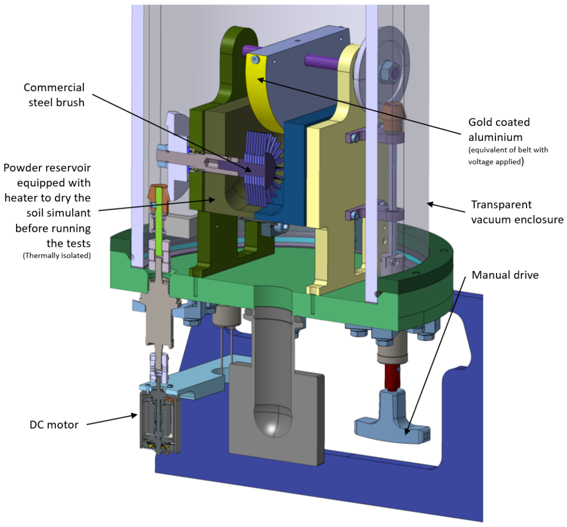

Figure 9: Design of the test setup for the regolith particle collection.

In the test runs, the rotation speed of the brushes was varied between 200 and 350 rpm, they operated between 5 and 10 s, and the bias voltage of the collection foils was varied between 0 V and –1,000 V.

For all these operation conditions we got acceptable collection efficiency of dust particles on the collection foil, and we found that the operation parameters of the sample handling system are not critical. A typical result of a dust collection run collecting dust on the collection foil is shown in Figure 11. The dust sticks to the collection foil well enough, so that its transport on the conveyer belt to the instrument is assured. The negative voltage bias on the collection foils was used because such a high-voltage power supply was readily available. Since the electric field causes an electric polarization of the particles resulting in an attractive force also a positive voltage bias of the conveyer belt will work, as has been demonstrated earlier [30,31].

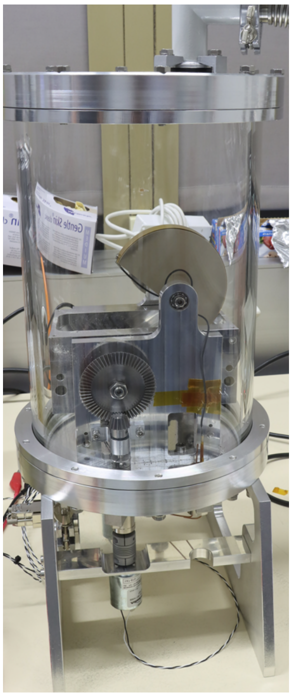

Figure 10: Test setup for the regolith particle collection.

5. SUMMARY

We prototyped all components for a LIMS instrument to be part of the science payload to be landed on the lunar surface on a robotic platform as part of the CLPS program of Artemis. Prototyping and testing of all crucial sub-units was successfully concluded. The LIMS instrument will analyze individual regolith grains from the vicinity of the landing site to derive the chemical composition of each grain, and to infer

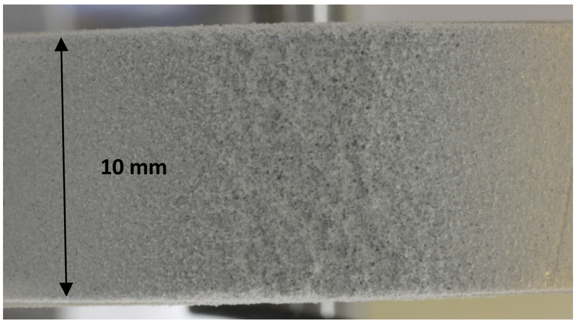

Figure 11: LHS-1 dust particles collected on the collection foil (the conveyor belt), using the test setup for regolith particle collection.

their mineralogy. These measurements address many of the scientific goals put forward for the Artemis program of NASA.

ACKNOWLEDGEMENTS

The financial support by the Swiss Space Office and the Swiss National Science Foundation is gratefully acknowledged.

REFERENCES

[1] G.H. Heiken, D.T. Vanniman, and B.M. French (1991). Lunar Sourcebook. Cambridge University Press, ISBN 978-0-521-33444-0.

[2] Y. Langevin and J.R. Arnold, The Evolution of the Lunar Regolith, Ann. Rev. Earth Planet Sci. 5 (1977) 449–489.

[3] J.J. Hart and J.D. Mitchell, Morpheus Lander Testing Campaign, IEEE Aerospace Conference, (2012), 1–12, doi: 10.1109/AERO.2012.6187304.

[4] V. Grimaudo, P. Moreno-García, A. Cedeño López, A. Riedo, R. Wiesendanger, M. Tulej, C. Gruber, E. Lörtscher, P. Wurz and P. Broekmann, Depth Profiling and Cross-Sectional Laser Ablation Ionization Mass Spectrometry Studies of Through-Silicon-Vias, Anal. Chem. 90(8), (2018), 5179-5186, DOI: 10.1021/acs.analchem.7b05313.

[5] D. Monserrat López, V. Grimaudo, G. Prone, A. Flisch, R. Zboray, T. Lüthi, M. Mayor, M. Fussenegger, P. Broekmann, P. Wurz, and E. Lörtscher, Automated, 3-D and Sub-Micron Accurate Ablation-Volume Determination by Inverse Molding and X-Ray Computed Tomography, Advanced Materials, 2200136 (2022), 11 pages, DOI: 10.1002/advs.202200136.

[6] S.K. Noble, L.P. Keller, and C.M. Pieters, Evidence of space weathering in regolith breccias I: Lunar regolith breccias, Meteoritics & Planetary Science 40(3), (2005), 397–408, DOI: 10.1111/j.1945-5100.2005.tb00390.x.

[7] C.M. Pieters and S. K. Noble, Space weathering on airless bodies, J. Geophys. Res. Planets, 121, (2016) 1865–1884, DOI: 10.1002/2016JE005128.

[8] J.R. Brophy, J. Castillo-Rogez and R.P. Casillas, Assessing Ceres' Past and Current Habitability, *2022 IEEE Aerospace Conference (AERO)*, 2022, pp. 1–15, DOI: 10.1109/AERO53065.2022.9843248.

[9] Artemis III, Science Definition Report, (2020), NASA/SP-20205009602

[10] P. Wurz, M. Tulej, A. Riedo, V. Grimaudo, R. Lukmanov, and N. Thomas, Investigation of the Surface Composition by Laser Ablation/Ionisation Mass Spectrometry, IEEE Aerospace Conference Big Sky, MT, USA, (2021), 50100, 15 pages, DOI: 10.1109/AERO50100.2021.9438486.

[11] M. Tulej, A. Riedo, M.B. Neuland, S. Meyer, D. Lasi, D. Piazza, N. Thomas, and P. Wurz, A miniature instrument suite for in situ investigation of the composition and morphology of extraterrestrial materials, Geostand. Geoanal. Res., 38 (2014), 441–466, DOI: 10.1111/j.1751-908X.2014.00302.x.

[12] U. Rohner, J. Whitby, and P. Wurz, (2003) Meas. Sci. Technol., 14, 2159–2164.

[13] U. Rohner, J. Whitby, P. Wurz, and S. Barabash, A highly miniaturised laser ablation time-of-flight mass spectrometer for planetary rover, Rev. Sci. Instr., 75(5), (2004), 1314–1322.

[14] A. Riedo, A. Bieler, M. Neuland, M. Tulej, and P. Wurz, Performance evaluation of a miniature laser ablation time-of-flight mass spectrometer designed for in situ investigations in planetary space research, Jou. Mass Spectr. 48 (2013) 1–15.

[15] A. Riedo, S. Meyer, B. Heredia, M.B. Neuland, A. Bieler, M. Tulej I. Leya, M. Iakovleva, K. Mezger and P. Wurz, Highly accurate isotope composition measurements by a miniature laser ablation mass spectrometer designed for in situ investigations on planetary surfaces, Planet. Space Sci. 87 (2013), 1–13.

[16] R. Lukmanov, M. Tulej, R. Wiesendanger, A. Riedo, V. Grimaudo, N. Ligterink, C. de Koning, A. Neubeck, D. Wacey, and P. Wurz, Multi-wavelength ablation/ ionisation and mass spectrometric analysis of 1.88 Ga Gunflint Chert, Astrobiology 22(4), (2022), 18 pages, DOI: 10.1089/ast.2019.2201.

[17] A. Riedo, M. Tulej, U. Rohner, and P. Wurz, High-speed strip-line multi-anode Multichannel Plate Detector System, Rev. Sc. Instr. 88 (2017), 045114, DOI: 10.1063/1.4981813.

[18] Grimaudo, V., P. Moreno-García, A. Riedo, S. Meyer, M. Tulej, M.B. Neuland, C. Gütz, S. Waldvogel, P. Wurz, and P. Broekmann, (2017) Anal. Chem., 89, 1632–1641.

[19] M.B. Neuland, K. Mezger, A. Riedo, M. Tulej, and P. Wurz, (2016), Meas. Sci. Technol., 27(3), 035904.

[20] V. Grimaudo, M. Tulej, A. Riedo, R. Lukmanov, N.F.W. Ligterink, C. de Koning, and P. Wurz, (2020) Rapid Comm. Mass Spectrom., 34:e8803 (2020), 11 pages, DOI: 10.1002/rcm.8803.

[21] V. Grimaudo, P. Moreno-García, A. Riedo, A. Cedeño López, M. Tulej, R. Wiesendanger, P. Wurz, and P. Broekmann, Review – Laser Ablation Ionization Mass Spectrometry (LIMS) for Analysis of Electrodeposited Cu Interconnects, Jou. Electrochem. Soc. 166 (2018), D3190–D3199, DOI: 10.1149/2.0221901jes.

[22] Riedo, A., M. Neuland, S. Meyer, M. Tulej, and P. Wurz, Coupling of LMS with fs-laser ablation ion source: elemental and isotope composition measurements, J. Anal. Atom. Spectrom. 28, (2013c) 1256–1269 (featured article).

[23] V. Grimaudo, P. Moreno-García, A. Riedo, M.B. Neuland, M. Tulej, P. Broekmann, and P. Wurz, High-resolution chemical depth profiling of solid material using a miniature laser ablation/ionization mass spectrometer, Anal. Chem. 87, (2015) 2037–2041, doi: 10.1021/ac504403j.

[24] M.G. Daly, O.S. Barnouin, C. Dickinson, J. Seabrook, C.L. Johnson, G. Cunningham, T. Haltigin, D. Gaudreau, C. Brunet, I. Aslam, A. Taylor, E.B. Bierhaus, W. Boynton, M. Nolan, and D.S. Lauretta, The OSIRIS-Rex Laser Altimeter (OLA) Investigation and Instrument, Space Sci. Rev. 212 (2017), 899–924, DOI: 10.1007/s11214-017-0375-3

[25] B. Farr, X. Wang, J. Goree, I. Hahn, U. Israelsson, M. Horanyi, Dust removal from a variety of surface materials with multiple electron beams, Acta Astronautica 200 (2022) 42–47, DOI: 10.1016/j.actaastro.2022.07.047

[26] A. Balogh, M. Bird, L. Blomberg, P. Bochsler, J.-L. Bougeret, J. Brückner, L. Iess, J. Guest, Y. Langevin, A. Milani, J.-A. Sauvaud, W. Schmidt, T. Spohn, R. von Steiger, N. Thomas, K. Torkar, H. Wänke and P. Wurz, BepiColombo—An interdisciplinary cornerstone mission to the planet Mercury. ESA-SCI(2000)1, Noordwijk, The Netherlands, European Space Agency (2000).

[27] P. Wurz, P. Tulej, R. Lukmanov, V. Grimaudo, S. Gruchola, K. Kipfer, C. de Koning, N. Boeren, L. Schwander, R. Keresztes Schmidt, N.F.W. Ligterink, and A. Riedo, Identifying biosignatures on Planetary Surfaces with Laser-based Mass Spectrometry, IEEE Aerospace Conference Big Sky, MT, USA, 21956099 (2022), 16 pages, DOI: 10.1109/AERO53065.2022.9843803.

[28] A. Riedo, V. Grimaudo, P. Moreno-García, M. Neuland, M. Tulej, P. Broekmann, and P. Wurz, Laser Ablation / Ionisation Mass Spectrometry: Sensitive and quantitative chemical depth profiling of solid materials, CHIMIA 70 (2016), 268–273, doi: 10.2533/chimia.2016.268.

[29] Exolith lab, 532 S. Econ Circle, Suite 100, Oviedo, FL 32765, USA

[30] X. Wang, J. Schwan, H.-W. Hsu, E. Grün, and M. Horányi, Dust charging and transport on airless planetary bodies, Geophys. Res. Lett., 43, (2016), 6103–6110, doi: 10.1002/2016GL069491.

[31] M. Onozuka, Y. Ueda, K. Takahashi, Y. Seki, S. Ueda, and I. Aoki, Dust removal system using static electricity, Vacuum, 47(6-8), (1996) 541-544.

BIOGRAPHY

Peter Wurz *has a degree in electronic engineering (1985), an M.Sc. and a Ph.D. in Physics from Technical University of Vienna, Austria (1990). He has been a post-doctoral researcher at Argonne National Laboratory, USA. Since 1992 at the University of Bern. He is Professor of physics and since 2015 head of the Space Science and Planetology division. He has been Co-I and PI for many science instruments for space missions of ESA, NASA, ISRO, CNSA, Roscosmos, and JAXA.*

Sébastien Hayoz *gained experience in different fields like electronics' development for Automotive, electronics' systems for Train Control Monitoring System (TCMS). Since February 2021, he is leading the electronics engineering team at the Space Research and Planetary Division and is involved for several instruments realized by the University of Bern.*

Daniele Piazza *has more than 20 years of experience in the design and development of space instruments. He has a Ph.D. in mechanical engineering from ETH Zurich and started his career in Formula 1. Since 2005 he leads the mechanical engineering group working on space instruments at the University of Bern.*

Timothy Bandy *has B.Sc. degree in mechanical engineering. Timothy has mainly worked in the defense, pharmaceutical fields before joining UBE. Since then he supported the development and AIV of BELA (BepiColombo), CHEOPS and CometInterceptor. Since then, he has worked as System Engineer for the PLATO TOU structure.*

Matthias Blaukovitsch *has a M.Sc. in Physics from the Technical University of Vienna, Austria (2016). He has been working on time-of-flight sensors specializing on diode lasers and is now appointed as an optical engineer at the University of Bern.*

Peter Keresztes Schmidt *received his B.Sc. and M.Sc. in Chemistry at the ETH Zürich, Switzerland. He is currently working as a PhD student in Bern, Switzerland, where he is developing a new the LIMS instrument for in situ studies on the lunar surface.*

Patrik Mändli *received a B.Sc. and a M.Sc. in electrical engineering and information technology, ETH Zürich, Switzerland. For seven years he worked in control, network and communications technology for all types of rail vehicles. Since March 2022, he is system engineer electronics for the LIMS instrument for CLPS.*

Benoît Plet *received his Ph.D. in Physical Chemistry from the University of Bordeaux, France, in 2007. After 15 years developing scientific instrumentation in industry, he has joined University of Bern, Switzerland, as project manager.*

Sven Riedo *received a B.Sc. in Electrical Engineering in 2022 from the University of Applied Sciences and Arts Western Switzerland. He is currently working as an electronic engineer at the University of Bern.*

Simon Studer *received his B.Sc. in Automotive Engineering in 2013 from the University of Applied Sciences Bern, Switzerland. He spent most of his time in Formula 1 before he joined as Mechanical Engineer to the Space Research and Planetary Sciences group of the University Bern.*

Marek Tulej *received a Ph.D. in Physical Chemistry from the University of Basel, Switzerland in 1999. After his post-doctoral period at Paul Scherrer Institute (PSI), Switzerland, he joined in 2008 the University of Bern as an instrument scientist for space missions, including Phobos-Grunt, Marco Polo-R, Luna-Resurs, and JUICE.*

Andreas Riedo *received his Ph.D. in Physics in 2014 from the University of Bern, Switzerland. In 2016 he received a SNSF fellowship that allowed him to continue his research in Astrobiology at the Leiden University, The Netherlands. He extended his stay at the Leiden University with a MCSA fellowship for another two years before he moved in 2019 to the Free University Berlin after receiving the prestigious Einstein fellowship. In 2020 he moved to University of Bern and is currently appointed as researcher and project manager within ESA's JUICE space mission.*

3.2 Sample Handling Concept for Analysis of Lunar Regolith

With the progression of the CLPS-LIMS project, a major change to the instrument's design was triggered by NASA by changing the responsibility regarding sample transport to the instrument, led to the development of a new Sample Handling System (SHS). As presented before, CLPS-LIMS was responsible to collect and process the sample from the lunar surface all the way to the LIMS measurement. Then, NASA decided to collect the sample themselves and provide a well-processed sample to the CLPS-LIMS instrument. Defining a reliable interface between the lander sample collection and CLPS-LIMS turned out prohibitive and it was decided that the lander is responsible for the coarse sample handling and CLPS-LIMS performs the fine sample preparation for the LIMS measurement. This concept is described in the following.

The new concept foresees that the CLPS-LIMS instrument is supplied by an external sample delivery system with lunar regolith. The sample delivery system (SDS) will be supplied by the lander vendor, with the responsibility of designing and operating it lying with the vendor. The CLPS-LIMS instrument must provide an interface at which it can receive the delivered sample and process it according to its needs. A set of requirements is posed towards the lander vendor, detailing how the sample must be delivered. These requirements include e.g. the total sample volume and the sample volumes per loading cycle. In addition, the maximum regolith grain size that the SDS may provide is specified, to ensure the functionality of the SHS.

The following publication describes the concept of the new SHS, and the related laboratory validation studies, which have been performed to prove its viability. The validation studies that I contributed focussed on the mass spectrometric analysis of lunar regolith simulant from which key parameters for the SHS could be derived. These are e.g. the maximally allowable sample roughness, such that the quality of LIMS measurements is not impeded. Additionally, the laboratory studies conducted on the regolith simulant, allowed to determine the minimally needed rotation speed of the sample carousel. As the LIMS measurements are destructive, thus consuming or displacing sample material, consecutive laser pulses applied on the same position, will lead to a decrease in mass spectrometric signal. The needed movement speed to counteract this signal decrease was determined in these studies and serves as a key requirement towards the design of the flight-capable SHS.

Sample handling concept for in-situ lunar regolith analysis by laser-based mass spectrometry

Peter Keresztes Schmidt
Space Research and Planetary Sciences,
Physics Institute, University of Bern,
Sidlerstrasse 5, 3012 Bern,
Switzerland
peter.keresztes@unibe.ch

Sébastien Hayoz
Space Research and Planetary Sciences,
Physics Institute, University of Bern,
Sidlerstrasse 5, 3012 Bern,
Switzerland
sebastien.hayoz@unibe.ch

Daniele Piazza
Space Research and Planetary Sciences,
Physics Institute, University of Bern,
Sidlerstrasse 5, 3012 Bern,
Switzerland
daniele.piazza@unibe.ch

Timothy Bandy
Space Research and Planetary Sciences,
Physics Institute, University of Bern,
Sidlerstrasse 5, 3012 Bern,
Switzerland
timothy.bandy@unibe.ch

Patrik Mändli
Space Research and Planetary Sciences,
Physics Institute, University of Bern,
Sidlerstrasse 5, 3012 Bern,
Switzerland
patrik.maendli@unibe.ch

Matthias Blaukovitsch
Space Research and Planetary Sciences,
Physics Institute, University of Bern,
Sidlerstrasse 5, 3012 Bern,
Switzerland
matthias.blaukovitsch@unibe.ch

Michael Althaus
Space Research and Planetary Sciences,
Physics Institute, University of Bern,
Sidlerstrasse 5, 3012 Bern,
Switzerland
michael.althaus@unibe.ch

Benoît Gabriel Plet
Space Research and Planetary Sciences,
Physics Institute, University of Bern,
Sidlerstrasse 5, 3012 Bern,
Switzerland
benoit.plet@unibe.ch

Sven Riedo
Space Research and Planetary Sciences,
Physics Institute, University of Bern,
Sidlerstrasse 5, 3012 Bern,
Switzerland
sven.riedo@unibe.ch

Simon Studer
Space Research and Planetary Sciences,
Physics Institute, University of Bern,
Sidlerstrasse 5, 3012 Bern,
Switzerland
simon.studer@unibe.ch

Olivier Studer
Space Research and Planetary Sciences,
Physics Institute, University of Bern,
Sidlerstrasse 5, 3012 Bern,
Switzerland
olivier.studer@unibe.ch

Michael Bieri
Space Research and Planetary Sciences,
Physics Institute, University of Bern,
Sidlerstrasse 5, 3012 Bern,
Switzerland
michael.bieri@unibe.ch

Marek Tulej
Space Research and Planetary Sciences,
Physics Institute, University of Bern,
Sidlerstrasse 5, 3012 Bern,
Switzerland
marek.tulej@unibe.ch

Andreas Riedo
Space Research and Planetary Sciences,
Physics Institute, University of Bern,
Sidlerstrasse 5, 3012 Bern,
Switzerland
andreas.riedo@unibe.ch

Peter Wurz
Space Research and Planetary Sciences,
Physics Institute, University of Bern,
Sidlerstrasse 5, 3012 Bern,
Switzerland
peter.wurz@unibe.ch

Abstract—**We present the current progress in developing a reflectron-type time-of-flight laser ablation ionization mass spectrometer (RTOF-LIMS) to allow for direct sensitive microanalysis of lunar regolith grains *in situ* on the lunar surface. The LIMS system will operate in the lunar south pole region on a CLPS mission within NASA's Artemis program.**

The concept for the regolith sample handling system, which is based on a carousel disk system with a cavity to hold the sample material, will be discussed in detail. Rotating the disk takes care of transporting the sample material from the sample inlet, into which a sample delivery system of the CLPS platform deposits the regolith, to the analysis position below the mass analyzer entrance and, subsequently, disposing the material after analysis is completed. Sample preparation is achieved by passive brushes and a shaping tool to create a sample surface with the necessary planarity. Accurate control of these parameters is important to ensure consistent laser ablation conditions during sample analysis and thus reproducible chemical composition determination of the sample material. The new sample handling system design has an improved acceptance range for larger regolith grain sizes up to ~ 1 mm Ø. This in turn reduces a possible sampling bias and should lead to a more representative analysis of the regolith's chemical composition. Sample disposal is realized by another set of brushes to clean out the cavity and to allow for new sample material to be deposited.

To verify the feasibility of the sample handling concept and guiding the development thereof, laboratory experiments on a lunar regolith simulant were conducted using a prototype LIMS system. This prototype system has capabilities representative of the flight instrument currently in development regarding the mass analyzer and optical sub-system. The laboratory and flight optical sub-system is based on a microchip Nd:YAG laser system (~ 1.5 ns pulse width, $\lambda = 532$ nm, 100 Hz laser pulse repetition rate, laser irradiance ~ 1 GW/cm^2), and custom-made laser optics to achieve a focal spot on the sample surface of ~ 20 µm. Consequently, the conducted measurements can serve as a qualification baseline for the flight instrument during ground-based tests.

979-8-3503-0462-6/24/$31.00

TABLE OF CONTENTS

1. INTRODUCTION

An instrument based on laser ablation ionization mass spectrometry (LIMS) for the chemical analysis of lunar regolith is currently under development. LIMS consist of a mass analyzer coupled to a pulsed laser system. The laser beam is focused onto the sample surface to obtain irradiances in the range of MW/cm^2 to TW/cm^2. This causes ablation of the sample material, and partial atomization and simultaneous ionization thereof [1]. Our LIMS instrument shall operate on a robotic lander platform to conduct autonomous *in-situ* measurements of the mineralogical, element and isotope composition of lunar surface material.

Our LIMS instrument is being developed for a mission within the Commercial Lunar Payload Services (CLPS) framework, which is a part of NASA's Artemis program. The lunar south pole region is being considered as landing site.

Regolith, the targeted sample material of our CLPS-LIMS instrument, covers the lunar surface with a thickness of 5 m to 10 m, depending on location [2], [3]. The regolith's grain size distribution could be inferred from regolith returned during the Apollo missions. About 90 wt% is larger than 10 µm, 50 wt% larger than 100 µm and 10 % larger than 1 mm [4]. Being an electrical insulator and with no protective lunar magnetosphere, the bombardment of the regolith with charged solar particles leads to electrostatic charging thereof [5]. When designing an instrument for operation on the lunar surface, such properties must be considered during the design phase. Furthermore, selection procedures for the correct grain size fraction of the measurement procedure must be implemented. Electrostatic charging of the sample material can have an influence on the instrument or cause contamination of surfaces, that ought to be clean of regolith [6]. In this contribution, we discuss how this is handled within the design of our CLPS-LIMS instrument and provide experimental results based on measurements conducted with lunar regolith analogue.

LIMS as a chemical analysis technique is suitable for direct determination of element composition and isotope ratios of the sample material, such as lunar regolith [1], [7], [8]. It is based on the ablation and subsequent ionization of the solids caused by a high-irradiance pulsed laser beam. The generated ions are separated according to their mass-to-charge ratio (m/z) and subsequently detected.

Our CLPS-LIMS instrument is based on a reflectron-type time-of-flight mass spectrometer ion-optical design (RTOF-MS) [9]–[11]. Laser ablation/ionization is accomplished by a frequency doubled Nd:YAG microchip laser ($\lambda = 532$ nm, $\tau \sim 1.5$ ns, 100 Hz pulse repetition rate). Positive ions in the ablated material are accelerated into the mass analyzer. For a more complete description of the CLPS-LIMS instrument and its subunits we refer the reader to the published design study [12].

Changes in the mission profile of CLPS-LIMS, namely the addition of a sample delivery system at the CLPS platform for sample collection from the lunar surface, resulted in a significant redesign of the instruments sample handling system (SHS), which is presented in the first part of this contribution. The concept design was validated and guided by laboratory experiments, which are described in the second part of this contribution.

Instrument Overview— The CLPS-LIMS system consists of two main parts, namely the Spectrometer Unit (SMU) and the Electronic Unit (ELU). In Figure 1 an overview of the current SMU design is shown. The SMU carries of the optical sub-system (OSS) on the top, which houses the laser source and the necessary beam shaping optics to generate a focused laser spot on the sample surface. The mass analyzer (MA) is mounted below the OSS and above the SHS.

All components of the instrument are attached to an ultra-stable structure made of sandwich panels with near-zero CTE CFRP face sheets and aluminum honeycomb, which acts also as the spacecraft interface.

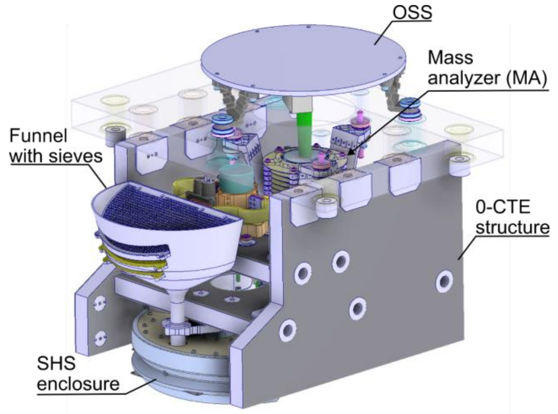

Figure 1: Overview of the current SMU design of the CLPS-LIMS instrument.

2. DESCRIPTION OF THE SAMPLE HANDLING SYSTEM CONCEPT

The CLPS mission profile foresees split responsibilities between sample collection from the lunar surface and delivery to a defined interface at the CLPS-LIMS instrument, and the subsequent sieving and fine manipulation of the sample material to prepare it for LIMS analysis. The CLPS lander platform will provide the sample delivery for the CLPS-LIMS instrument.

The external sample delivery system is required to provide a continuous flow or batched drops of 50–100 cm^3 of regolith with grain sized no larger than 5 mm.

The LIMS SHS accepts the collected material from the external sample delivery system (e.g., a robotic arm with a bucket end effector), sieves and shapes the material into an appropriate form for LIMS analysis. Subsequently, it presents the sample to the mass spectrometric system.

A 3D CAD drawing of the SHS's current design iteration is shown in Figure 2.

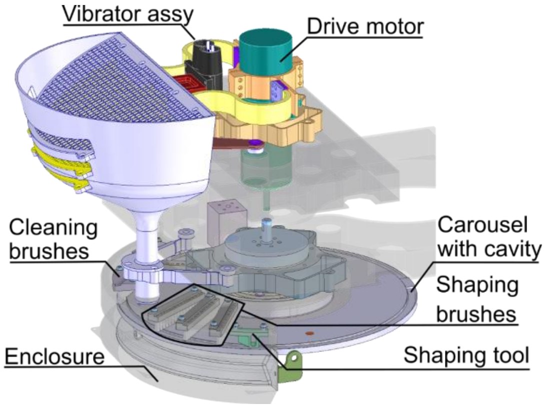

Figure 2: Close-up view of the sample carousel structure.

Conceptually, the SHS is built around a rotating sample carousel, which has an approximately 5 mm wide and 1.5 mm deep cavity along its outer edge. The externally delivered sample material is guided through a funnel structure into this cavity while the carousel is rotating counterclockwise. Following the sample deposition, a set of three brushes guides potentially spilled material from the carousel's main body towards the cavity. To enhance this process, the brushes are mounted rotated into the direction of rotation of the sample carousel. The brushes extend over the cavity as a first step in forming the sample surface and evenly distributing the sample material. For this purpose, the distance between the lower edge of the brushes and the carousel surface decreases across the set of brushes.

After the coarse shaping of the sample material by the brushes, an additional shaping tool further compresses the material and creates a surface with reduced roughness and porosity.

Rotating the carousel further, the now prepared sample material is moved to the measurement position of the CLPS-LIMS instrument. The sample is periodically advanced during analysis to present new material to the mass analyzer and avoid signal degradation due to displacement of the material caused by the laser-matter interaction and consumption of the sample material due to ablation.

After mass spectrometric analysis, the sample material is transported to the disposal structure. Here, another set of brushes removes the regolith from the cavity, making it ready to accept new sample material from the funnel. To aid the sample removal process, the sample cavity wall height is asymmetric with the outer wall being only 0.75 mm high. The brushes force the material over the outer edge of the sample cavity. Note, that a complete removal of sample material from the cavity is not necessary, since only the upper tens of micrometers of the sample material surface are investigated by LIMS.

Disposed sample material falls, by gravitational influence, to the bottom of the instrument enclosure, and passes through a slot present in the enclosure back onto the lunar surface. The slot is protected by a labyrinth structure to minimize radiative heat exchange between the inner part of the instrument and the lunar surface, hence the impact on the SMU's thermal design is kept minimal. This assures minimal accumulation of disposed sample material inside the instrument enclosure.

Actuation of the sample carousel is performed by a phySpace 32 stepper motor (Phytron GmbH, Gröbenzell, Germany), allowing for precise positional control of the rotation. A planetary gearbox is mounted onto the motor housing to increase effective torque of the carousel and reduce the rotation speed to the required levels. The pre-loaded drive bearings of the sample carousel are protected from lunar regolith using a labyrinth sealing system. Figures of merit of the drive system's current baseline design are listed in Table 1.

Table 1: Current figures of merit of the SHS drive system.

No. of steps per motor axle revolution	200 steps/rev
Drive motor torque	15 mNm
Total gear ratio	1:200
Carousel torque	3 Nm
Linear step size along sample cavity	14 µm

The torque requirements have not been experimentally verified yet and are at this time best estimates. A bread-board design of the carousel system is currently being built to accurately determine the needed torque to advance the sample material through the sample shaping and cavity cleaning sections of the carousel structure.

The minimal step size, with which the sample material can be advanced with, is given by the approximate diameter of the laser focus and thus the diameter of the analyzed area by the LIMS instrument. This has the advantage of not having to step the motor multiple times to reach a new sample area while also not wasting precious lunar sample material by having steps larger than the analyzed area. Consequentially, this reduces the duty cycle of the motor and thus power consumption and heat dissipation.

For initial position referencing a Hall effect or optical sensor is foreseen to be mounted to the top side of the carousel. No active position feedback is needed to keep track of the current rotation position of the carousel due to the fixed step sizes of the motor after initial referencing of the carousel position.

Sample surface quality and shaping tool—For optimal analysis of the lunar regolith with the LIMS instrument a sample surface with a defined height and small corrugation is necessary. Due to the ion optical design of the MA, the sample surface must have a distance of (0.6 ± 0.6) mm from the opening of the mass analyzer to achieve good collection of the ions generated the laser ablation. Furthermore, the required irradiance of the focused laser beam for sample ablation and ionization is only achievable in the same range. To account for any possible misalignment of the laser focus and the mass analyzer with respect to the nominal sample surface caused by thermo-mechanical distortion or external forces during launch and or landing, the sample planarity shall be better than ±0.2 mm when presented to the mass analyzer. The carousel will be designed to fulfill this constraint over full rotations of the carousel.

In Figure 3 the currently considered schematic designs for the sample shaping tools are shown. After forcing the regolith through beneath the shaping tool, the material should have the necessary planarity and reduced porosity required for analysis by LIMS. The appropriate tool design is currently being investigated using the SHS breadboard system (Figure 4). The knife edge tool (3) is currently favored due to its simple mechanical design. Due to the possibility of large grains getting stuck between the knife edge and the cavity, alternative solutions are being considered if the knife edge tool is proven to be not feasible. These might be a flexible Teflon lip tool (1) or a brush tool (2). Using a brush or Teflon lip could pose problems regarding insufficient compression and poor surface quality.

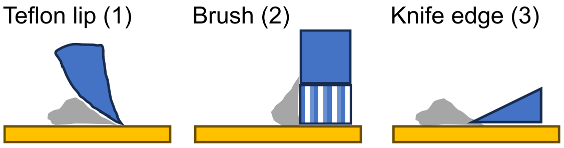

Figure 3: Schematic depiction of the shaping tools considered for the SHS. The carousel is shown in yellow with its nominal direction of rotation being to the right.

Launch lock—Unwanted movement of the carousel during launch, transit and landing are avoided by locking the carousel using a launch-lock pin. During the commissioning phase on the lunar surface, a spring-loaded, shape-memory alloy triggered pin puller is actuated allowing for motor-driven rotation of the carousel.

Funnel

The funnel serves as a drop zone for the CLPS platform's sample delivery system into which the collected lunar regolith is placed. Since the LIMS instrument is designed to handle only regolith with grain sizes of 1 mm and smaller, three sieves with decreasing mesh sizes (5 mm → 2 mm → 1 mm) are integrated into the funnel. It is defined that the sample delivery system is allowed drop regolith with grain sizes up to 5 mm to avoid clogging or damaging the sieves.

The sieves are slanted downwards away from the instrument body and cutouts in the funnel allow for the discarding of the unwanted fractions of lunar regolith.

To aid sieving and transport of the regolith material, an eccentric vibrator actuated by a brushed DC motor is attached to the funnel. The vibration frequency can be changed by increasing or decreasing the motor's rotation speed. This allows to tune the regolith flow through the funnel and hence onto the sample carousel. A voice coil vibrator has been considered, but due to the more complex control electronics required, the DC motor-based solution was chosen.

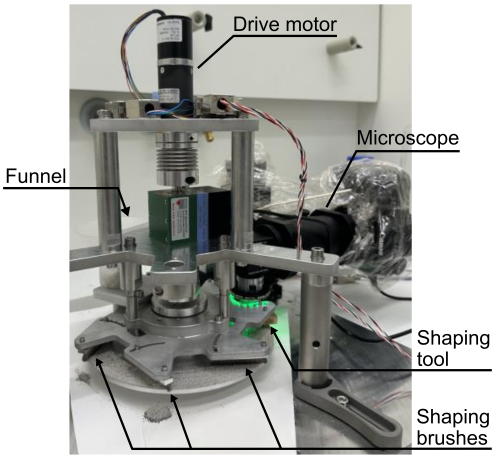

Figure 4: Sample handling system (SHS) breadboard to test different shaping tools and a custom microscope to quantitatively evaluate the resulting sample planarity.

Reference Samples

For post-landing checkout and calibration purposes two reference samples are foreseen. They are placed within a section of the outer perimeter of the sample carousel for which the sample cavity is interrupted. These samples will be analyzed first and, according to nominal planning only once, during the commissioning since their surface can become contaminated with lunar regolith during operations (see discussion below).

The first reference sample is a monolithic piece of AISI 316 L / 1.4435 stainless steel, which is glued into its respective cavity on the sample carousel. This material has been studied extensively with the laboratory prototype LIMS instruments and thus offers good comparability and evaluation of the performance of the LIMS system when deployed on the lunar surface. In addition, the well-defined surface of the steel reference sample reduces effects on the LIMS measurement stemming from deviations of the sample surface height, thus simplifying optimization procedures. Due to a low ablation rate of the steel, extensive measurement sequences (> 50’000 shots) can be performed on a single location of the sample without degradation of the spectral characteristics, reducing the size of the needed steel reference sample.

The second reference sample is lunar regolith analogue material pressed to a pellet. It is used for optimizing the operating parameters of the LIMS instrument (e.g., laser pulse energy, voltages applied to the ion optical system) as well as deriving calibration factors for all relevant species by using this matrix matched reference standard for the lunar regolith. Due to the low structural integrity of such a pressed pellet, it is sealed with a lid when the sample carousel is in its launch position.

When one of the reference samples is requested to be analyzed, the carousel is rotated in its nominal direction until the reference sample material is at the measurement location. This procedure is even feasible if the funnel still contains sample material while the reference materials pass below it. The last shaping brush is flush with the reference sample surface, thereby removing any potential regolith coverage that was deposited on top of the reference sample. If contamination of the reference sample is observed during subsequent analysis, one or multiple full rotations of the sample carousel can be initiated. This will empty the funnel and additionally the reference samples pass below the disposal and shaping brushes for additional cleaning of the surfaces.

Disposal of sample material and contamination control

Analysis of the lunar regolith with the CLPS-LIMS system consumes only a negligible amount of the sample material, in laser ablation mode in the range of fg – pg per laser shot [13], [14]. Most of the sample material entering the system will be disposed of unaltered. After analysis, the remaining material is discarded through a well-defined opening at the bottom of the instrument. Thus, appropriate positioning of the CLPS-LIMS instrument on the spacecraft has to be implemented to avoid potential contamination of other payloads with lunar regolith.

During sample material loading through the funnel and the sieving structure, regolith with too large grain sizes is removed through the openings at the front of the funnel (openings to the left, Figure 2). The disposal opening of the instrument and the funnel structure are in the XY-plane within ~60 mm of each other. No discharge from other parts of the instrument is expected.

To avoid contamination of the instrument with regolith other than introduced through the funnel, the instrument’s internal elements are protected partly by the structural assembly itself. The remaining openings are covered by epoxy impregnated glass fiber sheets. The second layer of protection consists of the multi-layer insulation (MLI) covering the instrument. Defined openings with sealed perimeters are foreseen for the funnel, which must be external of the MLI and the sample discharge opening. Internally the sections of the carousel where sample manipulation and shaping take place, are shielded by a top cover to contain regolith fines.

3. VALIDATION OF THE SAMPLE HANDLING SYSTEM CONCEPT

In this section we describe the experiments conducted on a prototype laboratory LIMS system and our findings, which helped guide the engineering choices made during the design phase of the SHS. All validation experiments were conducted using the lunar highlands simulant LHS-1 (Exolith Lab, Oviedo, FL, USA) as sample material. It is a high-fidelity lunar simulant, matching the chemical and geotechnical properties of lunar regolith found in the lunar highlands [15]. The mineral composition of the lunar simulant material is: SiO_2 (51.2 %), TiO_2 (0.6 %), Al_2O_3 (26.6 %), FeO (2.7 %), MnO (0.1%), MgO (1.6%), CaO (12.8 %), Na_2O (2.9 %), K_2O (0.5 %), P_2O_5 (0.1 %), and others (0.4 %) as given by XRF measurements. It is expected for the regolith found in the lunar south pole region to exhibit similar properties [16].

Stability of lunar regolith within the sample cavity

The lunar regolith must be able to keep its shape within the cavity of the sample carousel after its manipulation with the shaping brushes and the shaping tool for the correct functioning of the SHS. This is to ensure that the sample surface is still suitable for measurement using the LIMS instrument after the material is transported from the sample ingestion section to the analysis location.

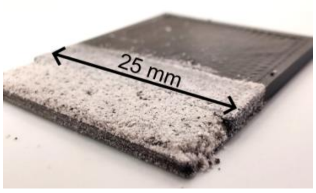

Figure 5: LHS-1 analogue material filled and shaped within a 3D printed linear strip of the carousel cavity profile (front). Some material is present outside of the cavity profile.

To test this, a 3D printed linear section with matching dimensions of the current cavity design was manufactured. It was coarsely filled with LHS-1, emulating the filling process the funnel and subsequently flattened to the height of the inner cavity wall using an L-shaped tool. The prepared cavity strip is shown in Figure 5. The sample retained its shape with no material flowing over the lower outer edge of the cavity. From optical inspection, the sample surface showed no major openings or cavities, and the sample planarity was compatible with the requirements for analysis using LIMS.

It remains to be tested whether potential vibrations during sample transport are degrading the sample surface quality, possibly requiring higher compression of the material. The cohesion of the used LHS-1 material is given with 0.311 kPa [15], whereas lunar regolith is expected to have cohesion values of 0.1 – 1 kPa [17] as encountered during the Apollo missions. With the cohesion of LHS-1 being on the lower end of the lunar regolith cohesion, using LHS-1 can be seen as a worst-case scenario. In addition, the higher angle of repose of regolith (LHS-1: 47.5°, lunar regolith: 58°) and the lower gravity on the Moon will lead to a more stable outer sample edge [18].

LIMS measurements of lunar regolith simulant

Measurements of the lunar analogue material were performed using a laboratory space prototype LIMS instrument [19]. For these measurements the LHS-1 sample material was filled into a AISI 316 L / 1.4435 stainless steel sample holder having 1 mm deep cavities. The prepared sample material in the holder is shown in Figure 6. To ensure sufficient planarity, the surface was levelled by moving the edge of a spatula over the sample material. Explicit compression of the material was avoided to simulate the worst-case scenario regarding porosity of the sample surface.

Optimization of the ion-optical voltage set of the ion-optical system was performed using the stainless steel holder itself as sample material. Ion-optical parameters were tuned to maximize signal intensity and mass resolution (*m/Δm*). This assures maximal sensitivity of the instrument and high spectral quality at the same time.

The sample planarity is a key factor for the quality of the obtained mass spectra. Because of the on-axis extension of the laser focus (Rayleigh length) there is a direct correlation between planarity and irradiance applied to the sample surface. A too low irradiance causes low material ablation rates and insufficient generation of ions. Additionally, element fractionation can be observed since elements with an higher ionization potential are not ionized efficiently due to the lower plasma plume temperatures [20]–[22]. This leads to low signal-to-noise ratios (SNR) and incomplete chemical information of the lunar regolith. On the other hand, a too high irradiance generates a too dense plasma at the ablation site as well as within the mass analyzer, resulting in space charge effects within the plasma plume and in the ion packets inside the analyzer, and thus reducing the mass resolution of the obtained spectra. This would make accurate chemical composition determination of the sample difficult.

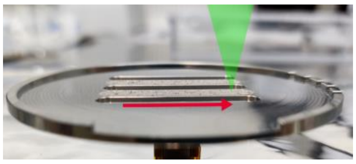

Figure 6: The stainless steel sample holder filled with LHS-1 lunar analogue material to test the sample-handling concept on the laboratory LIMS prototype instrument. The laser beam is schematically depicted as green cone and the sample movement direction during measurement is indicated by the red arrow.

The Gaussian beam propagation theory predicts a continuously increasing irradiance for a focused beam until the focus point is reached, after which the irradiance decreases again. To stay within an acceptable irradiance range for chemical analysis of the sample, the surface planarity must be appropriately controlled. Measurements using the laboratory setup were performed to determine the LIMS instrument's sensitivity regarding changes in laser irradiance *I*. Mass spectra at different laser pulse energies *E* were recorded and since *I* ~ *E*, direct correlations between *I* and spectral quality were obtained.

Figure 7 shows recorded mass spectra of LHS-1 at optimized laser irradiance (spectrum 1) and at 1.14x increased laser irradiance (spectrum 2), normalized to maximum signal intensity. The measurements were conducted while the sample was continuously moving underneath the mass

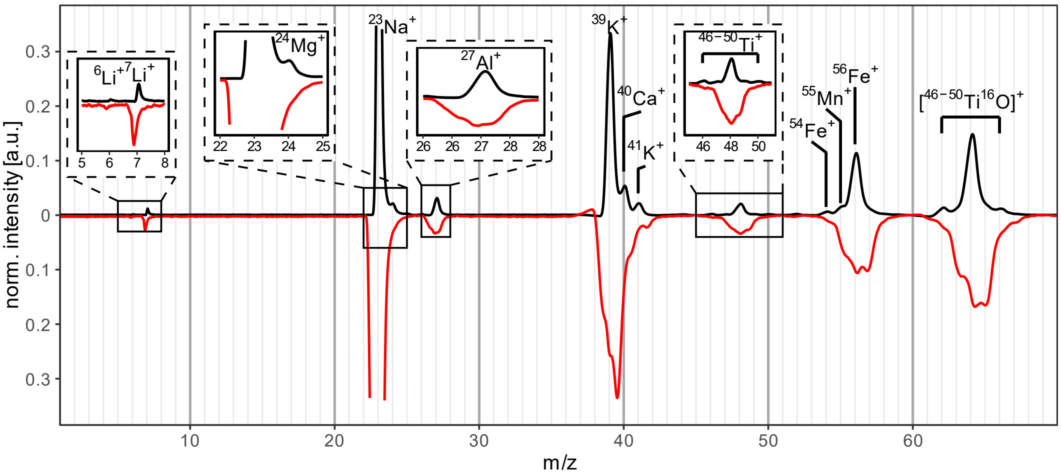

Figure 7: Mass spectrum of LHS-1 lunar analogue material measured using the laboratory LIMS setup. The upper mass spectrum (1) has been recorded with an optimized laser pulse energy, whereas the lower (inverted) mass spectrum (2) was recorded with 1.14 times higher laser pulse energy. Degradation of the spectrum quality by peak broadening is visible.

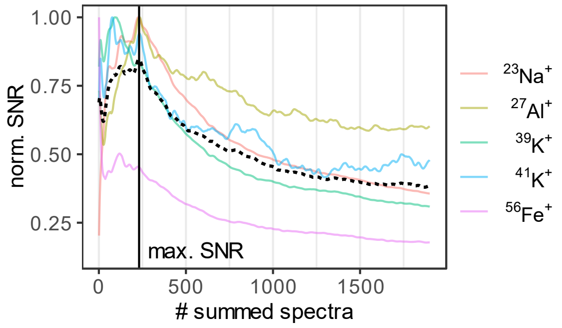

Figure 8: Normalized SNR of selected species with increased number of laser shots fired. The spectra were recorded on a single position, without moving the sample. The dotted line depicts the equally weighted mean. The maximal SNR was reached after 231 shots as indicated by the vertical line.

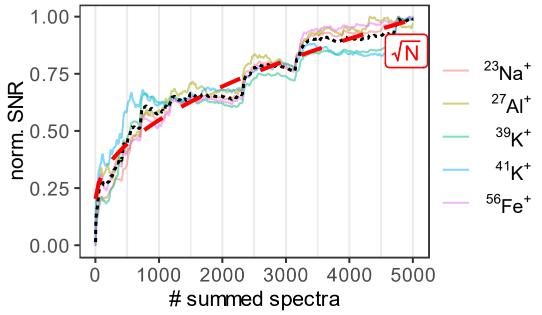

Figure 9: Normalized SNR of different species for increasing number of laser shots while the sample is continuously moving. The dotted line depicts the mean SNR. The dashed line the shows theoretical increase of SNR with the square root of summed mass spectra (*N*).

analyzer with a speed of ~0.8 mm/s. The recorded single laser shot spectra were filtered to only include spectra with a $^{23}Na^+$ signal having an SNR > 2. The filtered mass spectra were subsequently summed to obtain the final mass spectrum. For each energy level, about 5000 single shot spectra were recorded of which roughly 50 % matched the signal intensity criterium.

From the optimized spectrum (Figure 7, spectrum 1), all major elements present in LHS-1, except for Si and O, were detected. Additionally, peaks for some minor species, like $^6Li^+$ and $^7Li^+$ with the approximately correct isotope ratio of 1:10 are observed. These are not specified as compositing elements of LHS-1, since quantification by XRF, as used for the specification of LHS-1, is not able to detect Li. Mass spectrum (2), recorded with higher than optimal laser intensity, shows evident peak broadening. This masks the $^{24}Mg^+$, $^{41}K^+$, $^{54}Fe^+$ and $^{55}Mn^+$ peaks. Also, the isotopic structure of Ti is not discernible anymore.

From the known difference in laser irradiance between spectrum (1) and (2) and simulations of the laser beam propagation it can be derived that the sample planarity must not change by more than ±0.3 mm to ensure acceptable quality of the mass spectra. To allow for some safety margin, the sample planarity requirement was set to be ±0.2 mm.

Sample movement speed during analysis

LIMS measurements are destructive to the sample within the area of analysis. Consecutive laser shots applied at the same sample location will create an ablation crater and thus will lead to signal degradation eventually. To prevent this, new sample material must be continuously presented to the instrument. The signal degradation with respect to the amount of applied laser shots is highly material dependent. Crater formation is slower for a compact solid than for a loose grainy substance such as LHS-1 or lunar regolith [23].

The goal of the presented measurements was to determine the minimally needed rotation speed of the carousel to always have enough fresh sample material at the analysis location. Therefore, the SNR of the mass spectrometric signal with respect to fired laser shots without moving the sample was investigated. Figure 8 shows such an SNR trace at optimized analysis conditions (i.e., optimized laser energy). The SNR has been normalized to correct for the different absolute signal intensities due to the species having different concentrations in the sample material. Thus, the dotted trace shows the equally weighted mean of the SNR. For the initial accumulation of 231 single-shot mass spectra, an increase in SNR was observed. After that, not enough sample material was present at the analysis location to generate high enough signal to further increase the SNR. Instead, more noise than signal was added to the summed spectra, leading to a decrease in SNR from that point on. This measurement was repeated 2 times, with the maximum normalized mean SNR being reached on average after 200 laser shots.

With the LIMS instrument's nominal laser frequency of 100 Hz, the sample must be advanced with an average speed of at least 10 µm/s when a laser focus diameter of 20 µm is assumed. A ~1 Hz step frequency of the sample carousel's stepper motor is needed to reach this averages speed, as one step corresponds to 14 µm of sample advancement with the chosen gearing (see Table 1).

Figure 9 shows the SNR trace of a control measurement conducted with the same laser parameters as before, but with the sample moving at a constant speed of ~0.8 mm/s. With a continuously moving sample a decline in signal intensity is not observed. Consequently, the SNR continuously increases as more sample material is measured, closely following the theoretical SNR of $\sqrt{N}$, where N is the number of summed spectra.

Influence of the sample material's electrostatic charge

Regolith on the lunar surface is nominally electrostatically charged due to its exposure to solar UV radiation on the dayside, as well as the continuous stream of charged plasma particles impinging on the lunar surface [5]. The electrostatic potential on the sunlit surface ranges from a few volts positive up to +20 V [24].

To guarantee accurate operation of the mass analyzer's ion optical system, no potential difference between the system's reference ground and the sample material shall exist. This is to avoid unwanted disturbances in the electric fields used by the mass analyzer's ion optical system to extract ions from the plasma plume generated during measurements. Due to the potential electrostatic charging of the lunar surface, and thus the regolith sample material, preventive measures must be taken. To this end, the funnel structure, including the sieves are electrically conducting, and connected to instrument ground. This is also valid for the SHS carousel, as well as the sample shaping brushes. This ensures that the static electrical charge of the supplied lunar regolith can dissipate and the potential difference between instrument ground and sample material is minimized. Vibration of the sample material during sieving, and the sample shaping process leads to a large contact area of the sample material with grounded structures, thus achieving maximized potential equilibration.

Laboratory experiments were conducted to assess the sensitivity of the ion optical system to charged sample material through the application of a bias voltage to the sample material via the sample holder. A cavity of the prototype instrument's sample holder was filled with LHS-1 regolith simulant. Instead of connecting the sample holder to instrument ground, the holder was electrically isolated and connected to a bipolar power supply. Measurements were conducted while applying voltages of ±5 V, ±10 V and ±50 V to the sample. Additionally, reference measurements were performed while the power supply output was set to 0 V. For analysis, the faction of spectra having a mass peak of $^{23}Na^+$ with an SNR of larger than 2 was calculated. The results are shown in Figure 10. All measurements with bias voltage applied are within the spread of the reference measurements conducted at 0 V.

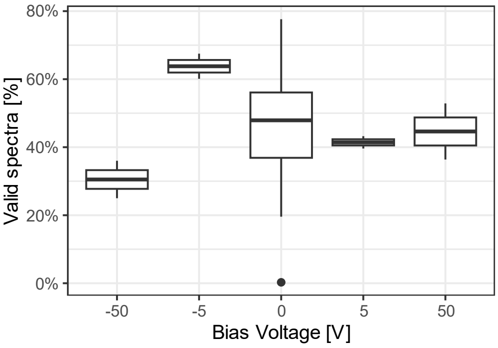

Figure 10: Ratio of spectra with a 23Na+ signal of SNR > 2 in dependence of applied bias voltage to simulate charged sample material.

Even at ±50 V, which corresponds to more than twice the expected potential of the unequilibrated lunar regolith, no significant decrease in signal intensity was observed. The spectral quality did however decrease, but we are expecting to be able to compensate for this by re-tuning the ion optical system.

4. SUMMARY

We described a sample handling concept for the analysis of lunar regolith using laser ablation ionization mass spectrometry (LIMS). The current design for integrating this concept into our CLPS-LIMS instrument is shown. Laboratory LIMS measurements on regolith analogue material were conducted to evaluate the sample handling concept and guide the implementation thereof. Resiliency of the system to electrostatic charging of the lunar regolith has been demonstrated. A complete breadboard of the SHS is currently being built, for the final version to be a part of the LIMS instrument which is scheduled to fly to the lunar south pole region within the CLPS program.

ACKNOWLEDGEMENTS

The financial support by the Swiss National Science Foundation and the Swiss Space Office is gratefully acknowledged.

REFERENCES

[1] P. Wurz, M. Tulej, A. Riedo, V. Grimaudo, R. Lukmanov, and N. Thomas, "Investigation of the Surface Composition by Laser Ablation/Ionization Mass Spectrometry," in *2021 IEEE Aerospace Conference (50100)*, Big Sky, MT, USA: IEEE, Mar. 2021, pp. 1–15. doi: 10.1109/AERO50100.2021.9438486.

[2] Y. Langevin and J. R. Arnold, "The Evolution of the Lunar Regolith," *Annu. Rev. Earth Planet. Sci.*, vol. 5, no. 1, pp. 449–489, May 1977, doi: 10.1146/annurev.ea.05.050177.002313.

[3] Y. Shkuratov, "Regolith Layer Thickness Mapping of the Moon by Radar and Optical Data," *Icarus*, vol. 149, no. 2, pp. 329–338, Feb. 2001, doi: 10.1006/icar.2000.6545.

[4] G. H. Heiken, D. S. McKay, and R. W. Brown, "Lunar deposits of possible pyroclastic origin," *Geochim. Cosmochim. Acta*, vol. 38, no. 11, pp. 1703–1718, Nov. 1974, doi: 10.1016/0016-7037(74)90187-2.

[5] T. J. Stubbs *et al.*, "Dependence of lunar surface charging on solar wind plasma conditions and solar irradiation," *Planet. Space Sci.*, vol. 90, pp. 10–27, Jan. 2014, doi: 10.1016/j.pss.2013.07.008.

[6] N. Afshar-Mohajer, C.-Y. Wu, J. S. Curtis, and J. R. Gaier, "Review of dust transport and mitigation technologies in lunar and Martian atmospheres," *Adv. Space Res.*, vol. 56, no. 6, pp. 1222–1241, Sep. 2015, doi: 10.1016/j.asr.2015.06.007.

[7] M. Tulej *et al.*, "CAMAM: A Miniature Laser Ablation Ionisation Mass Spectrometer and Microscope-Camera System for *In Situ* Investigation of the Composition and Morphology of Extraterrestrial Materials," *Geostand. Geoanalytical Res.*, vol. 38, no. 4, pp. 441–466, Dec. 2014, doi: 10.1111/j.1751-908X.2014.00302.x.

[8] A. E. Chumikov, V. S. Cheptsov, P. Wurz, D. Lasi, J. Jost, and N. G. Managadze, "Design, characteristics and scientific tasks of the LASMA-LR laser ionization mass spectrometer onboard Luna-25 and Luna-27 space missions," *Int. J. Mass Spectrom.*, vol. 469, p. 116676,

Nov. 2021, doi: 10.1016/j.ijms.2021.116676.

[9] U. Rohner, J. A. Whitby, and P. Wurz, "A miniature laser ablation time-of-flight mass spectrometer for *in situ* planetary exploration," *Meas. Sci. Technol.*, vol. 14, no. 12, pp. 2159–2164, Dec. 2003, doi: 10.1088/0957-0233/14/12/017.

[10] U. Rohner, J. A. Whitby, P. Wurz, and S. Barabash, "Highly miniaturized laser ablation time-of-flight mass spectrometer for a planetary rover," *Rev. Sci. Instrum.*, vol. 75, no. 5, pp. 1314–1322, May 2004, doi: 10.1063/1.1711152.

[11] A. Riedo, A. Bieler, M. Neuland, M. Tulej, and P. Wurz, "Performance evaluation of a miniature laser ablation time-of-flight mass spectrometer designed for *in situ* investigations in planetary space research: Miniaturised laser ablation tof mass spectrometer," *J. Mass Spectrom.*, vol. 48, no. 1, pp. 1–15, Jan. 2013, doi: 10.1002/jms.3104.

[12] P. Wurz *et al.*, "In Situ Lunar Regolith Analysis by Laser-Based Mass Spectrometry," in *2023 IEEE Aerospace Conference*, Big Sky, MT, USA: IEEE, Mar. 2023, pp. 1–10. doi: 10.1109/AERO55745.2023.10115714.

[13] V. Grimaudo *et al.*, "High-Resolution Chemical Depth Profiling of Solid Material Using a Miniature Laser Ablation/Ionization Mass Spectrometer," *Anal. Chem.*, vol. 87, no. 4, pp. 2037–2041, Feb. 2015, doi: 10.1021/ac504403j.

[14] M. B. Neuland, S. Meyer, K. Mezger, A. Riedo, M. Tulej, and P. Wurz, "Probing the Allende meteorite with a miniature laser-ablation mass analyser for space application," *Planet. Space Sci.*, vol. 101, pp. 196–209, Oct. 2014, doi: 10.1016/j.pss.2014.03.009.

[15] Exolith Lab, "LHS-1 Lunar Highlands Simulant Fact Sheet Dec. 2022." Dec. 2022. Accessed: Oct. 01, 2023. [Online]. Available: https://cdn.shopify.com/s/files/1/0398/9268/0862/files/lhs-1-spec-sheet-Dec2022.pptx.pdf

[16] P. D. Spudis, B. Bussey, J. Plescia, J.-L. Josset, and S. Beauvivre, "Geology of Shackleton Crater and the south pole of the Moon," *Geophys. Res. Lett.*, vol. 35, no. 14, p. L14201, Jul. 2008, doi: 10.1029/2008GL034468.

[17] J. K. Mitchell, W. N. Houston, R. F. Scott, N. C. Costes, W. D. Carrier III, and L. G. Bromwell, "Mechanical properties of lunar soil: Density, porosity, cohesion and angle of internal friction," *Lunar Planet. Sci. Conf. Proc.*, vol. 3, p. 3235, Jan. 1972.

[18] Z. Khademian, E. Kim, and M. Nakagawa, "Simulation of Lunar Soil With Irregularly Shaped, Crushable Grains: Effects of Grain Shapes on the Mechanical Behaviors," *J. Geophys. Res. Planets*, vol. 124, no. 5, pp. 1157–1176, May 2019, doi: 10.1029/2018JE005889.

[19] N. F. W. Ligterink *et al.*, "ORIGIN: a novel and compact Laser Desorption – Mass Spectrometry system for sensitive in situ detection of amino acids on extraterrestrial surfaces," *Sci. Rep.*, vol. 10, no. 1, p. 9641, Jun. 2020, doi: 10.1038/s41598-020-66240-1.

[20] K. H. Lepore, M. D. Dyar, and C. R. Ytsma, "Effect of Plasma Temperature on Major Element Prediction Accuracy From Laser-Induced Breakdown Spectroscopy," *Geophys. Res. Lett.*, vol. 50, no. 8, p. e2023GL102919, Apr. 2023, doi: 10.1029/2023GL102919.

[21] L. Torrisi, "Fractional ionization in plasmas produced by pulsed laser ablation," *Radiat. Eff. Defects Solids*, vol. 157, no. 3, pp. 347–356, Jan. 2002, doi: 10.1080/10420150212994.

[22] R. Huang *et al.*, "High irradiance laser ionization orthogonal time-of-flight mass spectrometry: A versatile tool for solid analysis," *Mass Spectrom. Rev.*, vol. 30, no. 6, pp. 1256–1268, Nov. 2011, doi: 10.1002/mas.20331.

[23] S. Wu, V. Karius, B. C. Schmidt, K. Simon, and G. Wörner, "Comparison of Ultrafine Powder Pellet and Flux-free Fusion Glass for Bulk Analysis of Granitoids by Laser Ablation-Inductively Coupled Plasma-Mass Spectrometry," *Geostand. Geoanalytical Res.*, vol. 42, no. 4, pp. 575–591, Dec. 2018, doi: 10.1111/ggr.12230.

[24] M. A. Fenner, J. W. Freeman Jr., and H. K. Hills, "The electric potential of the lunar surface," *Lunar Planet. Sci. Conf. Proc.*, vol. 4, p. 2877, Jan. 1973.

BIOGRAPHY

Peter Keresztes Schmidt *received his B.Sc. and M.Sc. in Chemistry at the ETH Zürich, Switzerland. He is currently working as a PhD student in Bern, Switzerland, where he is developing a new the LIMS instrument for in-situ studies on the lunar surface.*

Sébastien Hayoz *gained experience in different fields like electronics' development for Automotive, electronics' systems for Train Control Monitoring System (TCMS). Since February 2021, he is leading the electronics engineering team at the Space Research and Planetary Division and is involved for several instruments realized by the University of Bern.*

Daniele Piazza *has more than 20 years of experience in the design and development of space instruments. He has a Ph.D. in mechanical engineering from ETH Zurich and started his career in Formula 1. Since 2005 he leads the mechanical engineering group working on space instruments at the University of Bern.*

Timothy Bandy *has B.Sc. degree in mechanical engineering. He has mainly worked in the defense, pharmaceutical fields before joining UBE. Since then, he supported the development and AIV of BELA (BepiColombo), CHEOPS and CometInterceptor. He is now Systems Engineer for CLPS-LIMS.*

Patrik Mändli *received a M.Sc. in electrical engineering and information technology, ETH Zurich, Switzerland. For 7 years he worked in control, network and communications technology for all types of rail vehicles. Since March 2022, he is system engineer electronics for CLPS-LIMS.*

Matthias Blaukovitsch *has a M.Sc. in Physics from the Technical University of Vienna, Austria (2016). He has been working on time-of-flight sensors specializing on diode lasers and is now appointed as an optical engineer at the University of Bern.*

Michael Althaus *received a HTL & B.Sc. in Electrical Engineering from Lucerne University of Applied Sciences and Arts with specialization in Information Technology in 1999. He worked as a research engineer at ESEC SA in Switzerland and at the Centre for Advanced Materials Joining, University of Waterloo, Canada. Before joining the University of Bern in 2018 for the NIM (JUICE), the NGMS (Luna 27) and – lately – the CLPS-LIMS instruments, he worked as an R&D Senior SW/HW engineer in the industry.*

Benoît Plet *received his Ph.D. in Physical Chemistry from the University of Bordeaux, France, in 2007. After 15 years developing scientific instrumentation in industry, he has joined University of Bern, Switzerland, as project manager.*

Sven Riedo *received a B.Sc. in Electrical Engineering in 2022 from the University of Applied Sciences and Arts Western Switzerland. He is currently working as an electronic engineer at the University of Bern.*

Simon Studer *received his B.Sc. in Automotive Engineering in 2013 from the University of Applied Sciences Bern, Switzerland. He spent most of his time in Formula 1 before he joined as Mechanical Engineer to the Space Research and Planetary Sciences group of the University Bern.*

Olivier Studer *received his M.Sc. in Mechanical Engineering in 2023 from the University of Applied Sciences and Arts Northwestern Switzerland. Since September 2023 he is working as a mechanical design engineer on the sample handling system of CLPS-LIMS.*

Michael Bieri *received a B.Sc. in Electrical Engineering and Information Technology from the University of Applied Sciences Bern, Switzerland in 2022. Since Oct. 2022 is working at the University of Bern as software and electronics engineer on CLPS-LIMS and NGMS / Luna 27.*

Marek Tulej *received a Ph.D. in Physical Chemistry from the University of Basel, Switzerland in 1999. After his post-doctoral period at Paul Scherrer Institute (PSI), Switzerland, he joined in 2008 the University of Bern as an instrument scientist for space missions, including Phobos-Grunt, Marco Polo-R, Luna-Resurs, and JUICE.*

Andreas Riedo *received his Ph.D. in Physics in 2014 from the University of Bern, Switzerland. In 2016 he received a SNSF fellowship that allowed him to continue his research in Astrobiology at the Leiden University, The Netherlands. He extended his stay at the Leiden University with a MCSA fellowship for another two years before he moved in 2019 to the Free University Berlin after receiving the Einstein fellowship. In 2020 he moved to University of Bern and is currently appointed as researcher and project leader for CLPS-LIMS.*

Peter Wurz *has a degree in electronic engineering (1985), an M.Sc. and a Ph.D. in Physics from Technical University of Vienna, Austria (1990). He has been a post-doctoral researcher at Argonne National Laboratory, USA. Since 1992 at the University of Bern. He is Professor of physics, 2015–2022 head of the Space Science and Planetology division, and since 2022 director of the physics institute. He has been Co-I and PI for many science instruments for space missions of ESA, NASA, ISRO, CNSA, Roscosmos, and JAXA.*

3.3 Design and Testing of the Sample Handling System

The previously described sample handling concept based on a funnel interface, feeding delivered sample material onto a transport carousel, has been proven to provide sample material in a sufficient quality that makes analysis by LIMS possible. To improve on the design and provide the needed confidence that it will work under the challenging conditions of lunar surface operations, laboratory experiments with prototypes of the SHS have been conducted.

During surface operations, a fixed amount of sample material ($50\,\mathrm{cm}^3$ to $100\,\mathrm{cm}^3$ per loading operation) will be delivered to the CLPS-LIMS instrument by the external sample delivery system. With the available amount of sample material, one of the main performance parameters that needs to be optimised with regard to the SHS is its transport efficiency of lunar regolith. As the sieving during sample ingestion and sample surface shaping are lossy preparation processes, it is important to minimise these losses. The lower the internal losses, the more material is available for analysis by LIMS, thus enhancing the scientific return of the CLPS-LIMS instrument.

The following peer-reviewed publication describes the performed tests and optimisations to enhance the efficiency of the SHS and validate its overall functionality with respect to the expected conditions it will operate in.

© 2025 IEEE. Reprinted, with permission, from P. Keresztes Schmidt et al., ”Design and Testing of a Sample Handling System for Operation on the Lunar Surface”, *2025 IEEE Aerospace Conference*, Big Sky, MT, USA, 2025, pp. 1-14, doi: 10.1109/AERO63441.2025.11068749.

Design and testing of a sample handling system for operation on the lunar surface

Peter Keresztes Schmidt
Space Research and Planetary Sciences,
Physics Institute, University of Bern,
Sidlerstrasse 5, 3012 Bern,
Switzerland
peter.keresztes@unibe.ch

Sébastien Hayoz
Space Research and Planetary Sciences,
Physics Institute, University of Bern,
Sidlerstrasse 5, 3012 Bern,
Switzerland
sebastien.hayoz@unibe.ch

Daniele Piazza
Space Research and Planetary Sciences,
Physics Institute, University of Bern,
Sidlerstrasse 5, 3012 Bern,
Switzerland
daniele.piazza@unibe.ch

Timothy Bandy
Space Research and Planetary Sciences,
Physics Institute, University of Bern,
Sidlerstrasse 5, 3012 Bern,
Switzerland
timothy.bandy@unibe.ch

Patrik Mändli
Space Research and Planetary Sciences,
Physics Institute, University of Bern,
Sidlerstrasse 5, 3012 Bern,
Switzerland
patrik.maendli@unibe.ch

Matthias Blaukovitsch
Space Research and Planetary Sciences,
Physics Institute, University of Bern,
Sidlerstrasse 5, 3012 Bern,
Switzerland
matthias.blaukovitsch@unibe.ch

Michael Althaus
Space Research and Planetary Sciences,
Physics Institute, University of Bern,
Sidlerstrasse 5, 3012 Bern,
Switzerland
michael.althaus@unibe.ch

Benoît Gabriel Plet
Space Research and Planetary Sciences,
Physics Institute, University of Bern,
Sidlerstrasse 5, 3012 Bern,
Switzerland
benoit.plet@unibe.ch

Sven Riedo
Space Research and Planetary Sciences,
Physics Institute, University of Bern,
Sidlerstrasse 5, 3012 Bern,
Switzerland
sven.riedo@unibe.ch

Simon Studer
Space Research and Planetary Sciences,
Physics Institute, University of Bern,
Sidlerstrasse 5, 3012 Bern,
Switzerland
simon.studer@unibe.ch

Olivier Studer
Space Research and Planetary Sciences,
Physics Institute, University of Bern,
Sidlerstrasse 5, 3012 Bern,
Switzerland
olivier.studer@unibe.ch

Scott Trimble
Space Research and Planetary Sciences,
Physics Institute, University of Bern,
Sidlerstrasse 5, 3012 Bern,
Switzerland
scott.trimble@unibe.ch

Marek Tulej
Space Research and Planetary Sciences,
Physics Institute, University of Bern,
Sidlerstrasse 5, 3012 Bern,
Switzerland
marek.tulej@unibe.ch

Andreas Riedo
Space Research and Planetary Sciences,
Physics Institute, University of Bern,
Sidlerstrasse 5, 3012 Bern,
Switzerland
andreas.riedo@unibe.ch

Peter Wurz
Space Research and Planetary Sciences,
Physics Institute, University of Bern,
Sidlerstrasse 5, 3012 Bern,
Switzerland
peter.wurz@unibe.ch

Abstract—**Here we provide an in-depth description of the design concepts and verification strategy for the sample handling system (SHS) used for preparing lunar regolith samples for analysis by laser ablation ionization mass spectrometry (LIMS).**

The SHS is an integral part of a reflectron-type time-of-flight LIMS (RTOF-LIMS) system that allows for direct and sensitive chemical composition analysis of individual regolith grains *in-situ* on the lunar surface. The RTOF-LIMS measurements can provide the full element and isotope composition of the sample material (mass range up to m/z ~1,000) for each individual laser pulse applied to the sample surface.

The CLPS-LIMS instrument is manifested for a robotic mission (stationary lander) within NASA's Artemis Commercial Lunar Payload Service (CLPS) program to the lunar south-pole. The lander will provide upon request lunar regolith (grain sizes ≤ 5 mm) to the LIMS instrument's collection funnel for further sample manipulation by the instrument. The sample material is sieved in a two-stage process assisted by vibrating the funnel and sieve assembly at their first global resonance frequency. The sieving process removes grains with particle sizes larger than 1 mm, as these would interfere with achieving the required sample surface quality for reliable LIMS measurements. Control of the sample roughness is important to ensure consistent laser ablation conditions during sample analysis and thus reproducible chemical composition determination of the sample material.

The sieved sample material is deposited into a 1.5 mm deep and 5 mm wide channel at the edge of a rotating circular carousel disk with a diameter of 187 mm. The system creates, with the help of passive shaping brushes and a skimmer blade, a well-defined planar sample surface with height variations less than ±200 µm in > 90% of the conducted test runs. After chemical analysis by LIMS, cleaning brushes remove the remaining material from the channel and prepare it for new sample material delivered by the lander platform. The SHS system allows for indefinite sample material to be analyzed. Two

979-8-3503-5597-0/25/$31.00 ©2025 IEEE

reference samples are included along the edge of the carousel for calibration purposes of the chemical analysis performed by the LIMS instrument.

The SHS was tested and validated at inclinations up to ±10° off the nominal plane of operation, as an angled landing position of the lunar lander is possible. The observed overall sample utilization efficiency was influenced by losses during sieving and the intentional overfilling of the carousel channel. Effects on the sample surface quality have been studied and found to be within the requirements for subsequent analysis of the regolith by LIMS. Tests were conducted using regolith simulant with grain sizes of up to 5 mm (LHS-2, Space Resource Technologies, USA, complemented with larger grains). To test sieving efficiencies in the lunar gravity environment, cork grains with low specific mass were used to simulate the reduced gravity. Finite element analysis of the SHS shows compatibility with vibration loads as defined by NASA's General Environment Verification Standard (GEVS).

TABLE OF CONTENTS

1. INTRODUCTION

A Laser Ionization Mass Spectrometry (LIMS) instrument, designed to analyze the chemical composition of samples collected during an upcoming lunar mission, is currently under development. The LIMS instrument will operate on a robotic lander platform for conducting autonomous in situ measurements of lunar mineralogy, element composition, and isotope distribution without human intervention.

As part of NASA's Artemis program and its Commercial Lunar Payload Services (CLPS) framework, our team is working on developing the instrument, named "CLPS-LIMS", for upcoming missions with landing sites near the lunar south pole.

A major scientific goal of the Artemis program as outlined in the Artemis III Science Definition Team (SDT) report [1] is improving our understanding of the Earth-Moon system, such as the formation history and evolution of the Moon [2], [3]. Also, the lunar surface can serve as a time capsule preserving the history of impactors which were hitting the early Earth [4], [5], [6]. Sensitive chemical composition analyses and determination of isotope ratios of the lunar regolith grains will allow for a better understanding of the geochemical environment of the landing site [7]. These investigations directly address some of the questions formulated in the SDT report. Additionally, for a permanent human settlement on the lunar surface, local resources will have to be exploited [8] referred to as *in-situ* resource utilization (ISRU). To select, e.g., suitable building materials, the chemical makeup must be known [9], [10], [11]. The CLPS-LIMS instrument will deliver chemical composition information of bulk regolith as well as single grains.

The CLPS-LIMS instrument employs a pulsed laser system in conjunction with a mass analyzer to study the chemical composition of lunar regolith [12]. The laser beam is focused onto the sample surface to spot sizes of about 20 µm in diameter, resulting in irradiances in the range of MW/cm^2 to GW/cm^2, leading to ablation and simultaneous ionization of the material. The mass analyzer is based on a reflectron-type time-of-flight mass spectrometer (RTOF-MS) ion optical design [13], [14], [15]. The laser pulses are generated by a Nd:YAG microchip laser system employing second-harmonics generation ($\lambda = 532$ nm, $\tau \sim 1.5$ ns, 100 Hz pulse repetition rate). For a more in-depth description of the instrument's subunits, we refer the reader to the previously published studies [16], [17].

Instrument overview—A programmatic constraint of the mission is the strict adherence to the mechanical shock and vibration loads as defined by the General Environmental Verification Standard (GEVS) [18]. This is to decouple the requirements the payloads must fulfill from the, yet unknown, specific load environment the payloads will be subjected to during launch, transit and landing. This constraint excludes the possibility of a spacecraft (S/C) coupled loads analysis and the option to notch random loads at the S/C interface in case of high accelerations.

The instrument design published in [17] used a base structure (Main Support Structure, MSS) made of aluminum honeycombs sandwiched between near-zero coefficient of thermal expansion (CTE) carbon fiber-reinforced plastic (CFRP) sheets. These sheets provide the S/C interface as well as the mounting points of the different subassemblies. Structural finite element (FEM) analysis of this Spectrometer Unit (SMU) design (quasistatic analysis and full random analysis) showed structural loads at subassemblies exceeding limits when using input loads as specified by GEVS at the S/C interface as simulation input. The main cause identified was the 0-CTE structure highly amplifying the input loads. As targeted notching is out of scope, reducing the observed loads is only possible through structural changes to the MSS. Investigated design options were either stiffening the MSS and thus shifting the eigenfrequencies higher or softening the MSS to lower the eigenfrequencies. Both variants had the common goal to shift the MSS's eigenfrequencies into regions where GEVS input loads are lower. None of these approaches was successful and, consequently, a completely new mechanical design of the MSS became necessary. The new concept is based on a monolithic structure fabricated out of AlBeMet AM162. The material choice was based on the need for a thermally and mechanically stable, but lightweight structure. High thermal conductivity and heat capacity allow for uniform thermalization of the structure. It's mechanical characteristics, combined with its low CTE, make AlBeMet a good choice for a structure that must meet strict mechanical tolerances while being subjected to thermal changes. Additionally, AlBeMet's specific stiffness is higher than Aluminum or Titanium, making it more suitable for construction of GEVS loads compatible structures.

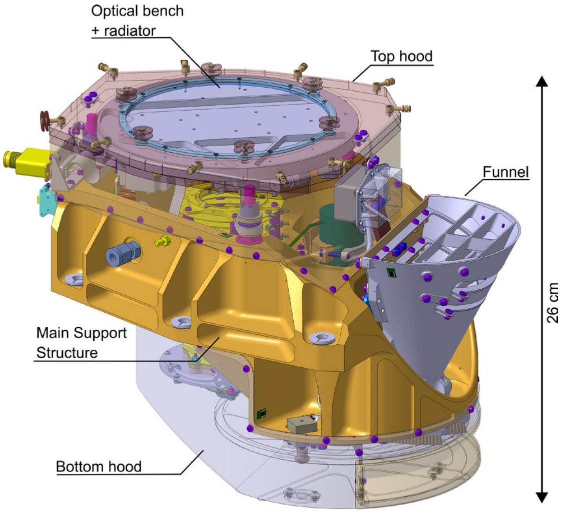

Figure 1: Overview of the current SMU design of the CLPS-LIMS instrument with a main support structure (MSS) fabricated out of AlBeMet AM162.

This monolithic design of the SMU is shown in Figure 1. The AlBeMet MSS is depicted in orange. All subassemblies, such as the mass analyzer (MA), the optical sub-system (OSS) and the sample handling system (SHS), are directly mounted to the MSS. The spacecraft interface is realized via inserts made of Ti6Al4V (Grade 5). These are individually dimensioned to compensate for residual machining tolerances of the MSS and pressed into the AlBeMet structure. The main design requirement was the need to keep random load amplifications at the subassemblies minimal. As the GEVS input loads prescribe high acceleration spectral densities between 50 Hz and 800 Hz [18], a minimum eigenfrequency of > 2000 Hz was defined for the MSS. Weight optimization of the MSS was performed using a geometry optimizer in combination with FEM analysis.

The SMU is encased in lightweight hoods fabricated out of glass fiber reinforced polymer (GFRP) for protection from lunar dust to which multilayer insulation (MLI) is attached via standoffs, serving as thermal barrier.

Radiative surfaces for heat dissipation serve multiple purposes. The optical bench (see Figure 1) functions simultaneously as the radiative surface for the laser and associated optics. To dissipate the heat produced by components within the SHS, the funnel on the SMU's side is used.

In a previous publication [17], we discussed the general sample handling concept of the CLPS-LIMS instrument. Since then, this concept has been refined and extensively tested and validated in a laboratory setting. In the following sections, an overview of the design choices made is given, as well as the verification procedures utilized to ensure the SHS fulfills its requirements.

2. DESCRIPTION OF THE SAMPLE HANDLING SYSTEM

The SHS's main functionality is to receive between 50 cm^3 and 100 cm^3 of coarse regolith from the lunar surface with grain sizes up to 5 mm. It prepares the sample for analysis with a surface planarity and roughness better than ±200 µm. This sample is continuously presented in front of the mass analyzer (MA) aperture for chemical analysis. The planarity requirement stems from the sample surface having to be within the focused region of the laser beam for laser ablation/ionization be able to take place.

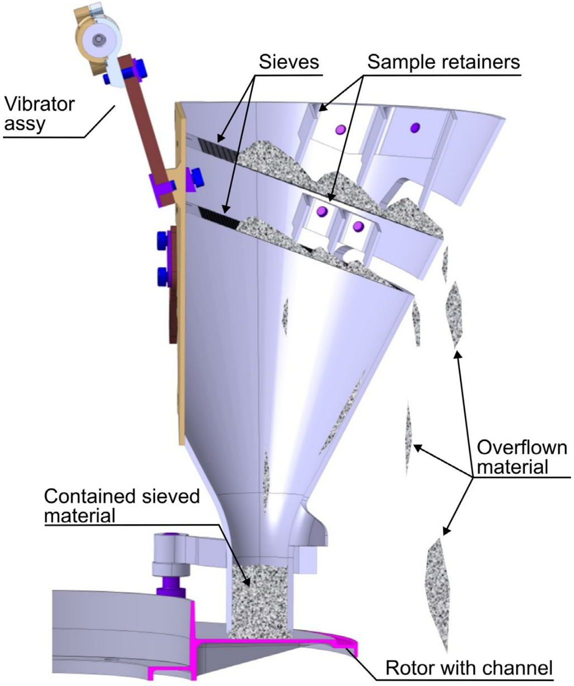

Figure 2: Graphic description of the funnel's principle of operation.

The lunar regolith is delivered via an external sample delivery system (SDS), which is part of the CLPS lander platform and thus out of scope of this instrument's design. The delivery system transfers the material into a drop-zone located above the funnel, which then collects and sieves the material as shown in Figure 2. The sieved material is dispensed onto a

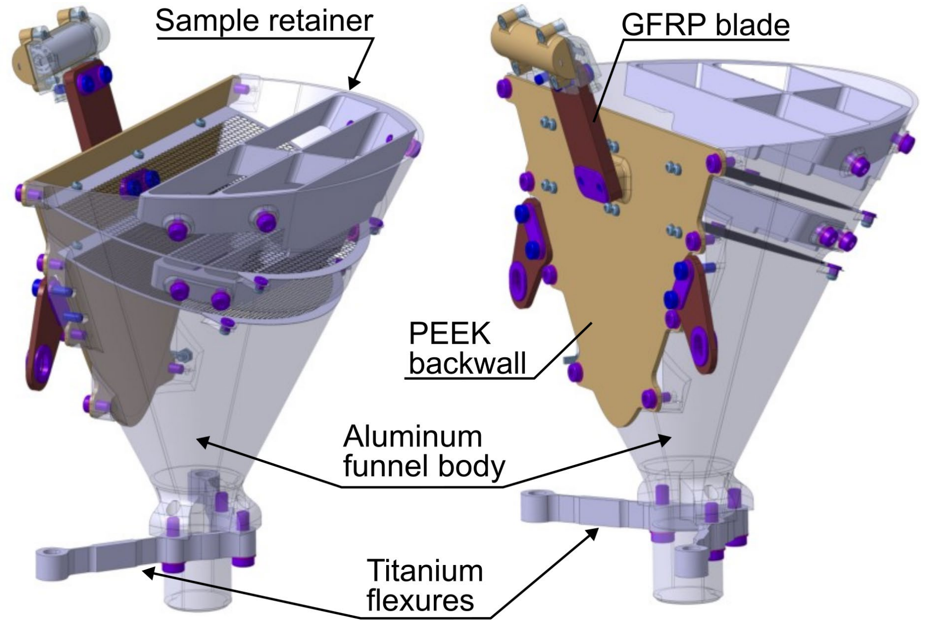

Figure 3: The current baseline funnel design of the CLPS-LIMS instrument.

rotating carousel which has an approximately 5 mm wide and 1.5 mm deep channel along its outer edge. A series of stainless-steel brushes push the material outwards into the channel and, in the process, completely fill the channel with the regolith sample. A skimmer compacts the sample and increases the surface quality before it is presented in front of the MA aperture. After analysis of the material, cleaning brushes remove the regolith from the carousel surface and empty the channel. The carousel rotates continuously during operation, continuously providing fresh sample material for chemical composition analysis.

The funnel, shown in Figure 3, with a large opening at the top is the interface for the CLPS provided SDS to dump the coarse sample material into. The funnel features two sieves that allow grains of 2 mm and 1 mm size, respectively, to pass towards the bottom of the funnel. Material which does not pass through the sieves falls out of openings on the side. These sieves are tilted at 20° to prevent stationary material clogging the funnel system. The tilt angle of the sieves allows for the lander to be tilted 10° relative to gravity vector in every direction without the material removal from the sieve surfaces being impeded. The sieves are made of woven metallic wires sandwiched in between metallic frames. Having woven wires should provide a degree of friction during launch and thus valuable dampening.

To facilitate sieving, a vibrator driven by a brushed DC motor (DCX10L Space; maxon Switzerland AG, Alpnach Dorf, Switzerland) is attached to the semi flexible, flat PEEK backwall of the funnel via a GFRP blade between the vibrator and funnel backwall. This is to amplify the deformation of the backwall and thus the agitation of the attached sieves. Each sieving process will take approximately 1 minute. The cables used to operate the vibrator have a shielding, which is also used to thermally connect the motor with the thermally controlled monolith, to ensure that non-operational temperature range is respected. The whole funnel is attached with flexible suspensions, to limit parasitic vibrations originating from the vibrator spreading throughout the LIMS instrument and beyond. These interfaces have slits and allowances for shims, allowing moving the funnel up and down relative to the carousel before final integration.

A retainer structure (see Figure 3) is added above the first sieve. This is used to avoid excessive sample material being lost due to sliding off the sieve during coarse sample delivery. The retainer also decreases the flow of sample material off the sieve during sieving and thus maximizes the sample material usage efficiency.

The carousel employed in the SHS has been fabricated from titanium, a material with good stiffness-to-mass ratio. To further enhance this property and maintain structural integrity even under demanding conditions, internal support beams at the bottom of the carousel structure were incorporated into the design. For calibration purposes of the chemical composition analyses using LIMS, two reference samples are integrated along the carousel's circumference, thus splitting the sample channel into two parts and making a position reference system necessary. For this reason, a tactile switch is mounted to the bottom side of the carousel within a dust protected enclosure, which is actuated once every full rotation. As a stepper motor is used to rotate the carousel, accurate positioning can be guaranteed after referencing the system once even with no additional encoders installed on the drive train, when respecting the motor's maximal stepping torque.

As the employed microchip laser system can potentially be damaged by direct back reflections from the carousel's surface, all surfaces that can be hit by the laser beam are tilted by 3° outwards. This ensures that any specular reflection from the carousel's surface is imaged outside of the laser by the optical system.

During launch and transit, unwanted carousel rotation is inhibited using a nD3PP-AL launch lock (DCUBED GmbH, Germering, Germany). It is disengaged after landing on the lunar surface.

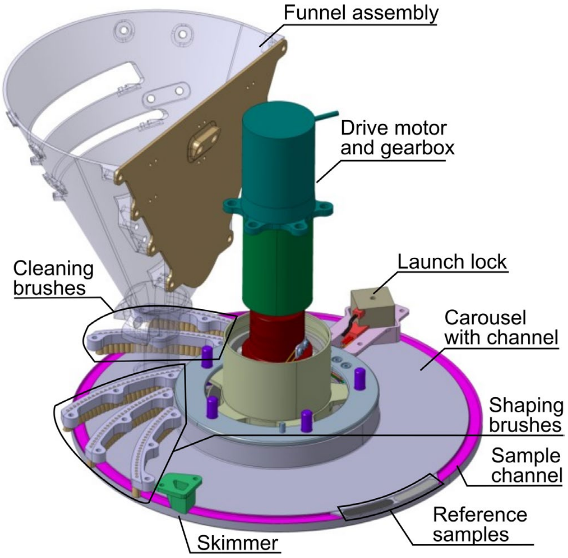

Figure 4: Overview of the SHS components. The vibrator structure is not shown in this figure.

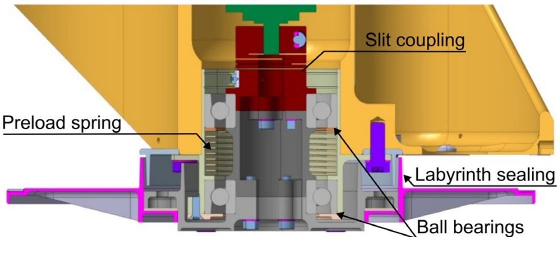

Figure 5: Close-up view on the SHS carousel drive train after the motor gearbox.

Drive train—A 2 phase stepper motor phySPACE 32-2-200-0,6-VGPL 32 (Phytron GmbH, Gröbenzell, Germany) with a matching 3-stage planetary gearbox are used to drive the carousel rotation. Space-application compatible Braycote (Castrol Ltd., Pangbourne, UK) lubricant is used to reduce friction and wear within. The gear has a high transmission ratio of 1:288 to maximize torque and position resolution per motor step. The carousel's drive bearings are shielded from lunar regolith contamination using a labyrinth sealing system, as shown in Figure 5.

Considering the diameter of the carousel disc and the position resolution after the gear, a single step will result in sample movement relative to the mass analyzer of 10 µm per step, which approximately matches the diameter of the laser beam's focal spot. The nominal stepper motor speed is ~10 Hz which leads to a complete rotation approximately every 90 minutes if a continuous measurement campaign is conducted.

The output torque (at 70% of maximum motor current) of 7.2 Nm (guaranteed by supplier to be applicable over the whole temperature range) is four times larger than the torque peaks measured during laboratory test campaigns with lunar regolith simulant.

The output shaft of the gear has a polygon shape for robust coupling with the carousel. A slit coupling design has been chosen to connect the polygon shaped gear shaft with the carousel. It can compensate for axis misalignment in angle and account for relative movement along the axis. Relative movement perpendicular to the axis cannot be compensated, instead the gear and the carousel have a tight sliding fit in the monolithic structure. The coupling is made of gold-plated titanium. The carousel's rotational bearings are made of steel rings and are equipped with ceramic balls within a phenolic resin cage. The bearings' outer diameter of 47 mm has been chosen to be reasonably large to absorb moments that originate from the carousel during launch and regolith grains being potentially crushed by the skimmer. This moment reduction is aided by a wave spring which is pushing the outer rings of the bearing apart.

3. TESTING AND VERIFICATION OF THE SAMPLE HANDLING SYSTEM DESIGN

Extensive testing has been conducted with lunar regolith simulant, both to iteratively optimize the subcomponents of the SHS and finally validate the integrated design. Initial testing and optimization were performed separately for the funnel and carousel subassembly. The following sections describe the procedures employed and how the results from the test influenced the system design.

The experiments were conducted using lunar regolith simulant from the LHS (i.e. lunar highland simulant) series (Space Resource Technologies, Oviedo, FL, USA) in engineering quality. Depending on the campaign, LHS-1E with grain sized up to 1 mm or custom LHS-2E with grain sizes extended up to 5 mm were used. The composition and structure of regolith at the lunar south pole landing site is expected to exhibit similar properties as the highland regolith [19]. Thus, this simulant is deemed a suitable proxy material for the conducted tests. The regolith simulant material was baked out at 110°C for 24 h, as humidity influences the geomechanical properties. The baked-out material was stored in a desiccator under vacuum until usage. While conducting the tests, the material was exposed to a non-humidity-controlled environment. After a day of testing, the material was baked out again.

Testing and Verification of the funnel

Ensuring efficient and reliable sample transport from the funnel to the SHS carousel is crucial for successful operation. This process starts with the sample material being dropped by the SDS onto the first sieve. The material's path must remain unobstructed under diverse conditions such as the spacecraft being tilted due to uneven or sloped landing sites. To guarantee proper sample handling in all foreseeable scenarios, various factors affecting this process have been investigated:

- Geometry of the funnel body and nozzle
- Sieve angle as well as sieving efficiency
- Vibration motor positioning

Evaluation of funnel and nozzle geometries—To identify the most effective funnel design, a series of breadboards (BB) were built and evaluated. Each BB was fabricated using either polylactic acid (PLA) or polyvinyl butyral (PVB) via fused filament 3D printing. Initially, simplified funnel shapes (geometry breadboards) were assessed to optimize material flow within the funnel (Figure 6). Funnel wall angles varied from 50° to 70° relative to the carousel plane, and for cylindrical designs, tube outlet diameters ranged from 12 mm to 24 mm. For the slotted funnel design, a slot width of 12 mm was tested.

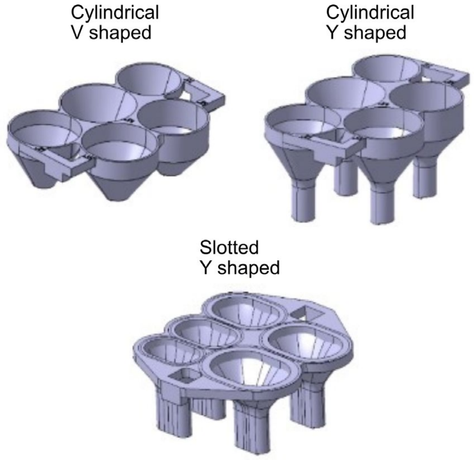

Figure 6: Overview of funnel geometries tested using the 3D printed breadboards.

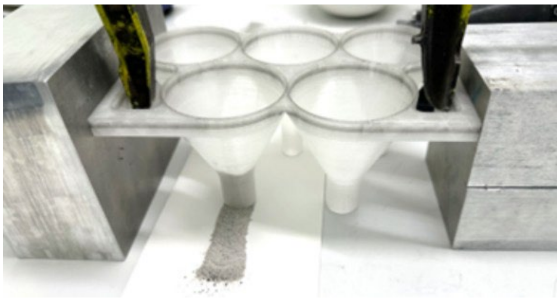

Figure 7: Test setup consisting of a series of 3D printed cylindrical Y funnel geometry breadboards. PVB was chosen as material as the surface quality can be improved by immersing it in isopropanol. The paper sheet was pulled continuously to simulate the carousel movement.

To assess the regolith outflow, the printed geometry BBs were fixed to aluminum blocks, maintaining a precise distance to the laboratory table. A sheet underneath the funnel nozzle mimics the movement of the carousel. After filling the funnel with regolith simulant, the sheet underneath is moved towards the front as shown in Figure 7, allowing the material to flow out of the funnel. The mass of dispensed material and the distance over which this happened, was measured to approximate the outflow rate.

The material behavior and the outflow rates of the different geometry types were measured and compared. For all following tests, LHS-1 regolith simulant was used. The outflow rate was defined as mass disposed per mm distance on carousel circumference.

Funnel designs with smaller tube diameters and smaller funnel angles often exhibit ratholing [20]. Ratholing refers to a condition where material flows only in a narrow central region of the funnel, while the surrounding material remains stationary and self-supporting. Despite ratholing, the material flow at the nozzle of the funnel can remain stable, as the surrounding material may collapse inward before any non-continuous funnel outflow occurs. At steeper funnel angles or larger tube diameters, ratholing becomes less likely, leading to the desired funnel flow behavior where some material is stagnant at the funnel wall while a larger volume flows simultaneously. Specifically, at a 70° funnel wall angle, continuous mass flow occurs across all diameters. In general, larger tube diameters and steeper funnel angles result in improved material flow through the funnel.

Many cylindrical V shaped funnels show bridging. The material does not create a hole in the middle of the funnel but supports itself and does not flow out. These phenomena can be seen with an outlet diameter of 12 mm at all funnel angles. Even the 50° and 55° funnel wall angles and 18 mm outlet diameter funnels show bridging. Generally, the V shaped funnels are problematic due to this phenomenon.

The material flow within the slotted funnel is promising, with mass flow occurring even at a 50° funnel wall angle, indicating that bridging or ratholing is highly unlikely. However, a challenge arises from the elongated outlet hole, where friction is created by jammed particles between the long edge and the sheet below. Consequently, testing was omitted for the 18 mm and 24 mm slot width concepts due to this issue. Outflow rates of the slotted 12 mm geometry BBs are comparable to the cylindrical Y shaped BB with 12 mm nozzle diameter, as the opening of both nozzles are similar. The friction effect was absent in the earlier cylindrical geometry tests since they lack the extended edge. Overall, the slotted design concept is deemed less favorable due to the particle jamming at the outlet, leading to torque peaks in the powertrain.

All funnel geometry breadboards were fabricated with two different outflow nozzle configurations, as shown in Figure 8. The variant with a flat opening requires a clearance of 1.5 – 2 mm to the carousel surface to allow for all expected grain sizes to be able to exit the nozzle. For the nozzle variant with the enlarged opening, the side on which material outflow is expected, is enlarged by 1.5 mm in the vertical direction. This enlarged opening allows larger grains to exit the funnel while maintaining a small clearance relative to the carousel. Thus, preventing material from spilling out on the sides of the nozzle and producing a clearly defined outflow geometry on the carousel.

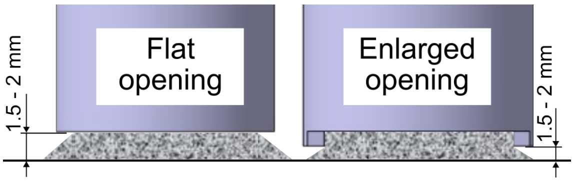

Figure 8: The two different nozzle configurations tested. The enlarged opening allows large grains to exit while reducing material spillage on the sides.

A cylindrical Y shaped funnel with a large tube outlet and a steep funnel angle emerged as the most promising geometry for optimal flow behavior within the funnel and efficient material outflow. This configuration facilitates a continuous material outflow without the need for vibration during carousel movement. The outflow rates rise with larger tube diameters, which reduces the carousel efficiency, as the sample channel in the carousel can be filled with a fraction of the incoming material. This challenge can be mitigated by positioning the funnel closer to the center of the carousel.

To validate the funnel behavior within a lunar gravity environment, the outflow tests were repeated with cork powder instead of lunar regolith simulant. The cork powder had a comparable grain size distribution and less than 1/6 the density of regolith simulant. The observed funnel outflow rate of the cork is comparable to the regolith simulant. No issues with ratholing or bridging were observed.

Evaluation of a complete funnel concept—Two funnel concepts were considered promising and designed in detail. The two concepts are subject to a tradeoff regarding outflow rate, funnel opening and available space. Both concepts have a flat back wall at the SMU monolith side and two 12° declining sieves. An Ø 18 mm nozzle was determined to be a good compromise between outflow rate and material flow continuity. The monolithic SMU design allows the funnel to move closer to the carousel center and thus keep the amount of dispensed material per carousel revolution constant while enlarging the nozzle diameter. The maximum funnel angle is limited by the minimum required drop zone surface for the SDS delivering the sample material and the required sieve area. The two concepts have maximum funnel wall angles of 63° and 70°, respectively. As a 70° funnel would create a too small drop zone (with the given height and the flat back wall), the available drop zone was therefore extended by having a smaller 55° angle (only in one direction) in the top section of the funnel (asymmetric design). The effective drop zone size is slightly larger than the required 80 mm x 80 mm. For the second concept, to avoid multiple funnel angles within one design, the overall funnel angle was reduced to 63° (symmetric design). This allows to have a sufficiently large opening at the top and sieve sizes within the available interior volume. The drop zone is comparable to the previous concept but is wider on the sides.

Both concepts were produced by additive manufacturing (3D printing) and equipped with representative sieves. The 63° model is shown in Figure 9. The vibrator was attached horizontally and vertically on the back wall and on the funnel side. For both funnels, attaching the motor on the side of the funnel led to almost no sieving, independent of the motor axis orientation and motor speed. The relatively stiff, round part of the funnel does not excite the sieves and thus no sieving occurs. Attaching the motor to the backwall led to adequate sieving results for the symmetric funnel. The same configuration on the asymmetric funnel did not work well and sieving took considerably longer. The vertical (parallel to funnel axis) attachment of the vibrator did not lead to efficient sieving results for both concepts. Tests have shown that the funnel backwall and the motor bracket will be excited by the vibrator at a specific eigenfrequency. This excitement leads to enhanced sieving results. The asymmetric funnel has a much smaller and hence stiffer backwall which reduces this excitement. To prove this theory, a much stiffer backwall (8 mm instead of 1.5 mm) was added to the symmetric BB. This stiffened backwall made the sieving impossible. A thin backwall is therefore required to have efficient sieving. As the flight-quality funnel will be manufactured out of aluminum, a more flexible material is needed for the backwall. The current baseline foresees PEEK as backwall material.

The tested BBs did differ in overall stiffness from the planned aluminum funnel. To detect potential problems due to this mismatch, a more representative BB regarding stiffness was printed with a 5 mm thick funnel body and a 1.5 mm thin backwall. This new BB showed comparable sieving results to the symmetric BB despite more representative stiffness.

A sieve angle of 12° is beneficial for efficiency as the lateral material outflow is moderate. An uneven landing site scenario might reduce this sieve angle to 2°, which is insufficient, as larger grains would remain stationary on the sieves. Therefore, a larger nominal angle of at least 20° is foreseen. The asymmetric funnel concept is not being pursued further due to limitations in sieving efficiency and the complicated manufacturing.

Figure 9: 3D printed funnel with 63° wall angle used to test and validate the sieving performance.

Optimization of the vibrator efficiency—The design of the funnel backwall and motor connection is important for efficient sieving. A main limitation of the previous funnel tests is the aluminum bracket used to mount the vibrator to the funnel. During vibration, motor and bracket are excited together which influences the system.

The aluminum bracket was replaced by lighter, 3D printed parts. Clamping the motor between two printed shells and bolting the assembly directly to the funnel backwall did not lead to efficient sieving results, independent of the vibrator frequency. The excentric forces are too small to excite the backwall efficiently. When adding a blade between motor shell and backwall, the sieving was very efficient, and comparable to the results with the aluminum motor bracket. The vibration motor mounted on a blade can be simplified as a damped harmonic oscillator. With the blade- and backwall thickness the eigenfrequency of the system can be tuned. A stroboscope was used to visualize the eigenmode of the system. A blade that is too thin leads to an unwanted torsion mode. By using a thicker blade, a bending mode can be achieved. For the flight design, the printed blade material will be replaced by glass fiber laminate.

Sample material retainers—Previous tests have shown that a significant percentage of material is ejected laterally out of the funnel, which otherwise would have been small enough to pass through the sieves. Especially when pouring a large scoop into the funnel, some material instantaneously flows out of the funnel at the first sieve. The material that does not exit laterally or falls onto the second sieve immediately, creates a cone, with an angle of repose between 43.1° to 45.8°, as given by the LHS-2 material specifications. At some point, the cone extends all the way to the end of the upper sieve. If more material is poured into the funnel, most of the additional material is ejected out of the funnel without having had the opportunity to be sieved. Laboratory tests have shown that the absolute amount of material passing the sieves, and therefore ending up inside the funnel, is mostly independent of the scoop size. Thus, the material usage efficiency of the overall system gets worse for large scoops. Two different countermeasures have been tested to increase the sample usage efficiency. In the first concept, the upper sieve was equipped with pillars which should prevent the material from outflowing, as shown in panel A of Figure 10. Alternatively, the second concept has blade shaped material retainers attached to the round section of the funnel, which are not in direct contact with the sieve (Figure 10, panel B). The pillar concept did not lead to a measurable efficiency increase. However, the blade concept increases efficiency. When pouring a large scoop into the funnel almost no material is ejected immediately. The clearance between sieves and retainers is critical and must be optimized to allow large grains to exit the funnel. When pouring a large scoop (118 g) into the funnel, these retainers lead to up to 10 g of additional material in the funnel. With this improvement, the sieving takes slightly longer as material remains longer on the sieves.

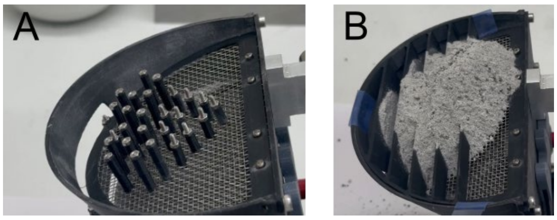

Figure 10: Sample retainer concepts based on pillar structures attached to the sieves (A) and blades attached to the funnel body (B).

Overall funnel efficiency—The amount of material passing the sieves mainly defines how much material can be analyzed by the mass analyzer. Small and large scoops (50 cm^3 and 100 cm^3) of LHS-2 extended up to 5 mm grain size were poured into the 3D printed, stiffness representative funnel with the blade vibrator to measure the efficiency of the optimized system. The whole funnel was tilted by 8° to reach a sieve angle of 20° as the BB is equipped with the 12° sieves. For these efficiency measurements, a retainer concept with three blades was used above the first sieve. A precise measurement of the sieving efficiency is challenging as many factors play a role, e.g. the position where the scoop is poured, the pouring height, the vibrator settings, etc. The total amount of material ending up in the funnel varied especially for large scoops. Six measurements with equal configuration led to results shown in Table 1. The overall efficiency for small scoops is higher than for large scoops. Some material does not reach the sieves themself, when a lot of material is present, but rather floats on the material that is still present on the sieves. This is especially noticeable on the second sieve. This limits the efficiency for large scoops. Most material is now lost on the second sieve. Introducing the retainers also on the second sieve might lead to a slight improvement. The additional complexity of this second retainer is currently deemed unnecessary, thus no second retainer is foreseen for the flight design.

Table 1: Determined sieving efficiencies for the optimized funnel design.

Scoop mass	Average material in funnel (range)	Efficiency
61 g (small scoop)	29.4 g (29 g – 31 g)	47 %
118 g (large scoop)	42 g (34 g – 49 g)	35 %

Verification of the carousel's functionality

The design verification for the funnel and brushes cannot be measured but are visually analyzed. Excessive material accumulation before brushes and inefficient channel cleaning has to be avoided. Various configurations were tested to find optimal parameters for the design.

The brush angle with respect to the radial direction can be changed from 10° to 50° on the BB. This influences how efficiently the dispensed material is pushed outwards towards the channel. Small angles lead to slow radial material flow. Hence, material accumulates before the brush. An unfavorable tilt of the carousel, as can be the result of the landing on the lunar surface, can even increase the material accumulation. A large brush angle increases the material outflow but requires longer brushes or even curved brushes. At 40° to 45° brush angles, sufficient material outflow was achieved, and no significant material accumulation was observed. The distance between carousel and brush (brush height) influences the amount of material that will be pushed outwards. To ensure that material accumulation before a single brush is acceptable and no material spills over the side of the brush, a sequence of three brushes with decreasing brush height is implemented on the SHS. The sequence of brush heights, which created similar material ejection volume at each brush, is 0.7 mm, 0.5 mm and 0.4 mm.

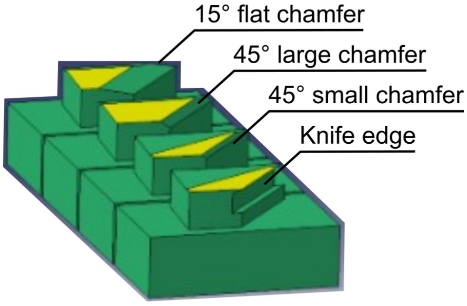

Figure 11: Various skimmer geometries that were tested on the SHS BB to ensure good sample compaction and planarity. Best results were obtained with the 15° flat chamfer skimmer, which ensure a flat sample surface and sample compaction.

Various skimmer geometries as shown in Figure 11 were tested. The three chamfered skimmers compact the sample and simultaneously eject excess material, whereas the knife edge skimmer rather cuts excessive material without sample compaction and pushes it off the carousel. Due to the brushes which already pre-shape the sample material, relatively little material must be removed by the skimmer. With a 45° angle between skimmer edge and a radial line passing through the skimmer, sufficient material flow was observed. As a compacted sample is beneficial for LIMS measurements, the knife edge skimmer is not considered for all further planarity measurements.

The cleaning brushes remove material from the carousel and from within the sample channel. Tests have shown that two brushes are required to sufficiently clean the carousel. One flat brush cleans the carousel surface (with 0.1 mm clearance). The second brush cleans the channel and the remaining particles on the carousel surface. The second brush is manufactured with a step to reach to the bottom of the channel. Some material remains in the channel, but this material is covered with pristine regolith material during the next sample delivery. Therefore, the channel must not be completely empty. For both brushes, the same angle (45°) can be used as for the shaping brushes.

Generally, the empirically determined settings with a 45° brush angle, skimmer and two cleaning brushes work well on the SHS BB. A test with 699 g of LHS-1 processed by the carousel was executed to simulate a complete lifetime. The amount equals 20 small scoops or 10 large scoops with an estimated funnel efficiency of 50%. The test showed no clogging or degradation on the brushes and the skimmer. All excessive material was removed, and no long-time material accumulation was detected.

Sample planarity and roughness verification

Sample planarity and roughness strongly affects the quality of obtainable mass spectra by the LIMS instrument. As such, a method to quantify and compare sample surface qualities prepared by the SHS breadboard system is needed. Several constraints and requirements had to be considered when designing the measurement system. For one, the loose nature of the sample material excluded tactile techniques and necessitated the use of optical profilometry techniques to determine the sample surface quality. As the profilometer had to be integrated into the SHS breadboard, the system had to be compact enough to fit onto the breadboard. Additionally, the profilometer's instantaneous field of view (FOV) should cover the width of the sample channel (~5 mm), to avoid the need for scanning movements and thus speed up the measurement.

A system based on focus variation microscopy was devised as it fulfilled all the constraints and was technically and cost-effectively realizable.

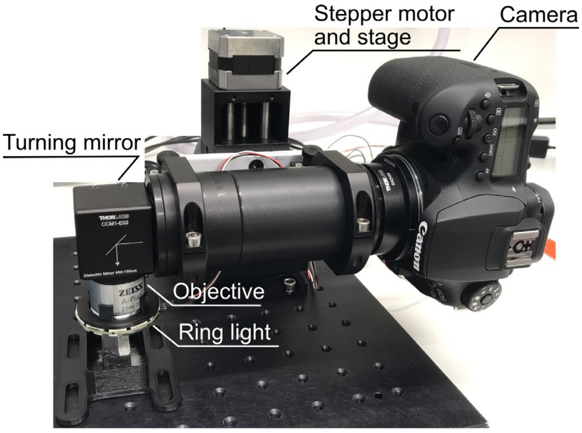

Figure 12: The microscope setup developed to measure the sample planarity as prepared by the SHS breadboard.

The principle of operation consists of taking a sequence of pictures with a shallow depth of field of the sample surface at different distances from the nominal sample surface. During data processing, regions of the images which are in focus at the respective distance are detected. This allows to construct a 3D profile of the imaged surface. The optical design is based on a Canon 90D DSLR camera featuring a large APS-C sensor (22.3 mm x 14.9 mm) compared to commercially available industrial vision cameras. This sensor size made it possible to comfortably design the microscope optics to accommodate for the large FOV with the required shallow depth of field. The imaging system of the microscope consists of 2.5x achromatic microscope objective (A-Plan 2.5x/NA 0.06, Carl Zeiss AG) and a corresponding 1x tube lens (164.50 mm FL, No. 425308-0000-000, Carl Zeiss AG). For illumination of the sample surface, a ring light consisting of 16 RGBW LEDs (NeoPixel Ring 2855, Adafruit Industries LLC) was attached through a 3D printed mounting assembly directly to the objective. The assembled microscope was mounted to a motorized vertical stage driven by a bipolar NEMA17 stepper motor with 200 steps per revolution, as shown in Figure 12. By driving the motor in full-step mode, a vertical resolution of minimally 2.5 µm between focus planes was realized. The stepper motor and the ring light were controlled using a microcontroller (Arduino UNO SMD, Arduino S.r.l.) combined with an H-bridge driver (Motor Shield 1438, Adafruit Industries LLC). The microcontroller receives commands from a controlling computer to initiate a certain vertical movement. Additionally, the DSLR camera was also connected to the computer and could be remote operated using the gPhoto2[1] software package. This allowed for fully automated recording of the image sequences.

Data analysis was performed using a custom MATLAB script. Using the externally developed *fstack* function[2], the respective in-focus pixels from each image in the focus stack could be extracted. A curvature correction using a 3rd degree polynomial function was performed on the height map to accommodate for the microscope not being perfectly perpendicular to the sample surface. The sample planarity can be extracted as the relative number of pixels within a predefined height range.

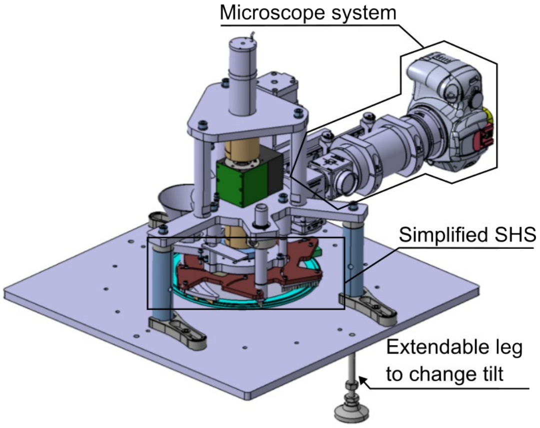

Figure 13: SHS BB setup with the integrated microscope for sample planarity measurements. The microscope can be positioned using a manual translation stage such that the objective is above the sample channel.

With the microscope system integrated into the SHS BB setup, the sample surface quality could be monitored over long periods of operation without user interaction. Analysis of the obtained image sequences resulted in distributions depicting the number of pixels in focus at a certain offset from the nominal surface height. Such a distribution for a reference sample can be seen in Figure 13. This sample was prepared manually in an equivalent fashion to samples which were measured by mass spectrometry and found to lead to acceptable results. Thus, a sample surface planarity of ±200 µm is deemed acceptable, as described in [17] as well. As comparison a sample with poor surface quality is shown in Figure 14. The large central hole is clearly visible in the 3D profile as well as in the broader depth distribution.

Surface planarity of the sample can mainly be influenced with the skimmer geometry. The two 45° chamfered skimmers (Figure 11) do not differ strongly and are expected to generate comparable planarity results, whereas the 15° chamfered skimmer is expected to behave differently regarding achievable planarity and roughness.

---

[1] http://www.gphoto.com

[2] https://github.com/joe-of-all-trades/fstack

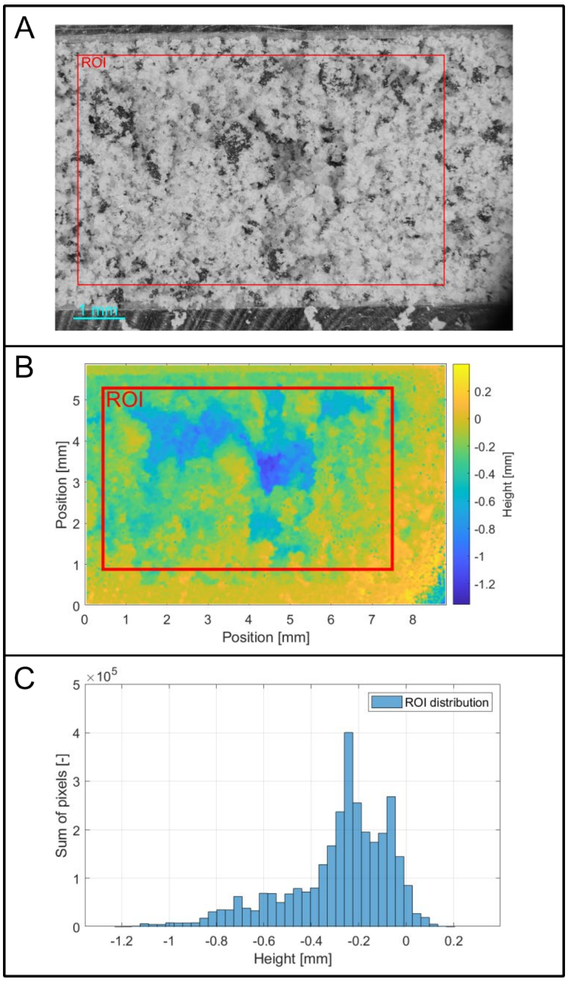

Figure 14: An example of a sample with poor sample surface quality as measured by the microscope setup. Panel A shows the focus-stacked composite image, for which the height profile is shown in panel B. The hole in the center of the region of interest (ROI) causes a wide sample height distribution (Panel C), and thus classified as poor sample surface quality.

Each skimmer was tested using an identical measurement procedure. The recorded image stacks consisted of 31 individual focus layers with step sizes of 75 µm, resulting in a total movement of 2.25 mm. During 1.5 carousel revolutions, a total of 160 height distributions were recorded. Brush heights and orientations are set to the previously optimized values. As sample material LHS-1 with a grain size distribution up to 1 mm was used.

The planarity measurement was started after a first initial rotation of 225° (~375 mm distance along the circumference), allowing for the channel to fill up with regolith simulant. After additional 25° (~40 mm distance) of rotation, the surface quality starts to rise, as can be seen in Figure 15. At this point, the filled part of the channel reaches the microscope. Rotating the carousel 25° further, the planarity is reaching a steady state. Clear differences between the 45° skimmers to the 15° skimmer are noticeable. The 15° skimmer prepared an average of 99% of the sample material with height variations less than the required ±200 µm. For the sample material prepared by the 45° skimmers only 95% of the analyzed area lies within the requirements.

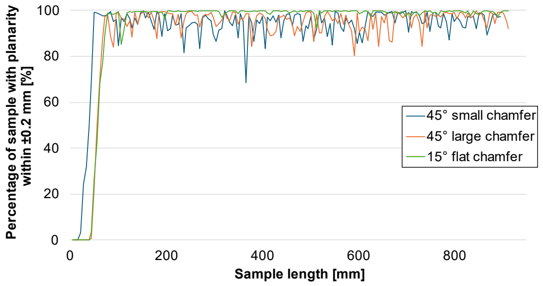

Figure 15: Measured percentage of the sample generated by different skimmer geometries that lie within the requirements.

Additionally, to the different skimmer geometries, the influence of potentially larger grain sizes on the sample height distribution was investigated. This is relevant since our tests revealed the possibility of elongated regolith particles with one dimension larger than the smallest sieve size (1 mm), to fall. For this purpose, the well-performing 15° skimmer was used to prepare a sample using LHS-2 regolith simulant, which was sieved with the funnel BB. A comparison of the results obtained with LHS-1 and sieved LHS-2 are shown in Figure 16. The average number of measured height profiles with a planarity within requirements decreased by 2% to 97% for the sieved LHS-2. In general, we observed that larger grains led to difficulties while preparing the sample. The larger grains preferentally get stuck in the carousel structures and cause grooves and holes within the sample surface, if they are pulled along as the carousel rotates.

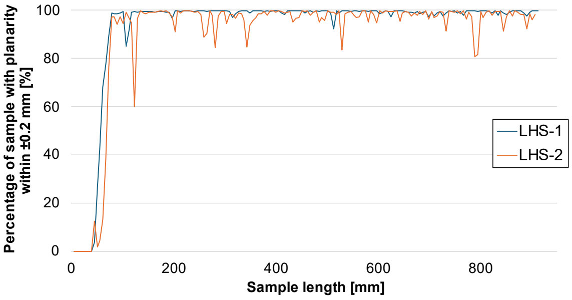

Figure 16: Planarity comparison between simulants of different maximum grain sizes.

As the sample preparation must work reliably even with lander tilts up 10°, planarity measurements were performed with the SHS BB being tilted 10° and 20°. At 10° tilt, the material flow on the carousel does not differ from the flat (0° tilt) tests. No material accumulation before brushes could be detected. At 20° inclination, a slight accumulation before the first shaping brush was observed. The material must be pushed upwards against gravity, which hinders the material outflow. It should be noted that this effect depends on the tilt direction. Performed planarity measurements, in both configurations using the 15° skimmer, showed no noticeable difference to the measurements performed with a flat SHS BB.

4. SUMMARY

In this contribution we present the challenges encountered while designing a Laser Ablation Ionization Mass Spectrometer (LIMS) to be launched on a CLPS mission to the lunar south pole for the *in-situ* chemical analysis of lunar regolith. Extensive design changes had to be carried out compared to our previous publications [16], [17], to ensure strict compliance with mechanical launch loads as described by NASA's GEVS. This required the introduction of a monolithic main support structure fabricated from AlBeMet AM162 to ensure high stiffness and thus low load amplifications at the subassemblies.

The instrument's sample handling system (SHS) has been extensively optimized, tested and validated using lunar regolith simulant. The tests performed with different funnel geometries led to optimized designs for all funnel elements such as funnel angle, funnel nozzle geometry and sieve vibrator mounting. The funnel geometry must be carefully chosen to avoid clogging effects, such as ratholing or bridging, and has to take into account the mechanical properties of the sample material, with the overall goal to increase the scientific return of the mission.

For the SHS carousel an efficient configuration of brushes and skimmers was found. This makes preparation of a planar sample surface possible, as it is required for stable laser ablation conditions using LIMS. The overall system has been tested and validated for lander tilts up to 10°.

ACKNOWLEDGEMENTS

The financial support by the Swiss Space Office through the ESA PRODEX program is gratefully acknowledged. The authors would like to thank the many people who made this instrument possible.

REFERENCES

[1] "Artemis III Science Definition Team Report," NASA, NASA/SP-20205009602, 2020. Accessed: Sep. 27, 2024. [Online]. Available: https://www.lpi.usra.edu/lunar/strategies/resources/Artemis-III-Science-Definition-Team-Report-2020.pdf

[2] J. Gross and K. H. Joy, "Evolution, Lunar: From Magma Ocean to Crust Formation," in *Encyclopedia of Lunar Science*, B. Cudnik, Ed., Cham: Springer International Publishing, 2016, pp. 1–20. doi: 10.1007/978-3-319-05546-6_39-1.

[3] G. Heiken, D. Vaniman, and B. M. French, Eds., *Lunar sourcebook: a user's guide to the moon*. Cambridge [England] ; New York: Cambridge University Press, 1991.

[4] K. H. Joy *et al.*, "Direct Detection of Projectile Relics from the End of the Lunar Basin–Forming Epoch," *Science*, vol. 336, no. 6087, pp. 1426–1429, Jun. 2012, doi: 10.1126/science.1219633.

[5] K. H. Joy, I. A. Crawford, N. M. Curran, M. Zolensky, A. F. Fagan, and D. A. Kring, "The Moon: An Archive of Small Body Migration in the Solar System," *Earth Moon Planets*, vol. 118, no. 2–3, pp. 133–158, Nov. 2016, doi: 10.1007/s11038-016-9495-0.

[6] K. H. Joy *et al.*, "The isotopic composition of volatiles in the unique Bench Crater carbonaceous chondrite impactor found in the Apollo 12 regolith," *Earth and Planetary Science Letters*, vol. 540, p. 116265, Jun. 2020, doi: 10.1016/j.epsl.2020.116265.

[7] A. A. Nemchin, R. T. Pidgeon, M. J. Whitehouse, J. P. Vaughan, and C. Meyer, "SIMS U–Pb study of zircon from Apollo 14 and 17 breccias: Implications for the evolution of lunar KREEP," *Geochimica et Cosmochimica Acta*, vol. 72, no. 2, pp. 668–689, Jan. 2008, doi: 10.1016/j.gca.2007.11.009.

[8] M. Anand *et al.*, "A brief review of chemical and mineralogical resources on the Moon and likely initial in situ resource utilization (ISRU) applications," *Planetary and Space Science*, vol. 74, no. 1, pp. 42–48, Dec. 2012, doi: 10.1016/j.pss.2012.08.012.

[9] G. Cesaretti, E. Dini, X. De Kestelier, V. Colla, and L. Pambaguian, "Building components for an outpost on the Lunar soil by means of a novel 3D printing technology," *Acta Astronautica*, vol. 93, pp. 430–450, Jan. 2014, doi: 10.1016/j.actaastro.2013.07.034.

[10] N. Leach, "3D Printing in Space," *Architectural Design*, vol. 84, no. 6, pp. 108–113, Nov. 2014, doi: 10.1002/ad.1840.

[11] A. Meurisse, A. Makaya, C. Willsch, and M. Sperl, "Solar 3D printing of lunar regolith," *Acta Astronautica*, vol. 152, pp. 800–810, Nov. 2018, doi: 10.1016/j.actaastro.2018.06.063.

[12] P. Wurz, M. Tulej, A. Riedo, V. Grimaudo, R. Lukmanov, and N. Thomas, "Investigation of the Surface Composition by Laser Ablation/Ionization Mass Spectrometry," in *2021 IEEE Aerospace Conference (50100)*, Big Sky, MT, USA: IEEE, Mar. 2021, pp. 1–15. doi: 10.1109/AERO50100.2021.9438486.

[13] U. Rohner, J. A. Whitby, and P. Wurz, "A miniature laser ablation time-of-flight mass spectrometer for *in situ* planetary exploration," *Meas. Sci. Technol.*, vol. 14, no. 12, pp. 2159–2164, Dec. 2003, doi: 10.1088/0957-0233/14/12/017.

[14] U. Rohner, J. A. Whitby, P. Wurz, and S. Barabash, "Highly miniaturized laser ablation time-of-flight mass spectrometer for a planetary rover," *Review of Scientific Instruments*, vol. 75, no. 5, pp. 1314–1322, May 2004, doi: 10.1063/1.1711152.

[15] A. Riedo, A. Bieler, M. Neuland, M. Tulej, and P. Wurz,

"Performance evaluation of a miniature laser ablation time-of-flight mass spectrometer designed for *in situ* investigations in planetary space research: Miniaturised laser ablation tof mass spectrometer," *J. Mass Spectrom.*, vol. 48, no. 1, pp. 1–15, Jan. 2013, doi: 10.1002/jms.3104.

[16] P. Wurz *et al.*, "In Situ Lunar Regolith Analysis by Laser-Based Mass Spectrometry," in *2023 IEEE Aerospace Conference*, Big Sky, MT, USA: IEEE, Mar. 2023, pp. 1–10. doi: 10.1109/AERO55745.2023.10115714.

[17] P. Keresztes Schmidt *et al.*, "Sample handling concept for in-situ lunar regolith analysis by laser-based mass spectrometry," in *2024 IEEE Aerospace Conference*, Big Sky, MT, USA: IEEE, Mar. 2024, pp. 1–10. doi: 10.1109/AERO58975.2024.10521190.

[18] *General Environmental Verification Standard (GEVS) for GSFC Flight Programs and Projects*, GSFC-STD-7000, Greenbelt, MD 20771., Apr. 28, 2021. [Online]. Available: https://standards.nasa.gov/sites/default/files/standards/GSFC/B/0/gsfc-std-7000b_signature_cycle_04_28_2021_fixed_links.pdf

[19] P. D. Spudis, B. Bussey, J. Plescia, J.-L. Josset, and S. Beauvivre, "Geology of Shackleton Crater and the south pole of the Moon," *Geophys. Res. Lett.*, vol. 35, no. 14, p. L14201, Jul. 2008, doi: 10.1029/2008GL034468.

[20] D. Schulze, *Powders and Bulk Solids: Behavior, Characterization, Storage and Flow*. Cham: Springer International Publishing, 2021. doi: 10.1007/978-3-030-76720-4.

BIOGRAPHY

Peter Keresztes Schmidt *received his B.Sc. and M.Sc. in Chemistry at the ETH Zürich, Switzerland. He is currently working as a PhD student in Bern, Switzerland, where he is developing a new LIMS instrument for in-situ studies on the lunar surface.*

Sébastien Hayoz *gained experience in different fields like electronics' development for Automotive, electronics' systems for Train Control Monitoring System (TCMS). Since February 2021, he is leading the electronics engineering team at the Space Research and Planetary Division and is involved for several instruments realized by the University of Bern.*

Daniele Piazza *has more than 20 years of experience in the design and development of space instruments. He has a Ph.D. in mechanical engineering from ETH Zurich and started his career in Formula 1. Since 2005 he leads the mechanical engineering group working on space instruments at the University of Bern.*

Timothy Bandy *has B.Sc. degree in mechanical engineering. He has mainly worked in the defense, pharmaceutical fields before joining UBE. Since then, he supported the development and AIV of BELA (BepiColombo), CHEOPS and Comet Interceptor. He is now Systems Engineer for CLPS-LIMS.*

Patrik Mändli *received a M.Sc. in electrical engineering and information technology, ETH Zurich, Switzerland. For 7 years he worked in control, network and communications technology for all types of rail vehicles. Since March 2022, he is system engineer electronics for CLPS-LIMS.*

Matthias Blaukovitsch *has a M.Sc. in Physics from the Technical University of Vienna, Austria (2016). He has been working on time-of-flight sensors specializing on diode lasers and is now appointed as an optical engineer at the University of Bern.*

Michael Althaus *received a HTL & B.Sc. in Electrical Engineering from Lucerne University of Applied Sciences and Arts with specialization in Information Technology in 1999. He worked as a research engineer at ESEC SA in Switzerland and at the Centre for Advanced Materials Joining, University of Waterloo, Canada. Before joining the University of Bern in 2018 for the NIM (JUICE), the NGMS (Luna 27) and – lately – the CLPS-LIMS instruments, he worked as an R&D Senior SW/HW engineer in the industry.*

Benoît Plet *received his Ph.D. in Physical Chemistry from the University of Bordeaux, France, in 2007. After 15 years developing scientific instrumentation in industry, he has joined University of Bern, Switzerland, as project manager.*

Sven Riedo received a B.Sc. in Electrical Engineering in 2022 from the University of Applied Sciences and Arts Western Switzerland. He is currently working as an electronic engineer at the University of Bern.

Simon Studer received his B.Sc. in Automotive Engineering in 2013 from the University of Applied Sciences Bern, Switzerland. He spent most of his time in Formula 1 before he joined as Mechanical Engineer to the Space Research and Planetary Sciences group of the University Bern.

Olivier Studer received his M.Sc. in Mechanical Engineering in 2023 from the University of Applied Sciences and Arts Northwestern Switzerland. Since September 2023 he is working as a mechanical design engineer on the sample handling system of CLPS-LIMS.

Scott Trimble received his M.Eng. in Electrical and Electronic Engineering from the University of Bristol, England. With 5 years of experience designing electronics for electrostatic applications, he joined the University of Bern in January 2023.

Marek Tulej received a Ph.D. in Physical Chemistry from the University of Basel, Switzerland in 1999. After his post-doctoral period at Paul Scherrer Institute (PSI), Switzerland, he joined in 2008 the University of Bern as an instrument scientist for space missions, including Phobos-Grunt, Marco Polo-R, Luna-Resurs, and JUICE.

Andreas Riedo received his Ph.D. in Physics in 2014 from the University of Bern, Switzerland. In 2016 he received a SNSF fellowship that allowed him to continue his research in Astrobiology at the Leiden University, The Netherlands. He extended his stay at the Leiden University with a MCSA fellowship for another two years before he moved in 2019 to the Free University Berlin after receiving the Einstein fellowship. In 2020 he moved to University of Bern and is currently appointed as researcher and project leader for CLPS-LIMS.

Peter Wurz has a degree in electronic engineering (1985), an M.Sc. and a Ph.D. in Physics from Technical University of Vienna, Austria (1990). He has been a post-doctoral researcher at Argonne National Laboratory, USA. Since 1992 at the University of Bern. He is Professor of physics, 2015–2022 head of the Space Science and Planetology division, and since 2022 director of the physics institute. He has been Co-I and PI for many science instruments for space missions of ESA, NASA, ISRO, CNSA, Roscosmos, and JAXA.

3.4 Electronics Unit (ELU)

In the following section, I provide a more detailed overview of the circuit boards within the Electronics Unit, of which the Elegant Breadboards (EBB) have been tested within the scope of this thesis.

3.4.1 Read-Out Electronics (ROE)

The acquisition system of the CLPS-LIMS instrument consists mainly of two parts: the detector with the mass analyser and the analogue to digital converter (ADC) responsible for digitising the acquired signal. These two systems are connected via $50\,\Omega$ impedance matched transmission lines to minimise signal distortions of the high bandwidth TOF signal.

The instrument's detector consists of two microchannel plates (MCP), which are mounted in a Chevron configuration. The detector design is based on a previous realisation for the laboratory LIMS instrument (Andreas Riedo, Tulej, et al. 2017). They register the impacting ions via secondary electron emission of the channel surfaces and this electron signal is amplified by further secondary electron emission, while a bias voltage of about $2\,\mathrm{kV}$ is applied across the MCP stack. The generated electrons are captured by an anode and conducted via a transmission line to the ADC, where a measurable voltage is generated over the $50\,\Omega$ termination resistor. Capturing the electrons from the MCP on the anode is aided by an additional bias voltage of $-300\,\mathrm{V}$ that is applied between the output side of the MCP stack and the anode, accelerating the generated electrons towards the anode. The MCP models manufactured by Photonis Scientific Inc., used for the laboratory and flight models of the CLPS-LIMS instrument, have already a long-standing heritage within the LIMS laboratory instrument on which the mass analyser is based on. The MCPs have an active area with a diameter larger than $40\,\mathrm{mm}$ (outer diameter of $50\,\mathrm{mm}$) and have a $7\,\mathrm{mm}$ diameter central whole, through which the ions from the entrance ion optics are guided. The plate's channels have a diameter of $8\,\mathrm{\mu m}$ with a bias angle of 8° and a L/D ratio of 60:1.

The detector anode consists of two electrically isolated, impedance matched concentric rings. This design is inherited from the LMS instrument (Andreas Riedo, Tulej, et al. 2017), allowing for an increased dynamic range, as the signal from one electrode can be subjected to high gain pre-amplification before digitisation. Thus, ion species with a low abundance can be detected with that channel. The signal from the second electrode is not amplified. Consequently, the signals with higher intensities can be simultaneously digitised without saturating the ADC. Detectors within ion-optical systems can be designed in two realisations: floating or non-floating. By having a floating detector, the whole detector assembly can be biased with respect to the other parts of the ion-optical system, allowing for more degrees of freedom in designing the ion-optical system. A disadvantage from this design is, that the signal lines must be AC coupled towards the data acquisition system to block the DC bias voltage. This necessitates HV decoupling capacitors on the detector itself, which typically have poor high-frequency characteristics and thus distort the ion signal. The ion-optical design of the laboratory LIMS system and thus also CLPS-LIMS mass analyser makes it possible to reference the detector to ground, meaning that the signal lines from the anodes can be DC connected to the acquisition electronics, as HV decoupling is not necessary. This design choice reduces the complexity of the detector significantly and ensures in the end a better signal quality than a HV AC coupled system could deliver. As the anode rings are impedance matched microstrip lines, the signal can be routed in a double-ended manner as a 100 Ω differential signal to the acquisition system, with the full current being measured. For simplicity and to rely on the heritage of the laboratory LIMS instruments, a 50 Ω single-ended architecture was implemented. For this one end of the anode is terminated with a 50 Ω resistor on the detector board. The other end connects to the transmission line towards the acquisition system. A SPICE[1] model of the signal path is shown in Figure 3.1. An anode ring is modelled as the transmission line T2 with a characteristic impedance $Z_0 = 42\,\Omega$, which is given by the specific geometry of the ring. The anode is terminated with a matched resistor R2 of the same value. The transmission line T1 with a characteristic impedance $Z_0 = 50\,\Omega$ is the coaxial signal cable to the ROE, where the transmission line is terminated by another matching resistor. The transient simulations showed no ringing with this design.

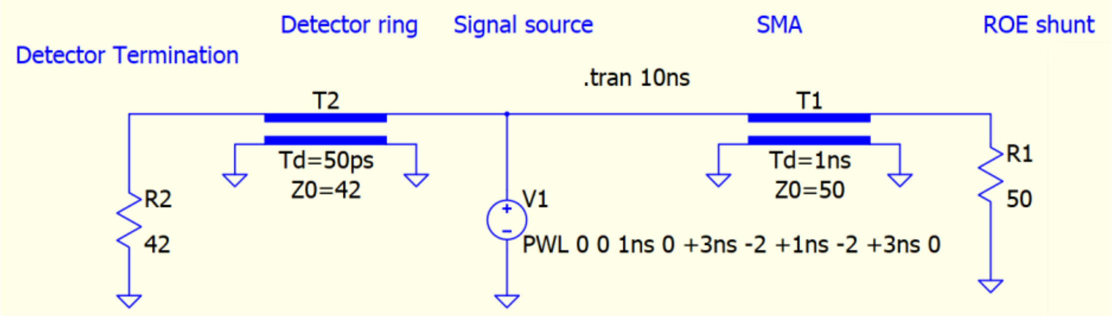

Figure 3.1: Simplified signal path of the detector system from the detector anode to the termination resistor of the acquisition system.

---

[1] Simulation Program with Integrated Circuit Emphasis. A programme with which the static and transient behaviour of electrical circuits can be simulated.

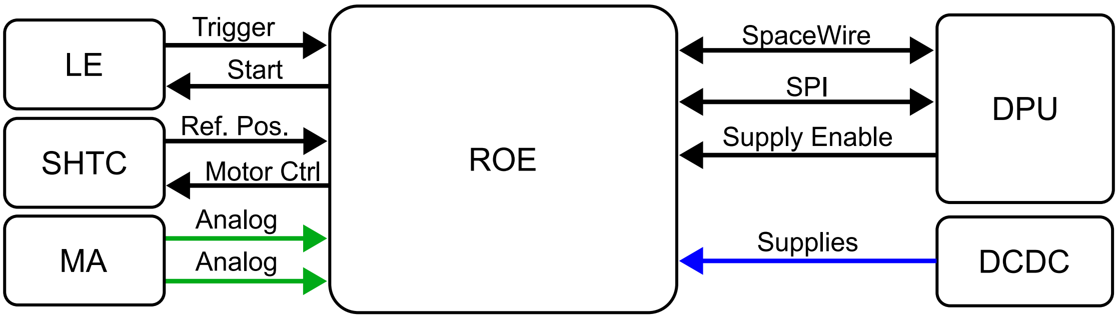

Figure 3.2: Block diagram of the Read-Out Electronics (ROE) showing the interfaces to the other sub-systems of the CLPS-LIMS instrument.

On one hand, the single-ended termination reduces the design and implementation complexity on the acquisition system side, as readily available designs for 50 Ω systems can be used. Additionally, only one coax cable per anode ring must be routed from the detector to the acquisition system. The downside of this design is the loss of half the signal within the termination resistor of the anode. This compromise was deemed acceptable, as the lost signal can be compensated by increasing the gain of the MCPs by increasing their bias voltage during operations.

As this overall design has been extensively tested within laboratory studies over more than a decade (A. Riedo, Bieler, et al. 2013), adoption of it for the CLPS-LIMS instrument meant a significant reduction in development time and risks.

The acquisition system consisting of ADC and associated frontend electronics, meaning signal transmission line termination, preamplifiers and filters, control electronics, such as an FPGA and memory for the digitised spectra, are located on the Read-Out Electronics (ROE) board. A block diagram how the electronic components integrate into the CLPS-LIMS instrument is shown in Figure 3.2.

In TOF Mass Spectrometry the beginning of a mass spectrum must be synchronised to a specific instance in time at which the generated ions are launched into the mass spectrometer for separation. In case of LIMS, this is the firing of the laser pulse. The laser used in the CLPS-LIMS instrument is a passively Q-switched laser, which can provide laser pulses on demand, but with 100s of µs variance in firing time. To obtain a reliable start pulse, a trigger signal generated by a photodiode within the laser head box is fed back to the ROE, allowing for precise synchronisation of the start of an acquisition.

Besides simple digitisation of single mass spectra, to reduce the downlink data rate of the instrument, it is important to have the possibility to co-add spectra from multiple laser shots into one spectrum. This resulting spectrum will have a better SNR and can then be downlinked to Earth, reducing the data rate requirements by a factor of $1/N$ where N is the number of co-added spectra.

After digitisation, the spectra are stored in memory located on the ROE and can be downloaded to Earth via the Data Processing Unit (DPU).

In addition to these classical functions of a high-speed digitiser, the ROE is responsible for controlling the rotation of the sample handling system carousel and is thus directly connected to the SHTC. This design choice was driven by the fact, that the ROE contains the only FPGA within the instrument. For the control of the carousel stepper motor drivers, pulse sequences with precise timings are necessary, which can be generated by said FPGA.

Based on the required described functionality, the following requirements have been derived for the ROE's design:

1. The sampling rate of the ADC must be sufficiently high to have enough samples per peak within the spectrum to allow for good quantification. The ion-optical design can produce peaks with FWHM down to about 2 ns. For integration of such a peak, with low errors, it is necessary to have at least 3 sample points. This leads to a minimal sampling rate of $1.6\,\mathrm{GS\,s^{-1}}$ per channel.

2. The bandwidth of the channels shall be $\geq 0.7\,\mathrm{GHz}$, so that signal degradation such as slower rise and fall times and thus peak broadening can be avoided. The bandwidth must be low-pass filtered depending on the chosen ADC sampling rate to $f_s/2$ to avoid aliasing effects according to the Nyquist-Shannon theorem.

3. For increased instantaneous dynamic range, the acquisition system must have to separate channels with differing gains to which each one of the anode rings is connected. The high gain (HG) channel shall have a full-scale range (FSR) of $-100\,\mathrm{mV}$ to $0\,\mathrm{mV}$ for the detection of trace elements. The low gain (LG) channel shall have an FSR of $-2\,\mathrm{V}$ to $0\,\mathrm{V}$ for the simultaneous detection of major species. As both channels will be subject to roughly the same input signal, depending on the ion-optical voltage set, the HG channel must be able to withstand $-2\,\mathrm{V}$ signal without damage or loss in performance.

4. Ion flight times within the MA up to m/z 250 with commonly used voltage sets are about 10 µs. With margin, this leads to a minimum spectrum length of 12 µs.

5. For the co-adding procedure to not reduce spectral quality it is important to minimise the timing jitter between spectra to be co-added. Added jitter will increase the FWHM of the peaks in the histograms, which directly translates into

a reduction of mass resolution, and hence the detection sensitivity of the system. The mass analyser is expected to produce peaks with FWHM of down to about 2 ns, as the width of a detected ion packet is limited by the laser system's pulse width of about 1.5 ns. This leads to the requirement for the peak-to-peak timing jitter from trigger input signal to the start of the acquisition, to be roughly an order of magnitude smaller, so that it can be neglected. Thus, the peak-to-peak jitter shall be $\leq$300 ps.

3.4.2 DCDC Board

The instrument is supplied by the spacecraft (S/C) with unregulated $(+28 \pm 4)$ V DC power. For the operation of the instrument electronics, multiple regulated DC voltages are necessary. It is the DCDC board's purpose to generate a general set of regulated voltages, which can be used by the other electronic modules of the LIMS ELU to generate point of load voltages as required (e.g. special voltages required by the ROE FPGA and ADC). Additionally, the DCDC board provides galvanic isolation from the S/C, and filters conducted electromagnetic emissions (EMI), both originating from the S/C and the downstream DCDC converters.

The DCDC board shall fulfil the following simplified list of requirements:

1. Provide inrush current control on the S/C input. This is required to limit the initial current draw of the instrument at power up in accordance with the limits imposed by the S/C manufacturer.
2. Provide a commonly used set of voltages, namely +12 V, +5 V, −5 V and +3.3 V.
3. Provide a galvanically isolated +12 V voltage with additional EMI filters on the output. This separate voltage line is used by the laser electronics, as its operation is expected to generate a substantial amount of noise on the power line. To not couple this noise into other subsystems, a separate isolated voltage line is required.
4. The DPU shall be able to switch the voltages on and off on command. A separate 3.3 V unswitched output shall be provided to power the DPU. This allows to power only the DPU in certain operation modes to reduce the overall power consumption of the CLPS-LIMS instrument.
5. The DCDC board shall provide HK data (output voltages, output currents, component temperatures) to the DPU.

3.4.3 HV/LV Power Supply

For the ion-optical system of the mass analyser to work, 12 independently regulatable DC low- and high voltages are necessary, which are supplied by the High Voltage Power Supply (HVPS). These are feeding the electrostatic lenses, as well as supply the bias voltage for the MCPs within the detector. In this context, voltages up to ±500 V are named low voltage, and voltages up to −2500 V are denoted as high voltage. The expected output currents of the channels are in the range of 10 µA, as the only expected current draw happens when the ion-optical elements, respectively their parasitic capacitance, is subjected to a change of potential. The MCPs do have a resistive load component of about 30 MΩ and thus a current draw of about 100 µA during operation. The respective voltage regulators must be sized accordingly.

The HVPS interfaces with the DPU using a Serial Peripheral Interface (SPI) bus. Using that bus, the DPU can set the requested output voltages and read back the measured output voltage, as well as housekeeping data.

The requirements for the HVPS channels are summarised in Table 3.1. They are based on values from voltage sets that are used on the laboratory LIMS instruments. As the ion-optical designs of the laboratory and flight instruments are nearly identical, this serves as a good base for the requirement specification.

Table 3.1: Summary of the required specifications for each HVPS channel with regard to voltage range and current consumption.

Channel Name	Operating range	Typical Current Consumption
Backplane (BP)	0 V to 500 V	10 µA
Reflectron 5 (R5)	−100 V to 100 V	10 µA
Reflectron 4 (R4)	−100 V to 100 V	10 µA
Reflectron 3 (R3)	−100 V to 100 V	10 µA
Reflectron 2 (R2)	−200 V to 0 V	10 µA
Reflectron 1 (R1)	−200 V to 0 V	10 µA
Drift Tube (DT)	−1500 V to 0 V	10 µA
Ion Snorkel (IS)	−500 V to 0 V	10 µA
Ion Lens (IL)	−2500 V to 0 V	10 µA
Ion Acceleration (IA)	−2500 V to 0 V	10 µA
MCP Front (DF)	−2500 V to 0 V	100 µA
MCP Back (DB)	−500 V to 0 V	100 µA

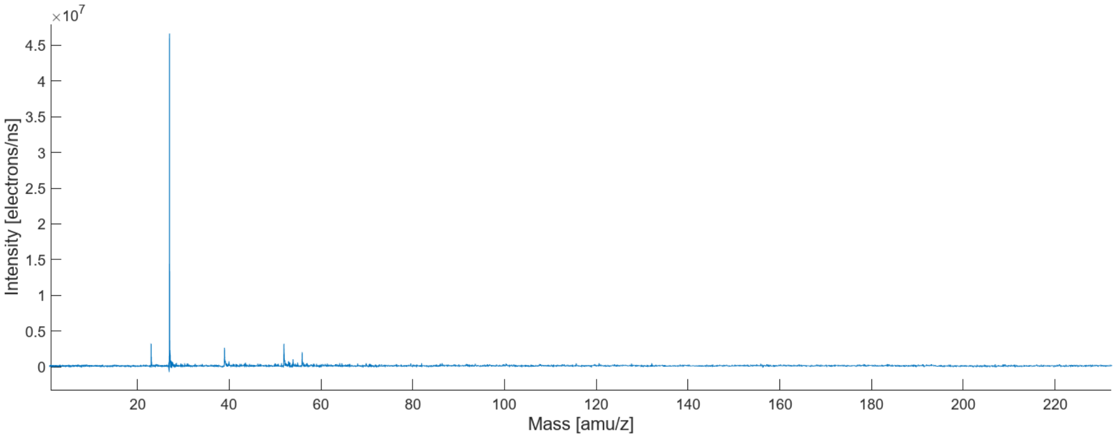

Recorded mass spectrum of the first laser shot fired with the fully assembled CLPS-LIMS EFM test setup in December 2024. The sample is 1.4435 stainless steel. The visible major peaks are $^{23}Na^+$, $^{27}Al^+$, $^{39}K^+$, $^{52}Cr^+$ and $^{56}Fe^+$, with the first three species being surface contamination.

4 Commissioning and Testing of the CLPS-LIMS Engineering Model

This chapter describes the commissioning and tests performed with various engineering models of different CLPS-LIMS subsystems. Additionally, a description of the used test setups and tools is given.

At the current stage of the project, enough subsystems were already procured in engineering quality to assemble a representative instrument to characterise the expected performance of the flight version. In addition, these tests serve to find design and manufacturing mistakes within the subsystem, so that they can be corrected for the future models. A third important goal is to gain hands-on measurement experience with the instrument, which shapes and refines the Concept of Operations design.

4.1 The EFM Test Setup

For the CLPS-LIMS project, a separate thermal vacuum chamber (TVC) has been designed and commissioned, which has the necessary volumetric capacity to house the assembled flight-like SMU and additional supporting components. The test setup is meant to evolve as the project progresses and more and more mature subsystems become

Table 4.1: Overview of the tested subsystems and their maturity levels.

Subsystem	Abbreviation	Maturity
Mass Analyser	MA	EFM
Optical Sub-System	OSS	EBB+
Read-Out Electronics	ROE	EBB
DC/DC Converter	DCDC	EBB
HV Power Supply	HVPS	EBB

available for testing. The current iteration of this setup is named the “EFM Test Setup”, due to the mass analyser engineering functional model (MA EFM) being one of the central devices under test (DUT).

In Table 4.1, an overview of the subsystems tested, and their maturity level is given. Subsystems that were not part of the testing procedure are the sample handling system (SHS) and the associated Sample Handling and Thermal Control board (SHTC), the flight-like Laser Electronics (LE), and the Data Processing Unit (DPU). The required functionality of these systems was replaced by appropriate laboratory equipment.

A block diagram of the DUTs and the necessary support equipment is shown in Figure 4.1. Housed within the TVC are the MA EFM and the OSS EBB+ including the Laser Head Box (LHB). The flight-design SHS with the sample carousel is replaced by a piezoelectrically actuated XYZ linear translation stage. This allows to mount different sample holders with various samples, which are used for performance characterisation and calibration measurements. The MA itself is not mounted to a monolithic support structure as during flight, but instead a simplified mounting jig has been designed and implemented.

As the EBB versions of the instrument’s electronic subsystems are not built for operation in vacuum, they are placed outside the TVC. Electrical connections between MA, OSS, and the electronic subsystems are realised through various vacuum feedthroughs.

The DCDC, HVPS and ROE are the main electronic subsystems, that are evaluated using this test setup. The DCDC is used to supply electric power to the HVPS and ROE. Since the DPU, LE, and SHTC are not powered by it the DCDC is not tested for the full power level. Tests of the HVPS are fully representative, as the ion-optical design of the MA is flight-like. This holds also true for the ROE. The LE is based on the commercial electronics of the laser manufacturer and thus is not fully representative of the flight design. It does have the necessary and compatible interfaces to be connected to the ROE, thus the interoperability between the two subsystems can be verified.

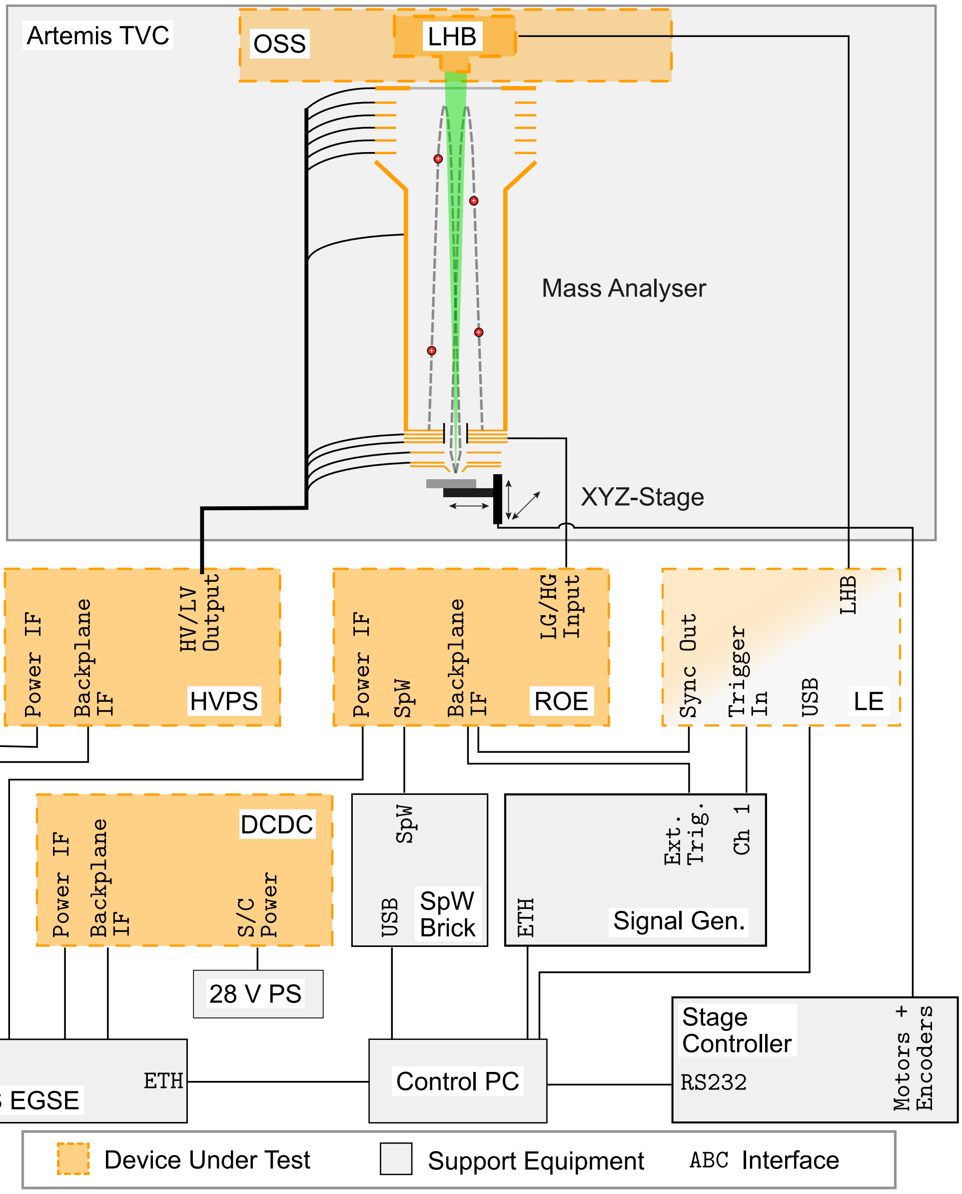

Figure 4.1: Overview of the EFM test setup with the sub-units under test marked in orange and additional support equipment marked in grey.

As no DPU is part of the setup, a control PC communicates with all the subsystems using the appropriate interfaces. For communication with the DCDC and HVPS, an EGSE box supplied by the subsystem manufacturer is utilised.

In the following subsections, the implementation of the sub-units and their tests are discussed in more detail.

4.1.1 Mass Analyser EFM

The used MA EFM, as shown in Figure 4.2 is, with regard to performance critical components, fully representative of the flight version. The optical entrance window was manufactured within the same batch as the window that will be used during flight. Thus, it is expected that the windows have the same optical transmission and same ion-optical performance. The ion-optical system design has been frozen before the EFM was manufactured. Electrode distances and shapes are therefore representative of the flight model. This includes the ceramic insulators between the electrodes. Changes are only expected, if issues arise during testing, that cannot be solved without changing the ion-optical design. The electrical design of the detector anode and MCP bias circuit are also not expected to change in the future.

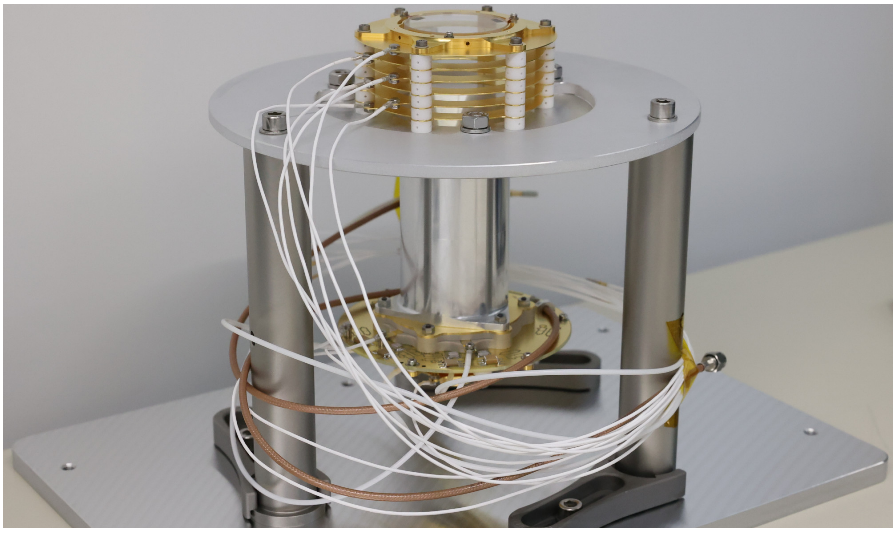

Figure 4.2: The CLPS-LIMS MA EFM, integrated and ready to be installed within the Artemis TVC setup for testing. The outer structure is the storage jig, which allows for safe handling and storage within a desiccator.

The MA EFM only differs in the outer, ion-optically non-active, shape of the drift tube, as the mechanical mounting between MA EFM and future models is different. Note, that in contrast to the other electrodes, the MA EFM drift tube is not gold coated. This was deemed an acceptable trade-off between production costs and representativeness. The coating improves the electrical conductivity of the ion-optical surfaces in order to dissipate local charges due to impinging ions quickly. As the ion flight paths are well confined within the drift tube, negligible collisions with the drift tube surface are expected to occur, thus no significant performance impact is expected from this difference. The MA EFM mounting system has been designed to allow for integration in the ORIGIN setup as well as into the Artemis TVC. This allowed for earlier testing and validation of the ion-optical design with the ORIGIN setup, before the TVC was fully commissioned. In contrast, the flight MA mounting design is optimised for integration into the AlBeMet Main Support Structure (MSS) and for conformance to NASA's General Environmental Verification Standard (GEVS) mechanical vibration levels and shock loads (*General Environmental Verification Standard (GEVS) for GSFC Flight Programs and Projects* 2021).

4.1.2 Optical Sub System EBB+

The OSS EBB+ as shown in Figure 4.3, consists of a flight-like and environmentally qualified Laser Head Box (LHB), and a beam guiding system, whose output, i.e. the characteristics of the beam in the focal spot, matches the requirements for sample ablation and ionisation. The output energy of the LHB can be modified in a range of 10 % to 100 % by adjusting the temperature of the SHG crystal. For the dynamic attenuation range to lie within the range needed for ablation and ionisation, static ND filters are placed after the output of the LHB. The OSS EBB+ is equipped with an absorptive neutral density (ND) filter with a transmission of 31.6 % (ND0.5), limiting the laser energy measured after the last optical element to 7.9 µJ.

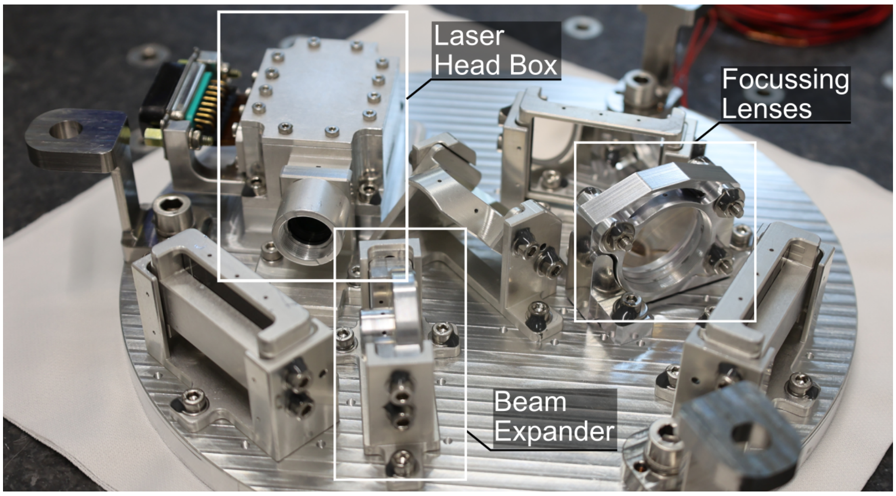

Figure 4.3: Image of the OSS EBB+ taken during its incoming inspection from the manufacturer. The tube mounted on the laser output contains ND filters, which are used to statically attenuate the laser beam, so the dynamic attenuation range can be optimised, so that the pulse energy range covers the required values for laser ablation and ionisation.

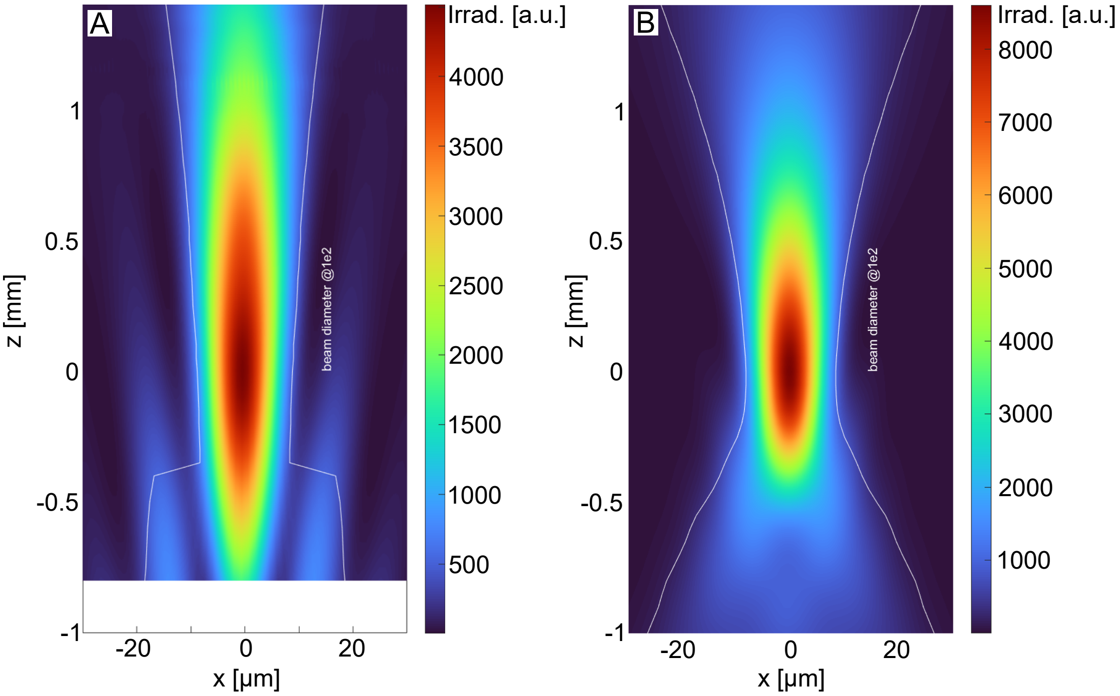

Figure 4.4: Beam profiles around the focal spot of the OSS EBB+ **(A)** and the OSS EQM **(B)**. The $1/e^2$ beam diameter is marked by the white lines.

No significant changes are expected to the LHB, and thus it can be seen as fully representative with regard to its optical parameters, such as pulse energy and stability, dynamic attenuation performance, and beam shape. In contrast, the beam guiding and shaping system is expected to be different in future models. This is mainly driven by difficulties of achieving compliance with GEVS loads with the current EBB+ design. Positioning of the optical elements is optimised, which allows for smaller optical elements overall. This reduces the size and mass of the optical holders, minimising the risk of slippage when subjected to high vibrational loads, thus achieving GEVS compatibility for the OSS. In addition, this design change will improve the optical performance of the OSS. Spherical aberrations present in the OSS EBB+ are minimised, leading to a more symmetrical beam profile around the focal spot as demonstrated through simulations. The beam profile of the improved EQM design has a significant reduction of side lobes, as shown in Figure 4.4, thus making the ablation and ionisation conditions above and below the focal spot symmetrical. The minimal beam waist remains unchanged at about 17 µm.

4.1.3 Read Out Electronics EBB

Based on the required functionality and the technical requirements described in Chapter 3, the manufacturer has designed and built three identical ROEs in EBB quality for testing and verification of the design. The ROE EBB with serial number 3 is shown in Figure 4.5.

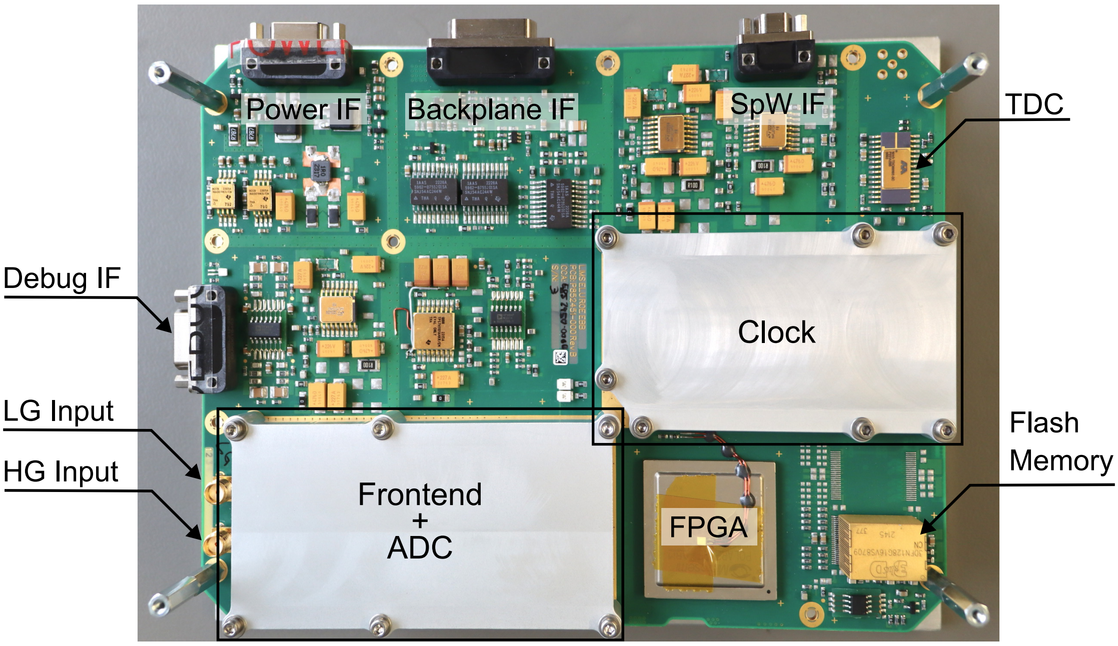

Figure 4.5: Top view of the ROE EBB S/N 3 with the most important sections and components marked. Under the EMC cover labelled "Frontend+ADC", the input LNAs, filters, and the high-speed ADC is located. The "Clock" EMC cover houses the main crystal oscillator and the clock generation IC.

The signal digitisation is performed by a Texas Instruments ADC12D1620QML high-speed ADC, which offers 12-bit resolution and $1.6\,\mathrm{GS\,s^{-1}}$ on two independent channels, allowing for the implementation of the LG and HG channel concept with a sufficiently high sampling rate for the expected signals. The ADCs inputs are fully differential with full-scale input ranges (FSR) of $\pm 400\,\mathrm{mV}$.

The implemented signal frontend as shown in Figure 4.6 serves mainly two purposes. It provides amplification in case of the HG channel or attenuation in case of the LG channel to match the expected input signal amplitudes to the FSR of the ADC. Additionally, it converts the single-ended signal from the anode into a differential signal that can be processed by the ADC. Signal level adjustments and differential conversion are provided by two Texas Instruments LMH5401-SP low-noise amplifiers (LNA), one per input channel. The amplifier on the LG path is configured with a gain of $-8\,\mathrm{dB}$, providing

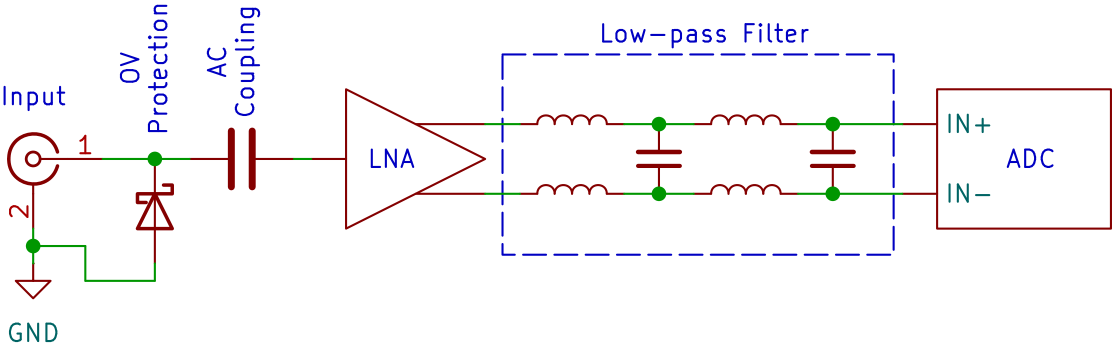

Figure 4.6: Simplified schematics of one channel of the ROE EBB frontend. The over-voltage (OV) protection diode is only placed on the HG channel.

sufficient attenuation by a factor of about 0.4 to match the −2 V to 0 V input signal to the FSR of the ADC. The HG amplifier is configured to provide 18 dB (factor about 8) of amplification, which matches the expected input signal of −100 mV to 0 mV to the FSR of the ADC. To avoid overdriving the HG LNA with signals greater than −100 mV, a fast, low-capacitance protection diode is placed in that signal path, which clamps the input signal before reaching the LNA. The amplifier gain-bandwidth product is specified with 6.5 GHz. Under optimal conditions, even with a gain of 18 dB of the HG channel, a bandwidth of 0.8 GHz should be achievable with this amplifier. It shall be highlighted that the ADC expects bi-polar signals centred around 0 V. This contrasts with the actual input signals provided by the detector. They are predominantly unipolar extending into the negative voltage range, as the detector only provides electrons. To be able to utilise the ADC's full range, including the positive range, the frontend electronics must apply a DC bias, shifting the amplified or attenuated signals, such that their expected midpoints are at 0 V. To keep the DC biased frontend design simple, the input signals are AC coupled into the frontend with a high-pass cutoff frequency of 10 kHz. After this signal conditioning, both signal paths are routed through 4^{th} order low-pass Butterworth filters in Cauer topology with a cutoff frequency of 700 MHz to suppress aliasing effects during digitisation.

The control logic of the ROE is implemented on a Microchip RTPolarFire RTPF500T FPGA. It interfaces with the ADC over a parallel LVDS bus. Towards the DPU a *SpaceWire* interface is provided. Additionally, it controls all the peripherals found on the ROE as well as the SHS carousel drivers, which are located on the SHTC board. As the FPGA is reprogrammable, a JTAG interface is provided for that purpose. Attached to the FPGA, are 16 Gbit flash memory provides storage for the recorded spectra before downloading.

The requirements of the ROE specify a peak-to-peak jitter between the laser synchronisation signal and the beginning of a spectrum to be $<$ 300 ps. The ADC has the possibility to process an external trigger signal and mark the sample at which it was registered. This mark could be evaluated by the FPGA and use the corresponding sample point as the first in the spectrum. Since with this solution the obtainable trigger jitter is directly derived from the ADCs sampling rate of $1.6\,\mathrm{GS\,s^{-1}}$, the jitter cannot be lower than $\pm 312.5\,\mathrm{ps}$, which corresponds to $f_s/2$. Thus, an alternative solution utilising a Time-to-Digital converter (TDC) was implemented. A TDC can measure the time difference between two signal edges to a very high resolution. In case of the chosen Magics TDC00002, a resolution of $<8\,\mathrm{ps}$ can be obtained. Using this architecture, the continuously read out samples from the ADC are stored within a ring buffer on the FPGA. The TDC is configured to measure the delay between the laser synchronisation signal and the next ADC sampling clock edge. Using this delay, the FPGA can align the spectra in time domain to each other in such a way that their respective zero-th sample point matches the time the laser was fired, as this marks the beginning of the spectrum. The alignment itself is done in two separate steps. To achieve a jitter better than $f_s/2$, a sub-sample alignment must be performed. For this, four digital fractional delay (FD) filter stages based on all-pass finite-impulse response (FIR) filters with phase delays of 312.5 ps, 156.25 ps, 78.125 ps, and 39.0625 ps are implemented in the FPGA. Using a lookup table, depending on the measured subsample delay by the TDC, the appropriate FD filters are activated. During coarse alignment, the FPGA shifts the fractionally delayed spectrum by full samples to remove the non-fractional delay introduced by the FIR filter architecture.

4.1.4 HV Power Supply EBB

The implemented design for the HVPS EBB is based on the generation of internal fixed low- and high-voltages which are connected via linear regulators to the output channels. All channels can source and sink current; thus, they are able to compensate for unwanted shifts in the ion-optical electrode voltages due to potentially impacting ions.

Internally, three low voltages ($-250\,\mathrm{V}$, $-125\,\mathrm{V}$, and $+125\,\mathrm{V}$) are generated by a switched DC/DC converter and a transformer with 3 secondary coils ("LV transformer" in Figure 4.7). Depending on the required output voltage range of the LV channels, the appropriate LV power supplies are connected to the high and low side of the regulators, thus achieving full four-quadrant regulation for the bi-polar channels and two-quadrant regulation for the unipolar channels.

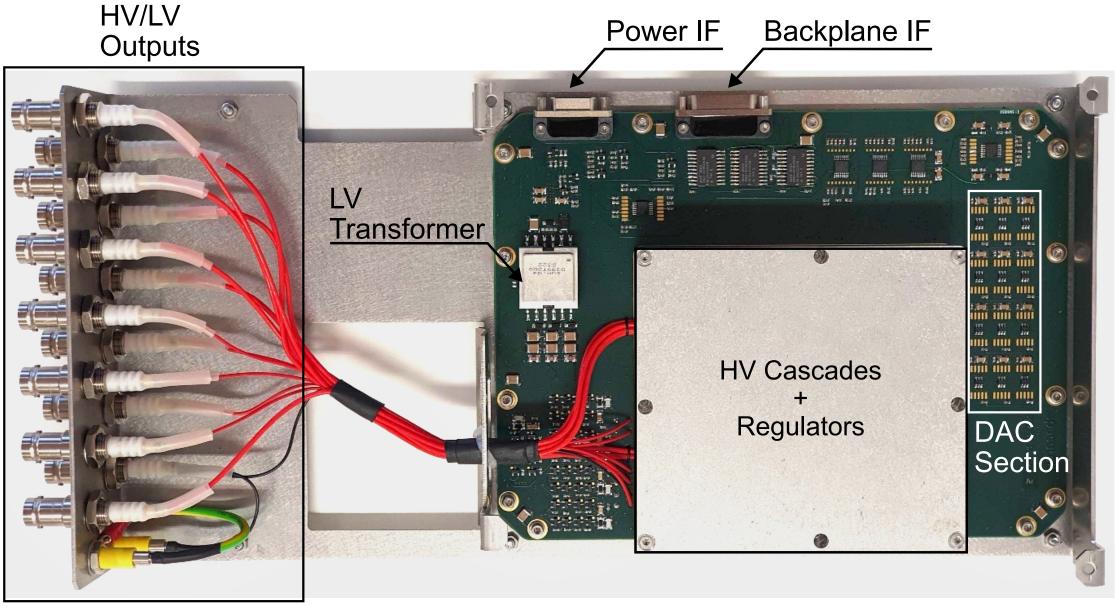

Figure 4.7: Top view of the EBB HV Power Supply board with the most important components and interfaces annotated.

The internal high voltages of −3600 V and +600 V are generated by a transformer-based DC/DC converter followed by two separate voltage multiplier cascades. Regulation is achieved by controlling two high-voltage optocouplers serving as linear regulators.

The MCP Front (DF) and Back (DB) channels are implemented in a way that controlling the DB voltage does not affect the voltage difference over the MCP stack, since $U_{DF} = U_{DF,set} + U_{DB,set}$. This allows to set the bias voltage between MCP stack and detector anode (DB) without changing the MCP gain, which is dependent on the voltage across the stack $\Delta U_{MCP} = U_{DF} - U_{DB}$.

4.1.5 DCDC Converter EBB

The DCDC EBB has been implemented based on the stated requirements in the previous chapter. A simplified block diagram is shown in Figure 4.8 and the actual board can be seen in Figure 4.9. The basic architecture is based on multiple DC/DC switching converters to provide the necessary output voltages of +12 V, +5 V, −5 V, and +3.3 V. Additional monitoring and switching circuits allows for measuring the output voltages and currents, as well as selectively disabling some voltages for low-power standby operations of the CLPS-LIMS instrument.

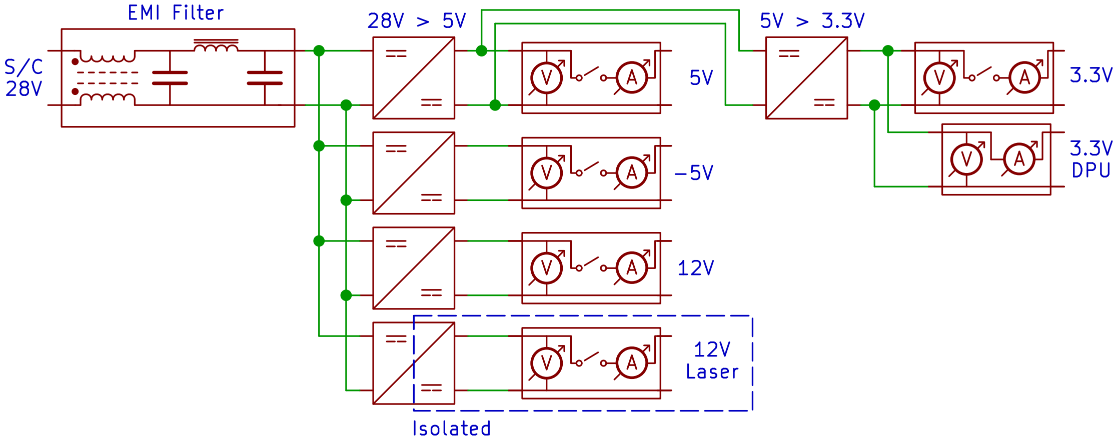

Figure 4.8: Simplified block diagram of the DCDC EBB showing the general architecture of the voltage supplies.

The (+28 ± 4) V DC input voltage supplied by the spacecraft is routed through an in-rush current limiting and overvoltage protection circuit. The former is to avoid any current spikes while powering on the instrument, which could trip overcurrent limits on the spacecraft and thus cut the instrument's power off. Overvoltage protection is implemented to protect the instrument from any potential voltage spikes originating from the spacecraft. Since the used DC/DC converters can back-feed noise into the S/C, an DVMC28 EMI filter from VPT, Inc. is placed between the protection circuity and the converters.

The utilised DC/DC converters are also commercial off-the-shelf (COTS) parts from VPT, Inc. (USA), allowing for a reduction in the development risk and cost of the DCDC EBB. In total, 5 such converters are needed to generate the output voltages. The +5 V, −5 V, and +12 V voltages are generated directly from the unregulated, filtered +28 V input voltage. An additional DC/DC converter is generating the isolated +12 V supply for the laser electronics, in order to avoid coupling of noise from the laser electronics into the other power lines. All these converters which are fed by +28 V are galvanically isolating, thus separating the S/C primary side from the instrument secondary side.

The +3.3 V supply is generated by a non-isolated buck converter from the +5 V supply. The +3.3 V supply is split into two outputs: one is in an always-on configuration, supplying the DPU. This allows the DPU to boot once the instrument is powered by the S/C. The other +3.3 V output, as well as all other outputs are switched and are only active if commanded by the DPU.

All output voltages and currents, as well as a temperature sensor placed on the board, are monitored and provided in the housekeeping data.

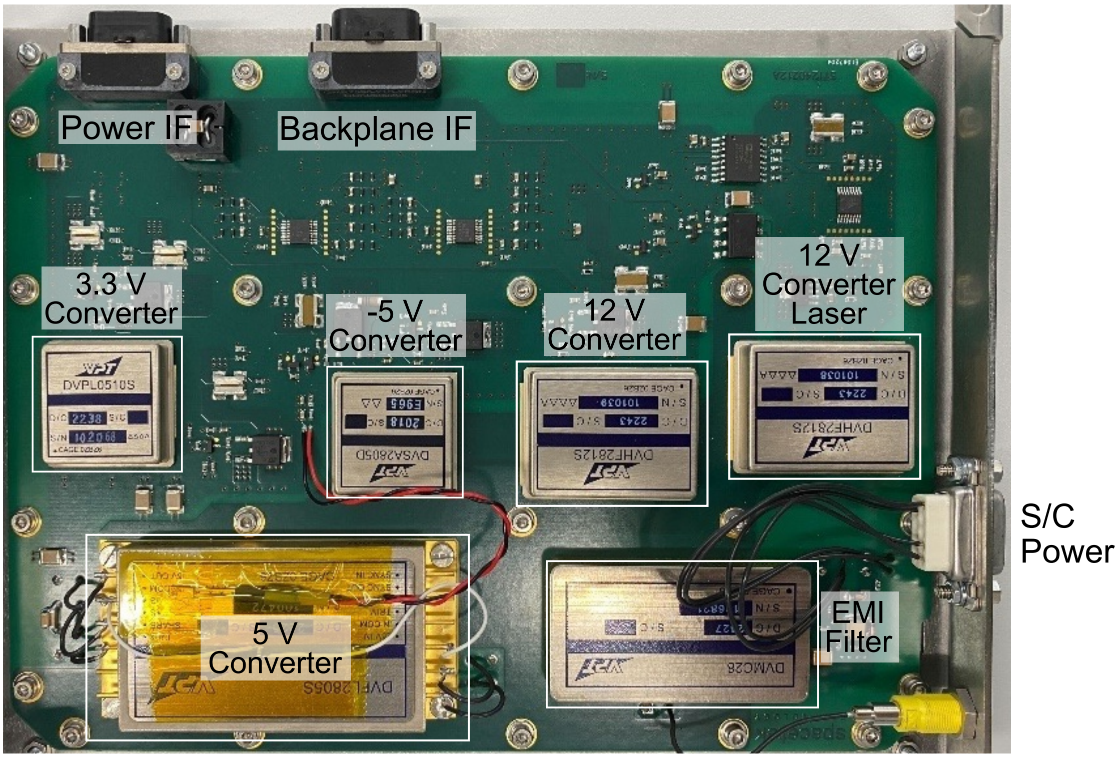

Figure 4.9: Top view of the DCDC converter board. The spacecraft will supply +28 V via the "S/C Power" connector. DC/DC converters provide the necessary regulated voltages to operate the instrument. Via the "Power I/F" connector the output voltages are distributed to the other CLPS-LIMS ELU boards. HK busses and digital signalling are routed via the "Backplane IF" connector.

4.1.6 The Artemis TVC

For CLPS-LIMS testing activities, a new thermal-vacuum chamber (TVC) was designed, built, and commissioned, called the Artemis TVC, which is shown in Figure 4.10. In its current iteration, it is suited for housing the MA EFM and OSS EBB+ with a laboratory sample stage instead of the flight SHS design, as well as a radiative heat exchanger to remove any excess heat from the OSS. In the future, the Artemis TVC will be adapted to house the full flight-like Spectrometer Unit (SMU), including reservoirs for lunar regolith simulant that can be dispensed into the SHS's funnel and LN2 shrouds for simulating lunar temperature conditions.

The TVC has internal dimensions of 0.66 m × 0.62 m × 0.72 m, and thus a total volume of $0.31\,\mathrm{m}^3$. It is mounted to a frame assembled from aluminium extrusion profiles, which provides additional mounting areas for the accessories needed to operate the setup. To create the vacuum levels of $<5\times10^{-7}\,\mathrm{hPa}$, necessary to operate the MA, a HiPace 300 M (Pfeiffer Vacuum AG, Switzerland) turbomolecular pump, backed by a HiScroll 12 scroll pump (Pfeiffer Vacuum AG, Switzerland) is attached to the chamber. The pressure in the vacuum chamber is monitored by a PKR 360 (Pfeiffer Vacuum AG, Switzerland) Pirani and cold cathode pressure gauge. It is connected to the interlock system of the HVPS, ensuring that high voltages can only be applied at low enough pressures, preventing damages to the system due to operator error or sudden vacuum loss.

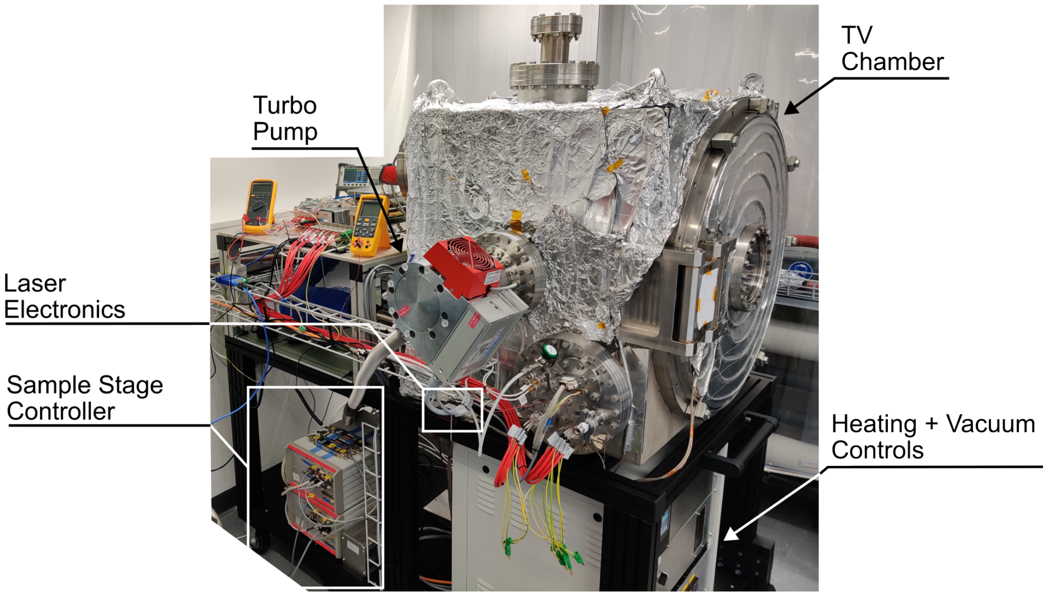

Figure 4.10: The CLPS thermal vacuum chamber (TVC) in which the engineering models of the SMU are tested. In the back the power supplies, read-out electronics, and other necessary accessories are visible.

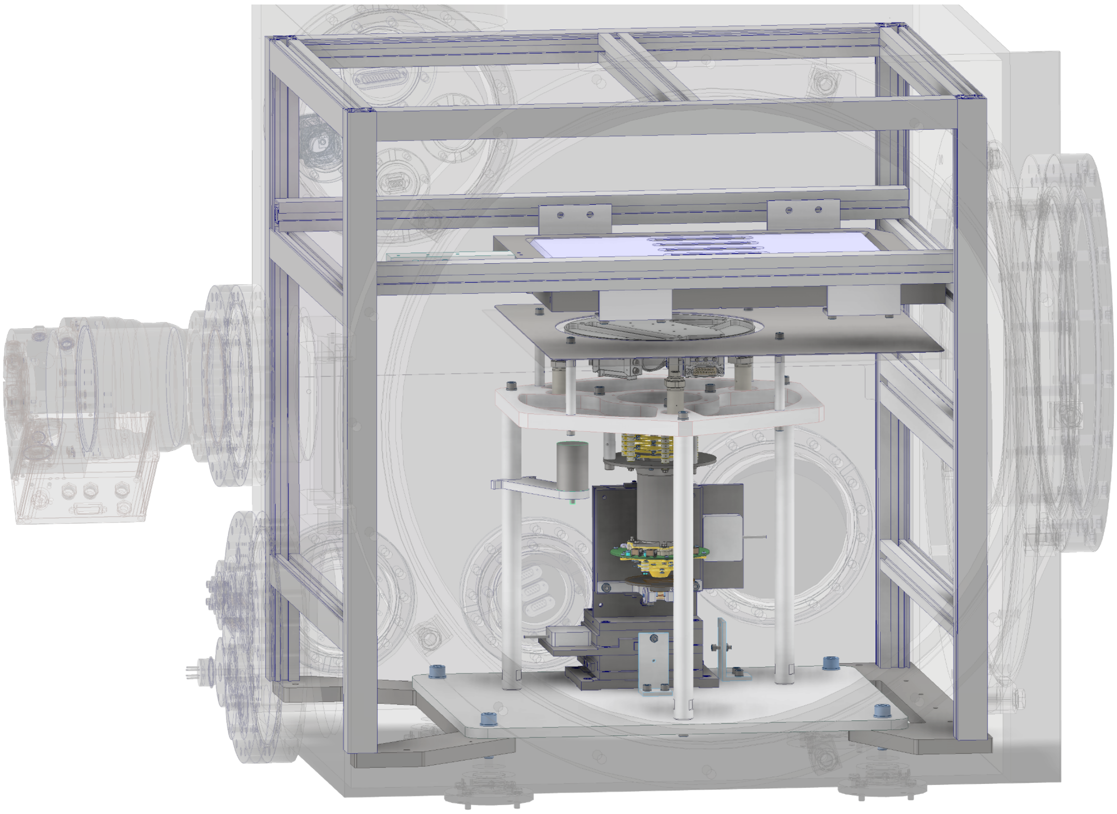

Figure 4.11: CAD model of the Artemis TVC in its current version for testing the MA EFM showing the internal mounting structure of the components.

Within the TVC, all structures are mounted to a supporting frame or a custom baseplate that is connected via studs to the vacuum chamber.

The OSS EBB+ and MA EFM are mounted to a connecting plate, ensuring the correct alignment of the two subsystems to each other. Above the OSS a heat exchanger is mounted, which couples radiatively to the OSS and can be cooled or heated by a thermostat outside the chamber. Below the MA, the XYZ linear translation stage can move an exchangeable sample holder for accurate positioning of the sample material within the system's laser focus for chemical composition analysis by mass spectrometry.

For future tests regarding magnetic susceptibility of the MA, an engineering model of the SHS drive motor was mounted at the same distance to the MA as it will have within the MSS. These tests should validate that the ion-optical system is immune to potential magnetic stray fields originating from the motor.

4.1.7 Electronic Support Equipment and Software

A space instrument is meant to be operated within the boundary conditions of a supporting spacecraft. The spacecraft is responsible for providing power to the instrument and a datalink through which it can communicate with the ground-based infrastructure. As no spacecraft is available during laboratory-based testing, additional devices substituting the functionality normally provided by the spacecraft are needed. In this context, these are summarised under the term Electronic Ground Support Equipment (EGSE).

The main component missing from this setup, whose functionality is indispensable to operate the instrument, is the DPU with a running application software. As the DPU is responsible for communicating with and controlling all the different electronic subsystems, appropriate replacements or simulators must be employed, which emulate the DPU's tasks.

The DCDC and HVPS can be controlled via a basic web-based interface, which runs on the EGSE box provided by the manufacturer. It allows for switching the different subsystems on and off and, in case of the HVPS, setting the requested voltages by communicating with the appropriate DACs and ADCs via an SPI bus. HK data can also be displayed and are additionally stored in an *InfluxDB*[1]. The stored HK data can be visualised using a *Grafana*[2] frontend.

The ROE uses a high-speed *SpaceWire* bus to communicate with the DPU, as high volumes of science data will be downlinked via this interface. To substitute the bus electrically, a SpaceWire Brick Mk4 (STAR-Dundee Ltd., United Kingdom) was used, connecting the ROE to a standard PC via USB. As the ROE was not supplied with any user-facing software by the manufacturer, the software library `roe-client` was designed and implemented in *Python*[3] based on the ROE's firmware documentation. On a low-level, the library implements the *SpaceWire RMAP*[4]-based interface, through which the ROE can be commanded. Based on the protocol implementation, higher level functions that abstract away common operations, such as startup and calibration of the ROE's systems and acquisition of spectra, were added. These functions allow the user to write scripts, that execute measurement procedures repeatably. On top of the `roe-client` library

---

[1] *InfluxDB* is a time-series database (TSDB) meant to store arbitrary values, primarily indexed by time of write. `https://www.influxdata.com/products/influxdb-overview/`

[2] *Grafana* is a web-based visualisation platform, to display data stored e.g. in TSDBs. `https://grafana.com/oss/grafana/`

[3] *Python* is an interpreted programming language. `https://www.python.org/`

[4] *SpaceWire RMAP* is a remote memory access protocol within the *SpaceWire* protocol stack. It allows for a *SpaceWire* node to access, read and write mapped memory of a remote *SpaceWire* node. It is standardised within ECSS-E-ST-50-52C.

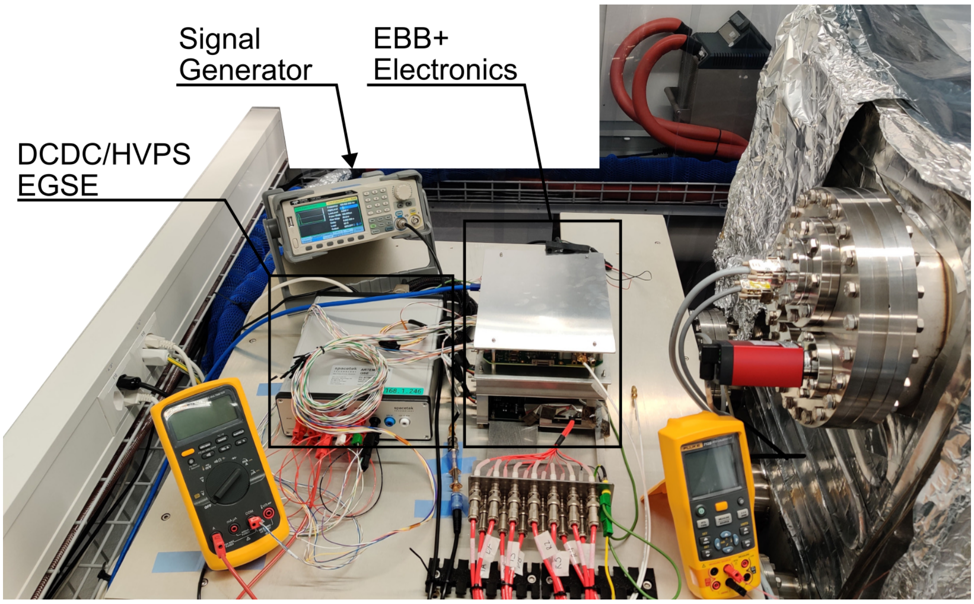

Figure 4.12: Overview of the EBB electronics as connected to the CLPS-LIMS thermal vacuum chamber. On the right, the HVPS, DCDC, and ROE are stacked and enclosed in the metal frame. On the left, the EGSE for the HVPS and DCDC is visible.

the graphical user interface (GUI) `roe-client-gui` based on *PyQt*[5] was developed. A screenshot is shown in Figure 4.13. The GUI allows setting up a basic measurement cycle and initiate the acquisition of spectra, which are displayed to the user in real-time. The acquired TOF spectra are stored on disk for further analysis.

For monitoring the HK data of the ROE, an electric interface based on a Raspberry Pico microcontroller board containing a RP2040 MCU (Raspberry Pi Ltd., United Kingdom), was developed. It interfaces with the dedicated SPI bus, which the ADCs responsible for collecting HK data within the ROE are using. Since the ADCs are connected to a shared bus, the chip select (CS) lines of the ADCs are connected to separate GPIO pins of the MCU. This allows to separately communicate with each ADC. An additional GPIO pin is connected to the `POWER_EN` pin of the ROE, allowing for power cycling the whole board by means of software. The firmware, written in C++ and running on the MCU, implements the specific SPI protocol of the used ADC128S102. A host computer can communicate with the MCU using a virtual COM port using a simple JSON based protocol, allowing it to read the ADC values and toggle the `POWER_EN` pin. The `roe-client` library contains the necessary abstractions to communicate with the MCU. Within `roe-client-gui` these abstractions are used to periodically read the ADC

---

[5] *PyQt* is a *Python* wrapper around the commonly used GUI framework Qt. `https://riverbankcomputing.com/software/pyqt/`

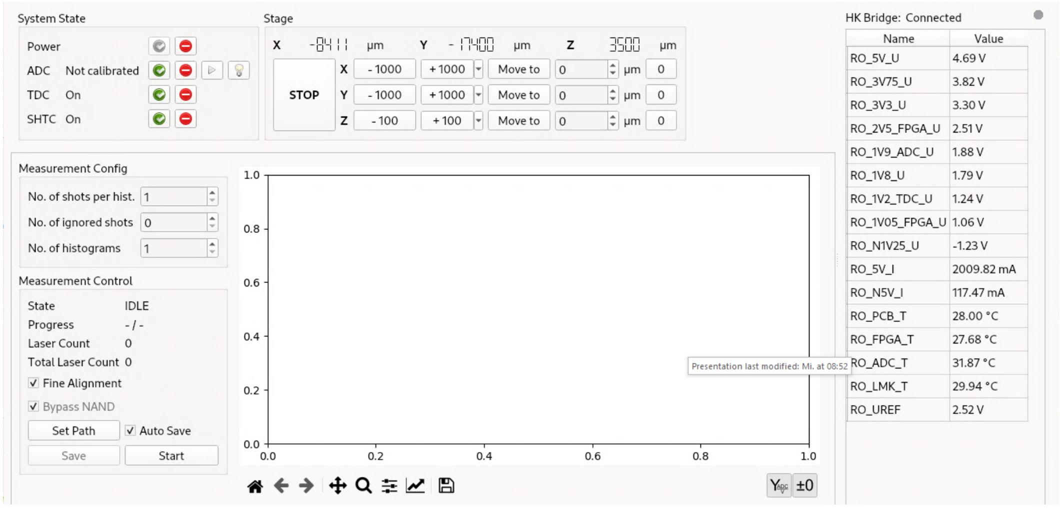

System State

Power

ADC Not calibrated

TDC On

SHTC On

Stage

X -8411 µm Y -17400 µm Z 3500 µm

X: Move to 0 µm, 0

Y: Move to 0 µm, 0

Z: Move to 0 µm, 0

Measurement Config

No. of shots per hist.: 1

No. of ignored shots: 0

No. of histograms: 1

Measurement Control

State: IDLE

Progress: - / -

Laser Count: 0

Total Laser Count: 0

☑ Fine Alignment

☑ Bypass NAND

☑ Auto Save

Presentation last modified: Mi. at 08:52

HK Bridge: Connected

Name	Value
RO_5V_U	4.69 V
RO_3V75_U	3.82 V
RO_3V3_U	3.30 V
RO_2V5_FPGA_U	2.51 V
RO_1V9_ADC_U	1.88 V
RO_1V8_U	1.79 V
RO_1V2_TDC_U	1.24 V
RO_1V05_FPGA_U	1.06 V
RO_N1V25_U	-1.23 V
RO_5V_I	2009.82 mA
RO_N5V_I	117.47 mA
RO_PCB_T	28.00 °C
RO_FPGA_T	27.68 °C
RO_ADC_T	31.87 °C
RO_LMK_T	29.94 °C
RO_UREF	2.52 V

Figure 4.13: Screenshot of the developed graphical user interface to control the ROE and sample stage.

values and using calibration values, convert the raw data to human-readable HK data like voltages, currents and temperatures. A list of the collected HK data is given in Table 4.2. The read HK values are displayed in the GUI and simultaneously forwarded to an *InfluxDB* for long-term storage and trend analysis. To access the recorded HK data, *Grafana* based dashboards were implemented, as can be seen in Figure 4.14.

The Laser Electronics (LE) used in this setup are not fully representative of the flight electronics in terms of functionality. The flight version will be able to generate laser bursts with a controllable count of shots. As the used LE is missing this feature, an external 33250A (Keysight Technologies, USA) function generator is configured to provide the appropriate trigger pulses to the LE. The signal generator is remote controlled by the `roe-client-gui` software and receives a trigger signal from the ROE when a burst shall be started. As the engineering LE are based on the manufacturer's commercial SB1 (Bright Solutions Srl., Italy) controller, it can be commanded by the previously developed `sb1-ctrl-gui` software (see Chapter 2), through which parameters such as the laser output energy can be set.

The final element to be controlled is the XYZ translation stage. Due to technical reasons, the supplied library that implements the communication protocol and provides a high-level C application programming interface could not be used. Based on the stage controller's documentation, a native implementation of the protocol in *Python* was developed. This allowed for a seamless integration of the stage into `roe-client-gui` and scripts, which allowed to automatise measurements that involved sample movement.

Table 4.2: Monitored HK values of the ROE

HK ID	Description	ADC Channel
`RO_5V_U`	Voltage of the incoming +5 V supply	CS: 0, Ch: 0
`RO_3V75_U`	Voltage of the +3.75 V supply for the LNAs	CS: 0, Ch: 1
`RO_3V3_U`	Voltage of the internal +3.3 V supply	CS: 0, Ch: 2
`RO_2V5_FPGA_U`	Voltage of the +2.5 V supply for the FPGA	CS: 0, Ch: 3
`RO_1V9_ADC_U`	Voltage of the +1.9 V supply for the ADC	CS: 0, Ch: 4
`RO_1V8_U`	Voltage of the internal +1.8 V supply	CS: 0, Ch: 5
`RO_1V2_TDC_U`	Voltage of the +1.2 V supply for the TDC	CS: 0, Ch: 6
`RO_1V05_FPGA_U`	Voltage of the +1.05 V supply for the FPGA	CS: 0, Ch: 7
`RO_N1V25_U`	Voltage of the −1.25 V supply for the LNAs	CS: 1, Ch: 0
`RO_5V_I`	Current of the incoming +5 V supply	CS: 1, Ch: 1
`RO_N5V_I`	Current of the incoming −5 V supply	CS: 1, Ch: 2
`RO_PCB_T`	Temperature of the PCB	CS: 1, Ch: 3
`RO_FPGA_T`	Temperature of the FPGA	CS: 1, Ch: 4
`RO_ADC_T`	Temperature of the ADC	CS: 1, Ch: 5
`RO_LMK_T`	Temperature of the clocking IC	CS: 1, Ch: 6
`RO_UREF`	Voltage of the LM4050 voltage reference	CS: 1, Ch: 7

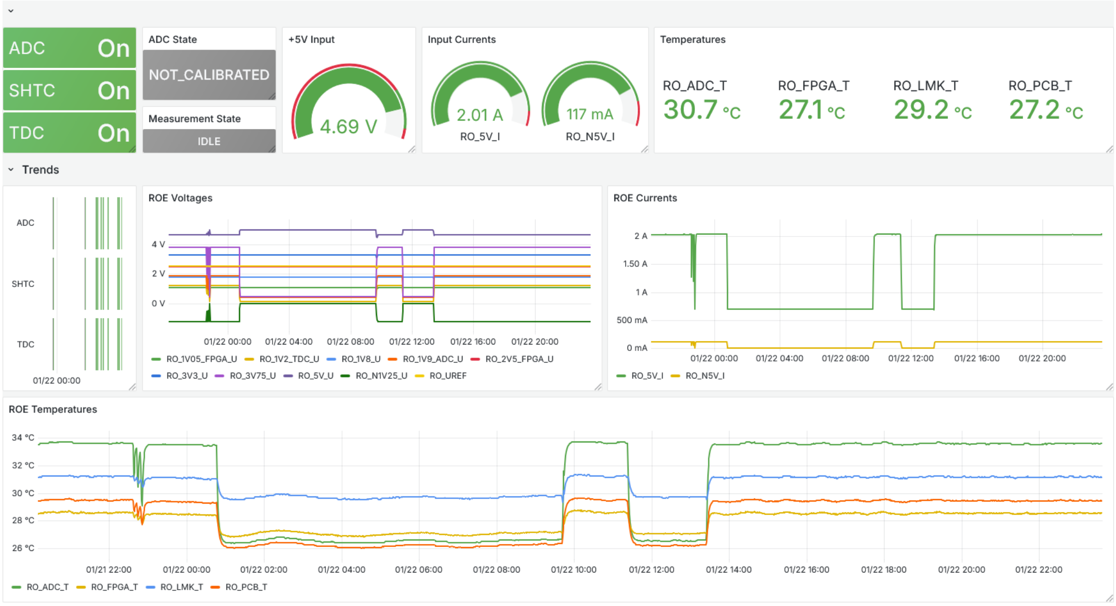

Figure 4.14: Screenshot of the ROE HK data monitoring system, based on an InfluxDB database with a Grafana frontend. This allows for displaying the current HK data as well as storing and reviewing trends, making it possible to establish correlations between occurring issues and the recorded data.

4.2 Commissioning and Characterisation of the ROE

The ROE for the CLPS-LIMS instrument is a custom-developed board. To ensure it performs in a manner that is in accordance with the technical specifications and thus does not degrade the spectral quality as produced by the mass analyser and detector system, characterisation measurements of the ROE were designed and performed.

4.2.1 Characterisation Setup

To provide a well-controlled and adjustable environment in which the performance of the ROE can be characterised, all external stimuli were generated by a set of arbitrary waveform generators (AWG), simulating the functionality of the laser electronics and the detector system. The general setup utilised is show in Figure 4.15.

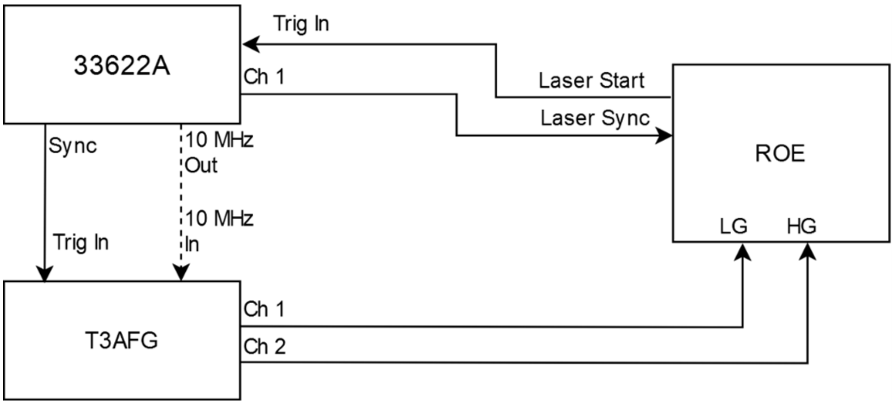

Figure 4.15: Schematic of the test setup, which was used to generate the external stimuli to characterise the ROE. Signals to the ROE were provided by two AWGs (Keysight 33622A, Teledyne LeCroy T3AFG).

A 33622A AWG (Keysight Technologies, USA) is responsible for generating the laser synchronisation pulses, which normally would be supplied by the photodiode within the LHB at the time a laser pulse is fired. The number of synchronisation pulses is configured according to the number of spectra the ROE expects for a measurement. The pulse train generation is triggered by the ROE using its “Laser Start” output, which is connected to the trigger input of the 33622A AWG.

Stimuli to the low- and high-gain channels of the ROE, and thus simulating the mass analyser’s detector system, are provided by a T3AFG500 AWG (Teledyne LeCroy, USA). This AWG has an output bandwidth of 500 MHz, making it the most suitable instrument available to generate the simulated high-bandwidth signals expected from the detector system.

As the “Laser Sync” pulse and the LG and HG signals are generated by two separate AWGs, appropriate timing synchronisation between them must be ensured. This is to minimise the jitter between the “Laser Sync” pulse and the LG and HG signals, and thus minimise the signal distortions when multiple spectra are co-added on the ROE. In addition to triggering the T3AFG with a low-jitter synchronisation signal from the 33622A, both AWG’s internal clocks are phase-locked together using the appropriate 10 MHz clock inputs and outputs. Using this setup, a reproducible jitter between the edges of the “Laser Sync” pulse and LG/HG signals of ∼100 ps std. dev. could be reached, as shown in Figure 4.16. As this jitter is about one order of magnitude smaller than the rise and fall times of the signals, contributions from this error can be neglected when co-adding signals into a single spectrum.

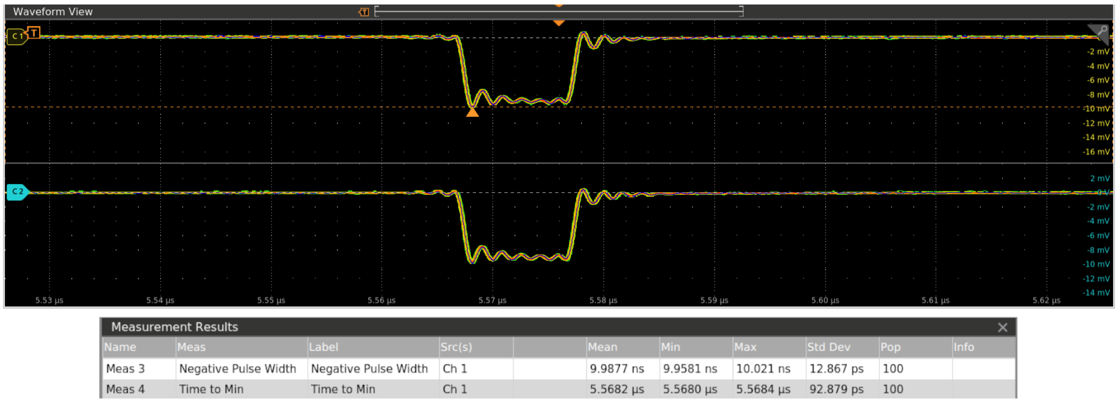

Name	Meas	Label	Src(s)		Mean	Min	Max	Std Dev	Pop	Info
Meas 3	Negative Pulse Width	Negative Pulse Width	Ch 1		9.9877 ns	9.9581 ns	10.021 ns	12.867 ps	100	
Meas 4	Time to Min	Time to Min	Ch 1		5.5682 µs	5.5680 µs	5.5684 µs	92.879 ps	100	

Figure 4.16: Oscilloscope measurements of the LG and HG signals using a Tektronix MSO64B. The oscilloscope was configured to trigger on the generated “Laser Sync” signal, thus being able to measure the jitter between the two signals.

4.2.2 Initial Commissioning of the ROE EBB

During the initial bring up of the ROE, communication between it and the `roe-client-gui` software was successfully established and status information could be read. HK data showed a current of about 0.6 A on the +5 V input supply (HK `RO_5V_I`) and 0 A on the −5 V supply (HK `RO_N5V_I`). This is in accordance with the expected values communicated by the manufacturer. Switching on the ADC and LNA power domain, the current on the +5 V input supply rose to 2.1 A A and the −5 V supply to 0.1 A. These values are also within the expected range.

First measurements with the now operational ROE connected to AWGs as signal sources, revealed several issues that needed to be addressed, before the ROE’s performance could be characterised properly.

Trigger misalignment First measurements performed with the ROE using the firmware version `v1.0.6` while co-adding spectra showed that LG and HG signal pulses, which should have the same delay from the “Trigger Sync” signal, were shifted with respect to each other as can be seen in Figure 4.17. The encountered delay was reproducibly 16 ADC samples long. The ROE manufacturer was notified about this issue and was able to reproduce it. Investigations on the manufacturer’s side revealed that the sampling concept with which the “Laser Sync” signal is detected, and thus the beginning of the spectrum is determined, is faulty. As in this implementation the “Laser Sync” signal is sampled by the on-board FPGA within its 100 MHz clock domain, indeed a sampling jitter of 16 to 32 ADC samples recorded at 1.6 GHz could occur.

The manufacturer was able to implement a solution within firmware version `v1.0.8`, without the need for hardware changes.

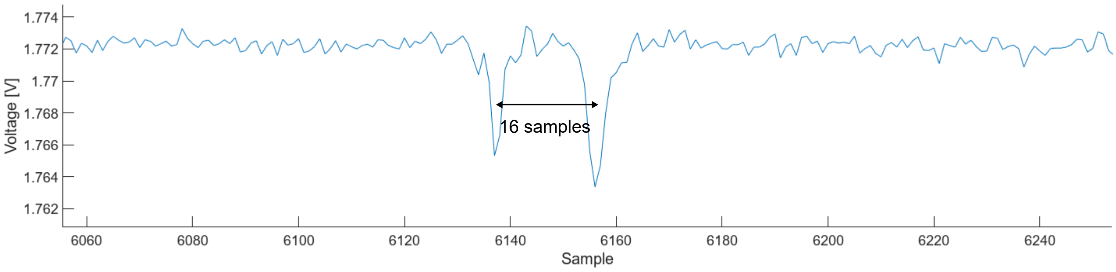

Figure 4.17: Spectrum of two co-added pulses on the LG channel. The generated peaks did have the same set delay counted from the beginning of the spectrum and thus should lie on top of each other.

Missed trigger signals It was observed that the ROE did not register every “Laser Sync” pulse within a measurement. This led to indefinite hang-ups of the ROE, as fewer spectra were recorded than the measurement configuration was set up to.

This issue could be traced back to the comparator used to register the “Laser Sync” pulses being configured with a very low threshold level of 50 mV. Resulting from a combination of not properly shielded connections within the test setup and the overall EM environment the ROE is in, enough noise could couple into the “Laser Sync” input and cause spurious trigger signals. As these were not timed in accordance with the expectations of the FPGA, invalid states within the firmware were encountered, leading to a hang-up of the FPGA.

The issue was resolved by increasing the comparator’s threshold level to 147 mV. This value is still low enough that the corresponding circuit on the laser electronics side can reach the necessary drive current. On the other hand, it is high enough to avoid any spurious trigger events with the environment the ROE is in.

Peak distortions on the HG channel Measurements with the HG channel of AWG generated pulses revealed serious signal distortions, as shown in Figure 4.18. The input stimulus generated by the AWG is a clean rectangular pulse with 1 ns rise and fall times, as was verified by oscilloscope measurements. The measured signal with the ROE showed a significant pre-pulse and undershoot on the falling edge. The distortion pattern was not in line with signal reflections due to possible impedance mismatches in the system. Nevertheless, connections external to the ROE were checked and could be excluded as source of the distortions. Non-linear effects within the LNA due to overdriving it could not be excluded, since it was operating at a high amplification of 18 dB. Investigations by the ROE manufacturer revealed an error in the initialisation sequence of the ADC, which was corrected in firmware version `v1.0.8`. With the new firmware, no distortions were detected any more.

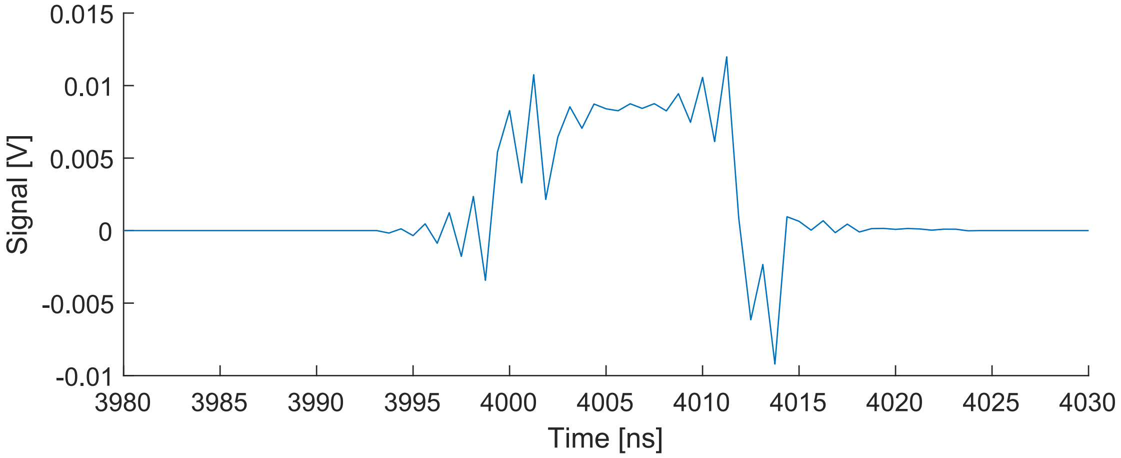

Figure 4.18: Rectangular pulse with 10 mV$_{pp}$ recorded with the HG channel of the ROE running firmware version `v1.0.7`. Signal distortions at the rising and falling edges are due to a faulty ADC initialisation sequence.

4.2.3 Noise Floor Characterisation

The achievable signal-to-noise ratio (SNR) with the ROE is directly related to the instrument's limit of detection (LOD) for a chemical species. Thus, for optimised performance, the SNR must be maximised. With the SNR being given by

$$SNR = \frac{A_{signal}}{\sigma_{noise}} \tag{4.1}$$

where A_{signal} is the signal amplitude and σ_{noise} is the standard deviation of the noise floor, it becomes evident that the SNR can be maximised in two ways. Increasing the signal amplitude will increase the SNR, which can be achieved by e.g., increasing the MCP gain. This method does come with limitations. A higher MCP gain leads to higher signal amplitudes of large abundance species, which can cause unwanted clipping during digitisation, thus limiting the instruments dynamic range. The other option to optimise the SNR is by decreasing the noise floor amplitude. This leads not only to a better LOD, but also to a higher instantaneous dynamic range of the instrument. With a given inherent noise of the instrument, the noise floor can be reduced by co-adding multiple spectra. In case the noise contribution is predominantly white noise, the noise floor decreases by $\sqrt{N}$, where N is the number of co-added spectra.

To understand the contributions of the ROE to the instrument's noise floor, characterisation measurements were performed. The characterisation setup was modified by terminating the ROE's LG and HG channel inputs with $50\,\Omega$ termination resistors. This ensures that only the internal noise of the ROE is captured. Triggering was performed as previously described with the 33622A AWG.

The standard deviation of the measured signal over the length of a nominal TOF spectrum is being used as a measure of the noise floor. The noise floor was measured at different numbers of accumulations. Initial measurements were performed at nominal operating conditions of the ROE EBB after all components were allowed to thermalise. The obtained results for the LG and HG channels, respectively, are shown in Figure 4.19 up to $N = 20\,000$. A linear correlation between $\frac{1}{\sigma_{noise}} \sim \sqrt{N}$ is evident in accordance with the predictions for white noise. For the HG channel, a non-linearity can be observed. Up to $N = 20\,000$, no significant flattening out of the data can be seen. This indicates that the noise floor at $N = 20\,000$ is still dominated by white noise, as contributions from harmonic noise cannot be minimised by accumulation of multiple spectra.

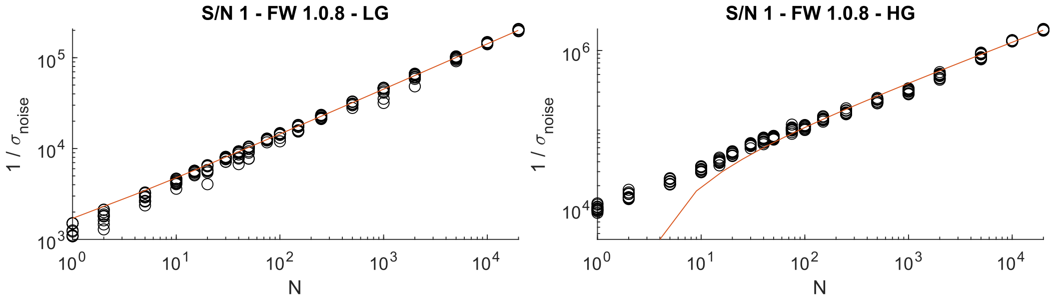

Figure 4.19: Inverse of the ROE's noise floor in relation to the square root of the number of accumulated spectra (N) for the LG and HG channel, respectively. The ROE was not additionally cooled ($T_{ADC} \sim 50\,°C$). The data are fitted with a linear function.

The measurements were repeated in the same configuration, with an additional electric fan being mounted onto the ROE. It provided a direct airflow over the FPGA and the frontend electronics EMC cover, which contains the ADC, thus, lowering the operating temperature of the ADC from +50 °C to +35 °C. The results in Figure 4.20 show a very similar trend to the case without cooling with no flattening of the curve up to $N = 20\,000$. However, the non-linearity observed on the HG channel in the hot case is not visible any more. No conclusive answer can yet be given to why this temperature dependence of the ADC response exists. The ADC used in the ROE EBB is an engineering quality model of the flight-model ADC12D1620QML-SP with a specified operating temperature of +25 °C, instead of the −55 °C to +125 °C operational range of the flight model. It cannot be ruled out that the observed behaviour of the ADC is a result of the engineering model's limited operational temperature range. Further investigations will have to be performed to better understand this phenomenon and ensure that it does not have a detrimental effect on the scientific performance of the CLPS-LIMS instrument.

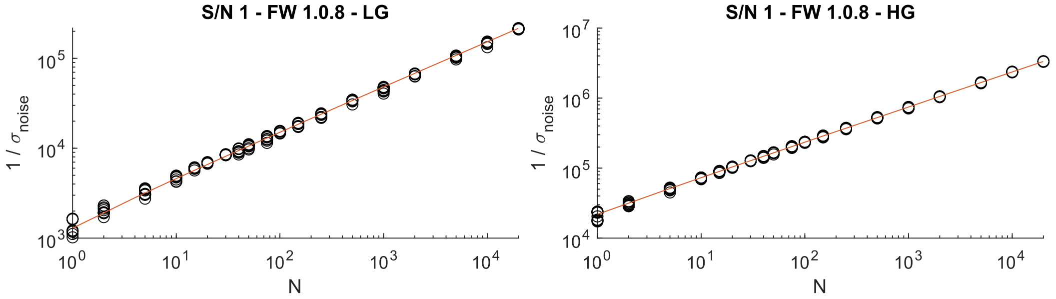

Figure 4.20: Inverse of the ROE's noise floor in relation to the square root of the number of accumulated spectra for the LG and HG channel, respectively. The ROE was additionally cooled by an electric fan ($T_{ADC} = 35\,°C$).

4.2.4 Dynamic Behaviour Characterisation

To gain an understanding of how the ROE behaves with various input stimuli applied to the LG and HG channel, the previously described characterisation setup with the T3AFG AWG providing the input signals was utilised.

All tests were conducted with self-similar rectangular pulses as input signals. Pulses with a rise and fall time of 1 ns and a width of 10 ns were used. The peak amplitudes were set to the FSR of the channels, being 2000 $\mathrm{mV_{pp}}$ for the LG channel and 100 $\mathrm{mV_{pp}}$ for the HG channel, respectively. The set rise and fall times are the minimum values the AWG can generate and match the expected rise and fall times of a peak generated by the mass analyser. For reference, the peak shape as generated by the AWG was measured using a Tektronix MSO64B oscilloscope. The obtained signal trace is shown in Figure 4.21 (left panel). Some ringing is visible at the transitions and can be attributed to be part of the signal generated by the AWG. By performing a Fast-Fourier Transform (FFT) on the time trace, its frequency spectrum is obtained (Figure 4.21, right panel). From this, the pulse's maximal frequency content was determined to be about 600 MHz.

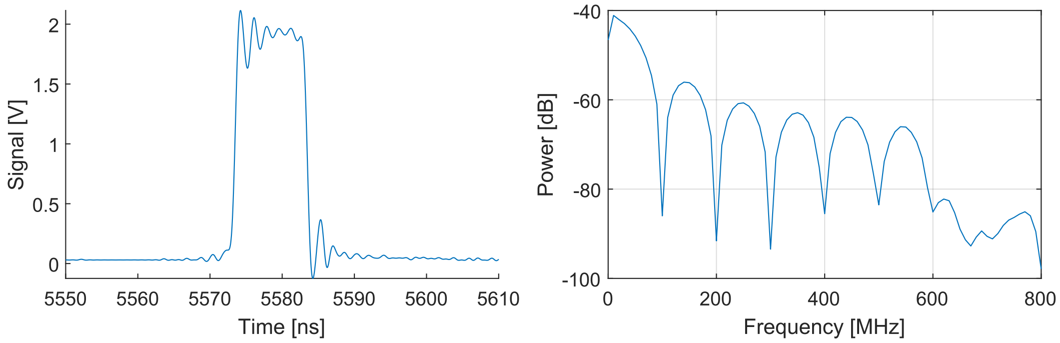

Figure 4.21: (Left) Input stimulus used for testing the LG channel with an amplitude of 2 $\mathrm{V_{pp}}$. **(Right)** FFT of the input stimulus.

Applying the appropriately scaled stimulus to the ROE's LG and HG channels results in the responses shown in Figure 4.22. Note, that the recorded data have been inverted to show positive pulses. The visible imperfections in the peak shape (ringing at the transitions) are already part of the AWG output and not part of the ROE response. No variations in the baseline before and after the peak are observable, even at input stimuli close to the channels' FSR. This is an important quality metric, as a non-flat baseline poses significant challenges when evaluating recorded mass spectra.

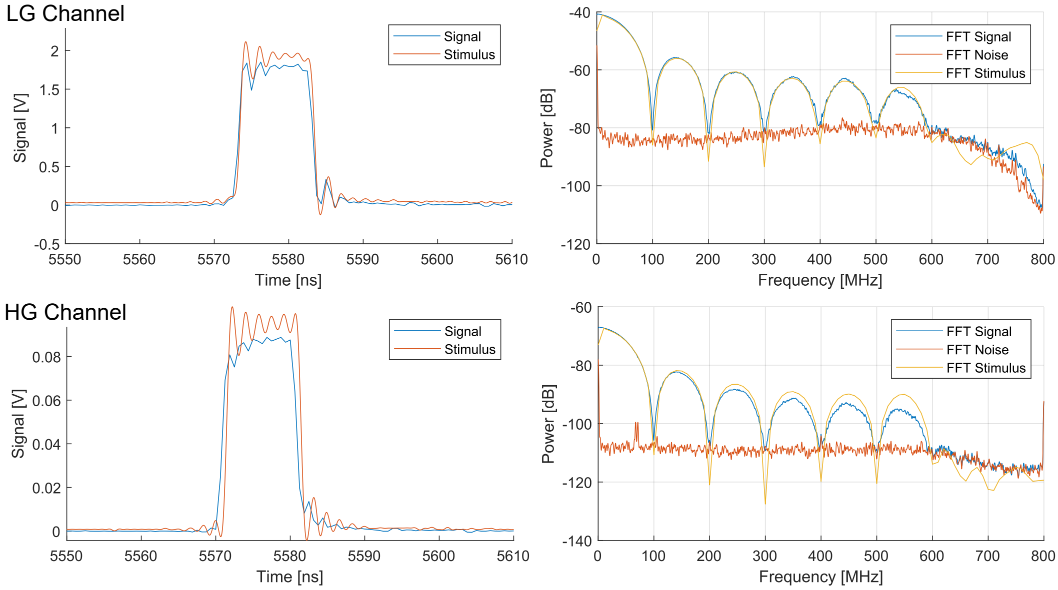

Figure 4.22: A 1 ns rise and fall time rectangular pulse recorded with the ROE's LG and HG channel, respectively. A reference measurement of the stimulus is shown additionally. The LG channel reproduces the stimulus correctly, whereas the HG channel shows increased rise and fall times.

For the recorded HG signal, a slight decrease in the transition steepness is observable in Figure 4.22. Comparing the frequency spectrum of the stimulus and the recorded signal, a significant attenuation of the higher frequency components >200 MHz can be seen. As the rise time is inversely proportional to the signal bandwidth, a reduction in bandwidth translates to an increase in rise time. Frequency response measurements of the ROE frontend performed by the manufacturer show a non-flat passband for the HG channel. Thus, this observation is in line with the provided data. As the bandwidth reduction will affect the spectral quality causing broadening, the ROE's signal bandwidth characteristics were explored in more detail and are described in the following Section 4.2.5.

In addition to the reproduction of input stimuli, the achievable dynamic range of the ROE's channels was investigated. The results are summarised in Table 4.3. The instantaneous dynamic range of both channels, i.e., without co-adding of spectra ($N = 1$), was found to be 61 dB, corresponding to about 3 orders of magnitude. Increasing N to 10 and 100, results in the expected improvement of the SNR by about 10 dB due to the decrease of the noise floor by a factor of $\sqrt{N}$. The SNR at $N = 1000$ is lower than theoretically predicted and lowered compared to the values obtained during the noise floor measurements. As the ROE's noise floor showed a linear decrease with respect to $\sqrt{N}$ up to $N = 20\,000$, it must be concluded that noise is contributed externally, e.g., from the AWG. With a lower noise signal source, a dynamic range of 90 dB (4.5 orders

Table 4.3: Measured dynamic range of the LG and HG channels in relation to the number of co-added spectra N.

N	$\sigma_{noise,LG}$	$A_{LG}/\sigma_{noise,LG}$	$\sigma_{noise,HG}$	$A_{HG}/\sigma_{noise,HG}$
1	1.7 mV	61 dB	79 µV	61 dB
10	0.55 mV	71 dB	23 µV	72 dB
100	0.18 mV	80 dB	8.6 µV	81 dB
1000	0.10 mV	86 dB	4.6 µV	86 dB

of magnitude) should be achievable at $N = 1000$. By using both channels in a combined fashion to detect high abundance species on the LG channel and low abundance species on the HG channel, a dynamic range of 4.5 orders of magnitude at $N = 1$ is feasible. At $N = 1000$ this increases to 6 orders of magnitude.

4.2.5 Bandwidth Characterisation

The pulsed signals generated by the mass analyser's detector system have an inherently high spectral content. This stems from the fast transition times in the low nanosecond range found in the signal. The recorded mass spectrum's possible quality is amongst others bounded by the bandwidth of the acquisition system, as a limited bandwidth translates to slower transition times, and thus lower mass resolution and ultimately lower detection sensitivity.

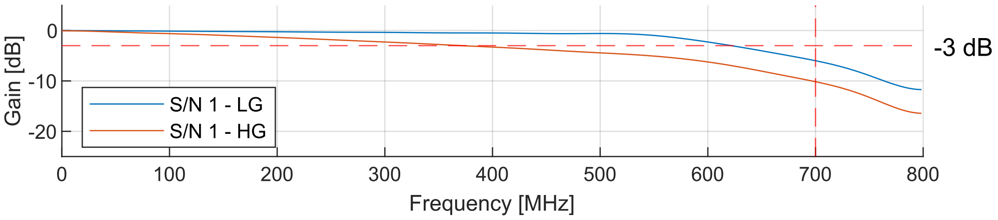

Figure 4.23: Frequency response of the ROE channel frontends, as determined by VNA transmission measurements between the input connector and the output of the anti-aliasing low-pass filter. The required −3 dB low-pass cutoff frequency at 700 MHz is marked.

The ROE's input bandwidth on the LG and HG channels was required to be 700 MHz (−3 dB low-pass cutoff) to not be a limiting factor in the signal chain. Results obtained during the characterisation of the ROE's dynamic behaviour and frequency response measurements of the channel frontends performed by the ROE's manufacturer revealed non-compliance with regard to the channels' bandwidth. In Figure 4.23 the frequency response of both channel frontends is shown with their maximal gain normalised to 0 dB. The LG channel has a flat passband up to 500 MHz and reaches its −3 dB point at 620 MHz. In contrast, the HG channel already starts attenuating below 10 MHz and reaches −3 dB gain at 370 MHz.

This deviation from the requirements prompted a more detailed analysis how the acquisition system's bandwidth influences the obtainable peak shapes of the CLPS-LIMS instrument. By performing in-silico analysis using simulated signals matching the detector system's expected output and filtering them using the ROE channels' frequency response, a general understanding of how the ROE EBB's limitations influence the recordable data quality was obtained. Three metrics describing the data's quality were investigated. An increase in the FWHM of a filtered peak leads to a worse mass resolution of the obtained mass spectrum, thus impeding data analysis and interpretation. The calculated Area Error is the difference between the area of the unfiltered peak obtained by numerical integration and the area of the filtered peak. Constant integration bounds of 1.5 FWHM are assumed. For quantitative chemical analysis of a mass spectrum, accurate integration of the peak attributed to a species is necessary. Thus, this error needs to be minimised. The *Max. Intensity Error* describes the difference between the maximum value of the unfiltered and filtered peak. A reduction in this maximum value impedes the detectability of peaks with intensities close to the noise floor.

As first order approximation, peaks produced by the instrument's detector system can be described by a Gaussian distribution with a width σ. For a Gaussian distribution the peak's FWHM is related to σ by

$$FWHM = 2\sqrt{2\ln 2\sigma} \approx 2.355\sigma \tag{4.2}$$

Since a TOF mass spectrometer's mass resolution M defined at FWHM is directly related to a peak's FWHM in the time domain by

$$M = \frac{m}{\Delta m} = \frac{t}{2\Delta t} = \frac{t}{2FWHM} \tag{4.3}$$

the simulated peaks used for the analysis are defined in terms of FWHM. All simulations were performed using a sample rate of 1.6 GS s^{-1}, matching the ROE's ADC sample rate. In Figure 4.24, peaks with varying FWHM are shown before and after being filtered by the measured ROE EBB's LG channel response. No significant broadening is detectable for the simulated peaks. As expected, the *Area Error* and *Max. Intensity Error* is maximal for the narrowest peaks, with the *Area Error* being −1.1 % and the *Max. Intensity Error* being −8 % for a simulated peak with FWHM of 1 ns. Figure 4.25 shows the identical analysis performed with the HG channel response. With the HG channel's lower cutoff frequency, the obtained errors for the high-bandwidth, low FWHM peaks are significantly higher compared to the LG channel. At FWHM of 1 ns, the peak's intensity is reduced by 24 %. Since the HG channel does not have a flat passband, the reduction in peak intensity is above 2 % for a peak with FWHM of 10 ns.

The shown data allow quantifying the impact of the acquisition system's bandwidth on the instrument's expected mass spectral quality. The shown reduction of a peak's maximum intensity can make the difference of detection and non-detection of a chemical species within the sample material, as this reduction translates directly to a reduction in SNR. With the CLPS-LIMS instrument's goal to detect and quantify trace elements within the lunar regolith, for which the ROE's HG channel is employed, mitigation strategies to counteract the shown deficiencies might have to be developed.

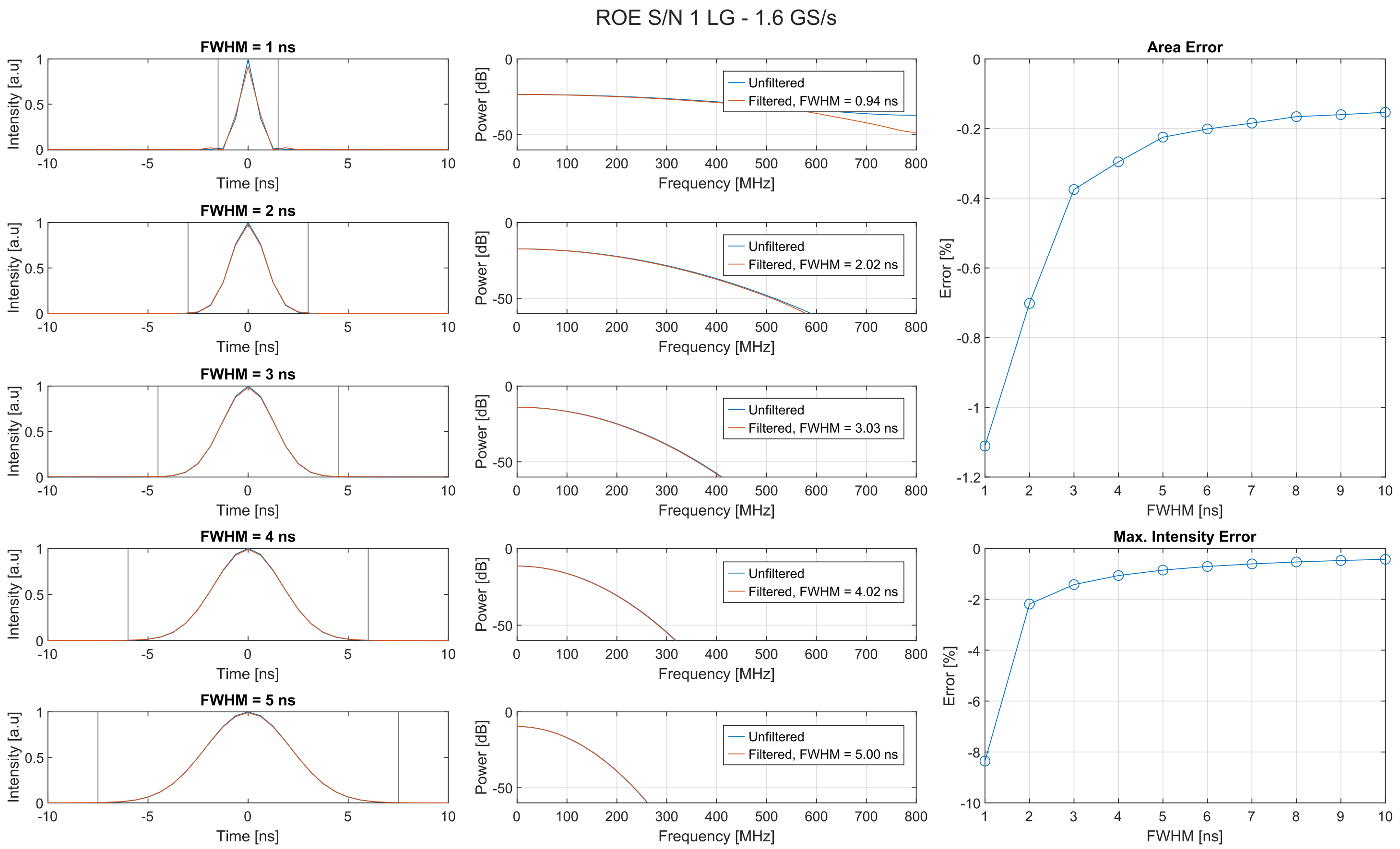

Figure 4.24: Simulated peaks modified by the ROE EBB's LG channel frequency response.

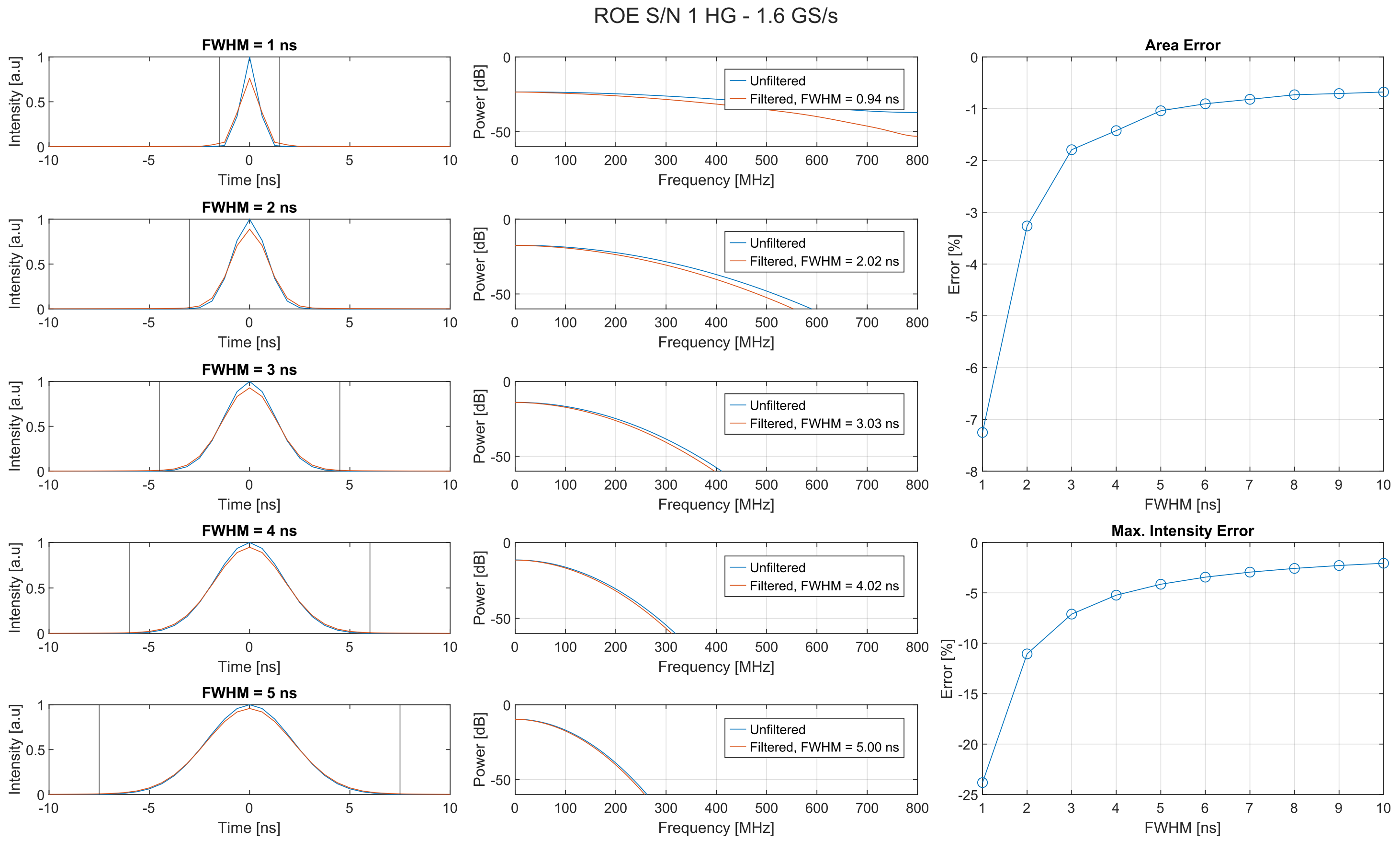

Figure 4.25: Simulated peaks modified by the ROE EBB's HG channel frequency response.

4.3 EFM Setup End-to-End Tests

After commissioning the complete EFM test setup, including all subsystems necessary to conduct LIMS measurements, the two prospective reference sample materials to be deployed with the CLPS-LIMS instrument were analysed. These were the first end-to-end tests the functionally equivalent subsystems of the CLPS-LIMS instrument were subjected to, proving the general functionality of the instrument's design.

Additionally, based on these measurements, the laser irradiance range required for successful ablation and ionisation of the sample materials was constrained. This analysis determines the types of the space-qualified ND filters to be procured for the instrument's flight version. Only if the LHB's static beam attenuation is properly sized, can the LHB's dynamic attenuation range of one order of magnitude be used to its full extent. Maximising the usable dynamic attenuation range is paramount to be able to correct for changes in the laser ablation and ionisation process. These changes can be caused by potential sample height variations, shifts in the optical system during launch and landing or simply the unknown optical absorbance efficiency of the sample material, which has an influence on the ablation efficiency.

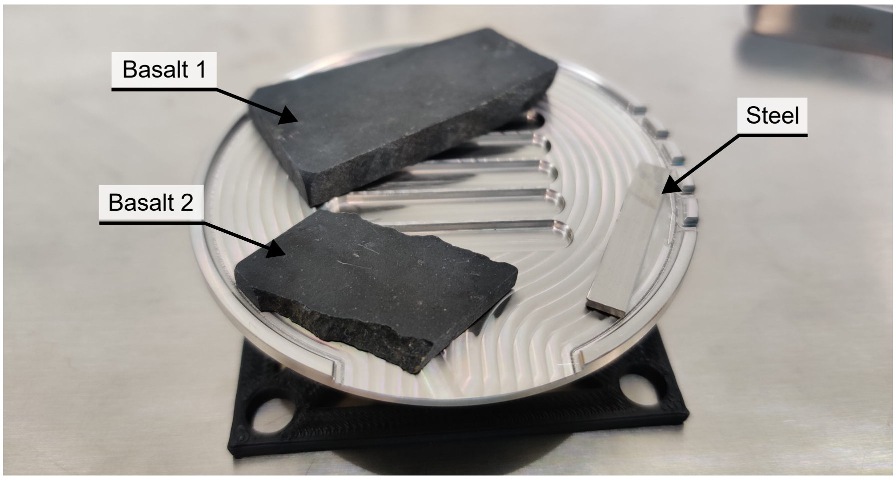

Figure 4.26: Sample holder with a stainless steel reference sample and two sections of different basalt rocks. “Basalt 1” is a less homogeneous, more crystalline basalt than “Basalt 2”.

A stainless steel sample (AISI 316L, 1.4435) similar to the one shown in Figure 4.26 will be used during the initial commissioning phase of the instrument on the lunar surface. During checkout, basic instrument health and performance parameters will be determined by performing LIMS measurements using this sample material. As it has a high homogeneity, extended measurements with a stable mass spectrometric signal can be performed, as needed for e.g., the optimisation of the ion-optical voltage set.

In addition to the steel reference sample, a geological reference sample will be part of the flight instrument. It serves as an external quantification standard. Using the calibration constants obtained by measuring it using the same instrument parameters and conditions that are used to analyse lunar regolith, it is possible to quantify the chemical composition of the regolith. For this purpose, the composition of the geological reference sample must be as close as possible to the assumed composition of the lunar regolith with regard to the major elements to reduce quantification errors due to differing matrix effects (Yu et al. 2009; B. Zhang et al. 2013). An additional constraint on the reference sample is, as with the steel sample, its spatial composition homogeneity to allow for stable measurements. Based on these requirements, basalt was chosen as the reference material. As the lunar regolith has a high basaltic content (Heiken et al. 1991), therefore this choice ensures good chemical compatibility. The rapid cooling of the low-viscosity lava from which basalts are formed leads to a highly homogeneous, amorphous structure with little crystalline inclusions. Additionally, to be able to survive the vibration and shock environment during the instrument's launch, the to be used reference sample must have sufficient mechanical stability to withstand the loads. A too weak material might break up during the launch, with fragments being liberated and damaging sensitive components within the instrument's spectrometer unit.

Two basaltic rocks, originating from Madagascar, were selected by the Institute of Geological Sciences, University of Bern, as potential reference samples. Both basalts are expected to have similar chemical compositions. They differ in grain size, with "Basalt 1" having a more crystalline structure and thus higher mechanical stability than "Basalt 2". As the more crystalline basalt's (Basalt 1) lower homogeneity is disadvantageous to analysis by LIMS, results of future vibration tests will determine if the more homogeneous basalt can be flown.

For analysis by LIMS, a section of about 5 mm thickness of each basalt was prepared. To remove potential surface contaminations both sections were sonicated for 5 min, each in ultra-pure water (MilliQ, Merck Millipore), isopropanol, and again ultra-pure water. The sections were fixed to the sample holder using carbon adhesive tape. In Figure 4.26 the sample holder with the basaltic samples is shown.

The initial measurements with the EFM setup were conducted using the steel sample, as this material's behaviour is well known from previous studies conducted during the prototyping phase of the project and known to exhibit well-behaved ablation and ionisation properties.

To verify the OSS alignment, more specifically the out-of-plane position of the laser focus spot, a scan along the optical axis (Z axis) with steel the sample was performed. The laser pulse energy was kept constant at an SHG temperature of $T_{SHG} = 26.0\,°\text{C}$, corresponding to a pulse energy of 0.8 µJ. This energy was chosen as it allows for the measurement of well resolved, not saturated mass spectra in the approximate focus point. The scan was performed starting at position $z = 0\,\mu\text{m}$ corresponding to the position where the sample surface is in contact with the mass analyser's aperture.

The peak areas of four selected species found in the stainless steel sample in relation to the distance from the mass analyser's aperture are shown in Figure 4.27, with the measured intensities shown in the top and the normalised intensities show in the bottom panel. All species show a similar behaviour with the ablation and ionisation process subsiding at the position $z_{min} \approx -1000\,\mu\text{m}$. At that position, the laser beam has diverged sufficiently, that the laser irradiance has dropped below the steel's ablation threshold. In the range of 0 µm to z_{min} the peak intensities show a local maximum at $z_{max} \approx -500\,\mu\text{m}$ and a global maximum at distances very close to the mass analyser ($|z| < 200\,\mu\text{m}$).

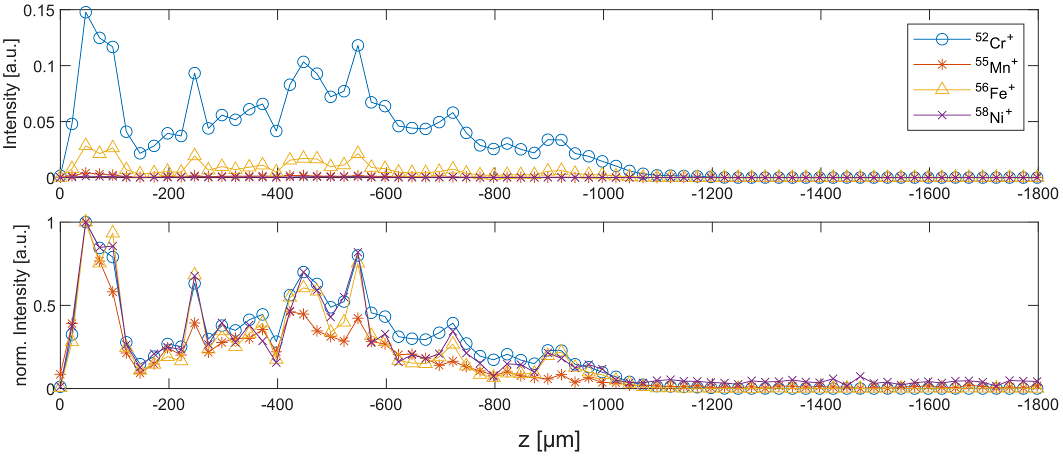

Figure 4.27: Mass spectrometric intensities of selected species present in the stainless steel sample depending on the sample's distance from the mass analyser's aperture z. Measured intensities are given in the top panel, while the bottom panel shows normalised intensities.

The optical focus of the setup has been determined to be at $z_0 = -245\,\mu\text{m}$ during the alignment procedure of the OSS. As a first order approximation, it is expected that the maximal peak intensities are being detected within the focal spot. The observed high-intensity area at $|z| < 200\,\mu\text{m}$ can be excluded from further interpretation. At those close distances to the aperture, the mass analyser's ion capture properties are different from those at the nominally required sample distance of $z_0^{ali} = -600\,\mu m$. The difference in distance between z_0 and z_{max} is about 355 µm. This observed difference can potentially be attributed to the increase in beam area above the laser ablation threshold counteracting the reduction of peak irradiance when moving the sample out of focus. The posed hypothesis cannot be proven or disproven with the collected data and will require further investigation to fully understand the phenomenon.

An important property of the instrument is the minimisation of the reliance of frequent calibration on an external standard for quantification purposes of the species within the sample material of interest. Such a recalibration can become necessary when the laser ablation and ionisation conditions change significantly, as this leads to a change in relative sensitivity coefficients (RSCs). Hence, the stability of the laser ablation conditions within the investigated region of interest are of high value for the quantitative analysis of the sample material. The lunar regolith sample surface, as prepared by the SHS, is expected to have a planarity of ±200 µm. Therefore, it shall be possible to measure the relative intensities of the species with a low variance within that region.

In Figure 4.28, intensity ratios referenced to $^{52}Cr^+$ across the investigated sample positions are shown. The calculated moving standard deviations of the ratios shown in the region $z_0^{ali} \pm 200\,\mu m$ are below 0.05, so that the upper limit of the quantification error resulting from the effects considered here is less than 5 %.

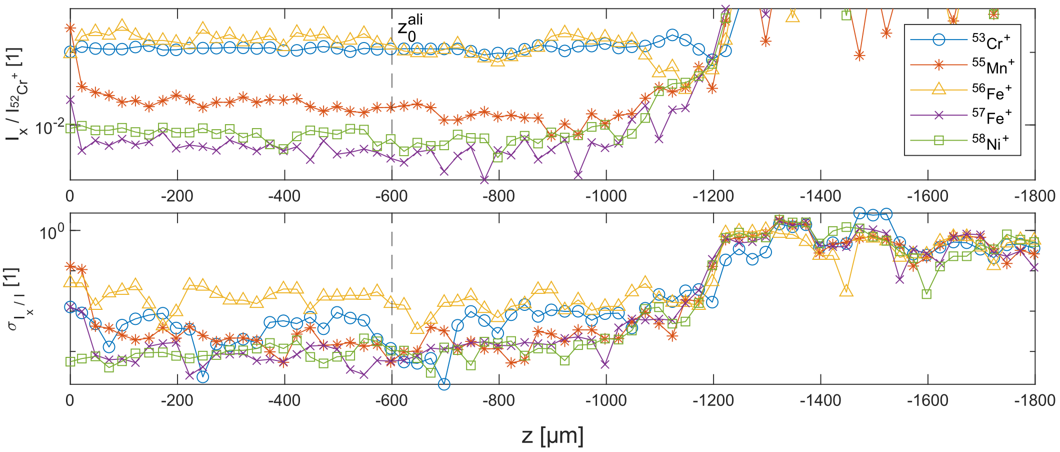

Figure 4.28: Intensities of selected species in the stainless steel sample referenced to $^{52}Cr^+$ (upper panel), and their variability given by the moving standard deviation with window length of 3 points (lower panel). Measured at different distances from the mass analyser aperture z. The nominal sample position of the SHS is marked with z_0^{ali}. Intensity ratios are stable up $z = 1200\,\mu m$, indicating stable ablation conditions in that range.

For the determination of the required irradiance I for optimal laser ablation and ionisation of stainless steel, the sample's behaviour at a fixed position z with varying laser pulse energies was studied. It is expected that below a certain energy, no species can be detected, as the obtained irradiance is below the threshold required for laser ablation and ionisation. Above a to be determined maximum energy threshold, a significant reduction in spectral quality is expected. As more and more ions are produced during ablation with increasing irradiances, the local ion concentration within the mass analyser's ion-optical system increases. Hence, space charge effects start to affect the ion packets, leading to a deterioration of the instrument's mass resolution.

The sample surface was positioned at $z = -400\,\mu\text{m}$, between the optical focus z_0 and z_{max}, as the resulting spectra were deemed qualitatively well resolved and stable at an SHG temperature of $T_{SHG} = 26\,°\text{C}$. Figure 4.29 shows a visual representation of the mass spectra's behaviour for varying laser energies. The shown mass range covers $^{52}\text{Cr}^+$ and $^{56}\text{Fe}^+$, the species showing peaks with the highest intensities. Since they appear at the lowest laser irradiances first, they are suitable to determine the ablation threshold. Visually, the ablation threshold is determined to be at $T_{SHG} \approx 26\,°\text{C}$. In Figure 4.30 the ratios of selected species referenced to $^{52}\text{Cr}^+$ are shown. Ratios above $T_{SHG} \approx 25.5\,°\text{C}$ show a low variability, thus stable laser ablation conditions above the corresponding irradiance can be assumed. This is in line with the visually determined threshold.

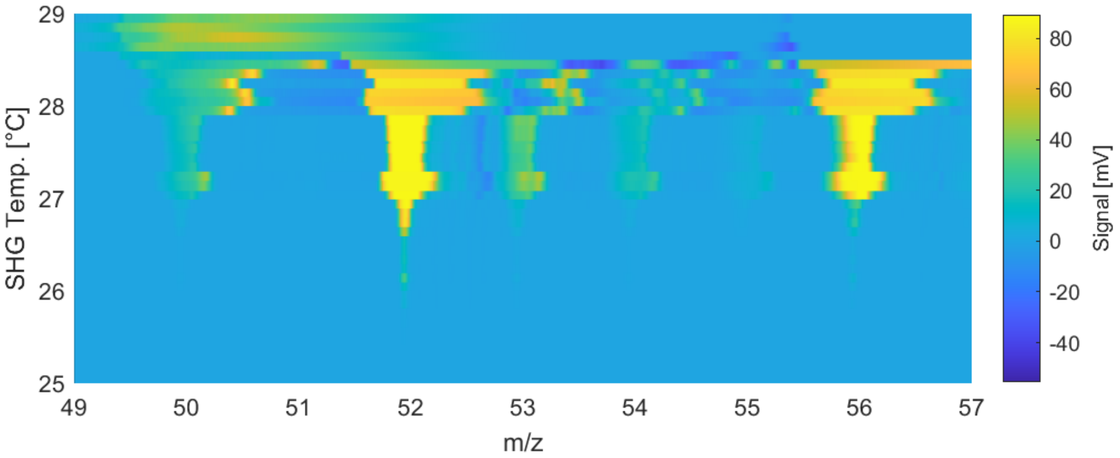

Figure 4.29: Mass spectra of the stainless steel reference sample at $z = -400\,\mu\text{m}$ and varying laser energies. Significant peak broadening is visible above 28 °C SHG temperature ($E = 1.4\,\mu\text{J}$, $I = 0.16\,\text{GW}\,\text{cm}^{-2}$).

The mass resolution starts deteriorating at $T_{SHG} > 27\,°\text{C}$ as can be seen from the broadened peaks visible in Figure 4.29. This observation is in line with the increasing variability in the ratios above that temperature as shown in Figure 4.30. At $T_{SHG} > 28\,^{\circ}\mathrm{C}$, significant peak broadening and shifts in the peak positions marks an absolute limit, as spectra of this quality cannot be analysed reliably any more. From this, the minimum ablation threshold can be estimated to be at $I^{steel}_{min} = 0.08\,\mathrm{GW\,cm^{-2}}$ and maximum tolerable irradiance at $I^{steel}_{max} = 0.16\,\mathrm{GW\,cm^{-2}}$ for the stainless steel.

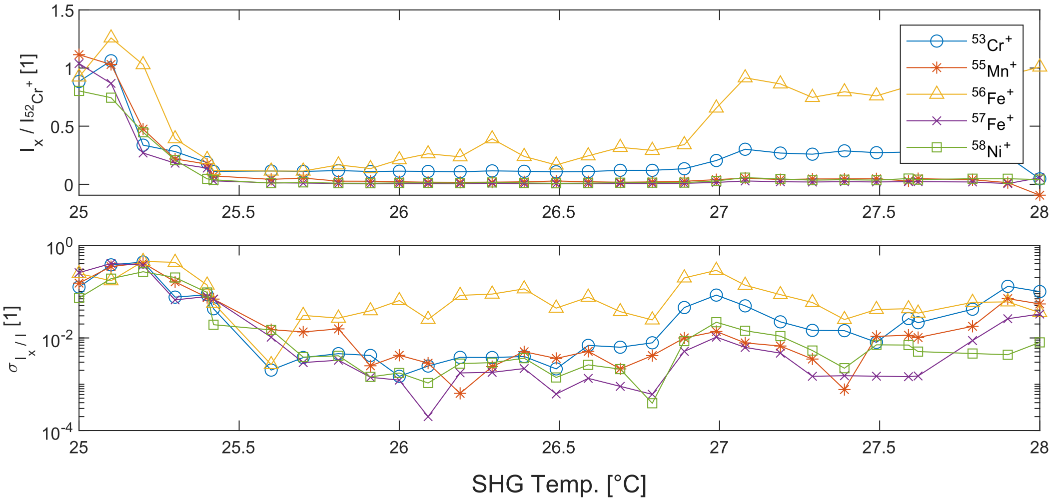

Figure 4.30: Intensities of selected species referenced to $^{52}\mathrm{Cr}^+$ (upper panel) and their variability shown as moving standard deviations (lower panel). Stainless steel reference sample measured at $z = -400\,\mu\mathrm{m}$.

Similarly to the energy threshold determination for the stainless steel reference sample, the maximally tolerable laser energy for the basalt sample was determined. As the basalt is a non-metallic material, both the lower and upper energy thresholds are expected to lie above the values of the stainless steel.

The measurements were conducted on the amorphous basalt sample (Basalt 2), as its higher spatial composition homogeneity is expected to produce more reproducible results. The energy scan was performed at $z = -410\,\mu\mathrm{m}$.

The mass spectra for the amorphous basalt for different laser irradiances are shown in Figure 4.31. At $T_{SHG} \approx 31.2\,^{\circ}\mathrm{C}$, corresponding to an irradiance of $0.40\,\mathrm{GW\,cm^{-2}}$, peak broadening and shifts in the peak positions are observed. As numerical analysis of the obtained spectra, such as the variability of the intensity ratios, didn't show clear trends, the upper energy limit was determined purely qualitatively by observing the recorded spectra while changing the laser energy. Deterioration of the spectral quality as previously described did commence in good agreement with the limit shown in Figure 4.31.

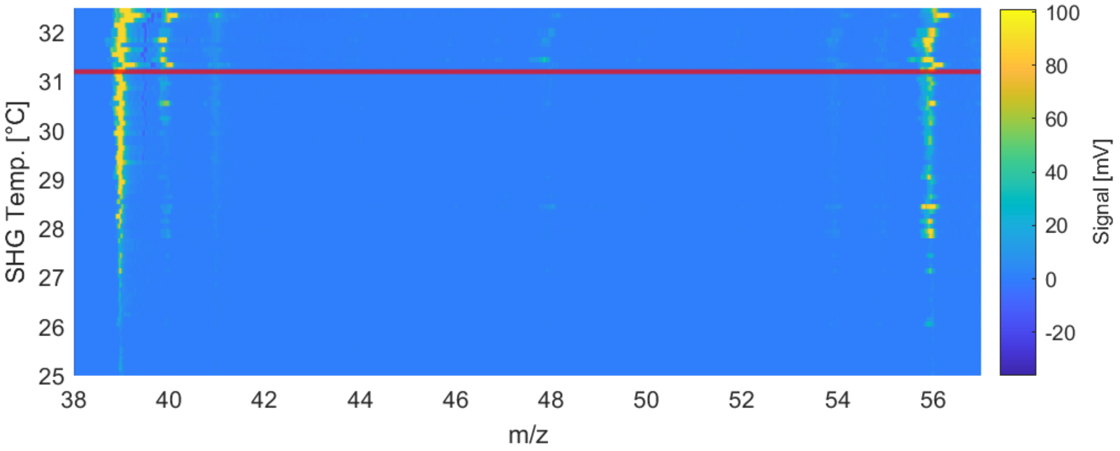

Figure 4.31: Waterfall plot of mass spectra recorded on “Basalt 2” at $z = -410\,\mu\text{m}$, and varying laser pulse energies. The spectrum quality deteriorates above an SHG temperature of 31.2 °C as marked by the red line.

As the chemical composition and colour, factors that influence the to be determined threshold energies, of the two basalts are identical, the obtained results are transferrable to “Basalt 1”. Studies using lunar regolith simulant as sample material (see Chapter 2) achieved good ablation results with $I_{regolith} \approx 0.2\,\text{GW}\,\text{cm}^{-2}$, thus showing comparable behaviour to the basalt sample.

Based on the obtained results, the initially foreseen irradiance range of $0.1\,\text{GW}\,\text{cm}^{-2}$ to $1.0\,\text{GW}\,\text{cm}^{-2}$ within the focus, is confirmed. With the current optical design and the worst-case in-axis sample misalignments of $z_0^{ali} \pm 600\,\mu\text{m}$, an irradiance range between $0.045\,\text{GW}\,\text{cm}^{-2}$ and $0.588\,\text{GW}\,\text{cm}^{-2}$ is obtainable. Thus, the baselined range fully covers the needed irradiances to conduct LIMS measurements on all three sample materials.

As mass spectra could be obtained on samples that are representative of materials the instrument will analyse during flight, the commissioning of the EFM test setup was successfully completed. These measurements could only be executed as all the subsystems, which are part of the EFM test setup, performed as intended without major impairments. Working engineering models of the subsystems boost the confidence in their respective implementations and allow the project to move forward in building a flight-ready instrument.

5 Conclusion

This thesis has outlined the critical steps undertaken to transform a laboratory-based Laser Ionisation Mass Spectrometer (LIMS) into a flight-ready instrument, capable of performing sensitive chemical analysis of lunar regolith. The data to be collected by the CLPS-LIMS instrument contributes to furthering our understanding of the Moon's composition and, more broadly, the history and evolution of our planetary system.

A key aspect of the instrument's development was the selection and testing of a suitable laser source, as well as the design of an optimised laser beam guiding and shaping system. This system forms the foundation for the optical system employed in the flight version of CLPS-LIMS. Furthermore, initial tests with lunar regolith simulant materials revealed challenges associated with mass spectrometric analysis in a regolith environment. Specifically, modifications to the mass analyser design were necessary to mitigate the risk of regolith grains interfering with the ion-optical system, ensuring reliable performance under expected lunar conditions.

Another critical factor addressed in this work was the potential issue of electrostatic charging of the lunar sample. It was demonstrated that the instrument can tolerate and operate effectively under such conditions, mitigating risks associated with charge accumulation in the harsh lunar environment. Additionally, the development of a self-cleaning sample handling system allows for the analysis of, in principle, an indefinite number of samples by continuously refreshing the sample surface. This approach represents a universal concept that could be adapted for other planetary instruments analysing regolith and requiring well-defined surfaces.

The successful demonstration of the CLPS-LIMS engineering model confirmed its capability to perform chemical analysis of the prospective reference materials. These advancements not only prepare the instrument for its deployment on the Moon but also pave the way for adaptations of the technology for future planetary exploration missions. Variations of the developed instrument could be applied to other solar system bodies such as Venus or Mars, where LIMS technology could focus on detecting and analysing organic molecules in the search for past or present extraterrestrial life.

Bibliography

Alikhanov, S G (Apr. 1957). “A NEW IMPULSE TECHNIQUE FOR ION MASS MEASUREMENTS”. In: *Soviet Phys. JETP* Vol: 4.

Anand, M., I.A. Crawford, M. Balat-Pichelin, S. Abanades, W. Van Westrenen, G. Péraudeau, R. Jaumann, and W. Seboldt (Dec. 2012). “A brief review of chemical and mineralogical resources on the Moon and likely initial in situ resource utilization (ISRU) applications”. In: *Planetary and Space Science* 74.1, pp. 42–48. ISSN: 00320633. DOI: `10.1016/j.pss.2012.08.012`.

Artemis III Science Definition Team Report (2020). Tech. rep. NASA/SP-20205009602. NASA. URL: `https://www.lpi.usra.edu/lunar/strategies/resources/Artemis-III-Science-Definition-Team-Report-2020.pdf` (visited on 09/27/2024).

Becker, Johanna Sabine (Dec. 2007). *Inorganic Mass Spectrometry: Principles and Applications*. 1st ed. Wiley. ISBN: 978-0-470-01200-0 978-0-470-51722-2. DOI: `10.1002/9780470517222`.

Boeren, Nikita J., Salome Gruchola, Coenraad P. De Koning, Peter Keresztes Schmidt, Kristina A. Kipfer, Niels F. W. Ligterink, Marek Tulej, Peter Wurz, and Andreas Riedo (Oct. 2022). “Detecting Lipids on Planetary Surfaces with Laser Desorption Ionization Mass Spectrometry”. In: *The Planetary Science Journal* 3.10, p. 241. ISSN: 2632-3338. DOI: `10.3847/PSJ/ac94bf`.

Boeren, Nikita J., Peter Keresztes Schmidt, Marek Tulej, Peter Wurz, and Andreas Riedo (Mar. 2024). *Towards biosignature detection on Icy Moons with ORIGIN*. Poster. DOI: `10.5194/egusphere-egu24-16084`. URL: `https://meetingorganizer.copernicus.org/EGU24/EGU24-16084.html` (visited on 01/07/2025).

– (Feb. 2025). “ORIGIN: Laser Desorption Ionization Mass Spectrometry of Nucleobases for In Situ Space Exploration”. In: *The Planetary Science Journal* 6.2, p. 28. ISSN: 2632-3338. DOI: `10.3847/PSJ/ad9de9`.

Brinckerhoff, W. B., G. G. Managadze, R. W. McEntire, A. F. Cheng, and W. J. Green (Feb. 2000). “Laser time-of-flight mass spectrometry for space”. In: *Review of Scientific Instruments* 71.2, pp. 536–545. ISSN: 0034-6748, 1089-7623. DOI: `10.1063/1.1150237`.

Brown, H.M., A.K. Boyd, B.W. Denevi, M.R. Henriksen, M.R. Manheim, M.S. Robinson, E.J. Speyerer, and R.V. Wagner (May 2022). “Resource potential of lunar permanently shadowed regions”. In: *Icarus* 377, p. 114874. ISSN: 00191035. DOI: `10.1016/j.icarus.2021.114874`.

Carrier, W. David (Oct. 2003). “Particle Size Distribution of Lunar Soil”. In: *Journal of Geotechnical and Geoenvironmental Engineering* 129.10, pp. 956–959. ISSN: 1090-0241, 1943-5606. DOI: `10.1061/(ASCE)1090-0241(2003)129:10(956)`.

Colwell, J. E., S. Batiste, M. Horányi, S. Robertson, and S. Sture (June 2007). “Lunar surface: Dust dynamics and regolith mechanics”. In: *Reviews of Geophysics* 45.2, 2005RG000184. ISSN: 8755-1209, 1944-9208. DOI: `10.1029/2005RG000184`.

Creech, Steve, John Guidi, and Darcy Elburn (Mar. 2022). “Artemis: An Overview of NASA’s Activities to Return Humans to the Moon”. In: *2022 IEEE Aerospace Conference (AERO)*. Big Sky, MT, USA: IEEE, pp. 1–7. ISBN: 978-1-6654-3760-8. DOI: `10.1109/AERO53065.2022.9843277`.

Critical decisions on Cosmic Vision (Nov. 2003). URL: `https://www.esa.int/Newsroom/Press_Releases/Critical_decisions_on_Cosmic_Vision` (visited on 02/27/2025).

Cudnik, Brian, ed. (2023). *Encyclopedia of Lunar Science*. Cham: Springer International Publishing. ISBN: 978-3-319-14540-2 978-3-319-14541-9. DOI: `10.1007/978-3-319-14541-9`.

Fenner, M. A., J. W. Freeman Jr., and H. K. Hills (Jan. 1973). “The electric potential of the lunar surface”. In: *Lunar and Planetary Science Conference Proceedings* 4. ADS Bibcode: 1973LPSC....4.2877F, p. 2877. ISSN: 0046-564X.

Garcia, Carmen C., Helmut Lindner, Alex Von Bohlen, Cedomil Vadla, and Kay Niemax (2008). “Elemental fractionation and stoichiometric sampling in femtosecond laser ablation”. In: *Journal of Analytical Atomic Spectrometry* 23.4, p. 470. ISSN: 0267-9477, 1364-5544. DOI: `10.1039/b718845e`.

General Environmental Verification Standard (GEVS) for GSFC Flight Programs and Projects (Apr. 2021). Greenbelt, MD 20771. URL: `https://standards.nasa.gov/sites/default/files/standards/GSFC/B/0/gsfc-std-7000b_signature_cycle_04_28_2021_fixed_links.pdf`.

George, Stuart P. et al. (Oct. 2024). “Space radiation measurements during the Artemis I lunar mission”. In: *Nature* 634.8032, pp. 48–52. ISSN: 0028-0836, 1476-4687. DOI: `10.1038/s41586-024-07927-7`.

Hapke, Bruce (May 2001). “Space weathering from Mercury to the asteroid belt”. In: *Journal of Geophysical Research: Planets* 106.E5, pp. 10039–10073. ISSN: 01480227. DOI: `10.1029/2000JE001338`.

Heiken, Grant, David Vaniman, and Bevan M. French, eds. (1991). *Lunar sourcebook: a user’s guide to the moon*. Cambridge [England] ; New York: Cambridge University Press. ISBN: 978-0-521-33444-0.

Hergenröder, Roland, Ota Samek, and Vanja Hommes (July 2006). “Femtosecond laser ablation elemental mass spectrometry”. In: *Mass Spectrometry Reviews* 25.4, pp. 551–572. ISSN: 0277-7037, 1098-2787. DOI: `10.1002/mas.20077`.

Hermann, J., L. Mercadier, E. Mothe, G. Socol, and P. Alloncle (Aug. 2010). “On the stoichiometry of mass transfer from solid to plasma during pulsed laser ablation of brass”. In: *Spectrochimica Acta Part B: Atomic Spectroscopy* 65.8, pp. 636–641. ISSN: 05848547. DOI: `10.1016/j.sab.2010.03.015`.

Karanam, Durga Prasad, Megha Bhatt, Amitabh A, Ambily G, Sachana Sathyan, Dibyendu Misra, Neeraj Srivastava, and Anil Bhardwaj (Aug. 2023). “Contextual Characterisation Study of Chandrayaan-3 Primary Landing Site”. In: *Monthly Notices of the Royal Astronomical Society: Letters*, slad106. ISSN: 1745-3925, 1745-3933. DOI: `10.1093/mnrasl/slad106`.

Kipfer, K. A., N. F. W. Ligterink, J. Bouwman, L. Schwander, V. Grimaudo, C. P. De Koning, N. J. Boeren, P. Keresztes Schmidt, R. Lukmanov, M. Tulej, P. Wurz, and A. Riedo (Feb. 2022). “Toward Detecting Polycyclic Aromatic Hydrocarbons on Planetary Objects with ORIGIN”. In: *The Planetary Science Journal* 3.2, p. 43. ISSN: 2632-3338. DOI: `10.3847/PSJ/ac4e15`.

Knott, K. (June 1973). “Electrostatic charging of the lunar surface and possible consequences”. In: *Journal of Geophysical Research* 78.16, pp. 3172–3175. ISSN: 01480227. DOI: `10.1029/JA078i016p03172`.

Li, Jin, Chengxiang Yin, Siyue Chi, Wenshuo Mao, Xiaohui Fu, and Jiang Zhang (Oct. 2024). “The Lunar Regolith Thickness and Stratigraphy of the Chang’E-6 Landing Site”. In: *Remote Sensing* 16.21, p. 3976. ISSN: 2072-4292. DOI: `10.3390/rs16213976`.

Ligterink, Niels F. W., Valentine Grimaudo, Pavel Moreno-García, Rustam Lukmanov, Marek Tulej, Ingo Leya, Robert Lindner, Peter Wurz, Charles S. Cockell, Pascale Ehrenfreund, and Andreas Riedo (June 2020). “ORIGIN: a novel and compact Laser Desorption – Mass Spectrometry system for sensitive in situ detection of amino acids on extraterrestrial surfaces”. In: *Scientific Reports* 10.1, p. 9641. ISSN: 2045-2322. DOI: `10.1038/s41598-020-66240-1`.

Ligterink, Niels F. W., Kristina A. Kipfer, Salome Gruchola, Nikita J. Boeren, Peter Keresztes Schmidt, Coenraad P. De Koning, Marek Tulej, Peter Wurz, and Andreas Riedo (June 2022). “The ORIGIN Space Instrument for Detecting Biosignatures and Habitability Indicators on a Venus Life Finder Mission”. In: *Aerospace* 9.6, p. 312. ISSN: 2226-4310. DOI: `10.3390/aerospace9060312`.

Mazur, J. E., C. Zeitlin, N. Schwadron, M. D. Looper, L. W. Townsend, J. B. Blake, and H. Spence (June 2015). “Update on Radiation Dose From Galactic and Solar Protons at the Moon Using the LRO/CRaTER Microdosimeter”. In: *Space Weather* 13.6, pp. 363–364. ISSN: 1542-7390, 1542-7390. DOI: `10.1002/2015SW001175`.

McIntosh, Eleanor C, James M D Day, Francis M McCubbin, Kathleen E Vander Kaaden, Ruan Hattingh, and Magali Porrachia (Apr. 2024). "Revisiting the Petrogenesis of Pyroclastic Glass Bead Deposits at the Apollo 15 and 17 Sites". In: *Journal of Petrology* 65.4, egae026. ISSN: 0022-3530, 1460-2415. DOI: `10.1093/petrology/egae026`.

O'Brien, P. and S. Byrne (Feb. 2021). "Physical and Chemical Evolution of Lunar Mare Regolith". In: *Journal of Geophysical Research: Planets* 126.2, e2020JE006634. ISSN: 2169-9097, 2169-9100. DOI: `10.1029/2020JE006634`.

Paige, David A. et al. (Oct. 2010). "Diviner Lunar Radiometer Observations of Cold Traps in the Moon's South Polar Region". In: *Science* 330.6003, pp. 479–482. ISSN: 0036-8075, 1095-9203. DOI: `10.1126/science.1187726`.

Pieters, Carle M. and Sarah K. Noble (Oct. 2016). "Space weathering on airless bodies: SPACE WEATHERING ON AIRLESS BODIES". In: *Journal of Geophysical Research: Planets* 121.10, pp. 1865–1884. ISSN: 21699097. DOI: `10.1002/2016JE005128`.

"Proceedings of the American Physical Society" (June 1946). In: *Physical Review* 69.11-12, pp. 674–674. ISSN: 0031-899X. DOI: `10.1103/PhysRev.69.674`.

Reitz, Guenther, Thomas Berger, and Daniel Matthiae (Dec. 2012). "Radiation exposure in the moon environment". In: *Planetary and Space Science* 74.1, pp. 78–83. ISSN: 00320633. DOI: `10.1016/j.pss.2012.07.014`.

Riedo, A., A. Bieler, M. Neuland, M. Tulej, and P. Wurz (Jan. 2013). "Performance evaluation of a miniature laser ablation time-of-flight mass spectrometer designed for *in situ* investigations in planetary space research: Miniaturised laser ablation tof mass spectrometer". In: *Journal of Mass Spectrometry* 48.1, pp. 1–15. ISSN: 10765174. DOI: `10.1002/jms.3104`.

Riedo, A., S. Meyer, B. Heredia, M.B. Neuland, A. Bieler, M. Tulej, I. Leya, M. Iakovleva, K. Mezger, and P. Wurz (Oct. 2013). "Highly accurate isotope composition measurements by a miniature laser ablation mass spectrometer designed for in situ investigations on planetary surfaces". In: *Planetary and Space Science* 87, pp. 1–13. ISSN: 00320633. DOI: `10.1016/j.pss.2013.09.007`.

Riedo, Andreas, Maike Neuland, Stefan Meyer, Marek Tulej, and Peter Wurz (2013). "Coupling of LMS with a fs-laser ablation ion source: elemental and isotope composition measurements". In: *Journal of Analytical Atomic Spectrometry* 28.8, p. 1256. ISSN: 0267-9477, 1364-5544. DOI: `10.1039/c3ja50117e`.

Riedo, Andreas, Marek Tulej, Urs Rohner, and Peter Wurz (Apr. 2017). "High-speed microstrip multi-anode multichannel plate detector system". In: *Review of Scientific Instruments* 88.4, p. 045114. ISSN: 0034-6748, 1089-7623. DOI: `10.1063/1.4981813`.

Rohner, Urs (June 2004). "Development of Highly Miniaturised Laser–Mass–Spectrometers for the in situ Analysis of Planetary Surfaces". Inaugural dissertation. Bern, Switzerland: University of Bern.

Rohner, Urs, James A Whitby, and Peter Wurz (Dec. 2003). "A miniature laser ablation time-of-flight mass spectrometer for *in situ* planetary exploration". In: *Measurement Science and Technology* 14.12, pp. 2159–2164. ISSN: 0957-0233, 1361-6501. DOI: `10.1088/0957-0233/14/12/017`.

Russo, Richard E., Xianglei Mao, Jhanis J. Gonzalez, Vassilia Zorba, and Jong Yoo (July 2013). "Laser Ablation in Analytical Chemistry". In: *Analytical Chemistry* 85.13, pp. 6162–6177. ISSN: 0003-2700, 1520-6882. DOI: `10.1021/ac4005327`.

Sanders, Gerald, William Larson, Kurt Sacksteder, and Carole Mclemore (Sept. 2008). "NASA In-Situ Resource Utilization (ISRU) Project: Development and Implementation". In: *AIAA SPACE 2008 Conference & Exposition*. San Diego, California: American Institute of Aeronautics and Astronautics. ISBN: 978-1-62410-002-4. DOI: `10.2514/6.2008-7853`.

Schonfeld, Julie (Oct. 2023). "Summary of the Contracted Deliveries of NASA Payloads to the Moon Via Commercial Lunar Payload Services (CLPS)". In: *2023 IEEE International Conference on Systems, Man, and Cybernetics (SMC)*. ISSN: 2577-1655, pp. 863–866. DOI: `10.1109/SMC53992.2023.10394001`.

Shkuratov, Y (Feb. 2001). "Regolith Layer Thickness Mapping of the Moon by Radar and Optical Data". In: *Icarus* 149.2, pp. 329–338. ISSN: 00191035. DOI: `10.1006/icar.2000.6545`.

Siegler, Matt, David Paige, Jean-Pierre Williams, and Bruce Bills (July 2015). "Evolution of lunar polar ice stability". In: *Icarus* 255, pp. 78–87. ISSN: 00191035. DOI: `10.1016/j.icarus.2014.09.037`.

Singh, Sunpreet, Gurminder Singh, Chander Prakash, and Seeram Ramakrishna (July 2020). "Current status and future directions of fused filament fabrication". In: *Journal of Manufacturing Processes* 55, pp. 288–306. ISSN: 15266125. DOI: `10.1016/j.jmapro.2020.04.049`.

Slabic, Ane, John E. Gruener, Rostislav N. Kovtun, Douglas L. Rickman, Laurent Sibille, Heather A. Oravec, Jennifer Edmundson, and Sean Keprta (Oct. 2024). *Lunar Regolith Simulant User's Guide: Revision A*. URL: `https://ntrs.nasa.gov/citations/20240011783`.

Smith, Marshall, Douglas Craig, Nicole Herrmann, Erin Mahoney, Jonathan Krezel, Nate McIntyre, and Kandyce Goodliff (Mar. 2020). "The Artemis Program: An Overview of NASA's Activities to Return Humans to the Moon". In: *2020 IEEE Aerospace Conference*. Big Sky, MT, USA: IEEE, pp. 1–10. ISBN: 978-1-7281-2734-7. DOI: `10.1109/AERO47225.2020.9172323`.

Spudis, Paul D., Ben Bussey, Jeffrey Plescia, Jean-Luc Josset, and Stéphane Beauvivre (July 2008). "Geology of Shackleton Crater and the south pole of the Moon". In: *Geophysical Research Letters* 35.14, p. L14201. ISSN: 0094-8276. DOI: `10.1029/2008GL034468`.

Stubbs, T.J., W.M. Farrell, J.S. Halekas, J.K. Burchill, M.R. Collier, M.I. Zimmerman, R.R. Vondrak, G.T. Delory, and R.F. Pfaff (Jan. 2014). "Dependence of lunar surface charging on solar wind plasma conditions and solar irradiation". In: *Planetary and Space Science* 90, pp. 10–27. ISSN: 00320633. DOI: `10.1016/j.pss.2013.07.008`.

Tulej, Marek, Niels F.W. Ligterink, Coenraad de Koning, Valentine Grimaudo, Rustam Lukmanov, Peter Keresztes Schmidt, Andreas Riedo, and Peter Wurz (Mar. 2021). "Current Progress in Femtosecond Laser Ablation/Ionisation Time-of-Flight Mass Spectrometry". In: *Applied Sciences* 11.6, p. 2562. ISSN: 2076-3417. DOI: `10.3390/app11062562`.

Tulej, Marek, Andreas Riedo, Maria Iakovleva, and Peter Wurz (2012). "On Applicability of a Miniaturised Laser Ablation Time of Flight Mass Spectrometer for Trace Elements Measurements". In: *International Journal of Spectroscopy* 2012.1. _eprint: https://onlinelibrary.wiley.com/doi/pdf/10.1155/2012/234949, p. 234949. ISSN: 1687-9457. DOI: `10.1155/2012/234949`.

Vondrak, Richard, John Keller, Gordon Chin, and James Garvin (Jan. 2010). "Lunar Reconnaissance Orbiter (LRO): Observations for Lunar Exploration and Science". In: *Space Science Reviews* 150.1, pp. 7–22. ISSN: 1572-9672. DOI: `10.1007/s11214-010-9631-5`.

Wang, Wenwen, Qi Jin, Xuejiao Chen, Hengyue Jiao, Wei Cai, Yu Lu, Tianyi Xu, and Yunzhao Wu (Jan. 2024). "Character and spatial distribution of mineralogy at the lunar south polar region". In: *Planetary and Space Science* 240, p. 105833. ISSN: 00320633. DOI: `10.1016/j.pss.2023.105833`.

Williams, J.-P., D.A. Paige, B.T. Greenhagen, and E. Sefton-Nash (Feb. 2017). "The global surface temperatures of the Moon as measured by the Diviner Lunar Radiometer Experiment". In: *Icarus* 283, pp. 300–325. ISSN: 00191035. DOI: `10.1016/j.icarus.2016.08.012`.

Yu, Quan, Rongfu Huang, Lingfeng Li, Lin Lin, Wei Hang, Jian He, and Benli Huang (June 2009). "Applicability of Standardless Semiquantitative Analysis of Solids by High-Irradiance Laser Ionization Orthogonal Time-of-Fight Mass Spectrometry". In: *Analytical Chemistry* 81.11, pp. 4343–4348. ISSN: 0003-2700, 1520-6882. DOI: `10.1021/ac900141z`.

Zayhowski, J.J. (2013). "Microchip lasers". In: *Handbook of Solid-State Lasers*. Elsevier, pp. 359–402. ISBN: 978-0-85709-272-4. DOI: `10.1533/9780857097507.2.359`.

Zayhowski, John J (2000). "Passively Q-switched Nd:YAG microchip lasers and applications". In: *Journal of Alloys and Compounds*.

Zhang, Bochao, Miaohong He, Wei Hang, and Benli Huang (May 2013). “Minimizing Matrix Effect by Femtosecond Laser Ablation and Ionization in Elemental Determination”. In: *Analytical Chemistry* 85.9, pp. 4507–4511. ISSN: 0003-2700, 1520-6882. DOI: `10.1021/ac400072j`.

Zhang, Shenyi et al. (Sept. 2020). “First measurements of the radiation dose on the lunar surface”. In: *Science Advances* 6.39, eaaz1334. ISSN: 2375-2548. DOI: `10.1126/sciadv.aaz1334`.

Acknowledgements

Everyone who read this far, I commend deeply.

First, I thank Prof. Dr. Peter Wurz for giving me the opportunity to carry out my doctoral studies in his research group. Thank you for your relentless behind-the-scenes support, as well as your personal and scientific advice. Further, my co-supervisor Prof. Dr. Marek Tulej deserves my gratitude for his support and the insights he shared with me over the last four years. Thanks for teaching me enough about lasers that I wouldn't look into one with the proverbial remaining eye. I'd like to extend my special thanks to PD Dr. Andreas Riedo, who played more than a small role in enabling me to start, stick with and ultimately finish this PhD project.

The developments presented in this dissertation wouldn't have been possible without the contributions of two groups of people. In that regard, I'd like to thank all my colleagues — past and present — of the LMS group. Especially:

(Very soon Dr.) Nikita Boeren, for not only sharing ORIGIN, drinks and food with me, but also being a great friend in every situation.

(Soon Dr.) Salome Gruchola, for your invaluable support in sifting through piles of data and pointing toward the needle in the haystack.

(Soon-ish Dr.) Luca Knecht, for pointing towards a world outside the office. Thank you for allowing me to be your sporty friend. Dr. Coenraad de Koning, for all our discussions at and outside of work, the knowledge transfer that went both ways, and always lending an ear in times of need.

The second group of people I'd like to thank are the members of the CLPS-LIMS team: Dr. Benoît Plet, Patrik Mändli, Sven Riedo, Michael Althaus, Michael Bieri, Scott Trimble, Sébastien Hayoz, Timothy Bandy, Matthias Blaukovitsch, Olivier Studer, Simon Studer, Dr. Daniele Piazza, Michela Gargano and Susanne Wüthrich. Thank you for seeing everything as a challenge with an eventual solution — I learned a lot from every single one of you.

I thank every member of the Space Research and Planetary Sciences division for providing the necessary support to build a space instrument like CLPS-LIMS and for having enough trust to let a young individual like me handle such equipment.

	Thank you
Rico Fausch	for all the discussions and the willingness to share an office
Audrey Vorburger	for the not only teaching me new things in the office, but also in the lecture room
Klaus Mezger	for answering all my geology related questions
Kristina Kipfer, Youcef Sellam, Samuel Wyler, Robin Bonny, Daniel Müller, Lorenzo Obersnel, Leander Schlarmann, Tim Mosimann, Parastoo Ghaznavi, Mohammed Tauseef	for your company in coffee breaks, during lunch, conferences and lectures
Thierry de Roche, Vincent Dor	for trying and sometimes succeeding in bringing the instrument to its limits
Harald Mischler	for transforming the ideas into reality, even on short notice
Heinz Tschumi, Werner Kellenberger, Sacha Häusler, Alexander Schläfli	for introducing me to the world of machining
Adrian Etter, Raphael Hänggi	for the discussions, tools and gizmos needed to get a setup running
Iljadin Manurung	for the constant supply of new electronics
Claudio Zimmermann	for the electrifying Friday afternoon discussions
Dora Zimmerer, Tina Rothenbühler, Fabienne Altenöder	for making sure the institute doesn't come to a grinding halt
Christoph Althaus, Charles Arn, Anton Güdel, Stefan Maurer, Vasco Vitacca, Franziska Stämpfli-Stalder	for keeping the ExWi up and running

Thank you Meli, Gunnar, Sebi, Fredi, Maike, Johannes, Paul and everyone else for your continuous support and friendship. Last but not least, my deepest gratitude goes to my family. A szüleim és családom feltétel nélküli támogatása és bátorítása felbecsülhetetlen értékű volt, és nélkülük nem lennék ott, ahol ma vagyok. Köszönöm!

List of Figures

List of Tables

A List of Abbreviations

AC	Alternating Current
ADC	Analogue to Digital Converter
BEX	Beam Expander
CLPS	Commercial Lunar Payload Service
COTS	Commercial Off-The-Shelf
CPU	Central Processing Unit
CTE	Coefficient of Thermal Expansion
DAC	Digital to Analogue converter
DC	Direct Current
DCDC	Direct Current to Direct Current converter
DPU	Data Processing Unit
EBB	Elegant Breadboard
EBB+	Elegant Breadboard with limited environmental testing
EFM	Engineering Functional Model
EGSE	Electronic Ground Support Equipment
ELU	Electronics Unit
EQM	Engineering Qualification Model
ESA	European Space Agency
FFT	Fast Fourier Transform
FPGA	Field Programmable Gate Array
FSR	Full-Scale Range
FWHM	Full Width at Half Maximum
GEVS	General Environmental Verification Standard
GND	GrouND
GSa	Giga Samples
HK	HouseKeeping
HG	High Gain
HV	High Voltage
HVPS	High Voltage Power Supply
IF	InterFace
LE	Laser Electronics
LG	Low Gain
LHB	Laser Head Box
LIMS	Laser Ionisation Mass Spectroscopy
LMS	Laser Mass Spectrometer
LNA	Low-Noise Amplifier
LRO	Lunar Reconnaissance Orbiter
LSS	Laser Sub System
LV	Low Voltage
LVPS	Low Voltage Power Supply
MA	Mass Analyser
MCP	Multi-Channel Plate
MS	Mass Spectrometry
MSS	Main Support Structure
NASA	National Aeronautics and Space Administration
ORIGIN	ORganics Information Gathering INstrument
OSS	Optical Sub System
PCB	Printed Circuit Board
PS	PowerSupply
RMAP	Remote Memory Access Protocol
ROE	Read Out Electronics
RX	Receive
S/C	SpaceCraft
SDS	Sample Delivery System
SHG	Second Harmonic Generation
SHS	Sample Handling System
SHTC	Sample Handling and Thermal Control

SNR	Signal-to-Noise Ratio
SPI	Serial Peripheral Interface
SpW	SpaceWire
TOF	Time-Of-Flight
TOF-MS	Time-Of-Flight Mass Spectrometer
TTL	Transistor-Transistor Logic
TVC	Thermal Vacuum Chamber
TX	Transmit
UART	Universal Asynchronous Receiver Transmitter
UV	UltraViolet
VIS	VISible
wt%	Weight-percent

B Regolith Simulant LHS-1 Datasheet

LHS-1 Lunar Highlands Simulant | **Fact Sheet**

002-01-001-0621

Simulant Name: LHS-1 Highlands Simulant
Simulant Type: General purpose
Reference Material: Average lunar highlands
Uncompressed Bulk Density: 1.30 g/cm^3
Mean Particle Size: 90 µm
Median Particle Size: 60 µm
Particle Size Range: <0.04 µm – 1000 µm

Geotechnical Properties

Grain Density: 2.75 g/cm^3
Void Ratio: 1.1
Porosity: 52.7%
[1]**Max Angle of Repose:** 47.5°
[2]**Cohesion:** 0.311 kPa
[2]**Angle of Internal Friction:** 31.49°

Geotechnical Property Sources

[1] (PDF) Comparing the Effects of Mineralogy and Particle Size Distribution on the Angle of Repose for Lunar Regolith Simulants (researchgate.net)

[2] 2038.PDF (usra.edu)

Mineralogy

As mixed.

Component	Wt.%
Anorthosite	74.4
Glass-rich basalt	24.7
Ilmenite	0.4
Pyroxene	0.3
Olivine	0.2

Safety

See SDS for details. Primary hazard is dust inhalation; wear a respirator in dusty conditions.

Bulk Chemistry

Relative abundances. Measured by XRF.

Oxide	Wt.%
SiO_2	51.2
TiO_2	0.6
Al_2O_3	26.6
FeO	2.7
MnO	0.1
MgO	1.6
CaO	12.8
Na_2O	2.9
K_2O	0.5
P_2O_5	0.1
LOI*	0.4
Total**	99.4

* Loss on ignition
** Excluding volatiles and trace elements

Photo credit Matthew Villegas. XRF data obtained by Hamilton Analytical Lab using fused bead sample preparation. Reflectance spectrum courtesy of Dr. Takahiro Hiroi, NASA RELAB, Brown University.

C SB1 Laser Controller Design

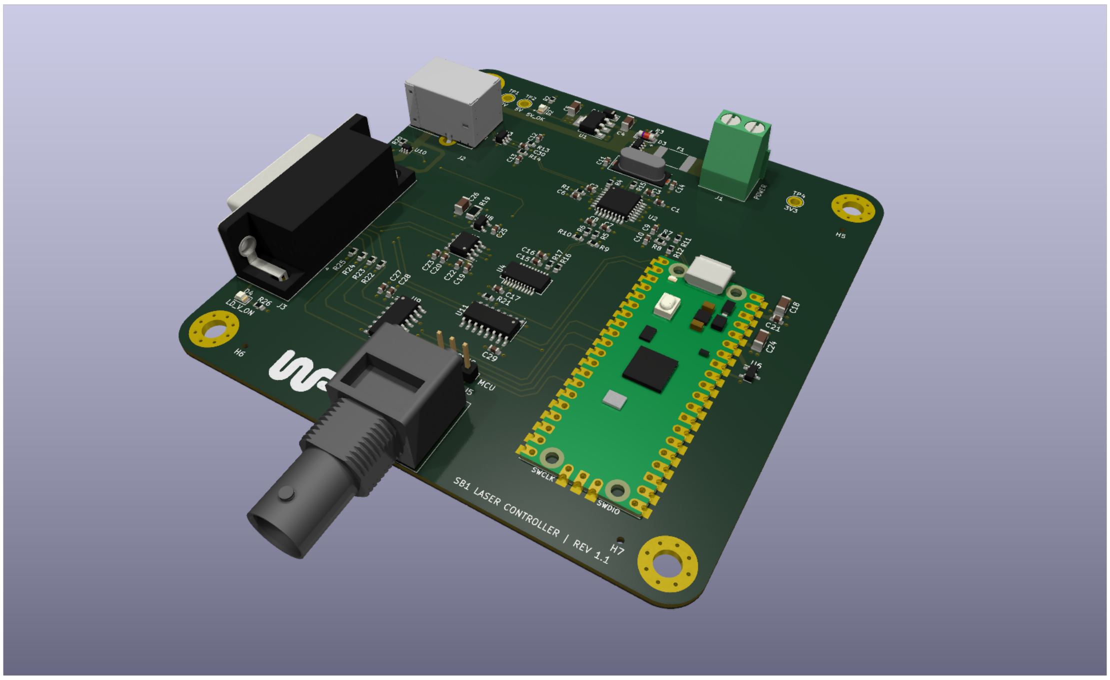

Figure C.1: 3D rendering of the designed SB1 controller board

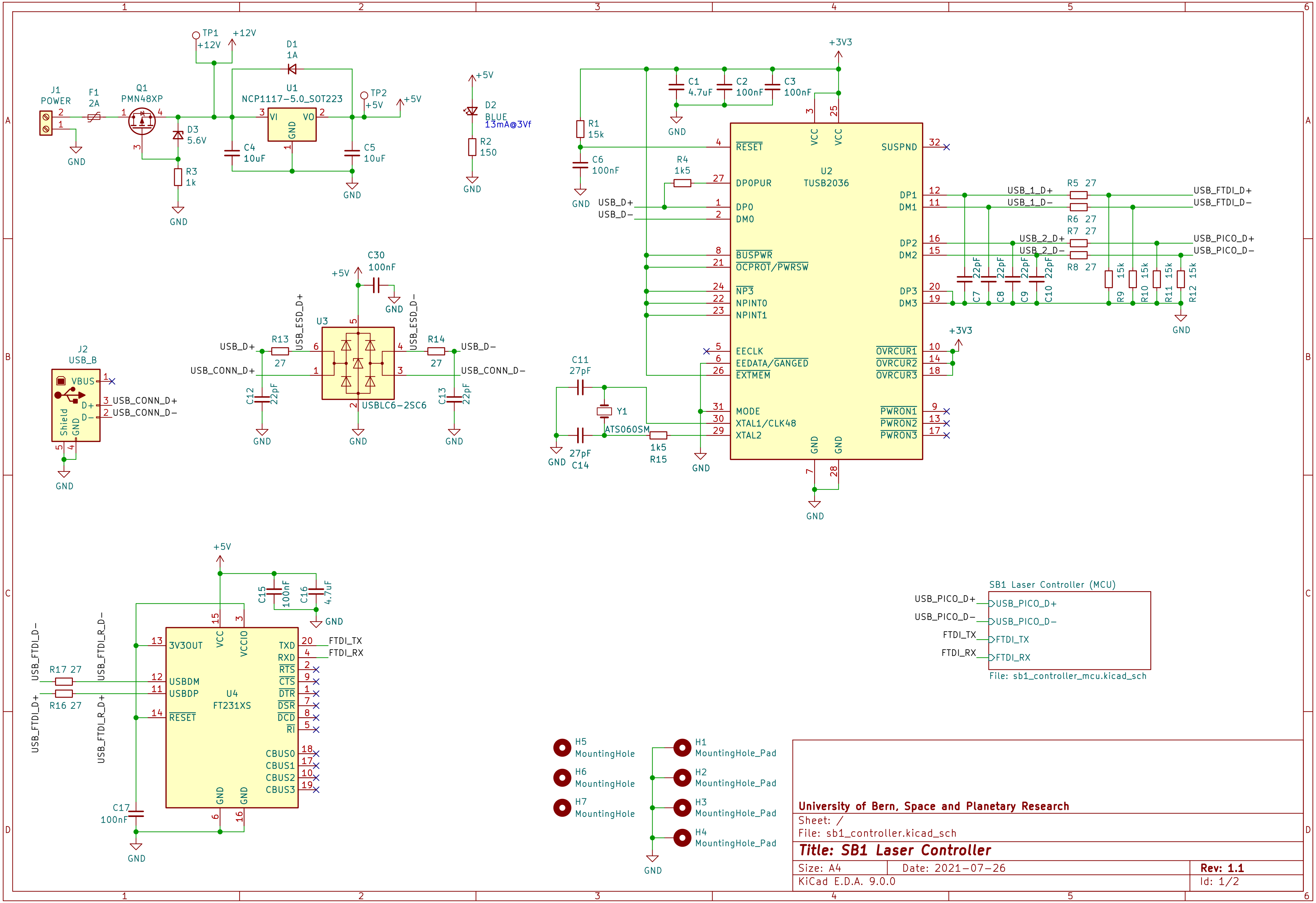

University of Bern, Space and Planetary Research
Sheet: /
File: sb1_controller.kicad_sch

Title: SB1 Laser Controller

Size: A4
Date: 2021-07-26
Rev: 1.1
KiCad E.D.A. 9.0.0
Id: 1/2

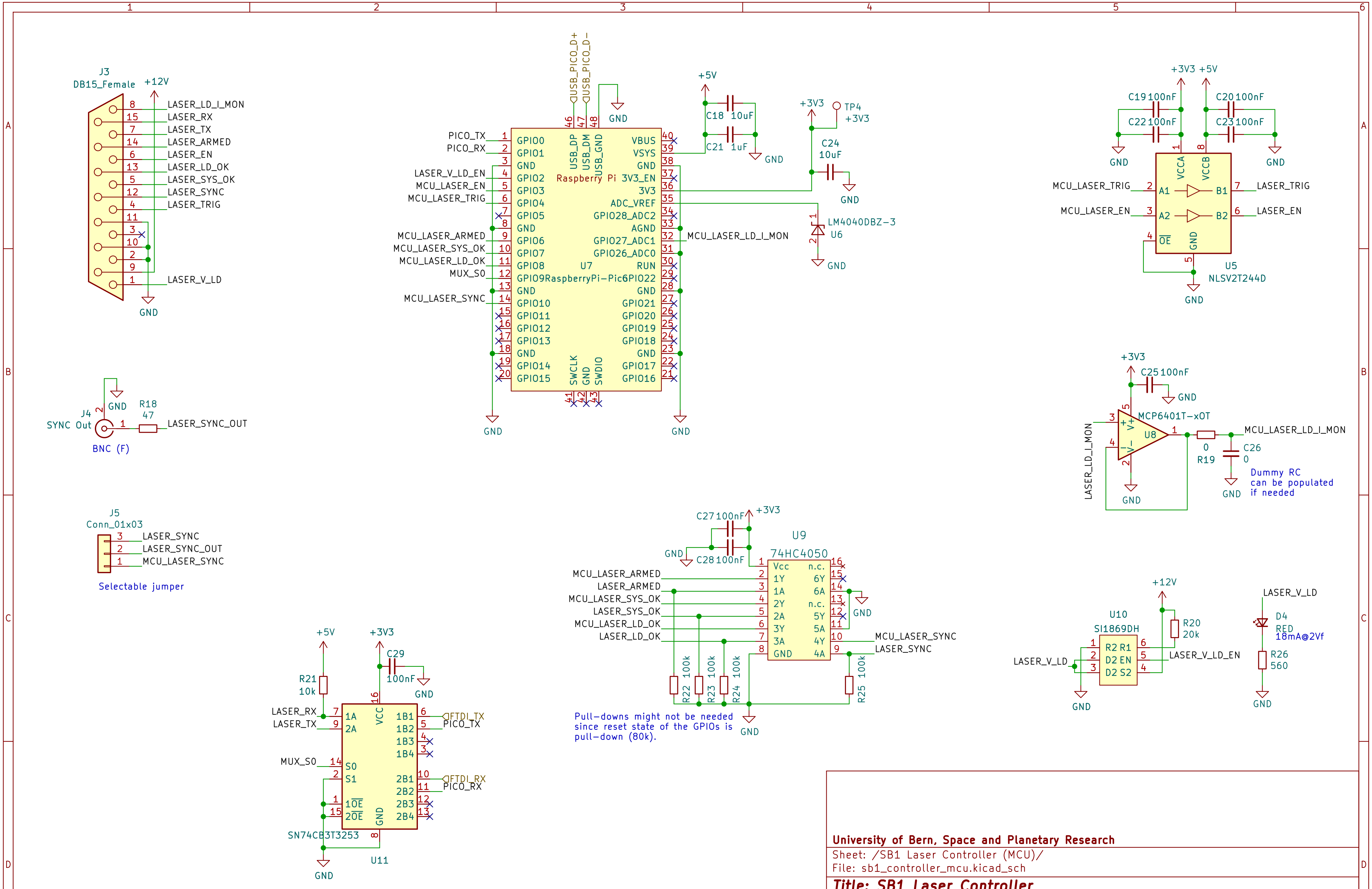

University of Bern, Space and Planetary Research

Sheet: /SB1 Laser Controller (MCU)/
File: sb1_controller_mcu.kicad_sch

Title: SB1 Laser Controller

Size: A4 | Date: 2021-07-26 | **Rev: 1.1**
KiCad E.D.A. 9.0.0 | Id: 2/2

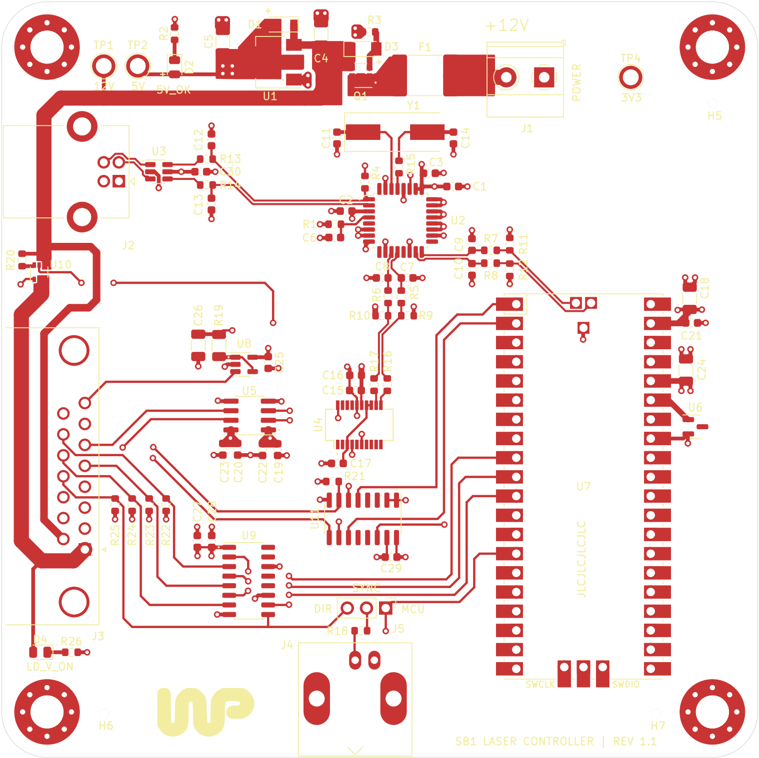

University of Bern, Space and Planetary Sciences

Sheet:

File: sb1_controller.kicad_pcb

Title: SB1 Laser Controller

Size: A4 | Date: 2021-07-26 | **Rev: 1**

KiCad E.D.A. 9.0.0 | Id: 1/4

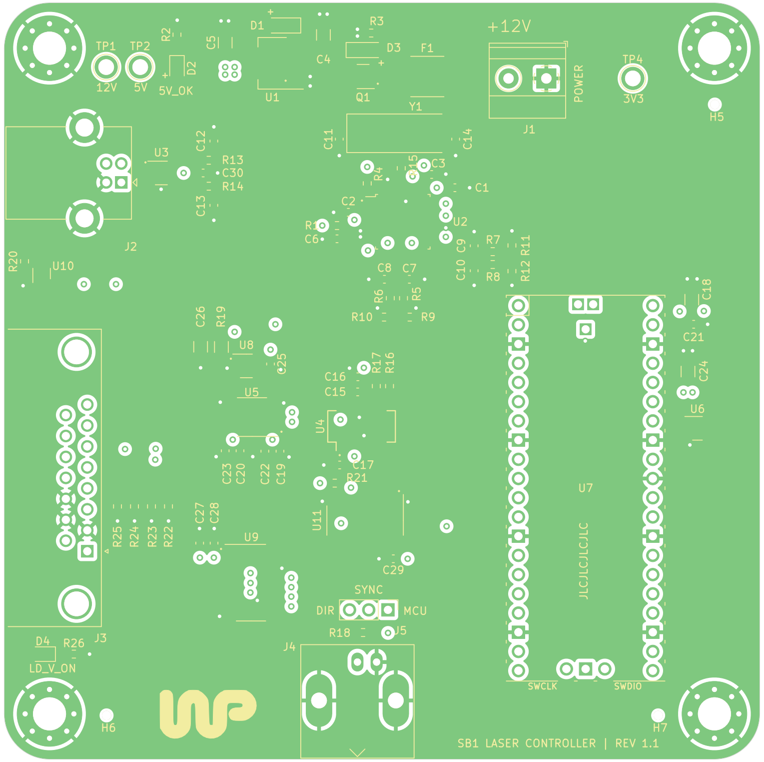

University of Bern, Space and Planetary Sciences
Sheet:
File: sb1_controller.kicad_pcb

Title: SB1 Laser Controller

Size: A4 | Date: 2021-07-26 | **Rev: 1**
KiCad E.D.A. 9.0.0 | Id: 2/4

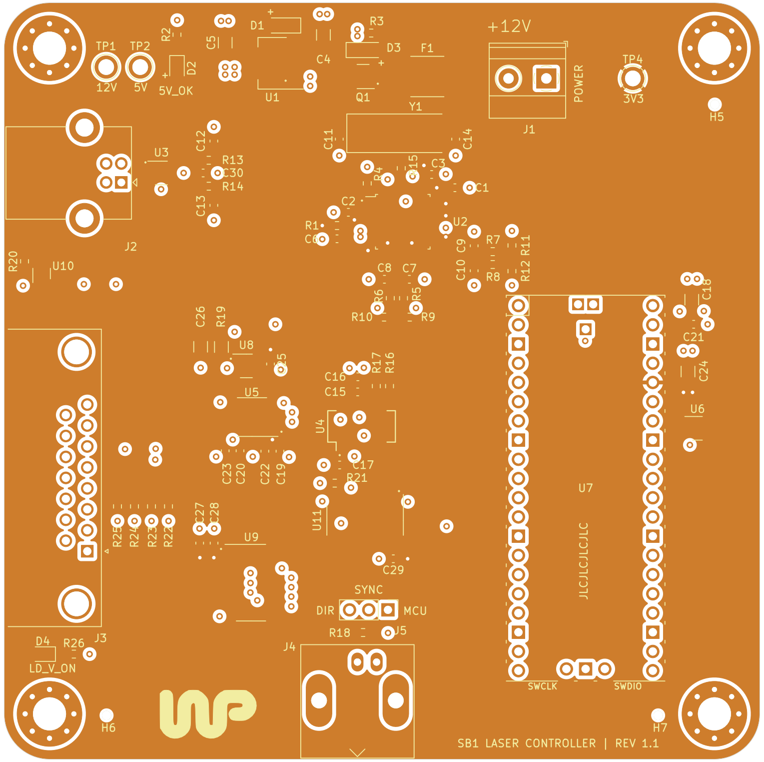

University of Bern, Space and Planetary Sciences
Sheet:
File: sb1_controller.kicad_pcb

Title: SB1 Laser Controller

Size: A4
Date: 2021-07-26
Rev: 1
KiCad E.D.A. 9.0.0
Id: 3/4

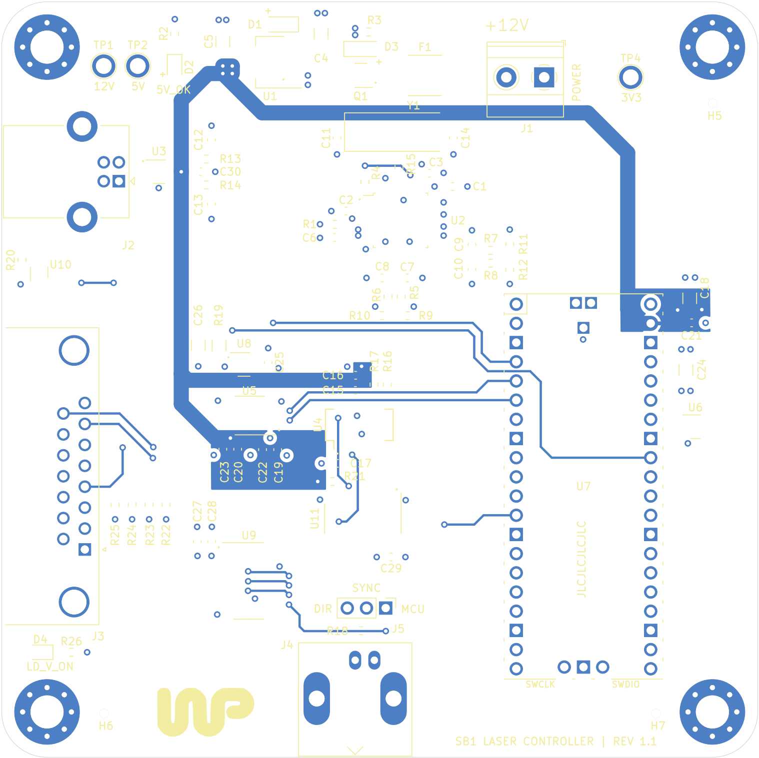

University of Bern, Space and Planetary Sciences

Sheet:
File: sb1_controller.kicad_pcb

Title: SB1 Laser Controller

Size: A4	Date: 2021-07-26	**Rev: 1**
KiCad E.D.A. 9.0.0		Id: 4/4

D List of Publications

Peer-reviewed Articles

[22] P. Keresztes Schmidt et al., “Design and testing of a sample handling system for operation on the lunar surface,” in 2025 IEEE Aerospace Conference, Big Sky, MT, USA: IEEE, Mar. 2025, submitted.

[21] A. Riedo, N. J. Boeren, P. Keresztes Schmidt, M. Tulej, and P. Wurz, “Life Detection Beyond Earth: Laser-Based Mass Spectrometry for Organics Detection on Solar System Objects,” Chimia, vol. 79, no. 1–2, pp. 70–76, Feb. 2025, doi: 10.2533/chimia.2025.70.

[20] Y. Sellam et al., “The search for ancient life on Mars using morphological and mass spectrometric analysis: an analog study in detecting microfossils in Messinian gypsum,” Front. Astron. Space Sci., vol. 12, p. 1503042, Feb. 2025, doi: 10.3389/fspas.2025.1503042.

[19] N. J. Boeren, P. Keresztes Schmidt, M. Tulej, P. Wurz, and A. Riedo, “ORIGIN: Laser Desorption Ionization Mass Spectrometry of Nucleobases for In Situ Space Exploration,” Planet. Sci. J., vol. 6, no. 2, p. 28, Feb. 2025, doi: 10.3847/PSJ/ad9de9.

[18] P. S. Garofalo et al., “Failed genesis of a Fe-skarn deposit caused by redox states of intrusion and wall rocks (Torre di Rio, Island of Elba, Italy),” Ore Geology Reviews, p. 106446, Jan. 2025, doi: 10.1016/j.oregeorev.2025.106446.

[17] A. Riedo et al., “Additive manufacturing in space research: hybrid mass analyser for laser ablation ionisation mass spectrometry,” J. Anal. At. Spectrom., p. 10.1039.D4JA00392F, 2025, doi: 10.1039/D4JA00392F.

[16] S. Gruchola, P. K. Schmidt, M. Tulej, A. Riedo, K. Mezger, and P. Wurz, “Autonomous Detection of Mineral Phases in a Rock Sample Using a Space-prototype LIMS Instrument and Unsupervised Machine Learning,” Planet. Sci. J., vol. 5, no. 12, p. 280, Dec. 2024, doi: 10.3847/PSJ/ad90b6.

[15] P. Keresztes Schmidt et al., “Sample handling concept for in-situ lunar regolith analysis by laser-based mass spectrometry,” in 2024 IEEE Aerospace Conference, Big Sky, MT, USA: IEEE, Mar. 2024, pp. 1–10. doi: 10.1109/AERO58975.2024.10521190.

[14] P. Wurz et al., “In Situ Lunar Regolith Analysis by Laser-Based Mass Spectrometry,” in 2023 IEEE Aerospace Conference, Big Sky, MT, USA: IEEE, Mar. 2023, pp. 1–10. doi: 10.1109/AERO55745.2023.10115714.

[13] P. S. Garofalo et al., “Fluid-rock interaction, skarn genesis, and hydrothermal alteration within an upper crustal fault zone (Island of Elba, Italy),” Ore Geology Reviews, vol. 154, p. 105348, Mar. 2023, doi: 10.1016/j.oregeorev.2023.105348.

[12] S. Gruchola et al., “Reduction of surface charging effects in laser ablation ionisation mass spectrometry through gold coating,” J. Anal. At. Spectrom., vol. 38, no. 7, pp. 1372–1378, 2023, doi: 10.1039/D3JA00078H.

[11] N. J. Boeren et al., “Detecting Lipids on Planetary Surfaces with Laser Desorption Ionization Mass Spectrometry,” Planet. Sci. J., vol. 3, no. 10, p. 241, Oct. 2022, doi: 10.3847/PSJ/ac94bf.

[10] M. Tulej et al., “Towards In-Situ Geochemical Analysis of Planetary Rocks and Soils by Laser Ablation/Ionisation Time-of-Flight Mass Spectrometry,” Universe, vol. 8, no. 8, p. 410, Aug. 2022, doi: 10.3390/universe8080410.

[9] N. F. W. Ligterink et al., “The ORIGIN Space Instrument for Detecting Biosignatures and Habitability Indicators on a Venus Life Finder Mission,” Aerospace, vol. 9, no. 6, p. 312, Jun. 2022, doi: 10.3390/aerospace9060312.

[8] L. Schwander et al., “Correlation Network Analysis for Amino Acid Identification in Soil Samples With the ORIGIN Space-Prototype Instrument,” Front. Astron. Space Sci., vol. 9, p. 909193, May 2022, doi: 10.3389/fspas.2022.909193.

[7] R. A. Lukmanov et al., “High Mass Resolution fs-LIMS Imaging and Manifold Learning Reveal Insight Into Chemical Diversity of the 1.88 Ga Gunflint Chert,” Front. Space Technol., vol. 3, p. 718943, May 2022, doi: 10.3389/frspt.2022.718943.

[6] P. Wurz et al., “Identifying biosignatures on Planetary Surfaces with Laser-based Mass Spectrometry,” in 2022 IEEE Aerospace Conference (AERO), Big Sky, MT, USA: IEEE, Mar. 2022, pp. 01–16. doi: 10.1109/AERO53065.2022.9843803.

[5] K. A. Kipfer et al., “Toward Detecting Polycyclic Aromatic Hydrocarbons on Planetary Objects with ORIGIN,” Planet. Sci. J., vol. 3, no. 2, p. 43, Feb. 2022, doi: 10.3847/PSJ/ac4e15.

[4] B. Marchesini et al., “Strain-induced trace element mobility in a quartz-sulphide vein system: An example from the ONKALO™ spent nuclear fuel repository (Olkiluoto, SW Finland),” Journal of Structural Geology, vol. 154, p. 104473, Jan. 2022, doi: 10.1016/j.jsg.2021.104473.

[3] M. Tulej et al., “Current Progress in Femtosecond Laser Ablation/Ionisation Time-of-Flight Mass Spectrometry,” Applied Sciences, vol. 11, no. 6, p. 2562, Mar. 2021, doi: 10.3390/app11062562.

[2] D. Rubatto et al., “Identification of growth mechanisms in metamorphic garnet by high-resolution trace element mapping with LA-ICP-TOFMS,” Contrib Mineral Petrol, vol. 175, no. 7, p. 61, Jul. 2020, doi: 10.1007/s00410-020-01700-5.

[1] C. Neff, P. Keresztes Schmidt, P. S. Garofalo, G. Schwarz, and D. Günther, “Capabilities of automated LA-ICP-TOFMS imaging of geological samples,” J. Anal. At. Spectrom., p. 10.1039.D0JA00238K, 2020, doi: 10.1039/D0JA00238K.

Columns

[1] P. Keresztes Schmidt, A. Riedo, and P. Wurz, “Back to the Moon - in situ Chemical Analysis on the Lunar Surface Using LIMS: Highlights of Analytical Sciences in Switzerland,” Chimia, vol. 76, no. 3, p. 257, Mar. 2022, doi: 10.2533/chimia.2022.257.

Conference Contributions

1. European Geosciences Union General Assembly, 14-19 April 2024, Vienna, Austria. Oral presentation, Title: In-situ sample handling and chemical analysis of lunar regolith by laser ablation ionisation mass spectrometry

2. European Geosciences Union General Assembly, 23-28 April 2023, Vienna, Austria. Oral presentation, Title: Instrumentation for laser ablation ionisation mass spectrometry on the lunar surface

3. European Winter Conference on Plasma Spectrochemistry, 29 January – 3 February 2023, Ljubljana, Slovenia, Poster presentation, Title: Laser ablation ionization mass spectrometry (LIMS) on the lunar surface

4. European Workshop on Laser Ablation, 12-15 July 2022, Bern, Switzerland. Poster presentation: Laser ablation/desorption mass spectrometry on the Moon

5. Swiss Chemical Society Fall Meeting, 10 September 2021, Virtual. Poster presentation, Title: Integration of a miniature microchip laser system into a laser desorption/ablation ionization mass spectrometer built for space applications

6. CHanalysis, 11-12 April 2019, Beatenberg, Switzerland. Poster presentation, Title: A Versatile Software Suite for Advanced Laser Ablation ICP-MS Element Imaging

Erklärung

gemäss Art. 18 PromR Phil.-nat. 2019

Name/Vorname: Keresztes Schmidt, Peter

Matrikelnummer: 14-941-108

Studiengang: Physik

Bachelor ☐ Master ☐ Dissertation ☑

Titel der Arbeit: Development of a Laser Ionisation Mass Spectrometer for in-situ investigations on the lunar surface

LeiterIn der Arbeit: Prof. Dr. Peter Wurz

Ich erkläre hiermit, dass ich diese Arbeit selbständig verfasst und keine anderen als die angegebenen Quellen benutzt habe. Alle Stellen, die wörtlich oder sinngemäss aus Quellen entnommen wurden, habe ich als solche gekennzeichnet. Mir ist bekannt, dass andernfalls der Senat gemäss Artikel 36 Absatz 1 Buchstabe r des Gesetzes über die Universität vom 5. September 1996 und Artikel 69 des Universitätsstatuts vom 7. Juni 2011 zum Entzug des Doktortitels berechtigt ist. Für die Zwecke der Begutachtung und der Überprüfung der Einhaltung der Selbständigkeitserklärung bzw. der Reglemente betreffend Plagiate erteile ich der Universität Bern das Recht, die dazu erforderlichen Personendaten zu bearbeiten und Nutzungshandlungen vorzunehmen, insbesondere die Doktorarbeit zu vervielfältigen und dauerhaft in einer Datenbank zu speichern sowie diese zur Überprüfung von Arbeiten Dritter zu verwenden oder hierzu zur Verfügung zu stellen.

Bern, 18.03.2025

Ort/Datum

Unterschrift